Study of carbonation in novel lime based materials

Pesce, Gianluca

Award date:
2014

Awarding institution:
University of Bath

Study of Carbonation

in

Novel Lime Based Materials

A thesis submitted by

Giovanni L. Pesce

for the degree of Doctor of Philosophy

University of Bath

Department of Architecture and Civil Engineering

March 2014

This thesis is dedicated to the memory of Prof. Tiziano Mannoni
in recognition of all he taught me.

1928 – 2010

Acknowledgements

Firstly I would like to thank Dr. Richard J. Ball, my supervisor, for his support and encouragement. He has provided me a large number of opportunities throughout this research project and for all these possibilities I am extremely grateful to him.

I would also like to thank my other supervisors: Prof. Peter Walker and Prof. Chris Bowen. I have always found them available for a discussion every time I needed, even at short notice. Dr. Guy Denuault and Ms. Mara Serrapede of the University of Southampton allowed me to work in a very pleasant environment every time I visited them for carrying out our tests on the pH measurements. I will always remember the time spent with them in setting up the system and the discussions we had until late in the evening.

Among the other members of the academic staff I would like to thank Prof. Geoffrey Allen of the University of Bristol for his guidance in this research and for the really pleasant scientific and non-scientific discussions. Professor Joao Rocha of the University of Aveiro (Portugal), Prof. Rajnish Kurchania of the Maulana Aznad National Institute of Technology (India), Prof. Khare Mukesh and Prof. Suresh Bhalla of the Indian Institute of Technology of Delhi (India) have always been very kind with me and have always found the time to discuss the results of my tests when I visited them in their respective laboratories.

Mr. David Odgers of Odgers Conservation Ltd. and Ms. Alison Henry of English Heritage have been very supportive partners during my research on nano-lime.

Among the staff of the Department of Architecture and Civil Engineering I would like to thank Mr. Graham Mott, Sophie, Neil, Will, Walter and David Montoya. Mr. Fernando Acosta of the Department of Chemical Engineering and Ms. Claire Ball of the Department of Mechanical Engineering have always been very kind and helpful. Dr. John Mitchels of the Microscopy and Analysis Suite spent a lot of time in teaching me the secret art of atomic force microscopy. For his patience and his passion I would like to thank him.

There are also other people that I do not have space to mention here but I would like

to let them know that all of them taught me something. Among them I would like to mention my “old” office mates: Dr. Hector Archila Santos, Dr. Tom Reynolds and Dr. Junzhe Wang (in rigorous alphabetic order!). For your friendship and your kindness I would really like to thank you.

To my parents I just want to say that I do not think I will ever be able to describe how much you have helped me. You have supported me in everything and taught me how to live a simple but respectable life. This work and all I achieved so far is dedicated to you. Elisabetta, my girlfriend, deserves a special thank you for having supported me in all moments of my “second” life as PhD student.

This research was funded by the Engineering and Physical Sciences Research Council, the main UK government agency for funding research and training in engineering and the physical sciences. A thank is due also to this institution. Thanks go to my industrial sponsors: Singleton Birch Ltd. and Ty Mawr Lime Ltd. that provided some of the materials needed to carry out the work. The the UK India Education and Research Initiative (UKIERI), an initiative that aims to enhance educational links between India and the UK, has provided me the chance to carry out research at the Indian Institute of Technology of Delhi (India) and at the Maulana Aznad National Institute of Technology (Bhopal, India). For this opportunity: thanks.

Abstract

This research advances the current understanding of the carbonation reaction in porous materials by investigating pH changes during the hardening process of lime, the role of pore-water in the dissolution process of calcium hydroxide and the effects of pore size on precipitation of calcium carbonate solid phases.

To achieve this, carbonation is studied within a thin film of an aqueous solution of calcium hydroxide, that simulates the conditions existing in porous media once most of the liquid water has evaporated. The research introduces novel approaches such as the use of specially manufactured micro-electrodes used to measure pH variations during the carbonation process. The effect of pore size on the solid phases precipitated by carbonation is investigated using a novel lime based material called *nano-lime*. Influence of pore-water on the hardening process of lime is studied in formulated lime using impedance spectroscopy: an electrochemical technique which is new in the study of lime based materials.

Overall, results demonstrate that the micro-electrodes can operate reliably in very alkaline environments such as those produced by the dissolution of lime. Their potentiometric response, in fact, was found to be Nernstian up to pH 14. Furthermore, the electrode response proved to be sufficiently sensitive and reproducible to differentiate, on the basis of pH, between the formation of calcite and vaterite. It is likely that these micro-electrodes are currently the only analytical tools capable of monitoring high pHs in confined places and, for this reason, they can be considered highly valuable for the study of chemical processes involving very alkaline waters. The study on the role of pore-water in the hardening process of formulated lime has, instead, demonstrated the potential of impedance spectroscopy as a non-destructive technique for real time *in situ* monitoring of the reaction between lime and hydraulic additives.

Publications

Some ideas and figures contained in this thesis have appeared previously in the following publications:

Papers in peer reviewed journals

- Serrapede, M., Denuault, G., Sosna M., Pesce, G., Ball R.J., 2013. Scanning electrochemical microscopy: using the potentiometric mode of SECM to study the mixed potential arising from two independent redox processes. Analytical Chemistry, 85(17), pp.8341-8346

- Pesce, G.L., Micheletto, E., Quarta, G., Uggè, S., Calcagnile, L., Decri, A., 2013. Radiocarbon dating of mortars from the baptismal font of the S. Lorenzo cathedral of Alba (Cuneo, Italy). Comparison with the thermoluminescence dating of related bricks and pipes. Radiocarbon, 55(3-4), pp.526-533

- Pesce, G.L., Morgan, D., Odgers, D., Henry, A., Allen, M., Ball, R.J., 2013. Consolidation of weathered limestone using nanolime. In: Proceedings of the Institution of Civil Engineers. Construction Materials 166 (4), pp.213-228

- Pesce, G.L., Ball, R.J., Quarta, G. and Calcagnile, L., 2012. Identification, extraction and preparation of reliable lime sample for the C14 dating of plasters and mortars with the method of “pure lime lumps”. Radiocarbon, 54(3-4), pp. 933-942

- Pesce, G.L.A., Ball, R.J., Bowen, C. R., Walker, P. and Allen, G.C., 2012. Characterization of lime/metakaolin paste using Impedance Spectroscopy. Key Engineering Materials, 517, pp.487-494

Papers in non peer-reviewed journals

- Raw-Rees, S., Pesce, G.L., Ball, R.J. and Fodde, E., 2012. Characterization of binders in the historic mortars and plasters from 1A Royal Crescent, Bath. The Journal of Building Limes Forum, 19, pp.28-37

Book chapters

- Pesce, G.L.A., Ball, R.J., 2012. Dating of Old Lime Based Mixtures with the "Pure Lime Lumps" Technique. In: D. Michalska Nawrocka, ed. 2012. Radiometric Dating, InTech, ISBN: 978-953-51-0596-1. Ch.2

Papers in conference proceedings

- Vecchiattini, R., Pesce, G.L., Quarta, G., Calcagnile, L., 2013. Sampling problems in the radiocarbon dating of old mortars and plasters with the "pure lime lumps" technique. In: Gabaglio, R. and Gulotta, D., eds. Built Heritage 2013. Monitoring Conservation and Management. Milan, Italy 18-20 November 2013. Milan (Italy):Politecnico di Milano

- Pesce, G. L., Ball, R. J., Bowen, C. R., Kurchania, R. and Bhalla, S., 2012. Monitoring hydration in lime - metakaolin composites. In: Ferreira, V. M., Dias, A. B., Afonso, A. S. and de Brito, J., eds. Congress of Innovation on Sustainable Construction (CINCOS'12). Aveiro, Portugal 20-22 September 2012. Aveiro (Portugal):University of Aveiro

- Pesce, G. L., Ball, R. J., Bowen, C. R., Kurchania, R. and Bhalla, S., 2012. Monitoring hydration in lime - metakaolin composites. In: Russell, M., ed. 32nd Cement & Concrete Science Conference. Belfast, United Kingdom 17-18 September 2012. Belfast:Queens University

- Vecchiattini, R. and Pesce, G.L.A., 2012. A Study on the Traditional Production of Lime: The Role of Oral Surces. In: Carvais, R., Guillerme, A., Nègre, V., Sakarovitch, J., eds. Proceedings of the 4th International Conference on Construction Industry – Nuts & Bolts of Construction History. Culture, Technology and Society, Paris, France 3-7 July 2012. Paris:Picard

- Pesce, G.L.A. and Vecchiattini, R., 2011. Technical regulations: limitations or resource? The case of building limes. In: Martines, R. and Biscontin, G., eds. Proceedings of the 27th International Conference on Science and Cultural Heritage. Bressanone, Italy 21–24 June 2011. Padua (Italy):Edizioni Arcadia Ricerche.

Contents

List of Figures

List of Tables

List of Algorithms

Abbreviations

Several acronyms and abbreviations have been used in this text. They have all been defined with their first instance of use but thereafter are referred to only in the abbreviated form. For reference, a list of the most commonly used acronyms and abbreviations is provided below.

Acronyms and definitions used in the lime market[1]

ACRONYM	FULL NAME	DEFINITION
CL	Calcium Lime	Calcium lime is an air lime consisting mainly of calcium oxide and/or calcium hydroxide without any hydraulic or pozzolanic addition
DL	Dolomitic Lime	Dolomitic lime is an air lime consisting mainly of calcium magnesium oxide and/or calcium magnesium hydroxide without any hydraulic or pozzolanic addition
FL	Formulated Lime	Formulated lime is a lime with hydraulic properties mainly consisting of air lime (CL) and/or natural hydraulic lime (NHL; see below) with added hydraulic and/or pozzolanic material. It has the property of setting and hardening when mixed with water and by reaction with carbon dioxide from the air (carbonation).
HL	Hydraulic Lime	Hydraulic lime is a binder consisting of lime and other materials such as cement, blast furnace slag, fly ash, limestone filler and other suitable materials. It has the property of setting and hardening under water. Atmospheric carbon dioxide contributes to the hardening process.
NHL	Natural Hydraulic Lime	Natural hydraulic lime is a lime with hydraulic properties produced by burning of more or less argillaceous or siliceous limestones (including chalk) with reduction to powder by slaking with or without grinding. It has the property of setting and hardening when mixed with water and by reaction with carbon dioxide from the air (carbonation).

[1] According to the BS EN 459-1, 2010

Main chemical species and compounds cited in the text

IUPAC NAME[2]	EMPIRICAL FORMULA	STATE OF MATTER[3]	CRYSTALLINE FORMS[4]	CRYSTAL SYSTEM AND CLASS NAME[5]	HARDNESS[6]	SOLUBILITY[7]
Calcium ion	Ca^{2+}	aq	-	-	-	exist only in solution
Calcium carbonate	$CaCO_3$	s	Calcite	System: Tr Class: Hex Sca or Rh	3	$0.00066^{(20)}$
			Aragonite	System: Or Class: Dipy	3.5	$0.00066^{(20)}$
			Vaterite	System: Hex Class: Dihe Dipy	3	$0.0011^{(25)}$
Calcium carbonate monohydrate	$CaCO_3 \bullet H_2O$	s	Monohydrocalcite	System: Tr Class: Tra	2-3	7.212[8]
Calcium carbonate hexahydrate	$CaCO_3 \bullet 6H_2O$	s	Ikaite	System: Mon Class: 2m	-	7.461[9]
Amorphous calcium carbonate	-	s	ACC	-	-	6.393[10]
Calcium hydroxide	$Ca(OH)_2$	s	Portlandite	System: Tr Class: Hex Sca	2.5-3	$0.160^{(20)}$
Carbonate ion	CO_3^{2-}	aq	-	-	-	exist only in solution
Carbon dioxide	CO_2	aq	-	-	-	-
Hydrogen ion	H^+	aq	-	-	-	exist only in solution
Hydrogen carbonate ion	HCO_3^-	aq	-	-	-	exist only in solution
Carbonic acid	H_2CO_3	aq	-	-	-	exist only in solution
Water	H_2O	l	-	-	0	-
Monosilicic or Orthosilicic acid	H_4SiO_4	aq	-	-	-	exist only in solution

[2] International Union of Pure and Applied Chemistry

[3] s = solid; g = gas; l = liquid; aq = aqueous solution

[4] Only the most common crystalline form of silica dioxide is listed. Silicon dioxide can also be found in amorphous state.

[5] System: Tr = trigonal; Or = orthorhombic; Hex = exagonal; Mon = monoclinic. Class: Hex sca = Hexagonal Scalenohedral; Rh = Rhomboedral; Dipy = Dipyramidal; Dihe Dipy: Dihexagonal Dipyramidal; Tra = Trapezohedral

[6] Hardness is measured by the resistance that a smooth surface offers to abrasion. The degree of hardness is determined by observing the comparative ease or difficulty which which one mineral is scratched by another. Numbers refer to the Mohs' relative hardness scale (Chemical Rubber Company, 2013-2014, 12-255)

[7] Aqueous solubility is expressed as the number og grams of the compound (excluding any water of hydration) that will dissolve in 100 grams of water. The temperature in ℃ is given as a superscript. From: Chemical Rubber Company, 2013-2014

[8] $-\log K_s^0$ at 25℃ from Brecevic and Kralj, 2007

[9] $-\log K_s^0$ at 25℃ from Brecevic and Kralj, 2007

[10] $-\log K_s^0$ at 25℃ from Brecevic and Kralj, 2007

Magnesium ion	Mg^{2+}	aq	-	-	-	exist only in solution
Magnesium carbonate	$MgCO_3$	s	Magnesite	System: Tr Class: Hex Sca	4	$0.18^{(20)}$
Magnesium hydroxide	$Mg(OH)_2$	s	Brucite	System: Tr Class: Hex Sca	2.5-3	$0.00069^{(20)}$
Hydroxide ion	OH^-	aq	-	-	-	exist only in solution
Silica dioxide	SiO_2	s	α-quartz	System:Tr Class: Tra	7	-

Abbreviated formulas according to the cement chemistry notation

ABBREVIATION	ACTUAL FORMULA	NAME	MINERAL PHASE
C	CaO	Calcium oxide or 'quick lime'	-
S	SiO_2	Silicon dioxide or silica	-
A	Al_2O_3	Aluminium oxide or Alumina	-
F	Fe_2O_3	Ion(III) oxide	-
H	H_2O	Water	-
$\overline{C}$ OR C	CO_2	Carbon dioxide	-
CSH gel (or C-S-H)	$(CaO)_x$•SiO_2•$(H_2O)_y$[11]	Calcium silicate hydrate	-
CSH(I)	$Ca_9(Si_6O_{18})(OH)_6$•$8H_2O$	Calcium silicate hydrate type 1	Poorly crystallized tobermorite-like
CSH(II)	$Ca_5Si_6O_{16}(OH)_2$•$8H_2O$	Calcium silicate hydrate type 2	Poorly crystallized jennite-like
C_2S	$2CaO$•SiO_2 *or* $Ca_2Si_2O_4$	Di-calcium silicate	Belite
C_2ASH_8	$Ca_2Al[(OH)_6AlSiO_2 - 3(OH)_{4-3}]$•$2,5(H_2O)$		Stratlingite or gehlenite hydrate
C_3A	$3CaO$•Al_2O_3 *or* $Ca_3Al_2O_6$	Tricalcium aluminate	-
C_3AS_3	$Ca_3Al_2(SiO_4)_3 - x(OH)4x$	Katoite	Hydrogrossular
C_3FH_6	$3CaO$•Fe_2O_3•$6H_2O$	hydrated calcium ferrite	Hydrogarnet
C_3FS_3	$3CaO$•Fe_2O_3•$3SiO_2$	-	Hydrogarnet
C_3S	$3CaO$•SiO_2 *or* Ca_3SiO_5	Tri-calcium silicate or Alite[12]	-
C_3AH_6	$3CaO$•Al_2O_3•$6H_2O$ *or* $Ca_3[Al(OH)_6]_2$	Katoite	Hydrogarnet
C_3ASH_6	-	-	Hydrogarnet
C_4AF	$4CaO$•Al_2O_3•Fe_2O_3 *or* $Ca_4(Al,Fe)_2O_{10}$	Tetra-calcium aluminate	Calcium aluminumferrite or Ferrite
C_4AcH_{11}	C_3A•$CaCO_3$•xH_2O[13]	Carboaluminate or Hydrated calcium carboaluminate	-
C_4AH_{13}	$4CaO$•Al_2O_3•$13H_2O$	Tetra calcium aluminate hydrate	Hydrogarnet
C_4AH_{19}	-	-	-
C_2AS	$2CaO$•Al_2O_3•SiO_2 *or* $Ca_2Al[AlSiO_7]$	Gehlenite	-

[11] x and y values may vary over a wide range (Hewlett, 2004, pp.243, 249).

[12] Alite is not a recognized mineral name

[13] x may vary between 1.5 and 3

1. Introduction

1.1. Lime and carbonation in the construction industry

Within the construction industry, the term *lime* has been used for centuries to describe a broad group of inorganic binders mainly composed of calcium oxides and/or hydroxides.

A more precise description of lime uses two classifications, air and hydraulic, to provide a better definition of these binders. Some limes harden only by reaction with air (hence the name *air lime)* whereas others harden by reaction with both, air and water (hence the name *hydraulic lime* is used).

The nomenclature highlights the fact that, despite the same general name, there are quite important chemical differences among limes. These originate from the difference in chemical composition of the stones used for lime production.

Traditional lime is produced by thermal treatment (heating) of more or less pure carbonate rocks in special kilns (figures 1.1 and 1.2). When a highly pure carbonate rock is used, the product of the thermal treatment is almost entirely calcium oxide. This compound reacts exothermically with water, forming calcium hydroxide known as air lime. When mixed with sand for use as a binder in construction, calcium hydroxide (i.e. the lime) reacts with atmospheric carbon dioxide and water vapor forming calcium carbonate that allows the lime to harden through a chemical process known as *carbonation*.

In contrast, when carbonate rocks containing relatively small amounts of impurities such as silica or clay are used in lime production other compounds such as belite can form inside the kilns by chemical reaction between calcium oxide and silica or alumina. These new compounds react with water to form new products that allow the lime to harden through a process called *hydration*. This material is known as hydraulic lime. Together with these compounds, however, in all hydraulic limes a certain amount of free calcium oxide (i.e. not bonded with silicate or aluminate) is present, providing a set by carbonation. This results in the double setting of this type of lime.

Air limes are currently sold in the form of dry powder (hydrated lime) or as a wet paste called lime putty (figure 1.3); historically, the latter was the only form available,

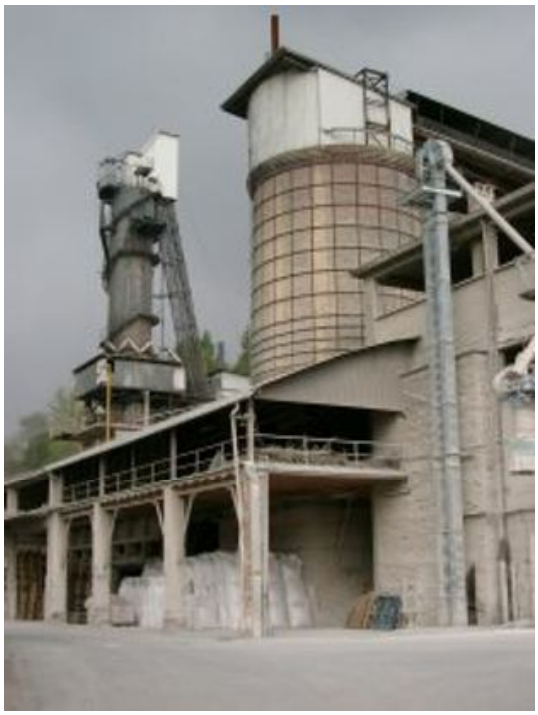

Figure 1.1.: Modern lime kiln at Piasco (Cuneo, northern Italy)

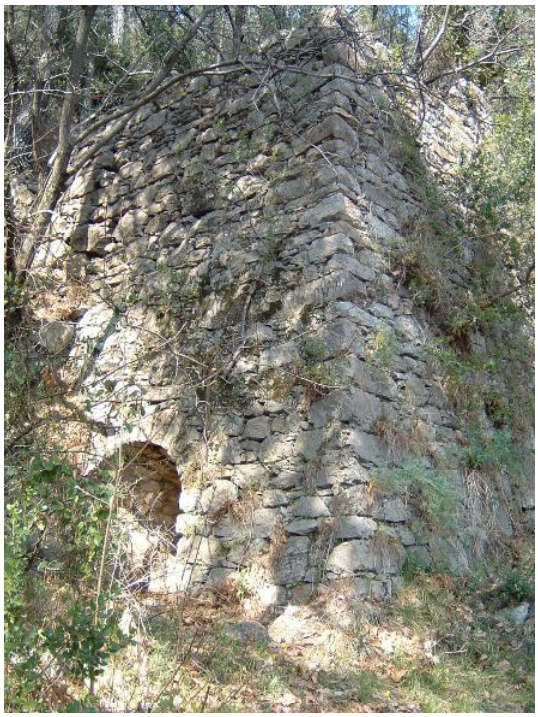

Figure 1.2.: Old lime kiln at Castiglione Chiavarese (Genoa, northern Italy)

Figure 1.3.: Lime putty (Piasco - Cuneo, northern Italy)

apart from quicklime (calcium oxide). Air lime is mainly used for plasters and renders because of the characteristics of the reaction that leads to hardening. Since it needs to be in contact with the air, mortars made with air lime cannot, in fact, be applied in layers of more than about 3 centimeters thickness, and this can be a problem in those cases where a more massive use of lime is required. Furthermore, the hardening process of air lime is associated with a quite significant mortar shrinkage that has to be controlled by choosing the right particle size distribution of sand. Despite these limitations, however, characteristics of mortars produced with these limes, such as breathability and elasticity, are unrivalled compared to the mortars that can be produced with hydraulic limes or cement.

Hydraulic limes, on the other hand, are sold in the form of dry powders where the calcium oxide is already converted to hydroxide by the addition of the minimum amount of water needed for this reaction, taking advantage of the high reactivity of this compound. Current European regulation EN 459-1 (published in 2010 and acquired by each EU member) classifies the hydraulic lime in three groups, depending on the content of hydraulic compounds. These products are preferred to air lime in the modern construction industry because mortars produced with these binders can be applied in various thicknesses, set more quickly (which reduces time on site) and almost no shrinkage. Characteristics of mortars prepared with hydraulic lime, such as elasticity and breathability, are lower than in mortars containing air lime but higher than in mortars made with cement.

Lime has been used for centuries for construction. In the area that includes Europe, Middle East and north Africa, lime is one of the oldest inorganic binders, after clay and gypsum. The oldest artifact containing lime found within this region is, in fact, a floor dated to 7000 B.C. that was unearthed in 1985 at Yaftah in Galilee (Israel; Rattazzi, 2007).

Over the centuries, this material was used by cultures such as Phoenicia, Egypt and Greece but was with the Romans that lime technology reached its maximum. With

the Romans, in fact, lime was used to build structures that are considered among the most remarkable buildings in the world such as the Pantheon. Built in 27 B.C. with a circular plan and a diameter of 43 meters, the dome that covers this temple remained the biggest cupola ever built until the 20th century and is still now the largest dome in the world made with un-reinforced concrete (Rattazzi, 2007).

After the fall of the Roman empire, during the late antiquity and the early middle age, the knowledge related to the use of lime was partially forgotten but in the late middle age a new renewed interest toward the lime came as a result of the rediscovery of old treatises such as the Vitruvius' *De Architecture*, written at the end of the 1st century B.C.

During the Renaissance, lime was widely used and new treatises were published such as *The Four Books of Architecture*, written by Palladio[1], describing lime technology from the firing process of carbonate rocks to the production of plasters and renders.

In the 18th century French architects and scientists laid the foundations of a renewed interest in this binder and, in particular, in the production and use of hydraulic limes. Work carried out by researchers such as De la Faye, Loriot and Rondelet allowed the rediscovery of the qualities of limes produced by the Romans and contributed to the development of the first scientific knowledge related to this material.

Thanks to this research, starting from the mid 18th century, a new inorganic binder destined to replace the lime was developed: cement (Rattazzi, 2007).

Since the very beginning of its development, characteristics of this product obscured those of lime which, as a results, fell into a new *dark age*. Lime was considered a product of old societies and the Age of Enlightenment, that emphasized reason over tradition, had already begun and needed new materials. It was probably also for this reason that the lime market started to reduce, almost to complete annulment (Torraca G., *Preface* in Rattazzi, 2007).

In the meantime, the cement industry developed new products such as Portland cement, which was characterized by higher strength and speed of set. Cement was easier to use than lime and proved to have superior mechanical properties which allowed construction of more and more ambitious buildings (in particular when used in conjunction with steel bars in reinforced concrete).

Starting from the beginning of the 20th century, however, some peculiar characteristics of cement mortars began to induce a more critical evaluation of the use of this material. One of the main problems was the compatibility with old structures built using lime mortars. Characteristics such as high stiffness and low breathability were in clear contrast with the corresponding characteristics of old mortars and this induced restorers and architects to look back to lime. Since then, lime has found a new dimension

[1] A detailed review of the descriptions of lime in treatise from 15th to 19th century is contained in: Arcolao, 1998.

which has led to a wider market.

Lime is of current interest not only because of its compatibility with old products but also because of its low-carbon footprint compared to other materials. At the very end of the last millennium, in fact, sequestration of carbon dioxide was identified as an important initiative for reducing climate change. Since then, several protocols such as the Kyoto agreement (1997) have been signed by the United Kingdom and many other countries for their commitment to the reduction of carbon dioxide emissions. Following these agreements, lime was identified as one of the key materials for substitution of cement (whose production introduces a very high amount of carbon dioxide in the atmosphere and, therefore, should be reduced or modified) because it has the ability to adsorb significantly high quantities of carbon dioxide during setting.

As a consequence of this renewed interest, lime production in United Kingdom, after the fall in the last decade caused by the economic downturn, since 2009 has seen a new increase, in which its export has grown by 76%. In 2012 more than 250,000 tonnes of lime produced in the United Kingdom were exported to areas such as South East Asia, Africa and Europe (British Lime Association, 2013).

Despite this growth, however, lime production still represents only a small market compared to cement. For instance, in 2006 (before the economic crisis) lime production in the United kingdom was about 1,600,000 tonnes per year (British Lime Association, 2013) whereas cement production was about 11,000,000 tonnes per year (Brown et al., 2008): almost 7 times more than lime.

Furthermore, lime production is mainly targeted at uses other than the construction industry, such as the iron and steel industry, environmental protection, agriculture and chemical industry. When employed in construction, lime is mainly used as a soil stabilizer for roads, in the foundations of new buildings, for stabilizing earthen dams and, a minor amount, for mortars and plasters[2].

It is probably for this reason that, to date, little funding has been invested in research on the development of lime for mortars and plasters and that several aspects of its hardening process still have to be investigated.

Research is needed if lime is to be more widely used and employed for more high-value uses than those currently described in the European standards. Research is needed, for instance, to demonstrate that new technical regulations should be developed to provide more precise rules on the use of lime in the construction industry than those contained in the European standards (e.g. uni-axial compressive tests on lime sample cannot be carried out with same rules used for cement since the two materials have completely different characteristics; Torraca G., *Preface* in Rattazzi, 2007).

[2]Information from the National Lime Association web site, available at URL: http://www.lime.org/uses_of_lime/construction/construction.asp.

Overall, this discussion shows that carbonation is an important chemical process of relevance to several construction materials that have been used for centuries. Carbonation is one of the main reactions in lime based building materials and is of current interest for the construction industry because of the ability to sequestrate carbon dioxide. Despite this importance, however, and because of the lack of research, the mechanism and the different variables that affect this reaction have not yet been completely understood.

Studies on carbonation have been carried out since the end of 18^{th} century, when Josef Black (1728-1799), Professor of anatomy and chemistry at the University of Glasgow (Scotland), for the first time isolated and identified the carbon dioxide that he called *fixed air*. He found that when limestone is heated or treated with acids, it produces a gas that he termed as *fixed air*. He, then, observed that the quicklime slaked with water reabsorbs the fixed air, producing the same initial compound: calcium carbonate (Rattazzi, 2007). These results stimulated new research such as that carried out by Bryan Higgins (1741-1818) that confirmed Black's observation and hypothesised that a similar phenomenon was responsible for the reduced reactivity of quicklime when left in contact with humid air for some time (Rattazzi, 2007).

Since then, several books and scientific papers have been written about the carbonation process showing that, although lime production is considered one of the simplest pyrotechnological processes (Mannoni and Giannichedda, 2003), several aspects of this material still have to be fully understood.

1.2. Objective of this thesis and the need for research

In this research, carbonation is studied within a thin film of water, in order to simulate the conditions existing in a porous medium such as the lime mortar once most of the liquid water has evaporated.

The research introduces novel approaches such as the use of nano-structured electrodes for measuring pH variations during carbonation.

The measure of acidity of aqueous solutions in building materials is one of the most important and difficult electrochemical measurements. Numerous chemical reactions, in fact, involve pH changes that can highlight processes otherwise difficult to monitor such as the well known problem of steel corrosion in reinforced concrete. Despite its importance, though, pH measurements in building materials are difficult due to the high pHs produced by some chemical compounds and the limitation of the most widely used pH-meters (e.g. large and unable to precisely measure very high pHs).

From a general point of view, it is possible to state that the reduction in the pH level

of pore-water in building materials is mainly due to carbonation. This reaction, in fact, transforms a compound that produces a very alkaline environment such as calcium hydroxide into a material such as calcium carbonate that produces environments with more neutral pHs.

Together with this, carbonation reduces a material's permeability and in lime based building materials this delays the setting process. This is due to the reduction in pore size caused by formation of compounds with larger volume than the initial one. The reduction in the pore size reduces the penetration of water and air that, in turn, affects the hardening process of lime.

The role of pore size on the compounds formed by this reaction, is investigated using a novel material: *nano-lime*. Nano-lime is the name of a commercially available product that is absorbed by porous media such as lime plasters or stones and acts as a consolidant through carbonation within the pores themselves. It was introduced about 10 years ago in the field of conservation of built heritage in order to provide a compatible consolidant for lime mortars and frescos but its application immediately showed some limitations. Nano-lime has the potential to provide chemically compatible treatments with carbonate materials and to produce improved consolidation compared to that achieved with traditional methods such as lime water and milk-of-lime. However, the exact behaviour of nano-lime is currently uncertain and widely debated. Some recent research, for instance, highlighted that different environmental conditions can affect the carbonation process of nano-lime producing less stable compounds than the compounds usually produced by the hardening process of traditional lime. Owing to their instability, these phases change over time and this can affect the overall result of the consolidation treatment.

Influence of pore-water on the hardening process of lime is studied in mixes of lime and hydraulic additives using techniques such as impedance spectroscopy that are relatively new in the study of lime based materials. Such techniques can play an important role in the modern construction industry by facilitating the on site analysis of water flow and allowing real time monitoring of hydration and carbonation.

Monitoring the hardening process of lime is an important activity of the building process. Among the data that should be collected (such as pH and temperature), the water content is one of the most important. Water is required for the two main reactions that allow lime to harden: carbonation and hydration. In carbonation water allows the reaction between the two main reagents (calcium hydroxide and carbon dioxide). In hydration, instead, water allows dissolution of solid phases and takes part in the formation of calcium silicate hydrates (the compounds that are the cause of initial hardening in hydraulic lime).

In practice, however, it is not possible to precisely measure *on site* the amount of

water contained within the lime mixtures non-destructively. As shown by this research, electrochemical impedance spectroscopy could be used as a non-destructive technique for real time *in situ* monitoring and the study of the water content in building materials.

1.3. Structure of the thesis

This thesis begins by providing a short definition of carbonation (chapter 2) that is assumed as a guiding principle in all research. Subsequently, within the same chapter is provided a summary of the most relevant results obtained in different fields in the study of carbonation, from the 20^{th} century to the most recent years. These are organized considering several aspects such as the reaction mechanism and the existence and the role of metastable phases, that are considered useful to provide a deep understand of this complex process. An original and critical discussion of carbonation in the different lime based materials currently used by the construction industry is also provided to conclude the chapter.

A description and discussion of the fundamental laws of chemistry describing carbonation are provided (chapter 3) presenting separately the three main phases involved: calcium hydroxide, carbon dioxide and calcium carbonate. This information is given together with the discussion of chemical calculations to provide an in depth knowledge of the influence of various factors such as temperature and pH on the chemistry of carbonation. Although this part presents some original studies, it is still based on a literature review of the most recent finding in the chemistry of aquatic systems and hydro-geochemistry. At the end of this chapter a detailed description of carbonation is presented as a summary of the results of chapters 2 and 3.

Following the introduction to carbonation, chapter 4 provides a description of the most distinguishing techniques employed in this research such as the nano-structured Pd-hydride micro-electrodes used to evaluate the pH change during carbonation and the use of PHREEQC (a computer program for simulating chemical reactions in natural water) for calculating the chemical characteristics of analysed solutions.

Chapter 5 gives a description of the experimental work carried out in applying the pH micro-electrodes to the monitoring of carbonation in porous media. This part details the experimental set up and, in particular, the specially manufactured electrodes and cell and shows the most relevant results obtained such as the possibility of distinguishing between formation of vaterite and calcite by considering the pH.

The following chapter (chapter 6) contains a description of the work carried out to study the tangible effects of carbonation in porous materials with a detailed illustration of the nano-lime.

The work carried out on the role of pore water in hydraulic lime and on the use of impedance spectroscopy for monitoring the hardening process in formulated lime is

reported in chapter 7.

At the end of this part, (chapter 8) the conclusions highlight the advancement in knowledge that has been gained from this research and introduces some suggestions for further work.

Following the conclusions, the thesis presents an appendix contains the results of experimental work on the radiocarbon dating of lime mortar. This work represents an important practical application of the knowledge acquired during this study on the carbonation process and presents an approach to the problem of radiocarbon dating lime mortars that can be a break-through in this research field.

1.4. Collaborations

This research has been a collaborative project between the Department of Architecture and Civil Engineering of the University of Bath, where most of the impedance spectroscopy tests were carried out, and The Electrochemistry Group of the University of Southampton where a system for the pH measurements with micro electrodes was set up. The University of Aveiro (Portugal) has supported this research making available the skills and equipment for the NMR analysis. English Heritage has kindly provided the nano-lime and supported the study of this new material. The research was funded by the Engineering and Physical Science Research Council (EPSRC reference: EP/I001204/1).

2. Literature review

2.1. A short definition of the carbonation reaction

Carbonation in lime based construction materials is the chemical reaction between calcium ions (Ca^{2+}) and carbonic ions (CO_3^{2-}) in aqueous solution that leads to the precipitation of a calcium carbonate solid phase ($CaCO_3$; De Silva et al., 2006; Cizer et al., 2012a,b). Carbonation is responsible for the strength in most of the lime based materials used in the construction industry (Van Balen, 2005; Moorehead, 1986) and is also the only reaction common to all types of lime, from the simplest *calcium lime* to the most complex products based on a mix of *natural hydraulic lime* and hydraulic additives (see paragraph 2.3)[1].

The reaction can be described by the following chemical model where the numbered list highlights the importance of the reaction order while the bullet point list highlights the existence of two different dissolution processes.

1. Dissolution of reactants in water:

    - dissolution of CO_2 in water (according to the model suggested in Morse and Mackenzie, 1990):

$$CO_{2(g)} \rightleftharpoons CO_{2(aq)} \tag{2.1.1}$$

$$CO_{2(aq)} + H_2O_{(l)} \rightleftharpoons H_2CO_{3(aq)} \tag{2.1.2}$$

$$H_2CO_{3(aq)} \rightleftharpoons HCO^-_{3(aq)} + H^+_{(aq)} \tag{2.1.3}$$

$$HCO^-_{3(aq)} \rightleftharpoons CO^{2-}_{3(aq)} + H^+_{(aq)} \tag{2.1.4}$$

[1] All the lime-related definitions used in this document such as *calcium lime*, *natural hydraulic lime* or *formulated lime* and their abbreviations (respectively: CL, NHL or FL) comply with the BS EN 459-1 2010. A short description of the main types of lime is reported in the list of abbreviations, at the beginning of this thesis.

- dissolution of calcium hydroxide ($Ca(OH)_2$) in water[2]:

$$Ca(OH)_{2(s)} + H_2O_{(l)} \rightleftharpoons Ca^{2+}_{(aq)} + 2(OH)^{-}_{(aq)} + H_2O_{(l)} \tag{2.1.5}$$

2. Reaction of calcium ions with carbonate ions in water:

$$Ca^{2+}_{(aq)} + CO^{2-}_{3(aq)} + H_2O_{(l)} \rightleftharpoons CaCO_{3(s)} + H_2O_{(l)} \tag{2.1.6}$$

From a chemical point of view, this reaction can be described as a two-steps process where the dissolution of reactants (CO_2 and $Ca(OH)_2$) precede the reaction of ions in water solution. The above description is preferable to the more common one:

$$Ca(OH)_2 + CO_2 \rightarrow CaCO_3 + H_2O \tag{2.1.7}$$

that does not highlights the complexity of the reactions involved and the very important role of water in the process.

2.2. Carbonation in the scientific literature

Precipitation of $CaCO_3$ solid phases is a process that has been widely investigated in several research fields such as chemistry, geology and engineering for a number of reasons such as the development of additives to medical supply, the use of $CaCO_3$ in food, paper, rubber, paint, plastic, printing ink, the development of biomedical implants and systems for drug delivery, the storage, transfer and oxidation of aquifers (Kitamura et al., 2002; Domingo et al., 2004; Sheng Han et al., 2006; Euvrard et al., 2004).

To date, much research have already been carried out and most of the results are available in the scientific literature.

Obviously, the interest in this process is different depending on the application field but results obtained in any research can be useful to reach a deeper understanding of this reaction. In order to do this, results obtained in fields of study other than the one of interest must be tailored to the specific needs. For instance, books describing the chemistry of groundwater report in great detail the dissolution process of $CaCO_3$ to illustrate solubility and mineral equilibria. The dissolution kinetic of carbonates is, thus, carefully described (e.g. Appelo and D., 2005, pp210-216) whereas $CaCO_3$ precipitation is simply described as *the backward term* in the dissolution equation (Appelo and D., 2005, p.217). For the construction industry it is more interesting and common to deal with the carbonate precipitation rather than with the carbonate dissolution so that

[2] A water molecule is reported in both sides of the equations in order to emphasize the role of this material in the whole process.

the *backward term* has to be studied with greater attention than the forward one but in any case the chemical principles remain unchanged.

Overall, it is possible to summarize that the main chemical reaction involved in the carbonation are described in great detail in the *carbonate equilibria* section (or: *carbonate and carbon dioxide*, *carbonate sediments*, etc.) of books published in the field of environmental chemistry, soil chemistry, geochemistry or hydro-geochemistry (e.g. Morse and Mackenzie, 1990; Appelo and D., 2005; Krauskopf, 1979; Ottonello, 1996) and the main principles are related to the chemistry of carbonic acid system (Loewenthal and Marais, 1978).

Within the construction industry, carbonation is discussed in several books describing lime and cement. Limiting the literature review to the books describing the lime it is possible to point out that the technological process of lime production and related chemical processes are described in detail in books such as Boynton (1966) or Oates (1998), that describe modern lime production. Studies on the traditional production of lime are reported in books such as Vecchiattini (2010) and Rattazzi (2007). The chemical processes in natural hydraulic lime (see paragraph 2.3.2), however, are not yet organically described in books specifically written on this topic but can be found in books on the chemistry of cement such as Hewlett (2004). The use of lime as a building material has been discussed in several publications such as Allen et al. (2003).

Looking in detail at the scientific papers currently available it is possible to state that the most recent research is focused on aspects such as the role of several factors on the whole mechanism (e.g. pH, temperature, relative humidity, presence of foreign ions), carbonation mechanism and kinetic, phase transformation, and adhesion mechanism of $CaCO_3$. The following paragraphs summarize the most recent findings related to these topics.

2.2.1. Factors affecting carbonation

Several factors and conditions control precipitation of $CaCO_3$ solid phases (Lopez-Arce et al., 2011; Montes-Hernandez et al., 2008). Among these, pH, temperature, relative humidity, supersaturation, CO_2 concentration, presence of other ions and additives in solution, and conductivity and magnetic fields are the most important.

pH

To date little research has been carried out on the effect of pH on the carbonation reaction. In 1990 Ogino et al. (1990) analysed the rate and mechanism of polymorphic transformation of vaterite and aragonite into calcite. These transformations were studied in water at temperatures between 25 and 80°C and with Ca^{2+} and CO_3^{2-} activity ranging from $10^{-2.5}$ M to $10^{-4.1}$ M and from $10^{-4.1}$ M to $10^{-5.7}$ M, respectively. Res-

ults showed that the transformation rate of vaterite to calcite was considerably retarded in solutions with very high pH (>10) and low concentration of total carbonate ion.

In 1998 Tai and Chen (1998) studied the polymorphism of $CaCO_3$ precipitated in solutions at constant composition. Factors affecting the formation of polymorphs such as solution pH, temperature, concentration ratio of components, supersaturation and ionic strength were studied. Results showed that at room temperature high-purity calcite and vaterite could be obtained respectively at pHs higher than 12 and at pHs lower than 10, while the maximum production of aragonite occurred around pH 11.

Four years later, Kitamura et al. (2002) studied the controlling factors and the crystallization mechanism of $CaCO_3$ polymorphs from $Ca(OH)_2$ suspensions by adding sodium carbonate (Na_2CO_3) solution. Results demonstrated that calcite precipitated from the beginning while aragonite began to precipitate when the molar ratio of Na_2CO_3/ $Ca(OH)_2$ was about 0.3. Alkaline solutions at pH higher than about 13.5 were though to be advantageous for the nucleation of aragonite. Aragonite crystallization was accelerated by decreasing the rate of Na_2CO_3 addition while calcite crystallized at high addition rates. Decreasing the addition rate, the volume of aragonite crystals with long needle-like morphology increased. Aragonite precipitation was also accelerated by increasing the solution volume and the stirring rate. In the meantime the amount of agglomerated fine particles of calcite decreased. According to Kitamura and colleagues, these results indicate that if the concentration of Ca^{2+} is close to the solubility of $Ca(OH)_2$ and the concentration of carbonate ions is low, crystallization of aragonite is favoured.

In 2006, Sheng Han et al. (2006) investigated nucleation, crystallization and transformation of vaterite at specific pH. They precipitated $CaCO_3$ particles by flowing $^{CO_2}/_{N_2}$ mixed gases into $CaCl_2$ solution. Results showed that the addition of ammonia (NH_3) locally induced high supersaturation as well as continuous formation of nuclei. This, in turn, promoted the growth and agglomeration of vaterite nuclei while inhibiting the transformation of vaterite to calcite. Overall, Sheng Han and colleague suggested that control of the pH is a way to obtain nearly pure vaterite.

More recently, Ma et al. (2010) studied the effects of pH and temperature on the crystallization of $CaCO_3$ in aqueous solutions containing a water soluble matrix of mother of pearls (WSM). Experiments were carried out at different temperatures and pHs using gas diffusion and titration. Results showed that the WSM could induce aragonite formation at different pH values, while the pH value had a clear influence on the calcite morphology rather than that of aragonite. The reason for this was thought to be the specific supersaturation and ionic strength related to different pH values. The solution temperature was found to have a relevant effect on the polymorph and morphology of $CaCO_3$ crystals.

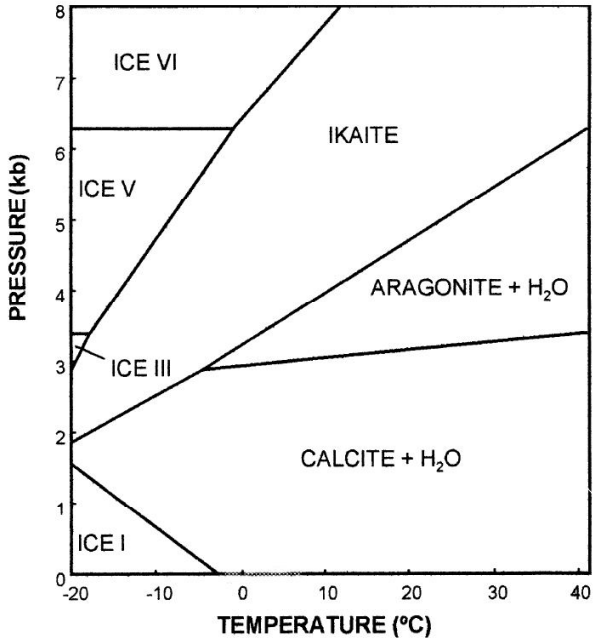

Figure 2.1.: Generalized pressure-temperature phase diagram for the $CaCO_3$ system in water between -20 and 40ºC (from: Lurio and Frakes, 1999, p. 1041).

Temperature

It is general knowledge that at 1 atm pressure and between 0 and 40ºC, temperature has little effect on the product of carbonation: calcite is the only stable polymorph under these conditions (figure 2.1). Despite this fact, however, several researchers evaluated the effect of temperature on the carbonation process. Small changes in the environment where carbonation takes place, in fact, can substantially modify the final product of the reaction. In systems where water activity is low, for instance, the stability fields represented in figure 2.1 are shifted to the right (Dutkiewicz and Jakubowska, 2002; Blandamer et al., 2005). Minerals such as ikaite, normally produced at high pressure or low temperature, can form metastably at surface pressure and temperatures between -1.9 and 7°C (Lurio and Frakes, 1999, p.1041).

In 1999 Vucak et al. (1999) studied the morphological development in $CaCO_3$ precipitation by the ethanolamine process at 30 and 60°C. According to their results, vaterite transforms to aragonite when passed from 30 to 60ºC. Furthermore, crystal aggregation is the mechanism that determines the overall particle size at 30°C, while crystal growth dominates at 60°C.

In the same year Gabrielli et al. (1999) investigated the nucleation and growth of $CaCO_3$ using an electrochemical scaling process. In their tests, $CaCO_3$ was electrochemically deposited onto gold electrodes of an electrochemical quartz crystal microbalance (QCM) using a CO_2-pure hard water under different conditions. Different polymorphs of $CaCO_3$ (calcite, aragonite or vaterite) were formed under different experimental conditions. Results showed that at room temperature calcite was predomin-

ant under the conditions which favoured a fast nucleation rate. On the contrary, vaterite was constantly obtained for experimental conditions leading to a slow nucleation rate. The temperature increase favoured the formation of either aragonite needles or vaterite crystallites with a different morphology.

Four years later, Yang et al. (2003) studied the $CaCO_3$ crystallization in ethanol-water solutions containing a mix of non-ionic and anionic surfactants. In this research, the effects of the ethanol-water volume ratio, the effect of surfactant concentration, and ageing temperature (30-90°C) on the $CaCO_3$ morphology and polymorphism were investigated. Results showed that a binary mixture (calcite-vaterite) and a ternary mixture (calcite-vaterite-aragonite) were produced, respectively, at less than 60°C and at high temperatures. Different ethanol/water volume ratios affected the habit with the production of spherical, plate-like, flower-like, and rod-like crystals. By adjusting the ethanol-water volume ratio it was possible to control the synthesis of nearly pure flower-like vaterite and rod-like aragonite.

Altay et al. (2007) studied the precipitation process of $CaCO_3$ using aqueous solutions of $CaCl_2$ with Na_2CO_3. Their tests were carried out over a range of mixing and ageing temperatures. According to their results, the amount of aragonite increased with temperature. The difference in the temperature of mixing and ageing had a small effects on the amount of aragonite formed. However with the decrease in the ageing temperature were observed some increase in the aspect ratio of the crystals. Shorter ageing times were found to favour aragonite formation.

In 2009, Chen and Xiang (2009) studied the synthesis of $CaCO_3$ polymorphs at 30-80°C in $CaCl_2$ and NH_4HCO_3 solutions with molar ratio of 1:1. Results showed that lamellar vaterite, a mix of vaterite, aragonite and calcite, and aragonite with whisker microsctructure were formed at different temperatures (30-40°C, 50-70°C and 80°C, respectively). Thermodynamic calculations showed that the ratio CO_3^{2-}/Ca^{2+} decreased with the increase of temperature. This was considered one of the reasons for the formation of the lamellar vaterite at 30-40°C and the aragonite whiskers at 80°C.

Relative humidity

According to Lopez-Arce et al. (2011), the scientific papers that describe the influence of relative humidity on the precipitation of $CaCO_3$ and its mineralogical characteristics are very scarce.

Cook and Batchelor reported in their book (Cook and Batchelor, 1996, p.343) that, according to a number of studies, approximately 50% relative humidity is optimal for carbonation in concrete. Shih et al. (1999) reported that in their tests $Ca(OH)_2$ reacted with CO_2 to form $CaCO_3$ only when the relative humidity exceeded 8%. Final conversion and reaction rate of $Ca(OH)_2$ were significantly affected by the relative humidity, slightly dependent on temperature and zeroth order dependent the CO_2 concentration.

The following year Beruto and Botter (2000) studied the formation of liquid-like H_2O adsorption layers on the $Ca(OH)_2$ crystals that, according to them, catalyses the $Ca(OH)_2 - CO_2$ reaction forming a non-protective layer. In their tests, porous $Ca(OH)_2$ particles were taken to the equilibrium with water vapour at a relative pressure ranging between 0.4 and 0.85 kPa and at temperature of 20°C. These particles were reacted with gaseous CO_2 at the same temperature and at a pressure of 0.65 kPa. Results showed that the $Ca(OH)_2$ particles were converted up to 85% into a non-protective layer of $CaCO_3$ which was distributed inside the pores of the initial particles. The same reaction with dry-$Ca(OH)_2$ powders converted up to 10% at a temperature of 100°C. According to these authors, the observed catalytic effect was dependent on the initial amount of water that was adsorbed by the particles. A minimum number of four layers of water adsorbed onto the $Ca(OH)_2$ particles was required to produce the catalytic effect.

Dheilly et al. (2002) studied the influence of storage conditions on the carbonation of powdered $Ca(OH)_2$. They stated that high relative humidity conditions with low levels of CO_2 and temperatures of about 10°C, favoured carbonation. For this reason, in their paper it is recommended to store the powdered lime at RH below 30% and at a temperature between 20 and 30°C.

Research carried out by El-Turki et al. (2007) showed that lime exposed to 97% RH was subject to a higher carbonation rate and carbonated completely compared to lime exposed to 65% RH. In this case, in fact, a small amount of $Ca(OH)_2$ was still detected at the end of the experiments.

Studies on the consolidation effect of nano-lime carried out by Lopez-Arce in 2010 (Lopez-Arce et al., 2010) have shown that high relative humidity conditions (75% RH) favours the consolidation process of nano-lime.

The following year, the same author carried out research to evaluate the influence of relative humidity on the carbonation of nano-lime and on the formation of $CaCO_3$ polymorphs (Lopez-Arce et al., 2011). Results showed that precipitation and transformation of $CaCO_3$ were strongly depended on the relative humidity: high RH (75%–90%) promoted formation of amorphous calcium carbonate (ACC), monohydrocalcite, vaterite, aragonite and calcite. At such relative humidities, carbonation was faster and particle size larger with higher crystallinity compared to the crystals formed at low RH (33%–54%). At low RH, instead, portlandite ($Ca(OH)_2$) and vaterite ($CaCO_3$) were the main solid phases formed. Carbonation was slower, the particle size smaller and the crystallinity lower.

CO_2 concentration

As the a reaction between Ca^{2+} and CO_3^{2-} ions occurs in aqueous solution, it is noteworthy that the CO_2 concentration can have an effect on the carbonation. Despite

this clear connection, however, the practical effects of the p_{CO_2} on carbonation is still matter of research.

In 1996 Cook and Batchelor (Cook and Batchelor, 1996, p.344) reported the results of a test on carbonation in cement specimens where exposure to an atmosphere containing 4 percent of CO_2 for one week was evaluated to be equivalent to carbonation under normal atmospheric conditions for one year.

In 2005, Han et al. (2005) studied the effect of flow rate and CO_2 content on the phase and morphology of $CaCO_3$. Calcium carbonate was prepared by bubbling a mixture of gas CO_2/N_2 into $CaCl_2$ solution. Results demonstrated that mainly vaterite was formed at a high flow rate or high partial pressure of CO_2. This was attributed to the slowing down of the vaterite to calcite transformation.

In the same year Van Balen (2005) studied the kinetics of the carbonation reaction at 20ºC. Different limes and p_{CO_2} were used to study the influence of these two variables. Results demonstrated that,within the test limits, the reaction speed was not dependent upon the CO_2 concentration.

In 2012 Cizer et al. (2012a) studied the phase and morphology evolution of $CaCO_3$ precipitated by carbonation of hydrated lime under different conditions ($p_{CO_2} \approx 10^{-3.5}$ atm at 60 % and 93 % RH; p_{CO_2} = 1 atm at 93 % RH). Results showed an initial precipitation of ACC which, in turn, transformed into scalenohedral calcite under excess Ca^{2+} ions. Because of their polar character, some faces of the scalenohedral crystals were thought to interact more strongly with excess Ca^{2+} than the faces of rhombohedral crystals and this was thought to have an effect that at some $^{Ca^{2+}}/_{CO_3^-}$ ratios ultimately promoted the stabilization of scalenohedral crystal faces. After the full consumption of Ca^{2+} ions and further dissolution of CO_2 the pH in the pore solution dropped and this was though to be the reason of the scalenohedral faces dissolution. This eventually resulted in re-precipitation of rhombohedral faces at close-to-neutral pH. This crystallization sequence was thought to progress through the depth of the carbonated layer and was thought to be strongly dependent on the degree of exposure to CO_2, which is controlled by pore structure (that affects the CO_2 diffusion). Both, the carbonation process and the scalenohedral-to-rhombohedral transformation were thought to be kinetically favoured in high RH and high p_{CO_2}. Supersaturation was thought to play a critical role on the nucleation density and size of $CaCO_3$ crystals.

In the same year Cizer and colleagues published another paper (Cizer et al., 2012b) on the reaction rate and the mineral phase modifications in carbonation of lime based building materials. In this research, the carbonation reaction of lime pastes was studied with an on-line carbonation set-up where the measurement of the amount of CO_2 consumed by $Ca(OH)_2$ was combined with the measurements of an *in situ* XRD analysis of portlandite and calcite. The reaction rates calculated using the net CO_2 uptake by $Ca(OH)_2$ and the rate calculated from the calcite precipitation were compared for

lime putty and lime hydrate pastes. Results indicated that carbonation is initially fast and controlled at the exposed surface. A strong limitation was found to be the CO_2 diffusion into the pore water. According to the same authors, the reaction, then, proceeded with a chemical-reaction controlled regime which was found to be faster than the previous step. This was followed by a transition to a CO_2-diffusion controlled regime. Drying and formation of the ACC on the $Ca(OH)_2$ faces were found to be a limiting effect for the calcite precipitation. The lime putty was characterized by a faster carbonation than hydrated lime and this was supposed to be due to the smaller particle size and morphology properties. In both cases the reaction rate was found to be independent of the CO_2 gas concentration.

In 2013 Visser submitted a paper (Visser, no date) describing the study carried out on the influence of the CO_2 concentration on the resistance to carbonation of concrete. Results showed that a change in CO_2 concentration does not change the carbonation process.The only effect of the high CO_2-concentration was considered a faster transport of the CO_2 molecules to the pore solution interface that increased the reaction process.

Supersaturation and Ca^{2+}/CO_3^{2-} ratio

Clarkson et al. (1992) studied the the spontaneous precipitation of $CaCO_3$ from highly supersaturated aqueous solutions with respect to calcite. According to their results the sequence of events during precipitation was strongly governed by the initial supersaturation and the temperature. At high supersaturation, the first-formed phase was ACC. This phase was observed only above a well defined ionic activity product and was homogeneously nucleated. Over the temperature range 16-50ºC, this amorphous phase had a solubility product (K_1) defined by the equation: $logK_1 = (1247/T)$–10.224. At concentrations insufficient to produce the amorphous phase, the first-formed solid that nucleated heterogeneously was calcite. Ikaite was formed only at temperatures below 25°C and subsequently transformed into vaterite. These two crystalline phases also resulted from the phase change of the ACC at higher initial supersaturation.

In 1996 Gomez-Morales et al. (1996) studied the precipitation of $CaCO_3$ from solutions characterized by the same initial supersaturation and different $[Ca]_T/([HCO_3^-]+[CO_3^{2-}])$ ratio. Unseeded and seeded experiments at 25ºC were carried out. Results showed that in unseeded experiments, the induction times (t_i) varied in the order: $t_i\,([Ca]_T/\sum C = 4) > t_i\,([Ca]_T/\sum C = 1/4) > t_i\,([Ca]_T/\sum C = 1)$. In seeded experiments the higher growth rates corresponded to runs where $[Ca]_T/\sum C = 4$ whereas the lower ones were observed in runs where $[Ca]_T/\sum C = 1/4$. The lower rate of nucleation (high t_i) and higher rate of growth were observed when $[Ca]_T/\sum C = 4$ and this was accounted for, respectively, by the formation of a lower concentration of ion pairs in the bulk solution as well as a higher concentration of $CaCO_3^0$ pairs on the crystal surface.

The year after van der Weijden et al. (1997) studied the influence of total calcium and total carbonate on the growth rate of calcite under seawater-like conditions. Results showed that the growth rate of calcite increased, increasing Ca^{2+} concentration, likely because of a higher supersaturation. At the same supersaturation and free activities of $CaCO_3$, the growth rate was faster when the concentration of the total carbonate was higher. This increase was explained with a contribution of HCO_3^- ion to calcite crystal growth.

In 2002, Rodriguez-Navarro et al. (2002) pointed out the role of pores size in the formation of supersaturated Ca solution in lime based mortars. Studying the Liesegang pattern developed in carbonated lime mortars, in fact, they highlight the fact that in pores with radius $<1\mu m$ $CaCO_3$ precipitates from solution with higher Ca concentration than in pores with radius $\geqq 1\ \mu m$. This is due to the Laplace effect of curvature that has also an effect on the nucleation rate, which is higher in smaller pores. Figure 2.2 shows how, according to Rodriguez-Navarro and colleagues, supersaturation and nucleation rates in the system $CaCO_3 - H_2O$ increases as the pore size decreases. In particular, high supersaturation and nucleation rates induce the formation of numerous and randomly scattered calcite particles characterized by nano-metric sizes and a colloidal non-equilibrium state. It is not clear if these particles are ACC, micro-crystalline calcite or one of the metastable precursors such as monohydrocalcite. Such small particles, however, have a high surface:volume ratio and, consequently, a high surface energy that can play a significant role in many chemical processes (Rodriguez-Navarro et al., 2002, p.2268). In the same paper, the same authors highlighted the fact that a large volume of pores with radius $>1\mu m$ enhanced capillary condensation of water. According to them this result is in agreement with the Kelvin equation (Rodriguez-Navarro et al., 2002, p.2269).

In 2009 Cizer (2009) studied the competition between carbonation and hydration in lime mortars. Results showed that calcite was the only $CaCO_3$ polymorph precipitated independently from the carbonation conditions. The conditions, instead, were found to have an important impact on the habit, size and morphology of the calcite crystals. The $[Ca^{2+}]/[CO_3^{2-}]$ ratio in the pore water, in particular, was found to determine the habit and the morphology of the calcite crystals. When $[Ca^{2+}]/[CO_3^{2-}] \approx 1$ the growth of the rhombohedral calcite crystals was favoured. Nonetheless, scalenohedral calcite crystals with a cracked and/or corroded surface were still observed in the sample thickness. Such a crystal surface feature was thought to be derived from the change in the ratio between Ca^{2+} and CO_3^{2-} ions with further diffusion of CO_2. According to Cizer, under such conditions the excess Ca^{2+} group in scalenohedron is balanced by the CO_3^{2-} ions. This eventually resulted in the formation of rhombohedral faces that contain equal amounts of Ca^{2+} and CO_3^{2-} ions.

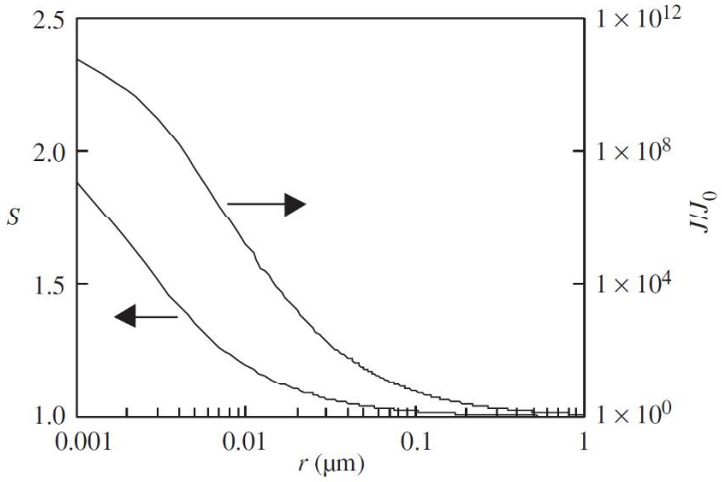

Figure 2.2.: Supersaturation (S) and nucleation rate (J/J_0) versus pore size (r) for the system $H_2O - CaCO_3$. For a specific pore size, the first curve indicates the supersaturation value (S) that can be sustained for that specific pore with respect to an initial supersaturation value of 1. The second curve indicates the variation of nucleation rate for S=2 with respect to the pore size (from: Rodriguez-Navarro et al., 2002, p.2267).

Other ions and organic additives

Magnesium One of the most important ions that should be considered in the study of $CaCO_3$ precipitation is magnesium (Mg^{2+}). Dolomitic lime, in fact, is an important sub-family of air limes characterized by a relevant presence of magnesium oxide (MgO) or hydroxide ($Mg(OH)_2$; between 5% and $\geq$30% according to BS EN 459-1, 2010, p.15). Research on the effect of this ion on carbonation started quite early. In 1976 Reddy and Nancollas (1976) studied the effect of magnesium, strontium and sulfate ions on crystallization of $CaCO_3$. Tests were carried out at 25ºC in supersaturated solutions containing 10^{-3} M sulfate ion, 10^{-4} M strontium ion, or 10^{-4} M magnesium ion. According to their results, all these ions yielded calcite crystals with an identical morphology to that obtained in the absence of ions. The addition of 10^{-3} M magnesium ions, however, resulted in calcite crystallites with a poorly developed crystal habit which gradually improved with aging. Subsequent analysis indicated that $CaCO_3$ formation involved an unstable amorphous phase that underwent subsequent transformation to aragonite and calcite.

In 1998 Tracy et al. (1998b,a) investigated the reaction rate of calcite sphere formation. Results showed that the Mg^{2+} and SO_4^{2-} impurities had an influence on the solid phase and morphology of precipitates. The calcite spheres were seen to precipitate initially in an amorphous form before going through a transition into an intermediate spherulitic morphology and finally developed into near-perfect spheres.

In 1998 Pokrovsky (1998) studied the homogeneous precipitation of calcium and magnesium carbonates in the $CaO–MgO–CO_2–H_2O$ system in supersaturated solutions. Results allowed him to calculate the order of $CaCO_3$ homogeneous nucleation

that was found to be equal to 4, while the surface energy of the $CaCO_3$ nucleus was measured to be 63 $^{mJ}/_{m^2}$. The main factor controlling the Mg content in the solid phase precipitated was found to be the saturation index of $MgCO_3$ in solution.

Meldrum and Hyde (2001) studied the morphological influence of magnesium and organic additives on the calcite precipitation. In their experiments, $CaCO_3$ was produced from saturated solutions of calcium bicarbonate ($Ca(HCO_3)_2$) in the presence of Mg and organic additives. Several concentrations of Mg and additives were investigated as well as the structure, composition and morphologies of the crystals. Results showed a very specific action of the organic additives in Mg-free solutions. This produced elongated single calcite crystals. In the presence of both Mg and organic additives, instead, a much wider range of calcite morphologies was observed. A transition from single crystal to aggregates was found to occur when the Mg concentration was increased. The increase of Mg in solution increased the $MgCO_3$ content in the crystals but this showed little correlation with the organic additive concentration.

In 2003 Loste et al. (2003) studied the role of magnesium in stabilising the ACC and controlling calcite morphologies. In their research they precipitated $CaCO_3$ from highly supersaturated Mg aqueous solutions. The precipitates were analysed over time with several techniques including X-ray diffraction and Fourier Transform Infrared Spectroscopy. Results showed that in all cases the ACC was the first phase formed. The Mg content in the ACC was calculated by the $^{Mg}/_{Ca}$ ratio in the solution and was found to increase systematically with the increase in $^{Mg}/_{Ca}$. ACC containing higher Mg concentrations was found to be significantly more stable than ACC with low magnesium. The crystalline phase produced on ACC transformation was found to be depending on the $^{Mg}/_{Ca}$ ratio. The ACC precipitated from solutions containing high concentrations of Mg crystallised producing high-Mg calcites (containing up to 47 mol% Mg), together with mono-hydrocalcite ($CaCO_3 \cdot H_2O$) and/or ikaite ($CaCO_3 \cdot 6H_2O$). The Mg content of the ACC phase also affected the precipitates' final morphology.

In 2004 Wei et al. (2004) studied the synthesis of $CaCO_3$ crystals from aqueous solutions containing sodium dodecyl sulfate (SDS), poly(N-vinyl-1-pyrrolidone; PVP), or SDS/PVP complexes. Formation of aragonite without Mg^{2+} ions at 26°C indicated that the initially formed ACC could turn into aragonite in the sedimentary phase. This suggested that the organic additives are the controlling factor in the nucleation and growth process of $CaCO_3$ crystals. The formation of hexagonal crystals matched the hexagonal cell of vaterite and suggested the colloidal-dispersion function of the SDS/PVP in the $CaCO_3$ crystallization process.

In 2005 Chen et al. (2005) studied the effect of magnesium on scale formation and, in particular, on the kinetics, habit and ratio of $^{Mg}/_{Ca}$ in the scale. The kinetics of $CaCO_3$ precipitation were studied with regard to precipitation in the bulk solution and as deposition on a metal surface. Mg^{2+} ions proved to have a greater inhibition effect on

bulk precipitation than surface deposition. Magnesium suppressed vaterite formation and the resulting precipitate was dominated by calcite. The $^{Mg}/_{Ca}$ ratio in the deposit was found to be proportional to the concentration of Mg^{2+} in the bulk solution. The distribution coefficient in surface deposition and in bulk solution was found to be a constant, independent of the concentration of Mg^{2+} ions in the bulk solution.

In 2008, Park et al. (2008) studied the effects of magnesium chloride ($MgCl_2$) and organic additives on the synthesis of aragonite by treating a suspension of $Ca(OH)_2$ with CO_2 gas. They found that in the presence of even a small amount of Mg^{2+}, Mg-calcite formed, but as the Mg^{2+} ion concentration increased, the amount of Mg-calcite decreased and the amount of aragonite increased. In the presence of 60 mol% $MgCl_2$, Mg-calcite was suppressed and only aragonite was formed. As the Mg^{2+} ion concentration increased, the aragonite longitude and aspect ratio was found to have decreased.

In 2009 Lin and Singer (2009) studied the effect of Mg^{2+} on the kinetics of calcite crystal growth. Experiments were carried out using calcite-seeded solutions. For the tests were employed five different solution compositions with the same degree of supersaturation (respect to calcite) but different $^{CO_3^{2-}}/_{Ca^{2+}}$ molar ratios. Results showed that in the presence of Mg^{2+}, the rate of the calcite crystal growth decreases linearly with the increases of Mg^{2+} concentration. By normalizing the crystal growth rate, the rate reductions in the five solutions converged to a single line. According to these authors, the widely used models (i.e. the *empirical degree of supersaturation model* and the simple *Langmuir adsorption model*) cannot explain the observed effects of the $^{Mg^{2+}}/_{Ca^{2+}}$ ratio on the inhibition of calcite crystal growth. On the contrary, a *competitive Langmuir adsorption* model involving Ca^{2+} and Mg^{2+} was found to better fit the experimental data.

Silica Silicic acid (H_4SiO_4) is another important compound that should be studied in order to evaluate its effects on the carbonation reaction in hydraulic limes (see paragraph 2.3.2 and 2.3.3). Unfortunately, to date little research has been carried out.

In 1995 Klein and Walter (1995) studied the interactions between dissolved silica (SiO_2) and carbonate minerals at 25-50°C. These were investigated under different experimental conditions. Results showed that in high ionic strength solutions maintained near equilibrium (with respect to calcite) at various p_{CO_2}, SiO_2 uptake onto calcite was irreversible and pH and time dependent. The rate of uptake was greatest during the first 5 hours and at lower pH (higher p_{CO_2}). Silica uptake was only nominally dependent on the Mg concentration and on the temperature, and was greater at high ionic strengths than in low-ionic-strength solutions. Adsorption of SiO_2 had no effect on the calcite precipitation rates. During recrystallization of aragonite and Mg-calcite in low-ionic-strength solutions, SiO_2 uptake values were similar to the values in near-equilibrium

experiments at high ionic strength. Despite considerable variation in the experimental carbonate equilibrium-disequilibrium, mineralogy and solution chemistry, SiO_2 uptake between 25 and 50°C was evaluated to be limited.

Lakshtanov and Stipp (2010) studied the kinetics of spontaneous precipitation of $CaCO_3$ from aqueous solution in the presence of dissolved SiO_2 by recording pH as a function of time. Results showed that presence of dissolved silica at concentrations below saturation with respect to the amorphous phase, decreased the induction time for $CaCO_3$ nucleation, but did not affect polymorphism. The surface free energy calculated agreed with values reported in the literature for vaterite and, consequently, suggested some degree of heterogeneous nucleation that could have occurred because of the relatively low degree of supersaturation used for the experiments. The ratio of Ca^{2+}/CO_3^{2-} activity was considered an important parameter for determining which $CaCO_3$ polymorph precipitated. At high Ca^{2+} to CO_3^{2-} activity ratios, almost all initial solid phase was vaterite, whereas at low ratios, a mixture of vaterite and calcite was observed. In solutions with low Ca^{2+} to CO_3^{2-} activity ratios, the presence of silica at concentrations above saturation with respect to amorphous silica led to formation of only calcite and influenced strongly the structure and morphology of the solid phases produced. At high Ca^{2+} to CO_3^{2-} ratios, the system behaviour did not differ from that without silica.

Conductivity and magnetic fields

It is already known that conductivity and magnetic fields can affect precipitation of $CaCO_3$ solid phases. In 1997 Wang et al. (1997) studied the influence of a magnetic field on the rapid onset of $CaCO_3$ crystallization. They carried out a series of experiments regarding the formation of $CaCO_3$ from super-saturated solutions. Results indicated that under specific conditions, in the presence of a magnetic field, the nucleation rate could be increased. This was observed as a rapid onset of crystallization within the bulk solution. As a consequence of this faster precipitation, Wang and colleagues found that the resultant crystals were greater in number, smaller in size and irregular in shape.

In 2003 Garcia Carmona et al. (2003) investigated the effects of the adjustment of the electrical conductivity (κ_{25}) on the morphology of the $CaCO_3$ particles precipitated from a suspension of $Ca(OH)_2$. They found a gradual morphological change from rhombohedral to scalenohedral shapes of calcite when the conductivity was increased from 1 to 7 $^{mS}/_{cm}$. The explanation they provided was the increase of both the supersaturation and the ratio between concentrations of charged species (Ca^{2+} and CO_3^{2-}) in solution as the κ_{25} set-point increased, prior to the precipitation process. Furthermore, the habit change was supposed to take place because of the increase of the Ca^{2+}/CO_3^{2-} ratio that could have had an effect on the growth rate of the rhombohedral {104} and

scalenohedral {21-1} faces.

In 2009 Watanabe and Akashi (2009) studied the formation of various polymorphs of $CaCO_3$ on porous membrane using an electrochemical approach. Their tests involved the use of an alternating current that could facilitate the crystallization of $CaCO_3$ polymorphs on a porous polymer membrane. A solution of $CaCl_2$ and Na_2CO_3 was filled in a glass cell and a porous membrane was interposed in the cell itself. A sine waveform of 10 Hz was applied to platinum electrodes using a high-speed bipolar power supply. In this manner, an alternating current was generated for 60 min. Versatile polymorphs of vaterite, aragonite, and calcite were formed on the membrane, showing that the alternating current induced the formation of various $CaCO_3$ polymorphs even in the absence of any additives.

2.2.2. Reaction mechanism and kinetics

Carbonation mechanism

Looking at the scientific literature currently available, it is possible to state that the main steps of carbonation have been defined and agreed by the majority of authors although some details are still debated. In 1993 Matsushita et al. (1993) studied the intermediate products of carbonation using X-ray photoelectron spectroscopy (XPS) on $Ca(OH)_2$ slurry. Results showed that the composition of the $Ca(OH)_2$ surface was almost the same as that of the bulk throughout the reaction process. Furthermore, their results supported the idea of the formation of an amorphous phase with formula: $Ca_{1+x}CO_3(OH)_{2x} \cdot yH_2O$ with $x > 0.05$ and $y = 0.6 - 0.8$, different from the ACC.

In 2000 Beruto and Botter (2000) studied the formation of a liquid-like H_2O adsorption layer on the surface of $Ca(OH)_2$ particles that catalyses the $Ca(OH)_2 - CO_2$ solid–gas reaction forming a non-protective solid product layer.

According to Dheilly et al. (2002), carbonation in powdered lime appears to follow three sequential steps: 1) formation of a thin layer of water from the atmosphere on the surface of the $Ca(OH)_2$ grains; 2) dissolution of the $Ca(OH)_2$ particles to form Ca^{2+} and OH^- ions together with the dissolution of gaseous CO_2 in the alkaline solution produced by the lime to form CO_3^{-2} ions; 3) precipitation of $CaCO_3$. Despite the fact that this mechanism is quite simple it provides a good starting point for the study of carbonation.

A more detailed study on the growth of $CaCO_3$ phases on the surface of $Ca(OH)_2$ crystals was carried out by Yang et al. (2003) that made a direct observation of the carbonation process on the surface of $Ca(OH)_2$ crystals in hardened cement paste using an AFM. The microscope was encapsulated in a glove-box and operated in contact mode at ambient temperature. Real-time measurements were performed in different conditions: 1) in pure N_2 atmosphere; 2) in $N_2 + H_2O$ atmosphere; 3) in $N_2 + CO_2$

atmosphere and 4) in $N_2 + CO_2 + H_2O$ atmosphere. In the $N_2 + H_2O$ atmosphere of 30–40% RH, a surface smoothing of $Ca(OH)_2$ crystals together with a more and more pronounced instability over the time was observed. No change was detected in the $N_2 + CO_2$ atmosphere, except for some very small grains that became smaller after two days. In the $N_2 + CO_2 + H_2O$ atmosphere, with about 26%–30% RH, on the surface of the $Ca(OH)_2$ crystals several small scattered spots were identified. These spots were found to be not very well linked to the surface. Under constant conditions (temperature, humidity and CO_2 content), these small spots grew and after a long-term exposition developed a specific spherical structure. This was interpreted as $CaCO_3$, produced by the surface carbonation process of the $Ca(OH)_2$ crystals.

According to Lawrence et al. (2007) who studied the effects of carbonation on the pore structure of non-hydraulic lime mortars, five stages are involved in the carbonation process of a lime based mortar: 1) diffusion of gaseous CO_2 through the pores of the mortar; 2) dissolution of the CO_2 in the pore water; 3) dissolution of $Ca(OH)_2$ in the pore water; 4) solution reaction between $Ca(OH)_2$ and CO_2 ; 5) precipitation of solid $CaCO_3$.

Cizer (2009) studied the competition between carbonation and hydration in the hardening process of lime. According to this author, the carbonation reaction proceeds in two stages that can be described as follow: 1) initial CO_2 uptake and 2) increased CO_2 uptake. During the first stage, CO_2 molecules are absorbed into the alkaline pore water on the sample surface. This starts the carbonation reaction producing precipitation of $CaCO_3$ solid phases. This stage includes a dormant period in which the rate controlling factor is the dissolution of $Ca(OH)_2$ and CO_2 in water. Test results showed that the dissolution rate of portlandite crystals in the lime putty proceeded faster than in the hydrated lime, probably because the higher specific surface area of the former. As a consequence, according to Cizer, CO_2 uptake and $CaCO_3$ precipitation in the lime putty pastes are kinetically faster than in the hydrated lime. The later stage of carbonation, as the CO_2 uptake increased, is controlled by the CO_2 diffusion through the sample thickness because water evaporation creates open pore space allowing diffusion paths for CO_2. With the increase in the CO_2 uptake, precipitation of $CaCO_3$ solid phases accelerates.

Carbonation kinetics

Carbonation kinetics have been discussed by several authors with slightly different results. In 2002 Dickinson et al. (2002) studied the interplay between kinetic and thermodynamic control of the $CaCO_3$ crystal growth by diffusion of gaseous CO_2 into an aqueous solution of $CaCl_2$. Results showed that the Ca^{2+} is the dominant species in producing thermodynamic growth of rhombohedral calcite, while kinetic growth is preferentially controlled by CO_2. This was evidenced by the formation of vaterite as

the p_{CO_2} increased for a given Ca^{2+} concentration.

In the same year, Kawano et al. (2002) studied the formation process of $CaCO_3$ from highly supersaturated solution by mixing $CaCl_2$ and Na_2CO_3 aqueous solutions at 20°C. Results showed that after an amorphous phase had formed, spherulitic vaterite and calcite in a rhombohedral shape nucleated simultaneously, but separately, and grew by forming a precipitate-free zone around them. This transformation was solvent-mediated and the measurement of the growth rate suggested that the rate-controlling process was the diffusion of elements in the earlier stage of this process, which then changed to surface kinetics.

In 2005 Van Balen (2005) studied the kinetics of carbonation reaction at 20ºC. Results suggested that the carbonation speed was dependent on the specific surface of the $Ca(OH)_2$ crystals.

The following year, De Silva et al. (2006) investigated the reaction kinetics, strength and microstructure in carbonate binders produced by reaction of hydrated lime with carbon dioxide. Their results showed that the rate of $Ca(OH)_2$ conversion to carbonate was enhanced by increasing gas pressure, but it decreased with increasing compaction of the initial mixture.

In 2011 Rodriguez-Blanco et al. (2011) studied kinetics and mechanisms of nano-particulate ACC transformation to calcite, via vaterite in a range of temperatures (7.5-25ºC) using Energy Dispersive X-ray Diffraction (ED-XRD) in conjunction with other techniques. The crystallization process was found to occur in two stages: 1) ACC particles rapidly dehydrate and crystallize forming individual particles of vaterite; 2) the vaterite turn to calcite through a dissolution and re-precipitation process of which the reaction rate is controlled by the calcite surface area. The second stage of the reaction was found to be approximately 10 times slower than the first.

2.2.3. Metastable phases and phase transformation

Formation of metastable phases and phase transformations is one of the key points in the study of carbonation. Despite the fact that calcite is the most stable $CaCO_3$ polymorph at room temperature and pressure, calcite crystallization is only the last step of a more complex mechanism that involves precipitation and formation of metastable phases.

In 1990, Ogino et al. (1990) found in their research that the transformations of vaterite and aragonite in calcite started from the dissolution of the metastable phases (vaterite and aragonite) followed by the growth of calcite. The rate-determining step was identified to be the growth of calcite for both transformations and the transformation rate constant they found was in good agreement with that of calcite growth from supersaturated solutions. The transformation rate of vaterite was found to be inde-

pendent of the activities of Ca^{2+} and CO_3^{2-} ions under most conditions but was also found to be considerably delayed in solutions at pH>10 and low total carbonate ion concentrations.

In 1997 Kralj et al. (1997) studied the kinetics of vaterite to calcite transformation in aqueous solution in the temperatures range 25-45°C and ionic strengths between 15 and 415 $^{mmol}/_{dm^3}$. In their tests, both vaterite and calcite precipitated spontaneously but vaterite was the only solid phase precipitated at the beginning. The transformation was found to be solution-mediated and the calcite growth was the rate-determining process.

A year later Spanos and Koutsoukos (1998) investigated the transformation of vaterite into calcite during precipitation of $CaCO_3$, under conditions of constant supersaturation at 25, 35 and 45°C and pH values of 8.5, 9.0 and 10.0. According their results, the transformation of vaterite into calcite over the temperature range considered, at relatively high supersaturation ratios (1.5–1.9), does not depend on pH and temperature but on the supersaturation. The transformation rate was found to decrease as supersaturation increased. On the basis of the kinetics results it was suggested that this transformation took place through vaterite dissolution, followed by calcite crystallisation. At relatively high supersaturation ratios the transformation was controlled by the dissolution of vaterite, whereas at lower supersaturation ratios (1.2–1.5) the rate of vaterite dissolution was similar to that of crystallisation of calcite.

Carmona et al. (2004) investigated the precipitation mechanism of chain-like calcite agglomerates. They carried out experiments by carbonating in a $Ca(OH)_2$ suspension at 20, 25 and 30°C, keeping the suspension conductivity at 5 mS/cm. Results demonstrated that the processes at 20°C and 25°C were similar, except in the final stage. The mechanisms, in fact, occurred via the surface and were composed by an initial precipitation of ACC followed by its transformation into calcite chain-like aggregates. These were only intermediate compounds that led to the formation of the final products constituted by spheroidal nano-sized calcite (at 20°C) and sub-micrometric chain-like calcite agglomerates (at 25°C). At 30°C, micrometric calcite of scalenohedral habit precipitated from the solution. According to these researchers, the change in the precipitation mechanism from preferentially via surface to preferentially via solution could be related to the $Ca(OH)_2$ surface area in the reaction mixture during the first steps of precipitation.

In 2005 Andreassen (2005) studied the formation mechanism and morphology in precipitated vaterite. The mixing of concentrated solutions of calcium nitrate ($Ca(NO_3)_2$) and Na_2CO_3 resulted in the formation of ACC which transformed within minutes to vaterite. Vaterite spheres nucleated and grew at a moderate relative supersaturation ratio, determined by the dissolution of the amorphous compound. The inner structure of these spheres exhibited the radiating pattern characteristic for spherulitic crystal growth. The final number of vaterite spherulites were typical for heterogeneous nucle-

ation processes.

In 2006 Nehrke and Van Cappellen (2006) studied the transformation of framboidal[3] vaterite aggregates into calcite. Their results suggested that the transformation into calcite occurred partly within the framboidal vaterite aggregate, leading to much higher transformation rates compared to the transformation of solid non-framboidal vaterite spherulites. The transformation from inside the framboidal vaterite led to the formation of single crystal calcite rhombs as observed for the transformation of non-framboidal vaterite spherulites.

In 2008 Xu et al. (2008) studied the roles of water and polyelectrolytes in the phase transformation of ACC. In their experiments, different ACC were prepared in absence and presence of polysodium 4-styrene sulfonate and polyacrylic acid. The transformation processes were investigated under different water concentrations. Results showed that ACC contained about 15% water. Under thermal transformation, that water was released from the ACC at temperatures above 100 °C. The $CaCO_3$ begun to crystallize at around 270–400°C forming calcite. The use of the polymer inhibited this crystallization process and the crystallization temperature moved toward higher values. These transformations allowed the study of the evolution steps of the ACC in different water–ethanol solutions. Results showed that the water could accelerate the transformation and crystallization of ACC. Furthermore, results showed that the increase of the quantity of water in the solvent phase always led to the promotion of the transformation kinetics. Interestingly, vaterite and aragonite, were produced in solution of low water content. However, addition of water could still make these crystals turn into calcite if enough time was provided.

2.2.4. Adhesion mechanism

One of the last subjects discussed in the scientific literature that have a particular importance on the development of new building materials, is the adhesion mechanism of $CaCO_3$. Unfortunately, to date only a few papers have been published regarding this subject. In 2002 Abdel-Aal et al. (2002) studied the adhesion mechanism of $CaCO_3$ using a quartz crystal micro-balance (QCM) with ion concentration measurements in which adhesion of crystals of $CaCO_3$ on the solid surface and its bulk precipitation were traced simultaneously. The adhesion mechanisms on the gold surface of the QCM sensor during the precipitation and transformation of $CaCO_3$ from highly supersaturated solution were obtained at 25°C. After several minutes of induction after the QCM sensor was inserted into the reaction solution, orthorhombic calcite nucleated and grew on the surface of the sensor. These processes were synchronized to the

[3] The term *framboid* describes a micro-morphological feature common to certain sedimentary minerals. The term is derived from the French *la framboise*, meaning *raspberry*, reflecting the appearance of the structure under investigation.

precipitation processes in the bulk solution, constituted by the transformation of ACC to calcite and vaterite and transformation of vaterite to calcite. When the QCM sensor was inserted into the suspension after the complete transformation of ACC, a thin disc of leaf-like vaterite grew on the surface, whereas the vaterite precipitated in solution was spherical. According to Abdel-Aal and colleagues, these adhesion processes were mainly controlled by the lattice ion activity product of the solution. In addition to these direct adhesions, the indirect adhesion of the crystalline $CaCO_3$ already precipitated in the solution was observed, although the contribution of this adhesion to the scaling was very small.

In 2005 Beruto et al. (2005) studied the binding mechanisms in the setting of Ca and Ca–Mg putty-limes in the temperature range between 15 and 30°C. Tests were carried out at 80% RH, under isothermal conditions, with a flux of wet N_2 containing 1% CO_2. Results showed that the binding mechanisms of $CaCO_3$ in the strengthening of the putty-lime systems was due to the interconnected texture formed from fine $CaCO_3$ crystallites during the precipitation process.

In 2006 De Silva et al. (2006) investigated the reaction kinetics, strength and microstructure in carbonate binders with the aim of establishing the characteristics of $CaCO_3$-based binders that are associated with strength (considered as an indicator of binder performance). Their results revealed that the crystalline state and the morphology of the carbonate formed, rather than the degree of conversion of $Ca(OH)_2$ into $CaCO_3$, are highly influenced by the binder strength.

2.3. Carbonation in lime based building materials

As already stated (see paragraph 2.1), carbonation is the only reaction common to all types of lime based materials for the construction industry. Considering the chemistry involved, these materials can be divided into four groups:

1. materials based on the sole use of *air lime* (both *calcium lime* and *dolomitic lime*);

2. materials based on mixtures of air lime and hydraulic additives. According to the classification contained within the European standard BS EN 459-1, these types of material can be found in both classes, the *formulated limes containing air lime* class or the *hydraulic limes cement free* (BS EN 459-1, 2010, p. 19);

3. materials based on the sole use of *natural hydraulic limes*;

4. materials based on mixtures of *natural hydraulic lime* and *hydraulic additives*. This type of material can be found within the class: *formulated limes* described in the BS EN 459-1 (2010, p. 19).

In this list, numbers highlight the complexity of chemical reactions, from the simplest group containing only air lime (group n.1) to the most complex group containing natural hydraulic lime and hydraulic additives (group n.4).

Groups 1 and 2 can be divided in sub-groups considering, once again, the complexity of the chemical reactions. Within the group n.1, in fact, it is possible to divide limes containing only $Ca(OH)_2$ from limes containing $Ca(OH)_2$ and $Mg(OH)_2$. Group 2, can be divided between mixtures containing silico-aluminate additives and mixtures containing only siliceous additives [4].

All the groups and the sub-groups are reported in figure 2.3 and 2.4 that summarise their main characteristics together with the main compounds and chemical reactions. The figures show that the carbonation reaction is common to all the group considered but also that the conditions where this reaction takes place are quite different among the different groups [5].

In the group of *air lime* containing calcium lime, for instance, carbonation is the only reaction whereas in the *formulated lime* containing NHL, this reaction takes place together with (or in competition with) other reactions and this can affect the whole hardening process.

Systems in figure 2.3 become more and more complex from the left, where the only compound is $Ca(OH)_2$, to the right, where mixtures of air lime and hydraulic additives

[4] A further degree of complexity would be achieved by considering the presence of $Mg(OH)_2$.
[5] In these figures, all possible reactions between binder and aggregate are disregarded.

are represented[6]. Figure 2.4 shows mixtures where the chemistry of reactions is even more complex from the *natural hydraulic lime* (left hand side) to the mixes of NHL with hydraulic additives (right hand side). This table should be joined on the left hand side to the figure 2.3. On its right hand side the chemistry of ordinary Portland cement should be represented. As well as the complexity of the main groups, also the complexity of sub-groups increases from left to right in all the tables.

In order to clarify the role of carbonation and the factors that can affect this reaction, a short description of the systems summarized in figure 2.3 and 2.4 is given in the following paragraphs.

2.3.1. Group 1: air limes

According to the BS EN 459-1 (2010, p.6), *air limes* are limes that combine and harden with atmospheric carbon dioxide. Consequently, all materials containing only air lime, carbonation is the main reaction (if not the only one).

As discussed in detail in the next chapter, calcium carbonate crystals can precipitate from the aqueous solution contained in lime and grow on the surface of $Ca(OH)_2$ crystals (figures 2.5 and 2.6) until the complete consumption of Ca^{2+} ions or, most commonly, until an external factor such as a lack of water or CO_2 or the impossibility for the $Ca(OH)_2$ to dissolve in water, occurs (Van Balen, 2005; Griffiths, 2011; Cizer, 2009; Cook and Batchelor, 1996; Cizer et al., 2012a).

The reaction is affected by several factors including pH of solution, $[Ca^{2+}]/[CO_3^{2-}]$ ratio, temperature and water content. If magnesium ions (Mg^{2+}) or other ions are in solution together with Ca^{2+} like in the dolomitic lime, crystallization of calcite is inhibited while aragonite precipitation is promoted (Lin and Singer, 2009; Krauskopf, 1979). Depending on the Mg^{2+}/Ca^{2+} ratio, $CaCO_3$ precipitated from the solution can assume different habits and form different crystalline structures such as ikaite, hydrated calcite and magnesium-calcite (Meldrum and Hyde, 2001; Loste et al., 2003). Finally, magnesium itself can react with water and dissolved CO_2 to form magnesium based phases such as one of the hydrate phases of magnesite (Meldrum and Hyde, 2001).

2.3.2. Group 2: formulated limes containing air lime and hydraulic limes cement free

In more complex systems such as those included in the *formulated lime containing air lime* class or in the *hydraulic lime cement free* class (respectively figure 2.4 and

[6] In the system *formulated lime containing air lime* (figure 2.3), the dolomitic lime behaves in almost the same manner as calcium lime but, as dolomite contains two alkaline earth metals (calcium and magnesium), more reactions can take place. Unfortunately, reactions of magnesium with silicate and aluminate are not yet completely understood.

Figure 2.3.: Schematic description of systems containing air lime and systems based on mixtures of air lime and hydraulic additives.

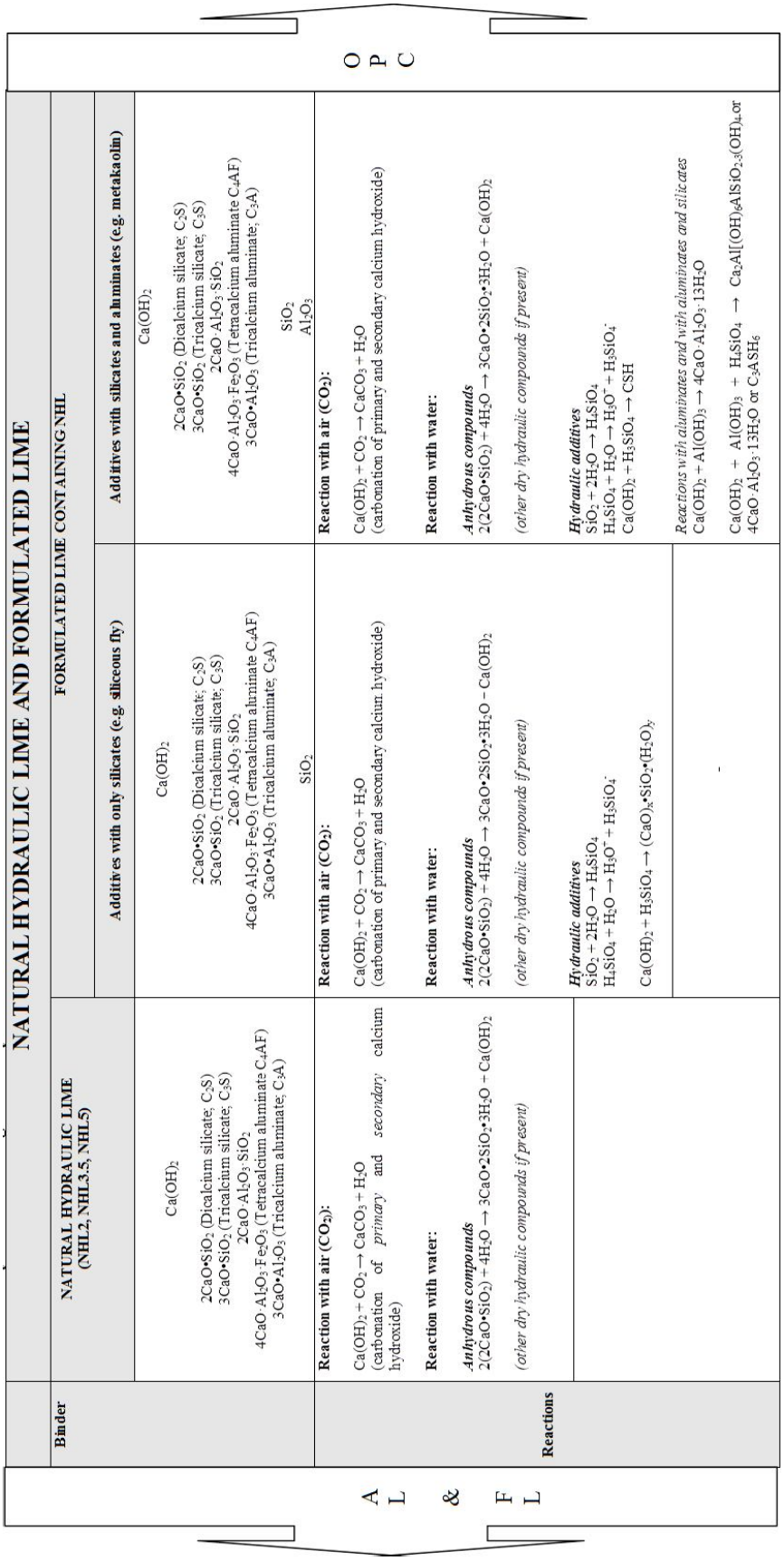

Figure 2.4.: Schematic description of systems containing natural hydraulic lime and systems based on mixtures of natural hydraulic lime and hydraulic additives.

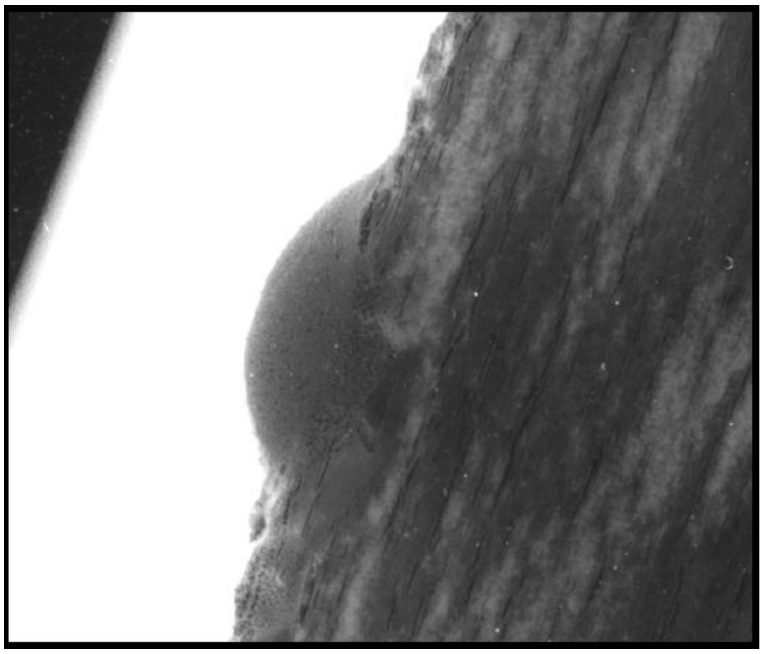

Figure 2.5.: TEM image of a cross section of a portlandite crystal (right hand side) with a nodule of $CaCO_3$ growing on its [0001] face (from: Griffiths, 2011, p.83 fig 6.6).

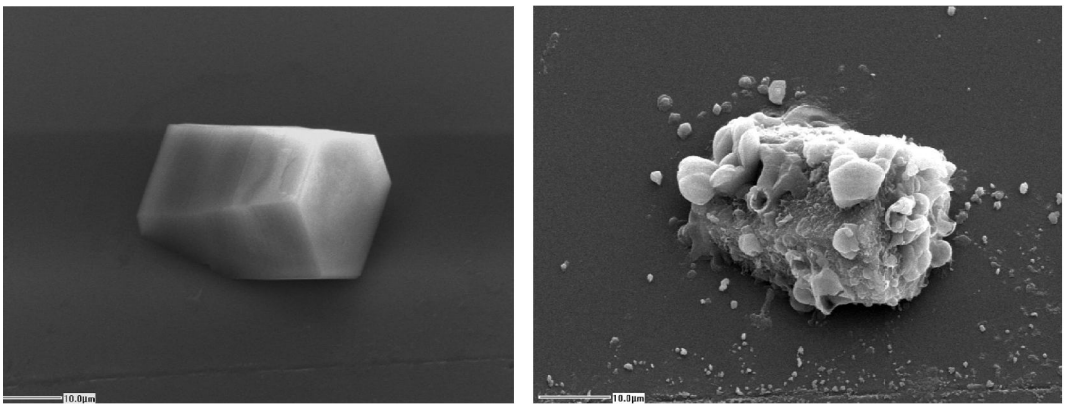

Figure 2.6.: Portlandite crystal before and after carbonation (from: Griffiths, 2011, p. 88 fig. 6.14 and p.90 fig. 6.16.

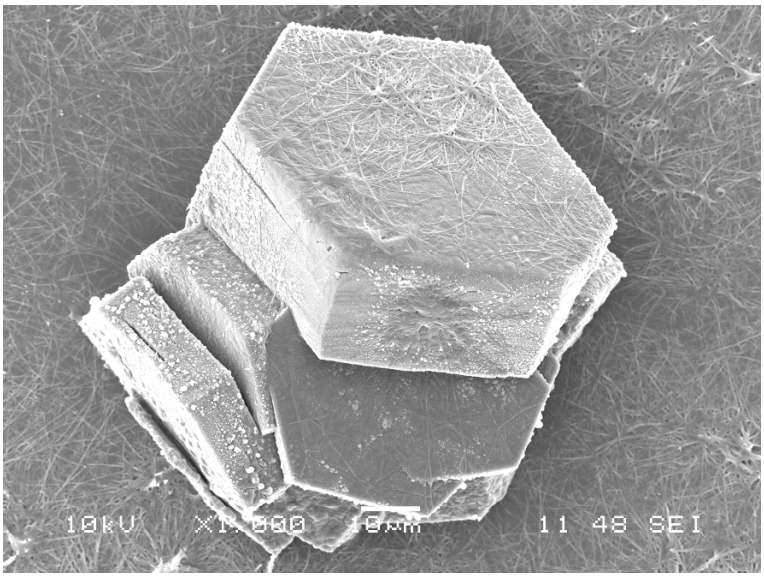

Figure 2.7.: Portlandite crystals on a glass substrate covered with CSH needles.

2.3; BS EN 459-1, 2010) air limes are mixed with hydraulic additives such as silica fume or siliceous fly ash. In these mixtures carbonation still happens but together (and very often in competition) with other reactions and compounds. More precisely, in these systems carbonation is still one of the main reactions because the amount of lime is usually no less than 50% of the binder fraction (Cizer, 2009), but it takes place together with the reaction between Ca^{2+} and silicic acid ($SiO_x(OH)_{4-2x}$) leading to the formation of calcium silicate hydrate compounds (CSH).

CSH is a family of amorphous or nearly amorphous hydrated compounds containing CaO and SiO_2 linked with water molecules. These compounds are supposed to determine the mechanical properties of mixes containing lime and pozzolanic additives. They have a variable stoichiometry (Chen et al., 2004) and their general formula can be written as:

$$CaO_x \bullet SiO_2 \bullet H_2O_y \tag{2.3.1}$$

with x and y values that may vary over a wide range (Hewlett, 2004, p. 243, 249).

Hydration mechanisms of pozzolanic additives are described as dissolution of silicate plates or chains in highly alkaline water ($pH \approx 12$) produced by the dissolution of $Ca(OH)_2$ with subsequent reaction in solution of the silicic acid (H_4SiO_4) with Ca^{2+} and precipitation of CSH compounds (figure 2.7).

CSHs assume two distinct semi-crystalline forms called $CSH(I)$ and $CSH(II)$. The former is a poorly crystallized tobermorite-like phase (Hewlett, 2004, p.495) whereas the latter is a poorly crystallized Jennite-like phase (Hewlett, 2004, p.243, 249)[7]. At a

[7] Tobermorite and Jennite are two calcium silicate hydrate minerals very common in hardened cement based mixtures.

micrometric scale, morphology of CSHs is quite changeable: they may, in fact, exist as fibres, flakes, honeycombs, tightly packed grains or seemingly featureless dense material (Hewlett, 2004, p.243, 255).

If the pozzolanic additives used together with lime contain not only silicon but also aluminium, such as the clay-based materials (e.g. metakaolin and brick powder), calcium aluminate hydrate (CAH) compounds can precipitate together with the CSH.

At first, this hydrate compound is a gel-like material but later a crystalline structure develops. In $Ca(OH)_2$ rich environments the main crystalline compound is C_4AH_{19}. This is a meta-stable, hexagonal crystal that, as hydration progresses, transforms into a more stable phase: katoite or C_3AH_6 or, again, $Ca_3[Al(OH)_6]_2$ with cubic arrangement (Hewlett, 2004, p.260). This conversion depends on several factors including the $^{CaO}/_{Al_2O_3}$ ratio and the presence of CO_2 (Hewlett, 2004, p.260). Furthermore, C_3AH_6 is one of the members of the hydrogarnet family that may produce solid solutions with other hydrated phases such as C_3FH_6 (hydrated calcium ferrite), C_3AS_3 and C_3FS_3 (Hewlett, 2004, p.260). For this reason, if it precipitates in a Si-rich environment, silicate-aluminate hydrated phases such as gehlenite hydrate (C_2ASH_8) can form[8].

Pozzolanic reactions are strictly linked to the so called *pozzolanic activity* that includes two parameters: maximum amount of lime that these materials can combine with, and rate at which such a combination happens. Both factors depend on the nature of additives (that can be quite different; Hewlett, 2004, p.471) such as the nature of active phases, SiO_2 content, lime:hydraulic compound ratio, specific surface area, water:solid ratio within the mix and temperature (Hewlett, 2004, pp.488-489). As a consequence it is possible to define only a general trend for the reactions.

Considering the CSH and CAH produced by hydration of brick powder in old lime mortars, it has already been observed that hydrated compounds generated by the hydration of discrete particles are generally concentrated in rings of several tens of microns thickness around the particles themselves (figure 2.8; Coutelas et al., 2004; Moropoulou et al., 2004; Baronio et al., 1997). For this reason, it is likely that the influence of this reaction on the carbonation is mainly at a local scale.

This type of hydration, which is different from the hydration of anhydrous silicates contained in NHL (described in the next paragraph), does not produce new $Ca(OH)_2$ but consumes Ca^{2+} ions by the reaction with Si and/or Al. Consequently this reaction can locally affect the $^{Ca^{2+}}/_{CO_3^{2-}}$ ratio with subsequent influence on the crystalline structure of $CaCO_3$.

Studies on spontaneous precipitation of $CaCO_3$ from aqueous solution in the presence of dissolved (amorphous) silica showed that in under-saturated solution (with regard to the silica) the induction time for $CaCO_3$ nucleation is decreased. In this

[8]Gehlenite is a meta-stable compound that tends to turn into hydrogarnet with time (Hewlett, 2004, p.496).

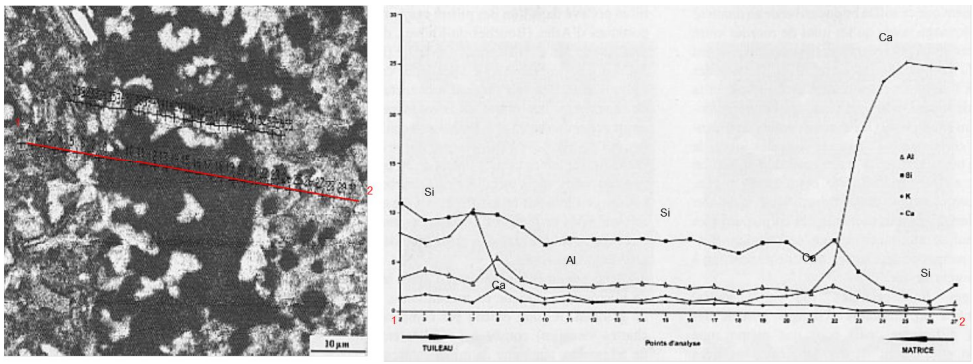

Figure 2.8.: Left hand side: Detail of the contact between a grain of crushed brick (grey area on the left hand side) and the lime (brighter area on the right). In the middle a transition zone is highlighted by the dark area (scale bar=10 microns). Right hand side: results of the EDX analysis for *Ca*, *Si* and *Al*. Measurements were taken from the crushed brick (left hand side) to the carbonated matrix (right hand side). Data show a high concentration of *Ca* and a low concentration of *Al* and *Si* in the area of lime while a high concentration of *Si* and low concentration of *Ca* is shown in the brick. The transition zone shows quite a high concentration of *Si* and *Al* (compared to the brick) and a low concentration of *Ca* (from: Coutelas et al., 2004).

context, if Ca^{2+}/CO_3^{2-} is high, vaterite is the main solid phase, whereas if the Ca^{2+}/CO_3^{2-} ratio is low, a mix of calcite and vaterite can be observed. On the contrary, if the concentration of amorphous silica is above saturation and Ca^{2+}/CO_3^{2-} ratio is low, calcite is the only polymorph but crystals are usually small and faceted (Lakshtanov and Stipp, 2010).

Finally, if alumina hydrated phases are in the system, they can react with $Ca(OH)_2$ and $CaCO_3$ to produce calcium alumina carbonate hydrate phases (C_4AcH_{11}; Cizer, 2009; Hewlett, 2004, pp.493-495) that also affect the carbonation product.

2.3.3. Group 3: natural hydraulic limes

According to the BS EN 459-1, a *natural hydraulic lime* is a lime with hydraulic properties produced by burning more or less argillaceous or siliceous limestone. It has the property of setting and hardening when mixed with water and by reaction with CO_2 from the air.

Mixtures containing natural hydraulic limes (NHL; figure 2.4) are completely different from the other limes previous discussed. NHLs, in fact, are more similar to cement than the lime previously described. These materials contain anhydrous compounds such as di-calcium silicate (C_2S or belite) and tri-calcium silicate (C_3S or alite; although to a lesser extent compared to the belite and to the C_3S content in cement). If the firing temperature is close to or exceeds 1200°C, also aluminium compounds such as tricalcium aluminate (C_3A) and tetra calcium aluminate (C_4AF) can be formed within the NHL. All these compounds do not exist in the lime systems previously described and have the characteristics to react quicker than hydraulic additives with water. Their behaviour and their interaction with the carbonation reaction can be understood

through the literature of cement chemistry.

In order to understand the role of carbonation in this type of lime, it is important to note that NHL2-type limes are richer in $Ca(OH)_2$ than the NHL5-type, where anhydrous calcium silicates are the main compounds. Consequently, carbonation is still one of the main reactions in feebly hydraulic lime (NHL2-type) whereas it is only a secondary reaction in highly hydraulic limes (NHL5-type).

Moreover, hydration of belite (and, in case, also of alite) produces new $Ca(OH)_2$ as a by-product. According to the *nucleation of* $Ca(OH)_2$ theory, in fact, as the $^{CaO}/_{SiO_2}$ ratio in the *CSH* is always lower than that of C_2S or C_3S, hydration of belite and alite is always associated with production of $Ca(OH)_2$ (Hewlett, 2004, p.248). This means that, as a result of the new Ca^{2+} production, a higher ratio $^{Ca^{2+}}/_{CO_3^{2-}}$ can be locally achieved (Hewlett, 2004, p.265) and this can affect the carbonation reaction according to the processes previously discussed or new $Ca(OH)_2$ crystals can be produced.

The $Ca(OH)_2$ produced by hydration of anhydrous compounds can lead to a new carbonation reaction that takes place with a certain delay compared with the reaction of $Ca(OH)_2$ embedded in the system since the beginning of the mixing process.

Finally, it must be pointed out that, if high firing temperatures are reached during NHL production, CaO particles produced by the decomposition of the $CaCO_3$ contained in the impure limestone, can sinter leading to a reduction in the hydration rate of CaO that affects the subsequent carbonation process.

2.3.4. Group 4; formulated lime containing NHL

Formulated limes (FL; figures 2.3 and 2.4) are binders with hydraulic properties mainly consisting of air lime and/or natural hydraulic lime with added hydraulic and/or pozzolanic materials (BS EN 459-1, 2010).

Chemistry of these mixtures is more complicated compared to the chemistry of all other groups. In order to make this complexity clear, the difference between the hydration reaction of hydraulic additives (e.g. fly ashes) and hydration reaction of anhydrous calcium silicate (e.g. belite) must be highlighted. Despite the fact that hydraulic compounds produced by hydration of belite (or alite) are considered similar to those produced by the hydraulic additives previously mentioned (Hewlett, 2004, p.493), in fact, some SEM and TEM images of hydrated pastes containing NHLs show morphologies that suggest different reaction kinetics and reaction mechanisms.

The morphologies of hydrated phases produced by the hydration of belite and alite suggest a direct reaction of anhydrous calcium silicate with water followed by a subsequent epitaxial growth of CSH needles on the surface of C_2S and C_3S particles that in this manner assume the shape of chestnut shells or see urchins (figure 2.9 left hand side). Reaction of hydraulic additives such as fly ash with air lime, instead, pro-

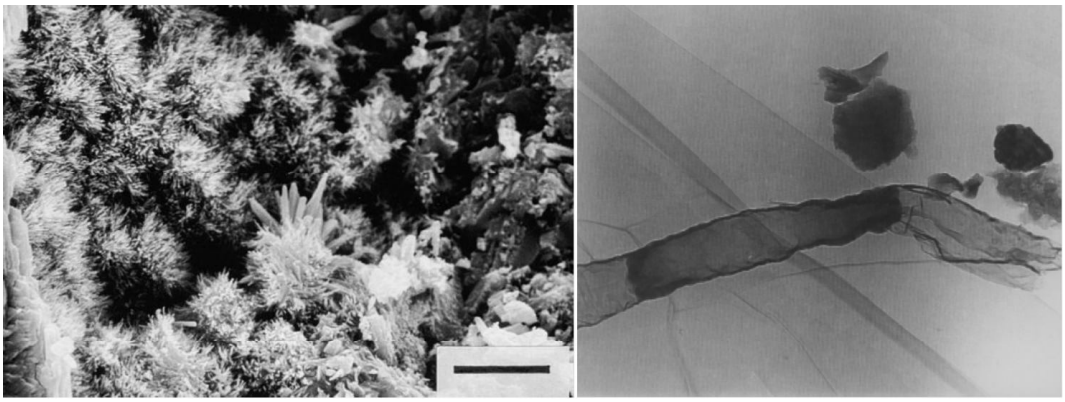

Figure 2.9.: Left hand side: SEM detail of the microstructure of CSHs in the matrix of an hydraulic mortar produced using NHL (scale bar=10 microns; Callebaut et al., 2001, p.400). Right hand side: TEM image of CSH and CSAH gel in a mortar containing brick fragments (magnification 30.000x; Moropoulou and Bakolas, 2000, p.45).

duces a dissolution process of silicates in water that lead to the reaction (in water) with $Ca^{2+}$and to the subsequent precipitation of CSH gel phases (figure 2.9 right hand side).

As a consequence, these morphologies lead to the hypothesis of not only different mechanisms but also different reaction rates: faster in the former and slower in the latter (Hewlett, 2004, p.490, 543). A confirmation of these differences comes from the list of hydration steps of cement containing fly ashes, reported by Franco Massazza in the chapter: *Pozzolana and Pozzolanic Cement* contained in one of the most important books on the chemistry of cement: *Lea's chemistry of cement and concrete* (Hewlett, 2004, p.471). In this list, even if the author suggests an overlap of the hydration reactions of clinker phases and fly ashes (that certainly occurs initially), the fly ash reaction is still reported to be active after 3 days, while the hydration of clinker is reported to be concentrated in the first ten hours (Hewlett, 2004, p.534).

Differences in the reaction mechanisms and kinetics are important in the study of the influence of these reactions on the carbonation process. If the carbonation takes place near particles of pozzolanic additives, absorption of Ca^{2+} ions by the CSH is not compensated by the release of Ca^{2+} as happens during the hydration process of C_2S. As a consequence, the habit of the $CaCO_3$ crystals can be affected. Similarly when the carbonation takes place near to belite (or alite) grains, whose hydration involve an enrichment of Ca^{2+} ions in solution, an increase of the $^{CaO}/_{SiO_2}$ ratio is produced with consequences on the formation of $CaCO_3$ newly formed phases.

Because hydration of belite takes place quicker than hydration of pozzolanic additives, it is also possible to suppose that, initially, $CaCO_3$ precipitates in a Ca^{2+}-rich environment leading to the rhombohedral habit of calcite, whereas later carbonation happens in a Ca^{2+}-poor environment leading to the formation of scalenohedral calcite.

Finally, as already seen, if the hydraulic reactions involve production of calcium aluminate hydrate, this compound can interact with $CaCO_3$ and $Ca(OH)_2$ to form

carboaluminate C_4AcH_{11}, whereas production of new $Ca(OH)_2$ by the hydration process of the C_2S silicates leads to a delayed carbonation affecting the microstructure of hardened specimens and their mechanical properties.

3. Chemistry of carbonation

3.1. Lime production and use

Traditional air lime[1] is produced from limestones with different levels of purity but essentially composed of $CaCO_3$ of geological origin. The limestone is burnt at around 900°C in special kilns to produce gaseous CO_2 and a solid phase forms composed of calcium oxide (CaO) otherwise known as *quicklime* (Boynton, 1966; Norman, 1961; Oates, 1998; Vecchiattini, 2010; Rattazzi, 2007; Goren and Goring-Morris, 2008), according to the following chemical equation:

$$CaCO_{3(s)} \overset{heat\ (900^{\circ}C)}{\longrightarrow} CaO_{(s)} + CO_{2(g)} \tag{3.1.1}$$

Subsequently, the quicklime undergoes a slaking process where it combines with water. The resulting exothermic reaction forms $Ca(OH)_2$ according to equation 3.1.2.

$$CaO + H_2O \rightarrow Ca(OH)_2 + heat \tag{3.1.2}$$

Depending on the amount of water added, several materials can be produced by slaking the quicklime. From the most to the least rich in water, the products available are (Boynton, 1966, pp.290-291):

- *lime water:* a saturated or unsaturated aqueous solution of $Ca(OH)_2$ without any solid phase.
- *Milk of lime* (or *whitewash*): an aqueous colloidal suspension of $Ca(OH)_2$ particles where the solid phase ranges between 1 and 20%.
- *Lime slurry:* a colloidal suspension of $Ca(OH)_2$ characterized by the consistency of a thick cream without body or plasticity with a $Ca(OH)_2$ content between 20 and 35%.
- *Lime putty:* a plastic moldable paste, sometimes described as a colloidal gel that contains between 30 and 40% of $Ca(OH)_2$.

[1] Here, the adjective *traditional* is added to differentiate the production process of the common lime from the production process of nano-lime discussed later in this thesis.

- *Dry hydrated lime:* a dry fine white powder that contains between 72 and 75% of $Ca(OH)_2$ and for this reason is the most concentrated form of lime.

All these forms of $Ca(OH)_2$ are commonly referred to as lime, although in chemistry the same term is also used when referencing CaO.

When mixed with water (if needed) and aggregate (e.g. sand), the $Ca(OH)_2$ within the mixtures hardens by reacting with atmospheric CO_2, resulting in the formation of $CaCO_3$ (from which the term *carbonation* is used), according to the equation 3.1.3.

$$Ca(OH)_2 + CO_2 \rightleftharpoons CaCO_3 + H_2O \tag{3.1.3}$$

Since $Ca(OH)_2$, CO_2 and $CaCO_3$ are the main compounds involved in this reaction, a detailed description of these is reported in the following paragraphs.

3.2. Calcium hydroxide

Calcium hydroxide is a non-combustible compound with chemical formula $Ca(OH)_2$, molar weight of 74.093 g/mol and density of 2.24 g/cm^3 at 20ºC.

Solubility in water at the same temperature is of about 1.7 g/l. Calcium hydroxide dissolution produces an alkaline environment with pH≈12.6 (Chemical Rubber Company, 2013-2014, 4-55). At atmospheric pressure it decomposes to form CaO in the temperature range from 450 to 500ºC, depending on the crystal size (Datta et al., 1969).

Calcium hydroxide can be found in nature in the form of colourless crystals or as a white powder. From a mineralogical point of view, it crystallizes in only one form called *portlandite*[2] that belongs to the trigonal-hexagonal scalenohedral system. Its habit is hexagonal and crystals can be both, elongated along the c axes or plate-like (sheet-form such as mica). They have a perfect cleavage along the {0001} faces and, consequently, their tenacity is sectile with a brittle fracture. Portlandite hardness is 2.5-3 (between gypsum and calcite) in the Mohs scale.

3.2.1. Solubility in water and pH

One of the most important characteristics of $Ca(OH)_2$ that allows its use in the construction industry is its solubility in water. Chemically, the $Ca(OH)_2$ is considered only slightly soluble in water (Johannsen and Rademacher, 1999) but, as shown in figure 3.1, carbonation lead to the formation of a more insoluble salt.

Despite this limited solubility, addition of pure water to solid $Ca(OH)_2$ causes dissolution (as said, to an extent of about 1.7 g/l) with diffusion of $Ca^{2+}$and OH^- ions

[2]The name comes from the fact that this compound is a common product of hydration of portland cement.

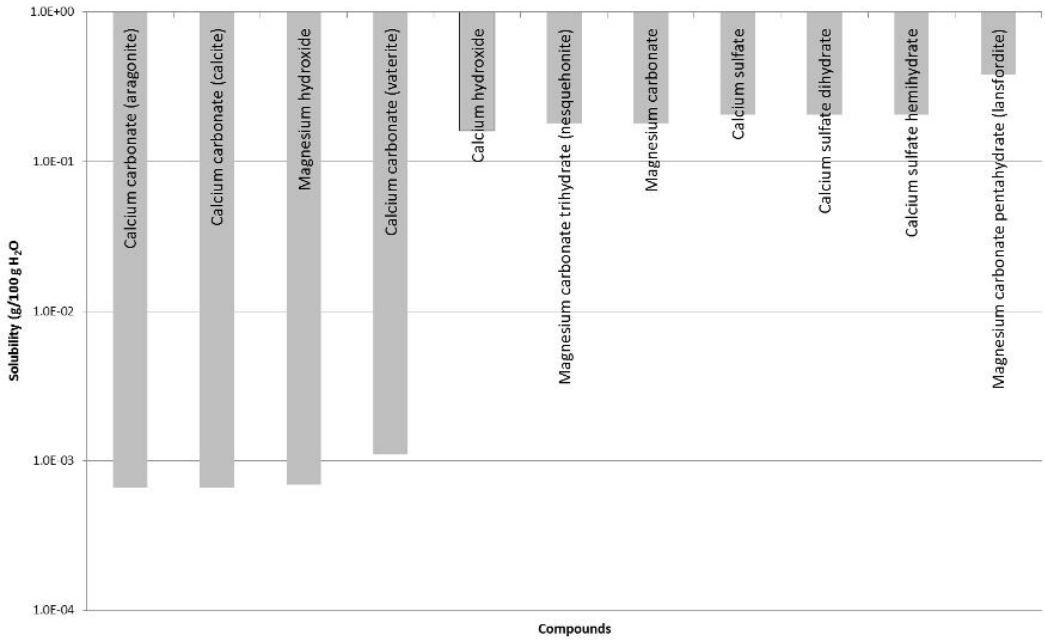

Figure 3.1.: Comparison of the aqueous solubility of different *Ca* and *Mg* compounds at 25°C. Solubility increases from left to right. The most insoluble compounds are the three $CaCO_3$ anhydrous polymorphs and magnesium hydroxide ($Mg(OH)_2$). Calcium hydroxide, in contrast, has solubility similar to the different forms of magnesium carbonate and calcium sulphate (e.g. gypsum; data from: Chemical Rubber Company, 2013-2014).

into the water. The equation for the dissolution of this mineral including the forward and a backward reaction is described in 3.2.1 (Johannsen and Rademacher, 1999, p.72; Pankow, 1991, p.230):

$$Ca\,(OH)_{2(s)} \rightleftharpoons Ca^{2+} + 2\,OH^{-} \tag{3.2.1}$$

According to this equation, the solubility constant of $Ca\,(OH)_2$ can be calculated as (Pankow, 1991, p.230):

$$K_{Ca(OH)_2} = \left\{Ca^{2+}\right\}\left\{OH^{-}\right\}^2 \tag{3.2.2}$$

where $\left\{Ca^{2+}\right\}$ and $\{OH^{-}\}$ are the concentration of calcium and hydroxyl ion, respectively.

Equation 3.2.2 states that crystals of $Ca(OH)_2$ dissolve until a specific value is reached ($K_{Ca(OH)_2}$), that is when the solvent is saturated with respect to the $Ca(OH)_2$ solid phase. The saturation state of an aqueous solution with respect to this mineral ($\Omega_{Ca(OH)_2}$) can be calculated as the ratio of the concentration product or ion activity to the stoichiometric solubility product, as shown in equation 3.2.3:

Table 3.1.: Aqueous solubility of $Ca(OH)_2$. Column on the right reports the percentage change in concentration at different temperatures (solubility data from: National Lime Association, no date, p.3).

Temperature [ºC]	Solubility [g/100g sat. sol.]	Moles of Ca^{2+} ions	$[Ca^{2+}]$ ions [%]
0	0.185	0.02497	100
10	0.176	0.02375	95.14
20	0.165	0.02227	89.19
25	0.159	0.02146	85.95
30	0.153	0.02065	82.70
40	0.140	0.0189	75.68

$$\Omega_{Ca(OH)_2} = \frac{\left\{Ca^{2+}\right\}\left\{OH^{-}\right\}^2}{K_{Ca(OH)_2}} \tag{3.2.3}$$

According to this equation, if $\Omega_{Ca(OH)_2} = 1$, the $Ca(OH)_2$ solid phase and the related solution are in equilibrium; if $\Omega_{Ca(OH)_2} < 1$, the solution is under-saturated with respect to the solid phase and, consequently, a mineral dissolution can occur until reaching the equilibrium; if $\Omega_{Ca(OH)_2} > 1$, the solution is supersaturated and precipitation of a new $Ca(OH)_2$ solid phase[3] occurs (Morse and Mackenzie, 1990, p.34).

As well as other minerals, the aqueous solubility of $Ca(OH)_2$ varies with temperature, as reported in table 3.1 and figure 3.2.

Using the solubility constant and the molar weight it is possible to calculate the dissolved moles of Ca^{2+} and OH^- ions in aqueous solutions in equilibrium with the solid phase. Considering, for instance, a solubility of $0.165\,g/100g(H_2O)$ at 20ºC (National Lime Association, no date, p.3; a similar value is reported by the Chemical Rubber Company, 2013-2014) the moles of Ca^{2+} ions dissolved in water at equilibrium are:

$$\frac{Aqueous\,solubility}{Molecular\,weight} = \frac{1.65}{74.093} = 22.26 \times 10^{-3}\,moles \tag{3.2.4}$$

According to equation 3.2.1 the dissolution of a mole of $Ca(OH)_2$ produces two moles of OH^- ions so that in a saturated solution at 20ºC there are 44.54×10^{-3} moles of OH^- ions.

Because the dissociation product of water (K_w) is constant for all water solutions (not only for the neutral ones), it is possible to calculate the pH of a saturated solution of $Ca(OH)_2$ as follows:

[3]Not necessary the same of the solid phase in contact with the solution. A typical example of this situation is the precipitation of calcite in an aqueous solution in contact with aragonite.

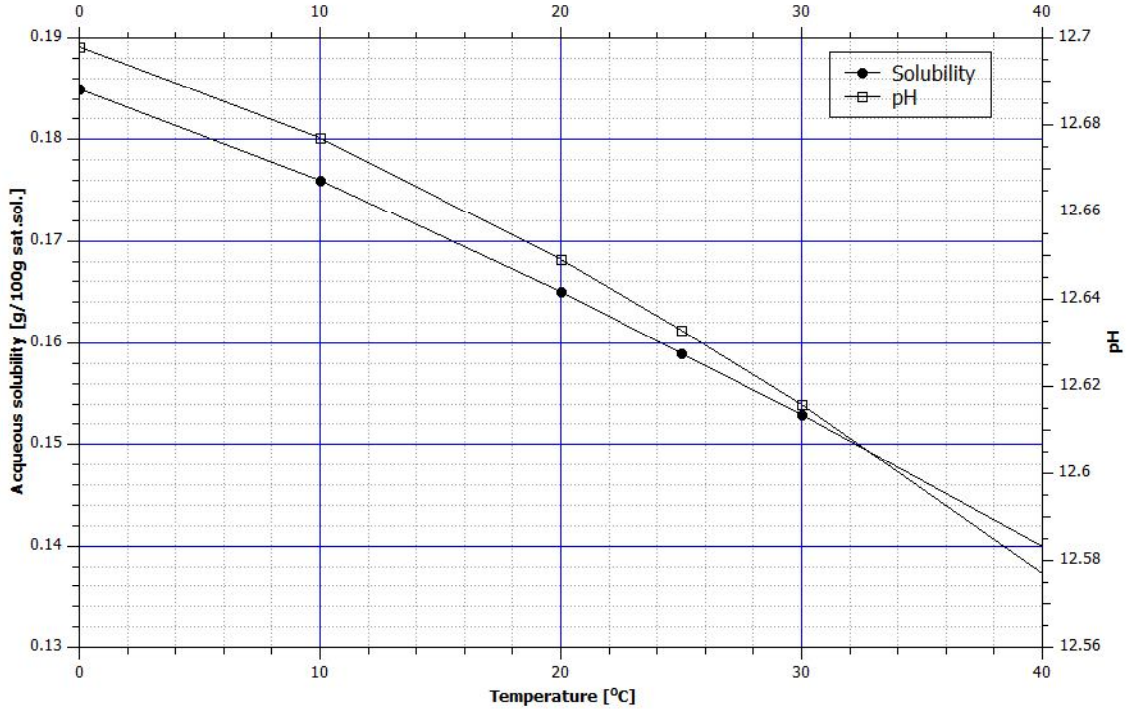

Figure 3.2.: Aqueous solubility of $Ca(OH)_2$ and pH of saturated aqueous solutions at different temperatures. Data from: National Lime Association, no date, p.3 and table 3.2.

Table 3.2.: pH of saturated solutions of $Ca(OH)_2$ at different temperatures.

Temperature [°C]	pH
0	12.698
10	12.677
20	12.649
25	12.633
30	12.616
40	12.577

$$pH = -\log\{H^+\} = -\log\frac{K_w}{\{OH^-\}} = \tag{3.2.5}$$

$$= -\log\left(\frac{10^{-14}}{44.54\times10^{-3}}\right) = -\log\left(2.25\times10^{-13}\right) = 12.65$$

where $\{H^+\}$ and $\{OH^-\}$ are the concentrations of protons and hydroxyls groups, respectively.

Since the aqueous solubility of $Ca(OH)_2$ varies with the temperature, the pH of a saturated solution of $Ca(OH)_2$ also varies with the temperature as shown in table 3.2 and figure 3.2.

Equation 3.2.5 can also be used to calculate the pH of an aqueous solution of

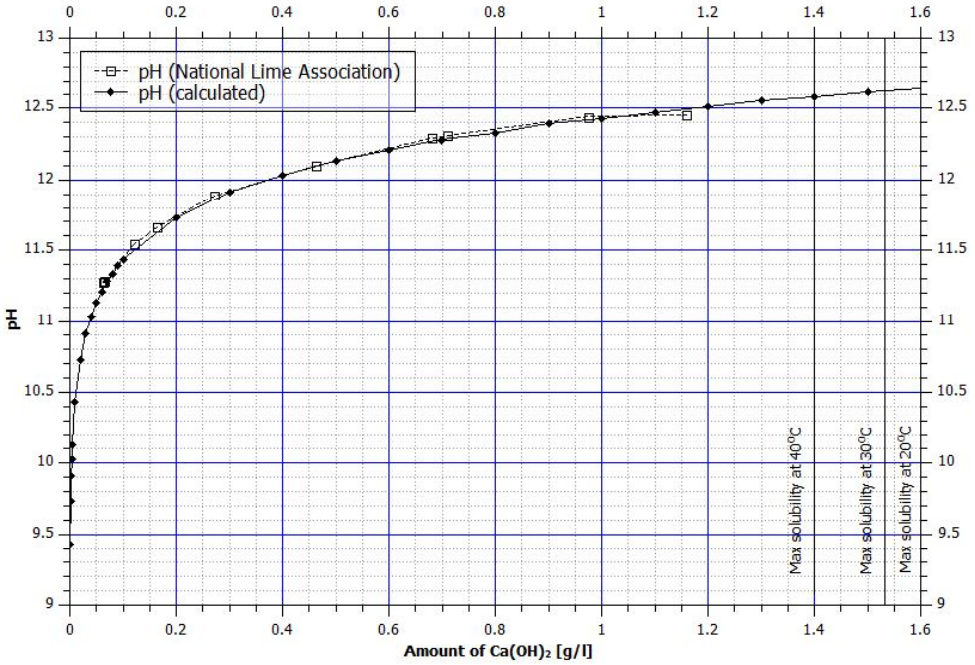

Figure 3.3.: *pH* variations related to different amounts of $Ca(OH)_2$. Comparison of the calculated data with the data published in: National Lime Association, no date, p.3.

$Ca(OH)_2$ when a specific amount of the solid phase is given, assuming that all the $Ca(OH)_2$ dissolves in water[4]. Figure 3.3 and table 3.3 show the results of these calculations (in figure 3.3 are also shown the data published by the National Lime Association (no date, p.2). Results demonstrate that, in an ideal case, even a very small amount of $Ca(OH)_2$ in a litre of water produces a very basic solution. A milligram of $Ca(OH)_2$, for instance, produces a *pH* of about 9.4 which is enough for increasing the CO_3^{2-} dissociation or solubility of silica in water (see figure 3.4).

As a consequence of this, the pH of an aqueous solution of $Ca(OH)_2$ reaches its equilibrium value (e.g. 12.65 at 20ºC) before the saturation state of Ca^{2+} ions in solution is reached (see paragraph 3.2.5 and figure 3.11).

A more complex study of the effect of temperature on the dissolution rate constants of $Ca(OH)_2$ was carried out by Johannsen and Rademacher who developed a thermodynamic model for the kinetics of $Ca(OH)_2$ dissolution in water (Johannsen and Rademacher, 1999). In their model they assumed that the Arrhenius concept can be used to describe the temperature dependence of the solubility constant for the forward (k_f, used in equation 3.2.6) and backward (k_b, used in equation 3.2.7) reactions (Johannsen and Rademacher, 1999, p.76):

[4]This is just an approximation because, as pointed out by Johannsen and Rademacher (Johannsen and Rademacher, 1999), the $Ca(OH)_2$ does not dissolve completely in water (see later in this chapter).

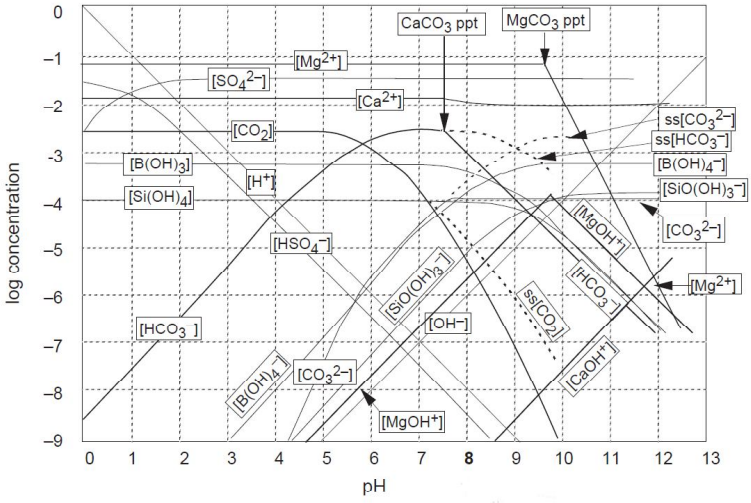

Figure 3.4.: Diagram of the major acid-base components in solutions with intermediate ionic strength. The dashed lines correspond to supersaturation with calcite (from: Lower, 1999, p.23)

Table 3.3.: *pH* variation related to different amount of $Ca(OH)_2$ as calculated according to equation 3.2.5.

Amount of lime [g/l]	*pH*	Amount of lime [g/l]	*pH*	Amount of lime [g/l]	*pH*
1.6	12.64	0.6	12.21	0.05	11.13
1.5	12.61	0.5	12.13	0.04	11.03
1.4	12.58	0.4	12.03	0.03	10.91
1.3	12.55	0.3	11.91	0.02	10.73
1.2	12.51	0.2	11.73	0.01	10.43
1.1	12.47	0.1	11.43	0.005	10.13
1	12.43	0.09	11.39	0.004	10.03
0.9	12.39	0.08	11.33	0.003	9.908
0.8	12.33	0.07	11.28	0.002	9.732
0.7	12.28	0.06	11.21	0.001	9.431

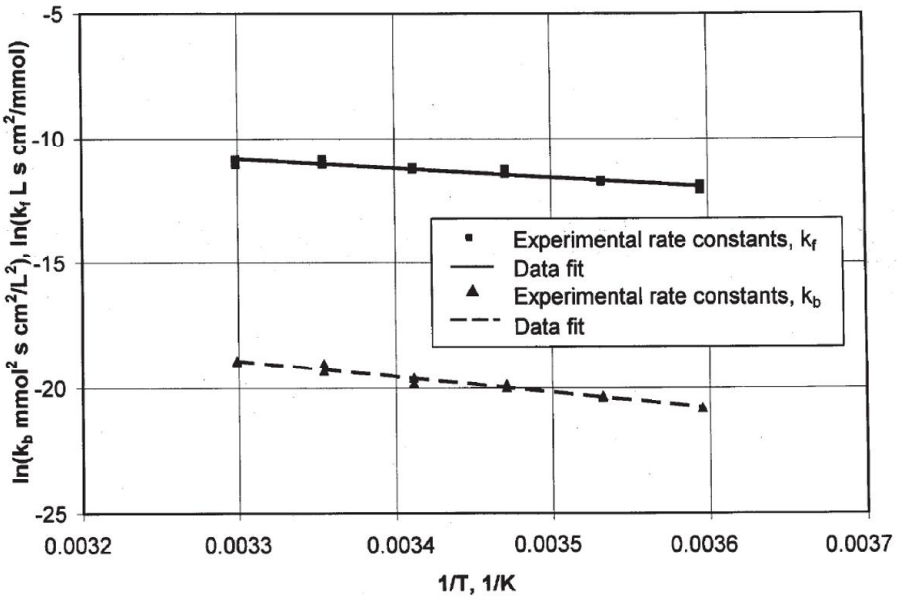

Figure 3.5.: Plot of k_f and k_b versus $1/T$ according to the Arrhenius equation (from: Johannsen and Rademacher, 1999, p.76)

$$\ln\left(\frac{k_{f_2}}{k_{f_1}}\right) = \frac{E_{Af}}{R}\left(\frac{T_2 - T_1}{T_1 \cdot T_2}\right) \tag{3.2.6}$$

$$\ln\left(\frac{k_{b_2}}{k_{b_1}}\right) = \frac{E_{Ab}}{R}\left(\frac{T_2 - T_1}{T_1 \cdot T_2}\right) \tag{3.2.7}$$

In equations 3.2.6 and 3.2.7, E_{Af} is the activation energy for the forward reaction (calculated to be 29.7±2.9 kJ/mol), E_{Ab} is the activation energy for the backward reaction, R is the gas constant and T_1 and T_2 are respectively the lowest and highest temperatures of the range of temperature in which the rate constant ratio is calculated. Figure 3.5 summarizes some of their findings.

3.2.2. Ionic strength and ion activity of saturated solution of $Ca(OH)_2$

As previously stated, the saturation state of a solution can be calculated as the ratio of the concentration product or ion activity to the stoichiometric product, according to equation 3.2.3. Ion activities generally give more accurate results when compared to concentration. The ion activity of a given specie, in fact, represents the number of ions of that specie that can be involved in chemical reactions since not all the ions in solution take part in the chemical processes.

The ion activity of a generic specie i^{th}, however, does not depend only on the concentration of the specie itself but also on the ionic strength of the solution where activity is calculated. In the case of a saturated solution of pure $Ca(OH)_2$ in pure water at 20°C

and 1 atm pressure, the ionic strength ($I_{Ca(OH)_2}$) can be calculated as follow:

$$I_{Ca(OH)_2} = \frac{1}{2}\left(\left\{Ca^{2+}\right\} \cdot z_{Ca^{2+}}^2 + 2\left\{OH^-\right\} \cdot (-z_{OH^-})^2\right)$$

where $\left\{Ca^{2+}\right\}$ and $\{OH^-\}$ are the concentration of calcium and hydroxyl ions and $z_{Ca^{2+}}$ and z_{OH^-} are the charges of the respective ions. Replacing the literal concentration with the actual values, the ionic strength becomes:

$$I_{Ca(OH)_2} = \frac{1}{2}\left\{0.0223 \cdot 2^2 + 2 \cdot 0.0223 \cdot (-1)^2\right\} = 0.0681\,(< 0.1) \tag{3.2.8}$$

According to this result, such types of solution can be considered diluted and, consequently, the activity of Ca^{2+} ions can be calculated using the Debye-Hückel or the Davies equations.

Using the Debye-Hückel equation, that is considered accurate up to a ionic strength of about 0.01, the activity coefficient of Ca^{2+} in solution ($\gamma_{Ca^{2+}}$) is calculated as follows:

$$\log \gamma_{Ca^{2+}} = \frac{-A\, z_{Ca^{2+}}^2\, I_{Ca(OH)_2}^{\frac{1}{2}}}{I_{Ca(OH)_2} + \mathring{a}\, B\, I_{Ca(OH)_2}^{\frac{1}{2}}} \tag{3.2.9}$$

where A and B are constants and a function of both, temperature and solution type, and $\mathring{a}$ is the approximate radius of the hydrated ion considered. Values for A and B in aqueous solution and values for $\mathring{a}$ are given in several books such as Morse and Mackenzie, 1990, p.13.

Alternatively, by using the Davies equation, which is considered accurate over the temperature range 0-50°C (Morse and Mackenzie, 1990, p.12) the the activity coefficient can be calculated as follows (starting from here the ionic strength of a $Ca(OH)_2$ aqueous solution is simply reported as I):

$$\log \gamma_{Ca^{2+}} = -0.5\, z_{Ca^{2+}}^2\, f(I) \tag{3.2.10}$$

where:

$$f(I) = \left(\frac{I^{\frac{1}{2}}}{1 + I^{\frac{1}{2}}} - 0.2I\right)\left(\frac{298}{t + 273}\right) \tag{3.2.11}$$

Table 3.4 shows the results of calculations for the activity coefficients and the ion activities of the Ca^{2+} ions within the temperature range 0-40°C[5]. Results are in agree-

[5] In the results obtained with the Debye-Hückel equation no correction with the "B-dot" method was applied (Ottonello, 1996, p.456).

Table 3.4.: Activity coefficient and ion activities of the Ca^{2+} ion in a saturated aqueous solution of $Ca(OH)_2$, calculated with the Debye-Hückel and Davies equations at different temperatures and 1 atm pressure. Values are compared with the concentration of Ca^{2+} ions in solution.

Temperature [°C]	Activity coef. (Debye-Hückel) [mole/l]	Ion activity (Debye-Hückel) [mole/l]	Activity coefficient (Davies) [mole/l]	Ion activity (Davies) [mole/l]	Concentration [mole/l]
0	0.4455	0.0111	0.3661	0.0091	0.0250
10	0.4469	0.0110	0.3857	0.0092	0.0238
20	0.4493	0.0100	0.4068	0.0091	0.0223
30	0.4556	0.0094	0.4289	0.0089	0.0207
40	0.4634	0.0088	0.4523	0.0085	0.0189

Table 3.5.: Percentage of the Ca^{2+} ions available for reactions compared to the total amount of ions in solution at different temperatures and 1 atm pressure. Ion activity is calculated with the Debye-Hückel and the Davies equations.

Temperature [°C]	Debye-Hückel	Davies
0	44.55	36.61
10	44.69	38.57
20	44.94	40.68
30	45.56	42.89
40	46.34	45.23

ment with those already published by other authors (Morse and Mackenzie, 1990, p.14, Ottonello, 1996, p.457, Garrels and Christ, 1965, p.63) and, as shown in table 3.5, because of several factors including temperature, ion charge and ionic strength of solution, the number of Ca^{2+} ions available in a saturated aqueous solution of pure $Ca(OH)_2$ is always less than a half of the dissolved ions. Furthermore, according to the Davies equation, at low temperatures ion activity is almost one third of the equivalent concentration at the same temperature.

Figure 3.6 shows that, because of the temperature factor (second term in equation 3.2.11), the effect of temperature is less relevant on the ion activity than on the solubility of $Ca(OH)_2$: the difference in the ion activity between 0 and 40°C is, in fact, approximately 6.5% while considering the concentration the difference is about 24.4%.

An alternative method for calculating the ionic strength and activity coefficient has been proposed by Johannsen and Rademacher (1999). These two authors suggested to also considering the $CaOH^+$ ion pair in the calculations[6] using mass action concepts to calculate the relationship between solubility constants and species in solution. In this method the solubility product of the $CaOH^+$ ion pair (K_{CaOH^+}) is calculated as

[6]No clear evidence has been found on the existence of the di-hydrated calcium oxide ($CaO \cdot 2H_2O$) specie in solutions of $Ca(OH)_2$, as was previously suggested by some researchers (Haslam et al., 1924). For this reason this specie will not be considered in this study.

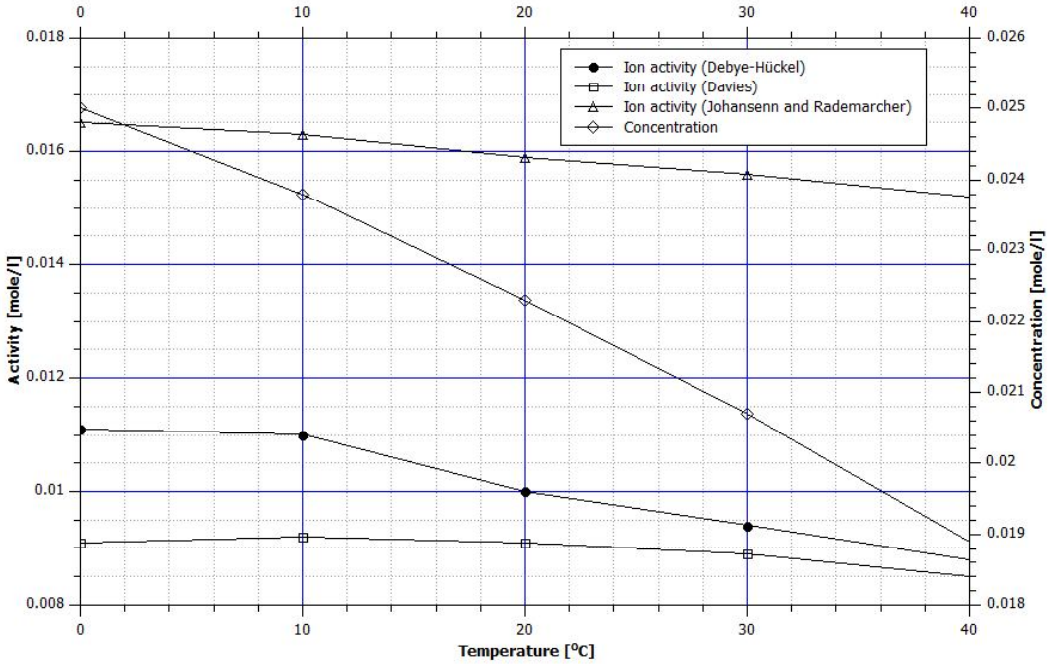

Figure 3.6.: Variation of the ion activity and concentration with the temperature. Data calculated according to the Debye-Hückel and Davies equation and to the Johannsen and Rademacher's method .

follows:

$$\frac{\left\{Ca^{2+}\right\}\cdot\left\{OH^{-}\right\}}{\left\{CaOH^{+}\right\}}\cdot f^{4}=K_{CaOH^{+}} \tag{3.2.12}$$

where $\left\{Ca^{2+}\right\}$, $\left\{OH^{-}\right\}$, $\left\{CaOH^{+}\right\}$ are the concentrations of the calcium and hydroxide ion and of the $CaOH^{+}$ ion pair, respectively, and f is the activity coefficient. $K_{CaOH^{+}}$ (considered to be the thermodynamic equilibrium constant) and f can be calculated, respectively, as:

$$\lg K_{CaOH^{+}}=-1.299+260.388\left(\frac{1}{T_0}-\frac{1}{T}\right) \tag{3.2.13}$$

$$\lg f=\frac{-0.5\sqrt{I}}{1+1.4\sqrt{I}} \tag{3.2.14}$$

The ionic strength I contained in the equation 3.2.14 can be calculated as follows:

$$I=0.5\left\{4\left\{Ca^{2+}\right\}+\left\{CaOH^{+}\right\}+\left\{H^{+}\right\}+\left\{OH^{-}\right\}\right\} \tag{3.2.15}$$

According to this procedure, since the ionic strength is a function of the concentration of ionic species and vice versa, an iterative calculation procedure must be used

Table 3.6.: Ionic strength and ion activity coefficients in the temperature range 0-40ºC calculated according to Johannsen and Rademacher (1999).

Temperature [°C]	$[CaOH^+]$	$[Ca^{2+}]$	I	f	Calculated K_{CaOH^+}	Supposed pH	Calculated pH
0	0.0084	0.0165	0.0622	0.8083	0.0418	12.698	12.6182
10	0.0074	0.0163	0.0601	0.8104	0.0452	12.677	12.6030
20	0.0064	0.0159	0.0572	0.8136	0.0485	12.649	12.5815
25	0.0059	0.0156	0.0556	0.8154	0.0502	12.633	12.5686
30	0.0054	0.0152	0.0538	0.8174	0.0519	12.616	12.5550
40	0.0045	0.0144	0.0499	0.8220	0.0553	12.577	12.5226

to simultaneously determine both the specie concentrations and the ionic strength (Johannsen and Rademacher, 1999, p.73).

The iteration includes an initial estimation of the pH value and the subsequent calculation of the $\{CaOH^+\}/\{Ca^{2+}\}$ ratio using equation 3.2.12. Then, the calculation of $\{Ca^{2+}\}$ and $\{CaOH^+\}$ can be carried out using equation 3.2.17, where $\{Ca\}_T$ is the concentration of the total calcium ions in solution.

Subsequently, the ionic strength is calculated using equation 3.2.15 and the activity coefficient can then be estimated using equation 3.2.14. Finally, the pH can be calculated using equation 3.2.16 and compared with the initially estimated value:

$$2\{Ca^{2+}\} + \{CaOH^+\} + \{H^+\} = \{OH^-\} \tag{3.2.16}$$

$$\{Ca\}_T = \{Ca^{2+}\} + \{CaOH^+\} \tag{3.2.17}$$

The iteration should be conducted until the difference between the estimated and the calculated pH is less than the desired value (Johansenn and Rademarcher reached a difference of less than 0.001; Johannsen and Rademacher, 1999, p.73).

Results of this iteration for the temperature range considered in this study are reported in table 3.6. In contrast to the calculation of Johannsen and Rademacher that used the concentrations of Ca^{2+} ions measured by electrical conductivity as total concentration of Ca^{2+} ions, in these calculations the ion concentration of a saturated solution of $Ca(OH)_2$ was used. Furthermore, as the initial pH was used the pH of the saturated $Ca(OH)_2$ solution at different temperatures as reported in table 3.2. Calculation was iterated five times before the final result was reached.

Results show that even considering the presence of the $CaOH^+$ ion pair, the ionic strength of a saturated aqueous solutions of $Ca(OH)_2$ remains in the range of diluted solutions.

The calculated solubility constant for $CaOH^+$ ion pair is very close to those found by other authors through laboratory based tests (Bates et al., 1959) however the activity

Algorithm 3.1 PHREEQC script to calculate ion activity of different species in $Ca(OH)_2$ saturated aqueous solutions.

```
SOLUTION 1

temp 20
pH 7 charge
pe 4
redox pe
units mmol/kgw
density 1
Ca 100 Mol/kgw portlandite 0
-water 1 # kg

END
```

Table 3.7.: Values of the ionic strength, ion activities and pH in a saturated aqueous solutions of $Ca(OH)_2$ calculated by PHREEQC in the temperature range 0 to 40ºC. Database used *llnl.*

Temperature [°C]	$[CaOH^+]$	$[Ca^{2+}]$	I	$\{Ca_T\}$	Final pH
1	0.01828	0.004877	0.05214	0.0322	13.242
10	0.008185	0.006011	0.04591	0.0219	12.985
20	0.003299	0.006378	0.04162	0.01652	12.564
25	0.002112	0.006350	0.03978	0.01495	12.372
30	0.001364	0.006239	0.03806	0.01378	12.190
40	0.0005885	0.005895	0.03480	0.01207	11.850

coefficient calculated in accordance with the Johannsen and Rademacher's method is almost double that of the activity coefficients found using the Debye-Hückel and Davies equations (table 3.6 and figure 3.6). The effect of temperature on the ion activity is less relevant than on the ion concentration.

Nowadays, several computer programmes can be used to carry out these calculations. These take into account additional variables including the density of water at different temperatures and electron activity (*pe*). PHREEQC is recognized as one of the most powerful of these. With a simple script such as that reported in algorithm 3.1, in a matter of seconds it is possible to calculate pH, ionic strength, total alkalinity, concentration and activity of all species in solution (in the case of the simulation carried out with the script 3.1, ion activity was calculated for: OH^-, H^+, H_2O, Ca_T, Ca^{2+}, $CaOH^+$, $H_{(0)}$, H_2, $O(_0)$ and O_2) and were calculated also for the different solid phases potentially present with relative saturation index. In this simulation, 1 kg of water is reacted with an infinite reservoir of portlandite at 20ºC in order to reach equilibrium (represented by the value 0 after the name of the mineral) in absence of CO_2 and other solid phases. Some of the results of these calculations in the temperature range considered are reported in table 3.7 and figure 3.7. Results confirm that the ionic strength is within the range of diluted solutions and that the effect of temperature on the activity of Ca^{2+} ions is less relevant that on the concentration of Ca ions.

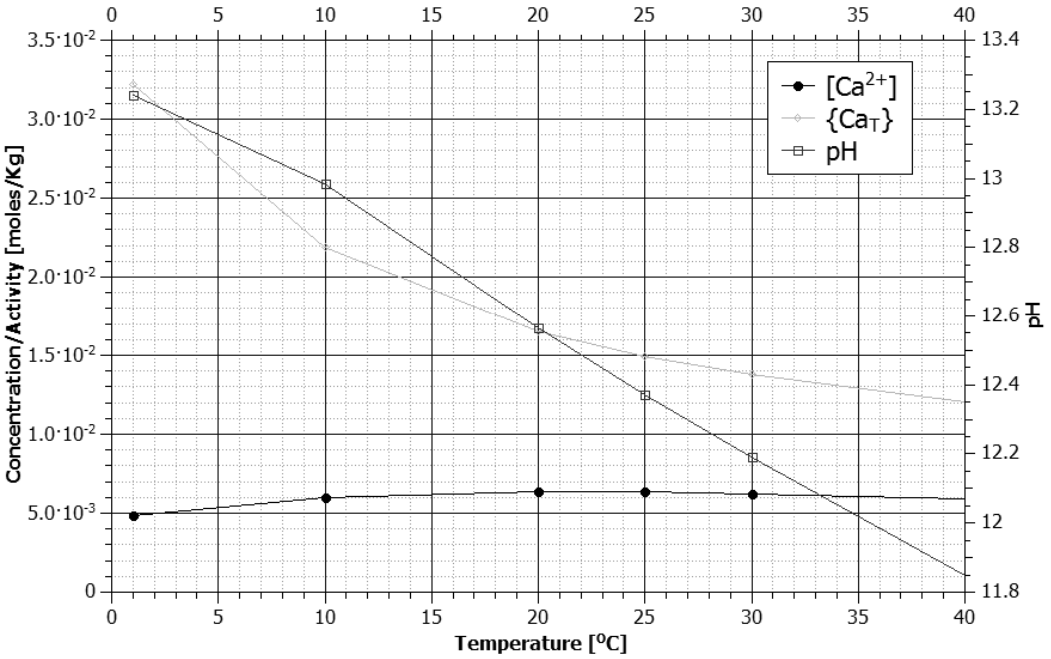

Figure 3.7.: $[Ca^{2+}]$, $\{Ca_T\}$ and pH in a saturated aqueous solutions of $Ca(OH)_2$ as calculated by PHREEQC in the temperature range 0 to 40ºC.

3.2.3. Solid phase concentration and solubility of $Ca(OH)_2$

Results of the Johannsen and Rademacher experiments showed that the quantity of dissolved $Ca(OH)_2$ in their tests was always smaller than the dosed amount (Johannsen and Rademacher, 1999, p.74, 76 and fig.4 p. 77; figure 3.8). As they pointed out, this behaviour had already been found by other researchers and was supposed to be related to the reduction in the total surface area available for the reaction (Johannsen and Rademacher, 1999, p.75). According to them, in fact, if a single particle of $Ca(OH)_2$ dissolves in water, the dissolution reaction takes place on all the surface exposed to the water. On the contrary, if a group of particles closely packed together dissolves in water, the surface available for the reaction is only that in contact with water, while the contact surface among the particles does not react. Presence of this contact surface is supposed to be the cause of the reduction in the amount of $Ca(OH)_2$ that can dissolve in water.

In a bucket of lime putty or in a mortar, most particles are in contact with each other, tightly packed by the weight of the particles and water above them. Mobility of water trapped between the particles is reduced and, consequently, this pore water soon becomes saturated with Ca^{2+} ions so that the dissolution of more $Ca(OH)_2$ is inhibited.

Besides this effect, the reduced solubility of the majority of the limes currently used by the construction industry, is also due to their $CaCO_3$ content. This contamination is

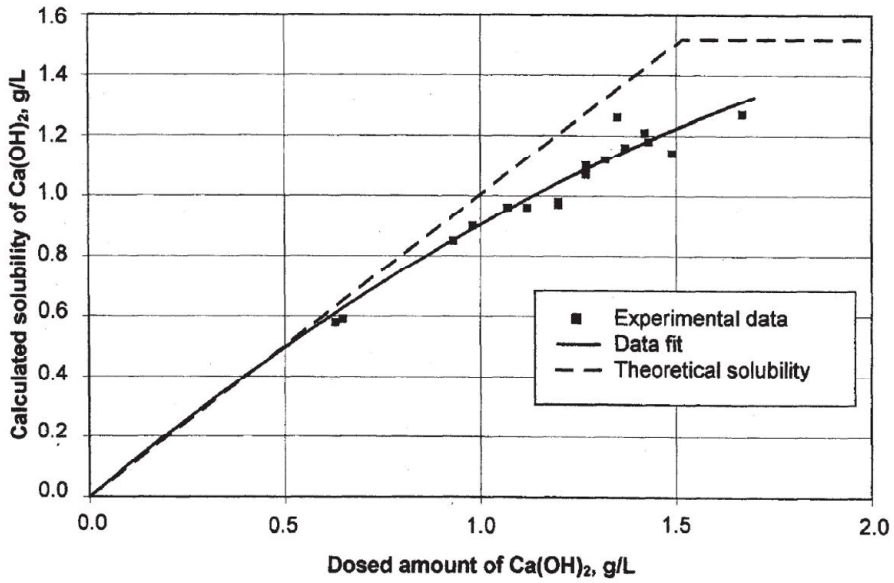

Figure 3.8.: Calculated solubility versus the dosed amount of $Ca(OH)_2$ at 25°C (from: Johannsen and Rademacher, 1999, p.77) .

due to the reaction of $Ca(OH)_2$ with the CO_2 contained in the atmosphere during the productive process and during the storage of lime (Mascolo et al., 2010, p.2364).

3.2.4. Particle size and solubility of $Ca(OH)_2$

Together with the effect of dosage and temperature on the dissolution rate of $Ca(OH)_2$, Johannsen and Rademacher also studied the effect of the particle size. From a thermodynamic point of view, the effect of grain size on the solubility of solids is already well known: the solubility constant of a solid phase with respect to its area can be modelled by an exponential equation such as (Morse and Mackenzie, 1990, p.50):

$$K_{sp} = K_b \, e^{E_S A} \tag{3.2.18}$$

where:

$$K_b = \frac{-\triangle G_r^0}{RT} \tag{3.2.19}$$

and:

$$E_s = \frac{\sigma}{RT} \tag{3.2.20}$$

In equations 3.2.18, 3.2.19 and 3.2.20, K_{sp} is the solubility of the generic solid, $\triangle G_r^0$ is the standard free energy of the reaction, R is the gas constant, T is the absolute

temperature, σ is the surface free energy per unit area and A is the surface area of the solid per mole.

This equation suggests that the solubility of a solid increases exponentially with the increase of the surface area and, consequently, with a reduction of the particle size. For most solids the influence of excess surface free energy becomes relevant when the particles are under 0.1 microns in diameter[7] (Morse and Mackenzie, 1990, pp.49-50).

According to the model applied by Johannsen and Rademacher, where the particles were considered spherical in shape, the $Ca(OH)_2$ solubility ($K_{(Ca(OH)_2)_S}$), instead, can be described by the following equation (Johannsen and Rademacher (1999, p.76)):

$$K_{(Ca(OH)_2)_S} = (5.214 - 0.0124T) \cdot \exp(0.0313/d) \tag{3.2.21}$$

where d is the particle diameter (in microns) and T is the absolute temperature.

According to their results, the concentrations calculated from the experimental data were always lower than the theoretical values and, furthermore, a dependence of the solubility on the dosed amount of $Ca(OH)_2$ was found. Despite these differences between theoretical and experimental values, this calculation can provide a clue as to the impact of the particle size on the solubility of $Ca(OH)_2$ that, as these authors already pointed out, becomes evident when the diameter of the particles is less than approximately 0.5 μm (figure 3.9; Johannsen and Rademacher, 1999, p.76).

According to this equation, particles of $0.15\mu m$ diameter, such as the nano-lime crystals produced by IBZ-Salzchemie GmbH & Co.KG (IBZ-Salzchemie GmbH, no date), are 20% more soluble (figure 3.9) than the most common particle of 2 μm diameter tested by Johannsen and Rademacher (Johannsen and Rademacher, 1999, p.74 tab. 3).

3.2.5. $Ca(OH)_2$ dissolution mechanism and kinetics

According to Ritchie and Xu (1990), the mechanism of $Ca(OH)_2$ dissolution proceeds in two steps: 1) dissolution of $Ca(OH)_2$ into Ca^{2+} and OH^- ions; 2) diffusion of Ca^{2+} and OH^- ions into the bulk solution. Between these, the ion diffusion in solution is the rate controlling step. This is a zeroth order process that is in agreement with the results of the tests carried out by several authors (e.g. Giles et al., 1993, p.120).

According to the same authors, the fact that the diffusion step governs the reaction rate, implies that the dissolution step is at equilibrium. This, in turn, implies that there must be a film of solid $Ca(OH)_2$ on the reacting lime surfaces which is in equilibrium with Ca^{2+} and OH^- ions in solution (Ritchie and Xu, 1990, p.385).

[7] Regarding this point, it is important to note that, according to Morse and Mackenzie, even a few particles in a group mainly composed of much larger particles can significantly influence the solubility measurements (Morse and Mackenzie, 1990, pp.49-50).

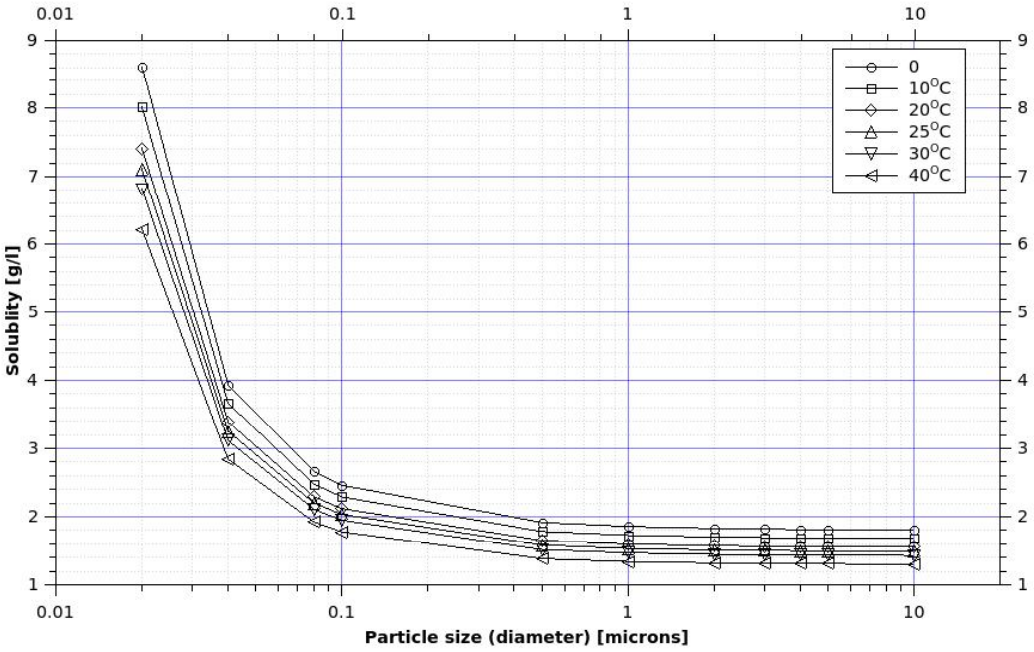

Figure 3.9.: $Ca(OH)_2$ solubility calculated at different temperatures according to the Johannsen and Rademacher's equation and plotted versus the particle size .

A general rate law describing the change in solute concentration produced by a dissolution/precipitation process is given in equation 3.2.22 (Appelo and D., 2005, p.162).

$$R = k\frac{A_0}{V}\left(\frac{m}{m_0}\right)^n g(C) \tag{3.2.22}$$

In this equation, R is the reaction rate (expressed in $mol \cdot l^{-1} \cdot sec^{-1}$), k is the specific rate for the same equation ($mol \cdot m^{-2} \cdot sec^{-1}$), A_0 is the initial surface area of the considered mineral (in m^2), V is the volume of solution in contact with the solid phase (in m^3), m_0 is the initial moles of mineral and m is the moles of the same mineral (in this case $Ca(OH)_2$) at a specific time (Appelo and D., 2005, p.162).

In this model, the dissolution rate depends mainly on the specific rate and on the ratio A_0/V. The factor $(m/m_0)^n$ accounts for changes in the reactive surfaces during the process. According to Appelo and D. (2005, p.162), for a monodispersed population of uniformly dissolving spheres n=2/3, while for polydispersed crystals the population n becomes a function of the initial grain size distribution and, consequently, its value can acquire values up to 3.4. Finally, $g(C)$ is a function that accounts for the effects of solution composition on the rate (e.g. pH and distance from the equilibrium).

A similar equation was used by Appelo and D. (2005, p.164) to model the kinetic dissolution of quartz in water using PHREEQC. Details of the model used are reported in equation 3.2.23.

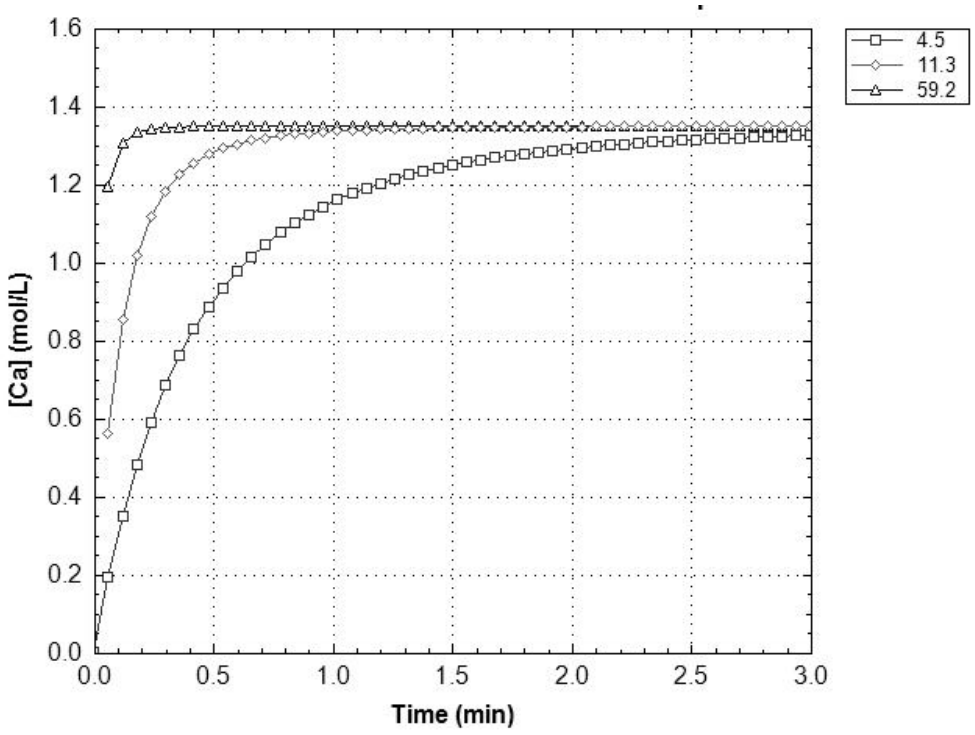

Figure 3.10.: Kinetic dissolution of portlandite with three different surface area: 4.5, 11.3 and 59.2 $^{m^2}/_{g}$ as calculated by PHREEQC using algorithm 3.2 .

$$\frac{dSi}{dt} = \left(\frac{A_0}{V}\right) \cdot \left(\frac{m}{m_0}\right)^{0.67} \cdot k \cdot (1 - SR) \tag{3.2.23}$$

In this equation Si is the concentration of H_4SiO_4 (in $^{mol}/_{l}$), t is the time (in s), A_0 is the initial surface of quartz (in m^2), V is the solution volume (in l) in contact with the solid phase, m is the remaining mass of quartz (in mol), m_0 is the initial mass of quartz (in mol), k is the rate constant and SR is the saturation rate for quartz.

The same equation can be used to model the dissolution kinetics of portlandite, as shown in figures 3.10. Algorithm 3.2 shows the code used to calculate these kinetics.

In this example the dissolution of three different limes was modelled: a two years old lime putty with a surface area of 4.5 $^{m^2}/_{g}$ and a water content of 47.7%; a 16 years old lime putty with a surface area of 11.3$^{m^2}/_{g}$ and a water content of 32.4%; a lime with particle size similar to the mean particle size of nano-lime. Data for the lime putties were taken from Hansen et al. (1999) while the surface area of nano-lime was calculated considering an average diameter of 150 nm (IBZ-Salzchemie GmbH, no date) and a ratio height:diameter of 1:10. A specific rate constant of 5.020×10^{-6} was used according to the *CRC Handbook of Chemistry and Physics* (Chemical Rubber Company, 2013-2014), a value of 1.3 was used for n and as saturation rate for portlandite was acquired the value contained into the *phreeqc* database.

Results obtained with this simulation are in agreement with those obtained by Jo-

Algorithm 3.2 Kinetic dissolution of portlandite calculated with PHREEQC.

```
# Kinetic dissolution of Portlandite
#
RATES
Portlandite
# d qu / dt = (A0 / V) * (m / m0)^0.67 * k * (1 - SI_po)
# Specific rate k from: Bullard1 J.W., Enjolras E., George W.L., Satter?eld S.G. # and Terrill J.E., (2010) A parallel reaction-transport model applied to cement
# hydration and microstructure development, Modelling Simul. Mater. Sci. Eng., 18, pp.1-16 # doi:10.1088/0965-0393/18/2/025007.
# k = 7.2^-6 mol/m2/s (25 C)
# A value of 5.020^-6 is reported in: Baysinger G. (2012). CRC Handbook of Chemistry and Physics.
# PhD Thesis, Rensselaer Polytechnic Institute # A0, initial surface of portlandite (m2) recalc's to mol/s
# V, solution volume in contact with A0
# A0 and V from: Hansen F., Tagle A., Erder E., Baron S., Connel S., Rodriguez-Navarro C. and
# Van Balen K. (2000), Effects of ageing on lime putty, in: Bartos P., Groot C. and Hughes J.J. (eds), PRO 12: International RILEM
# Workshop on Historic Mortars: Characteristics and Tests. RILEM publications, pp. 197-206
# Putty's Age (years) Surf. Area (m2/g) Water content (%)
# 2 4.5 47.7
# 16 11.3 32.4
# Fres 22.3 -
# 14 (months) 24.0 -
#
-start
1 A0 = parm(1)
2 V = parm(2)
10 rate = (A0 / V) * (m/m0)^1.3 * 5.02^-6 * (1 - SR("Portlandite"))
20 save rate * time
-end
KINETICS
Portlandite
-formula Ca(OH)2
-m0 13.49 # initial moles of portlandite (1 mol = 74.0932 g => 1.349 mol = 100 g
-parms 4500 0.477 # Surface area and Volume of water in contact with portlandite
-time_step 3 minutes in 50 # 50 time steps
INCREMENTAL_REACTIONS true
SOLUTION 1
temp 25
pH 7
pe 4
redox pe
units mmol/kgw
density 1
water 10 # kg
USER_GRAPH
-chart_title "Kinetic dissolution of Portlandite - effect of particle size"
-axis_titles "Time (min)" "[Ca] (mol/L)"
-axis_scale x_axis 0 10
# -axis_scale sy_axis 0 13
-initial_solutions true
-headings Surface_area 4.5
-start 10 graph_x total_time / 60 # time in years on x-axis
20 graph_y tot("Ca") # parameter on y-axis # 30 graph_sy -la("H+")
-end
END
KINETICS 2
Portlandite
-formula Ca(OH)2
-m0 13.49 # initial moles of portlandite
-parms 11300 0.324 # Surface area and Volume of water in contact with portlandite
-time_step 3 minutes in 50 # 50 time steps
INCREMENTAL_REACTIONS true
USE solution 1
USER_GRAPH
-headings Surface_area 11.3
-start 10 graph_x total_time / 60 # time in years on x-axis
20 graph_y tot("Ca") # parameter on y-axis
-end
END
KINETICS 3 # NANOLIME
Portlandite # NANOLIME
-formula Ca(OH)2 # NANOLIME
-m0 13.49 # initial moles of portlandite
-parms 59182 0.324 # Surface area and Volume of water in contact with portlandite
-time_step 3 minutes in 100 # 50 time steps
INCREMENTAL_REACTIONS true
USE solution 1
USER_GRAPH
-headings Surface_area 59.2
-start 10 graph_x total_time / 60 # time in years on x-axis
20 graph_y tot("Ca") # parameter on y-axis
-end
```

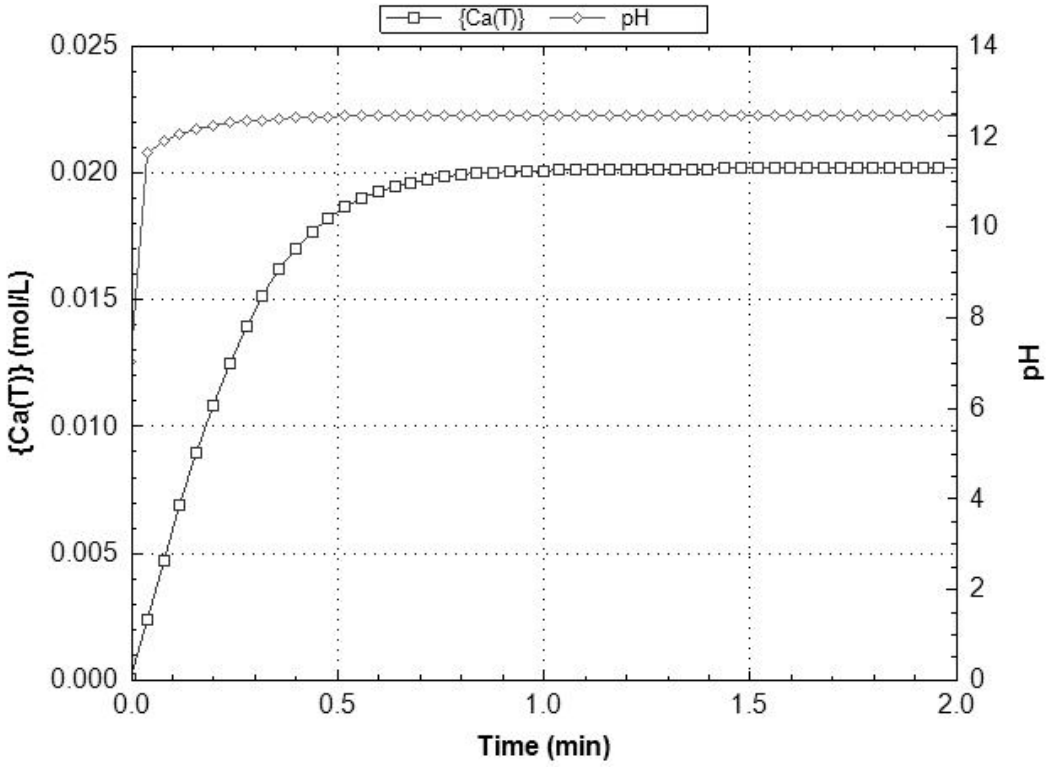

Figure 3.11.: Dissolution kinetic of portlandite with surface area: 4.5 $^{m^2}/_{g}$. Comparison with the pH change produced by the dissolution same solid phase.

hannsen and Rademacher (1999, p.77) using both, theoretical and experimental values and show that, according to this model, limes containing particles with high surface area dissolve quicker than lime with larger particles. Figure 3.10, in particular, shows that after 30 seconds, the amount of Ca^{2+} ions dissolved in water by the nano-lime-like particles is approximately 35% more then the amount of ions dissolved by the particles of a 2 years old lime putty.

A similar algorithm can also be used to evaluate the pH change in an aqueous solution of $Ca(OH)_2$ during the dissolution of portlandite crystals. Figure 3.11 was automatically produced by PHREEQC using the algorithm 3.3 where portlandite particles with surface area of 4.5 $^{m^2}/_{g}$ are dissolved in water using the same condition reported for the previous model. In this simulation, though, the *pitzer* database was used instead of the *phreeqc* database. Results show that, according to the calculations carried out in paragraph 3.2.1, the pH reaches its equilibrium value before than the calcium in solution reaches the saturation state.

3.2.6. $Ca(OH)_2$ re-crystallization in water

The forward and backward reactions that describe the dissolution and re-precipitation of $Ca(OH)_2$ reported by Johannsen and Rademacher (see equation 3.2.1) suggest that even when the water surrounding the lime (such as the water in the lime putty) reaches a

Algorithm 3.3 Kinetic dissolution of portlandite and related pH values calculated with PHREEQC

```
# Kinetic dissolution of Portlandite
#
RATES
Portlandite
-start
1 A0 = parm(1)
2 V = parm(2)
10 rate = (A0 / V) * (m/m0)^1.5 * 5.02^-6 * (1 - SR("Portlandite"))
20 save rate * time
-end
KINETICS
Portlandite
-formula Ca(OH)2
-m0 13.49 # initial moles of portlandite (1 mol = 74.0932 g => 1.349 mol = 100 g
-parms 4500 0.477 # Surface area and Volume of water in contact with portlandite
-time_step 2 seconds in 50 #50 time steps
INCREMENTAL_REACTIONS true
SOLUTION 1
temp 25
pH 7
pe 4
redox pe
units mmol/kgw
density 1
water 10 # kg
USER_GRAPH
-chart_title "Kinetic dissolution of Portlandite"
-axis_titles "Time (min)" "{Ca(T)} (mol/L)" pH
-axis_scale x_axis 0 2
-axis_scale sy_axis 0 14
-initial_solutions true
-headings Surface_area {Ca(T)} pH
-start 10 graph_x total_time # time in years on x-axis
20 graph_y tot("Ca") # parameter on y-axis
30 graph_sy -la("H+")
-end
END
```

chemical equilibrium with the solid phase, a dissolution and re-precipitation processes continuously occurs between the water and lime.

At equilibrium only the net rate of the reaction (R) is zero but not necessarily the forward (k_f) and the backward (k_b) rate constant (Johannsen and Rademacher, 1999, p.72):

$$R = k_f - k_b \cdot \left\{Ca^{2+}\right\} \cdot \left\{OH^{-}\right\}^2 \tag{3.2.24}$$

The only constrain in this equation is that:

$$k_f = k_b \cdot \left\{Ca^{2+}\right\} \cdot \left\{OH^{-}\right\}^2 \tag{3.2.25}$$

Under such conditions, a continuous recrystallization of portlandite crystals takes place even if lime is left undisturbed, in absence of CO_2.

k_f and k_b are temperature dependent and, according to the results obtained by Johannsen and Rademacher, this recrystallization process is facilitated by low temperatures (figure 3.5; Johannsen and Rademacher, 1999, p.76).

According to the results already obtained by a few groups of researchers, the recrystallization process involves an important size reduction and a significant morphological change with the development of plate-like crystals that contribute to an increase in the overall surface area (Rodriguez-Navarro et al., 1998; Mascolo et al., 2010).

The mechanism underneath this change is driven by the difference in solubility of the different crystal faces (Mascolo et al., 2010, p.2366 and Cazalla et al., 2000, p.1070) that can be explained as follows (Rodriguez-Navarro et al., 1998, p.3034).

The equilibrium shape of a crystal with surface energy for the i^{th} face γ_i, is such that the ratio between the surface energy and the the distance from the centre of the crystal to the i^{th} face r_i is constant. This can be described by the following equation:

$$\frac{\gamma_i}{r_i} = constant \tag{3.2.26}$$

The equilibrium habit of $Ca(OH)_2$ consists of hexagonal plates where the distance from the centre to the pinacoidal faces $\{0001\}$ is always less than the distance from the centre to the prism faces $\left\{10\bar{1}0\right\}$ and $\left\{10\bar{1}1\right\}$ so that:

$$r_{\{0001\}} < r_{\left\{10\bar{1}0\right\}} or\, r_{\left\{10\bar{1}1\right\}} \tag{3.2.27}$$

Consequently, from the equations 3.2.26 and 3.2.27 it is possible to verify that:

$$\gamma_{\{0001\}} < \gamma_{\left\{10\bar{1}0\right\}} and\, \gamma_{\left\{10\bar{1}1\right\}} \tag{3.2.28}$$

Because of the solubility (S) of a single face is given by the equation:

$$RT \ln \left[\frac{K}{K_0} \right] = \frac{2\gamma_i V_m}{r_i} \tag{3.2.29}$$

where K_0 is the equilibrium solubility, R the gas constant, T the temperature and V_m the molar volume, it is clear that the higher the surface energy, the higher the solubility (Rodriguez-Navarro et al., 1998, p.3034).

In the case of a prismatic $Ca(OH)_2$ crystal with a non-equilibrium habit, it will be, for instance,:

$$r_{\{10\bar{1}0\}non-equilibrium} > r_{\{10\bar{1}0\}equilibrium}$$

and, consequently:

$$\gamma_{\{10\bar{1}0\}non-equilibrium} > \gamma_{\{10\bar{1}0\}equilibrium}$$

This will result in an increase of the solubility of prismatic faces in non-equilibrium that will start to dissolve.

This dissolution leads to an erosion of the crystals with a subsequent supersaturation of the solution close to the crystal itself. As a consequence, a nucleation/recrystallization process of sub-micrometer portlandite particles on the faces of the crystal takes place. Because these particles precipitate in near-equilibrium conditions, they have well developed $\{0001\}$ faces and small $\{10\bar{1}0\}$ faces.

This dissolution process is more intense along the weak foliation planes, perpendicular to the c-axes and this produces the separation of thin hexagonal plates from the existing elongated crystal (Rodriguez-Navarro et al., 1998, p.3034 and Mascolo et al., 2010, p.2366).

The most recent model describing this change, is based on the attainment of the lowest total surface energy and is described by Mascolo et al. (2010). According to this model, this chemical process leads to the formation of large plate-like crystals with well developed $\{0001\}$ faces at the expense of smaller prismatic crystals, according to the so called Ostwald ripening effect (figure 3.12).

Separation of the hexagonal plates from the prismatic crystals increases the $Ca(OH)_2$ surface area. The increased surface area, in turn, increases the $Ca(OH)_2$ solubility which is controlled by the diffusion of Ca^{2+} and OH^- ions away from the crystal surface (Giles et al., 1993) but this increase is partially compensated by the growth of some large crystals, in conformity with the Ostwald effect (Mascolo et al., 2010, p.2366).

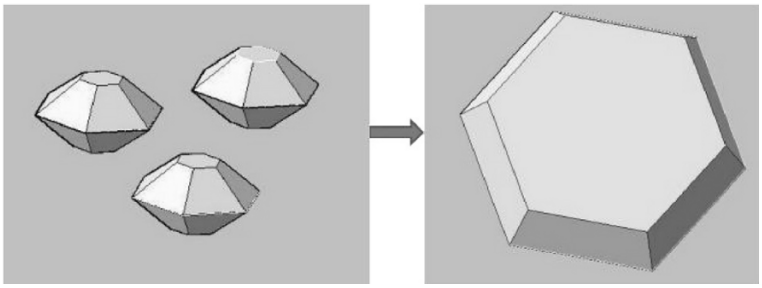

Figure 3.12.: Schematic illustration of the evolution of small prismatic portlandite crystals in a single large hexagonal crystal (from: Mascolo et al., 2010, p.2368).

An experimental evaluation of the increase in surface area achievable with the ageing of portlandite crystals is provided by Cazalla et al. (2000) who in their research found that for equal crystal sizes, plate-like crystals with a height:length ratio of 1:10 (i.e. the same ratio of nano-lime crystals) have a surface area about 5 times larger than prismatic crystals with 1:1 height:length ratio. In particular, it has been measured that the plate-like crystals contained in a lime putty aged 14 years have a surface area of $102.6 m^2/g$ whereas the prismatic crystals contained in a fresh hydrated lime have a surface area of $22.2 m^2/g$ Cazalla et al. (2000, p.1072).

Figure 3.13 shows a plot of the calculated surface area versus the diameter of the portlandite crystals in the case of crystals with 1:1 length:height aspect ratio and in the case of 10:1 length:height aspect ratio (plate-like crystals). The figure is derived from that published by Cazalla (Cazalla et al., 2000, p.1072 fig.3). The equations used to plot the surface area are indicated within the plot.

The figure shows that the increase in surface area is more relevant for particles with smaller diameters: for instance, in the dimensional range of nano-lime ($0.150 \mu m$ mean diameter), the difference between the surface area of a plate-like crystal and of a crystal with a 1:1 aspect ratio is 10 times bigger than in particles of 2 microns diameter.

Overall, the transformation occurring in the portlandite crystals during ageing in excess water are considered to be the reason for the higher plasticity, workability[8] and ability to retain water[9] of the lime putty, compared to the other forms of hydrated lime (Rodriguez-Navarro et al., 1998; Cazalla et al., 2000; Mascolo et al., 2010; Margalha et al., 2012).

[8] Research on the effect of ageing on the rheological properties of lime putty has been carried out by Atzeni and colleagues and published in: Atzeni et al., 2004.

[9] Research on the effects of ageing on lime putty showed that the water retained in a 16-year lime putty is more strongly adsorbed on the portlandite crystals than the water adsorbed in a 2-year putty (Hansen et al., 1999, pp.203-204). Finally, regarding the water retained in the lime putty it is important to highlight that, according to some researchers, the high water retention in the aged lime putty may induce crack formation on drying in the mortar with high binder:aggregate ratio (Cazalla et al., 2000, p.1075).

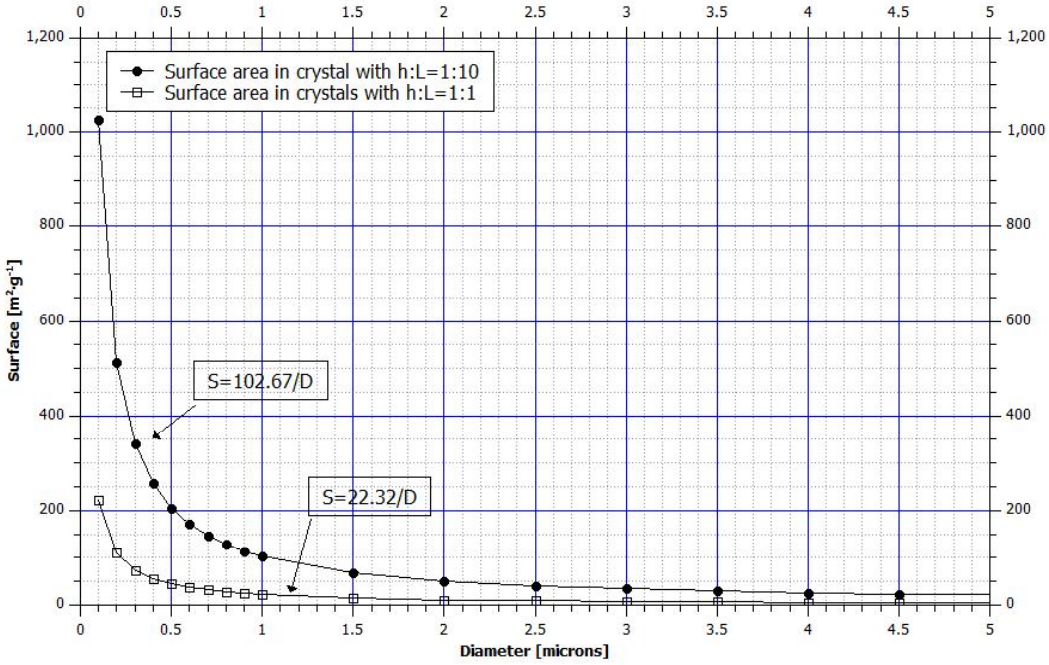

Figure 3.13.: Calculated surface area versus diameter of the portlandite crystals (modified from: Cazalla et al., 2000, p.1072 fig.3).

O=C=O

Figure 3.14.: Lewis figure of the carbon dioxide molecule

3.3. Carbon dioxide

Carbon dioxide is a compound with chemical formula CO_2 that at standard temperature and pressure is in the form of a gas. Its molecule is symmetrical with the carbon atom located in between and on the same axes of the two oxygen atoms (figure 3.14). It occurs naturally in nature and takes part in a number of reactions. Its concentration in the atmosphere changes during the seasons and with geographical location and it is so low that this is considered a *trace gas*. For the calculations considered in this document, however, the concentration of atmospheric CO_2 is assumed to be $350 ppm$ ($= 0.0350\%$) in dry air.

3.3.1. Solubility in water

One of the characteristics of CO_2 that make this gas useful in the construction industry is its solubility in water that only depends on the p_{CO_2}. Pure water at 25°C in equilibrium with non polluted air containing $350 ppm$ of CO_2, for instance, has a concentration of aqueous carbon dioxide ($CO_{2(aq)}$) of $1.146 \times 10^{-5} M$ (Manahan, 2000, p.59).

When in water, the CO_2 react to form more complex compounds. An aqueous solu-

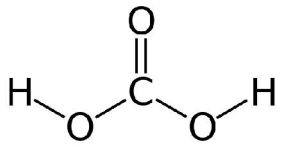

Figure 3.15.: Lewis figure of the carbonic acid molecule.

tion of carbon contains both $CO_{2(aq)}$ and hydrated carbonic acid ($H_2CO_{3(aq)}$) molecules. Conversion of $CO_{2(aq)}$ to $H_2CO_{3(aq)}$ is described in equation 2.1.2 where the forward reaction is relatively slow while the backward one (dehydration) is much faster. At room temperature and pressure, only about 3% of the $CO_{2(aq)}$ reacts to form $H_2CO_{3(aq)}$ (Ottonello, 1996, p. 472).

It is interesting to notice that while the $CO_{2(aq)}$ molecule has a linear structure, the $H_2CO_{3(aq)}$ has a trigonal planar structure (figure 3.15) where the molecular orbitals are formed by the hybrid atomic orbitals sp^2.

Using the rate constants of the forward and backward reactions in equation 2.1.2 it can be calculated that at room temperature and pressure and under stable conditions the ratio $^{CO_{2(aq)}}/_{H_2CO_{3(aq)}}$ is close to 600 (Ottonello, 1996, p. 472, Appelo and D., 2005, pp.179-180). Nevertheless in some calculations (such as those involved in the chemistry of carbonates) $CO_{2(aq)}$ is considered as if it is fully converted into $H_2CO_{3(aq)}$ without distinction between the linear and the planar trigonal structure (Ottonello, 1996, p. 472).

3.3.2. The CO_2-carbonic acid system

As already stated carbonation is the chemical reaction between Ca^{2+} and CO_3^{2-} in aqueous solution. The CO_3^{2-} ion in the chemistry of water is part of the more complex *carbonic acid system* which derives from the dissolution of CO_2 in water and which includes, other than the carbonate itself also the chemical species: bicarbonate ion (HCO_3^-), undissociated carbonic acid (H_2CO_3), dissolved carbon dioxide ($CO_{2(aq)}$) and in many instances, exchange with gaseous carbon dioxide ($CO_{2(g)}$). The relationship among these different chemical species is represented by the equations 2.1.1-2.1.4 (Morse and Mackenzie, 1990, p. 1). This reaction system highlights two important issues related to the carbonic acid system:

- the hydrogen ion involved in reactions 2.1.3 and 2.1.4, is an important chemical species and this is indicative of the role played by the carbonic acid system in influencing the pH and buffer capacity of water;

- the activity of the carbonate anion (equation 2.1.4) plays an important role in determining the degree of saturation of water with respect to carbonate minerals

and, consequently, their precipitation or dissolution as represented by the following equation (Morse and Mackenzie, 1990, p. 34, Krauskopf, 1979, p. 52, Ottonello, 1996, p. 471 and Manahan, 2000, p.59):

$$CaCO_{3(s)} + CO_{2(aq)} + H_2O_{(l)} \rightleftharpoons Ca^{2+}_{(aq)} + 2HCO^{-}_{3(aq)} \tag{3.3.1}$$

Determination of the concentration or activity of the carbonate ion is not an easy task but nevertheless is necessary for the interpretation of a number of chemical processes occurring in nature (Morse and Mackenzie, 1990, p. 1). To simplify the calculations, in the following paragraphs the Plummer and Busenberg approach will be used used where the equation 2.1.2 and 2.1.3 are combined as follows (Morse and Mackenzie, 1990, p.1):

$$CO_{2(aq)} + H_2O_{(l)} \rightleftharpoons HCO^{-}_{3(aq)} + H^{+}_{(aq)} \tag{3.3.2}$$

According to the equations 2.1.1, 2.1.4 and 3.3.2, the relative proportion of the different species can be, once again, calculated using the equilibrium constant. As previously said, if thermodynamic constants are used, activities must be used instead of the concentrations (Morse and Mackenzie, 1990, p. 2).

The equilibrium constants of the carbonic acid system as previously discussed, can be calculated as follow:

$$K_H = \frac{\left[CO_{2(aq)}\right]}{p_{CO_2}} \tag{3.3.3}$$

$$K_1 = \frac{\left[HCO^{-}_{3(aq)}\right]\left[H^{+}_{(aq)}\right]}{\left[CO_{2(aq)}\right]\left[H_2O_{(l)}\right]} \tag{3.3.4}$$

$$K_2 = \frac{\left[CO^{2-}_{3(aq)}\right]\left[H^{+}_{(aq)}\right]}{\left[HCO^{-}_{3(aq)}\right]} \tag{3.3.5}$$

Constants K_H, K_1, K_2 are temperature and pressure dependent.

Rearranging equation 3.3.3, 3.3.4 and 3.3.5 allows calculation of the activities of aqueous CO_2, HCO^{-}_3 and CO^{2-}_3 ions:

$$\left[CO_{2(aq)}\right] = K_H\, p_{CO_2} \tag{3.3.6}$$

$$\left[HCO_{3(aq)}^{-}\right] = K_H K_1 \left(\frac{p_{CO_2}\left[H_2O_{(l)}\right]}{\left[H_{(aq)}^{+}\right]}\right) \tag{3.3.7}$$

$$\left[CO_{3(aq)}^{2-}\right] = K_H K_1 K_2 \left(\frac{P_{CO_2}\left[H_2O_{(l)}\right]}{\left[H_{(aq)}^{+}\right]}\right) \tag{3.3.8}$$

The use of equations that define the activities related to concentration by the activity coefficient, make it possible to express the above calculated activities as concentrations. With the exception of high ionic strength solutions, it is possible to assume that the activity of water as unity eliminating the relative term ($\left[H_2O_{(l)}\right]$). Equations 3.3.6, 3.3.7 and 3.3.8 then become:

$$\left\{CO_{2(aq)}\right\} = K_H \left(\frac{1}{\gamma_{CO_{2(aq)}}}\right) p_{CO_2} \tag{3.3.9}$$

$$\left\{HCO_{3(aq)}^{-}\right\} = K_H K_1 \left(\frac{1}{\gamma_{HCO_{3(aq)}^{-}}}\right)\left(\frac{p_{CO_2}}{\left[H_{(aq)}^{+}\right]}\right) \tag{3.3.10}$$

$$\left\{CO_{3(aq)}^{2-}\right\} = K_H K_1 K_2 \left(\frac{1}{\gamma_{CO_{3(aq)}^{2-}}}\right)\left(\frac{P_{CO_2}}{\left[H_{(aq)}^{+}\right]}\right) \tag{3.3.11}$$

In these equations, the activity of the hydrogen ion ($\left[H_{(aq)}^{+}\right]$) is usually obtained from pH measurements although their relationship is complex (Morse and Mackenzie, 1990, p 4).

The relative distribution of the chemical species of the carbonic acid system is commonly presented as a function of pH relative to $\sum CO_2$ in a plot known as a Bjerrum diagram (figure 3.16; Morse and Mackenzie, 1990, p.7).

The diagram shows that the point of equal concentration of $CO_{2(aq)}$ and HCO_3^- is at $pH = pK_1$ and the point of equal concentrations of HCO_3^- and CO_3^{2-} ions is at $pH = pK_2$. It is also clear that over the pH of a saturated solution of $Ca(OH)_2$ in water ($\approx$12.6), CO_3^{2-} is the most abundant specie (Morse and Mackenzie, 1990, p. 7). According to the same diagram and to the calculations carried out in paragraph 3.2.1, CO_3^{2-} is the most abundant specie in solution even when only 40 milligrams of $Ca(OH)_2$ are dissolved in a litre of water.

From the fundamental equations previously described it is possible to derive the equations required to calculate the activity of CO_3^{2-} using any pair of the four quantities: pH, p_{CO_2}, carbonate alkalinity (A_c) and total CO_2 ($\sum CO_2$). For instance, equation 3.3.12 allows calculation of $\left[CO_3^{2-}\right]$ knowing $[H^+]$ and $\sum CO_2$ as follow:

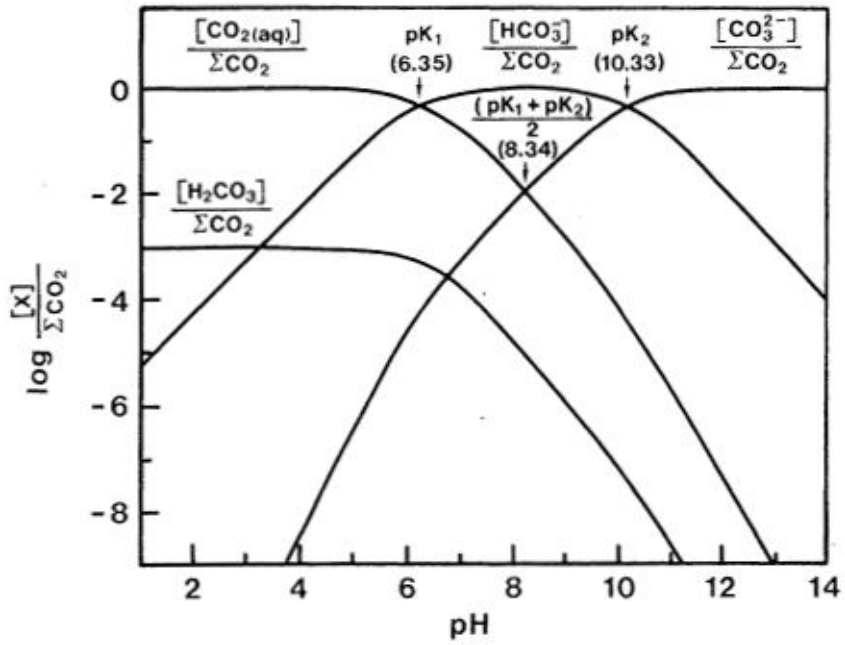

Figure 3.16.: Bjerrum diagram for the relative proportion of different species in the carbonic acid system at 25°C, for the case where all activity coefficients are equal to 1 (from: Morse and Mackenzie, 1990, p. 8).

$$\left[CO_3^{2-}\right] = \sum CO_2 \, \gamma_{CO_3^{2-}} (1 - x - y) \tag{3.3.12}$$

where:

$$x = \frac{[H^+]^2}{[H^+]^2 + \left(\frac{\gamma_{CO_2}}{\gamma_{HCO_3^-}}\right) K_1 \, [H^+] + \left(\frac{\gamma_{CO_2}}{\gamma_{CO_3^{2-}}}\right) K_1 K_2} \tag{3.3.13}$$

$$y = \frac{K_1 \, [H^+]^2}{\left(\frac{\gamma_{HCO_3^-}}{\gamma_{CO_3^{2-}}}\right) [H^+]^2 + K_1 \, [H^+] + \left(\frac{\gamma_{HCO_3^-}}{\gamma_{CO_3^{2-}}}\right) K_1 K_2} \tag{3.3.14}$$

where K_1 is the point of equal concentration of $CO_{2(aq)}$ and HCO_3^- , K_2 is the point of equal concentrations of HCO_3^- and CO_3^{2-} ions, $[H^+]$ is the proton activity and γ_X is the activity coefficient of related species in solution.

The other derived equations are reported in Morse and Mackenzie (1990, pp.8-10).

In theory it should be possible to deal with all carbonate chemistry in a number of solutions simply by knowing the appropriate activity coefficients and how parameters such as temperature and pressure affect them. In practice, the treatment of activity coefficients under varying set of conditions has been shown to be difficult for most problems of interest (Morse and Mackenzie, 1990, p.27) where computer programs such as PHREEQC can play a really important role.

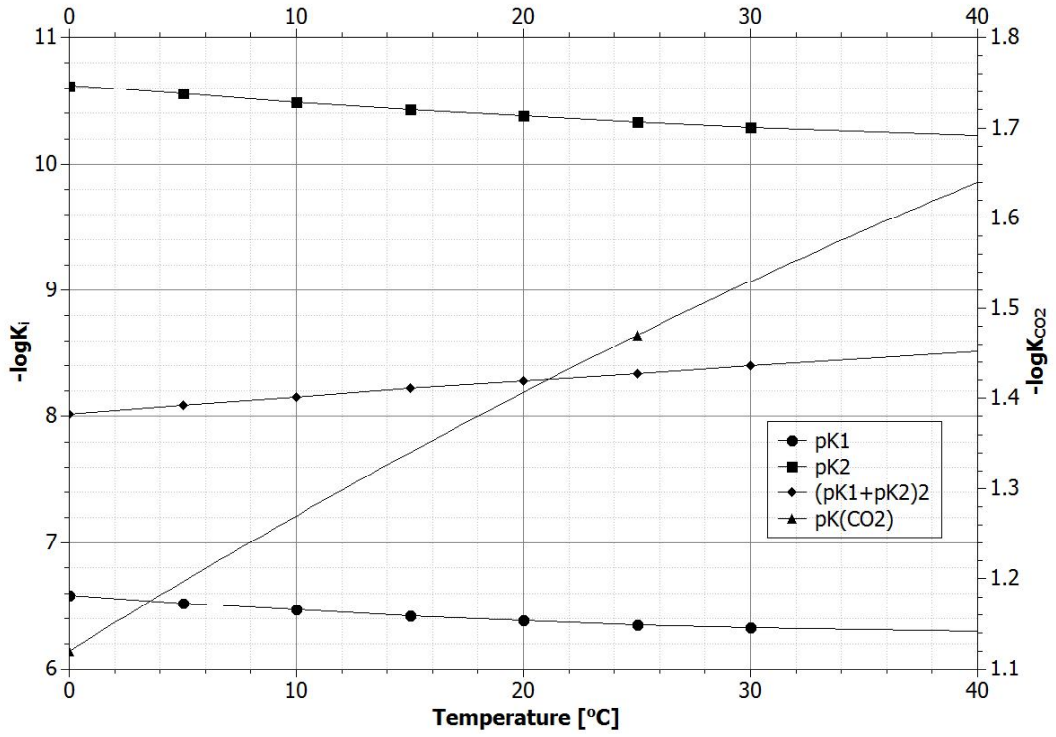

Figure 3.17.: Effect of temperature on the carbonate equilibrium constants pK_1, pK_2, $\frac{(pK_1+pK_2)}{2}$ and pK_{CO_2} showed in figure 3.16. Data are reported in: Garrels and Christ (1965, p.89).

Effects of temperature and pressure on the equilibrium constants Figure 3.17 shows the effect of temperature on the carbonate equilibrium constants pK_1, pK_2, $\frac{(pK_1+pK_2)}{2}$ and pK_{CO_2}. The graph shows that increasing the temperature moves the equilibrium constant pK_2 towards more acidic pHs (from 10.38 at 20°C to 10.22 at 40°C). Because the pH tends to reduce while the carbonation reaction proceeds, the movement of pK_2 towards more acidic pHs suggests that at higher temperatures the CO_3^{2-} ions are available for reaction with Ca^{2+} ions for a longer time. In the meantime also the pK_1 equilibrium constant moves towards more acidic pHs while the $\frac{(pK_1+pK_2)}{2}$ constant moves toward more basic pHs reducing the range of influence of the HCO_3^- ion. This analysis suggests that when considering the species in the carbonic acid system, an increase in temperature favours the carbonation reaction.

3.3.3. Effect of CO_2 dissolution on the pH

As soon as pure degassed water comes in contact with the air, gaseous species including atmospheric CO_2 dissolve until a new equilibrium is reached. Methods for quantifying this dissolution process and the activity of the ionic species involved, are based on an iteration similar to the one already described for the calculation of ionic strength and ion activity coefficients in $Ca(OH)_2$ saturated aqueous solutions.

The method is clearly described by Morse and Mackenzie (1990, pp.57-58). For

this calculation they assume as initial conditions: water with $pH = 7$, total alkalinity $A_t = 0$, $p_{CO_2} = 330 \mu atm$, no Ca^{2+} ions in solution and no change in the total alkalinity.

Because the pH is fixed and is equal to 7, it is possible to state that $\{H^+\} = 10^{-7}$ (as well a $\{OH^-\}$). Moreover, because H^+ and OH^- ions are not involved in ion pairing reactions, their ion activity calculated from the Davies equation are equal to their concentration.

Since A_t is known (equal to 0) and cannot change by the addition of only CO_2, the general equation for A_t can be used to calculate the pH under different p_{CO2} .

This can be done using the equations for the equilibrium relations in the carbonic acid system and expressing the alkalinity in terms of p_{CO2} (known value) and $[H^+]$ considered as the unknown value. The general equation used by Morse and MacKenzie for A_t is:

$$A_t = \left(\frac{K_H K_1 p_{CO_2}}{\gamma_{HCO_3^-} \gamma_{H^+} [H^+]} \right) + 2 \left(\frac{K_H K_1 K_2 P_{CO_2}}{\gamma_{CO_3^{2-}} \gamma_{H^+}^2 [H^+]^2} \right) + \left(\frac{K_W}{\gamma_{H^+}^2 [H^+]} \right) - \left[H^+ \right] = 0 \tag{3.3.15}$$

This equation can be rearranged to the more convenient form:

$$A_t = \left[H^+ \right]^3 - \left[H^+ \right] + \left[\left(\frac{K_H K_1 p_{CO_2}}{\gamma_{HCO_3^-} \gamma_{H^+}} \right) + \left(\frac{K_W}{\gamma_{H^+}^2} \right) \right] - 2 \left(\frac{K_H K_1 K_2 p_{CO_2}}{\gamma_{CO_3^{2-}} \gamma_{H^+}^2} \right) = 0 \tag{3.3.16}$$

where all the variables are already described in the previous paragraph.

Because it is known that following the dissolution of CO_2 in pure water, pH decreases (the water becomes more acidic), Morse and MacKenzie made an initial estimation of the final pH. In this estimation they assumed that the concentration of both OH^- and CO_3^{2-} ions would have been relatively small in acid conditions and, consequently, the pH would have been near the square root of the HCO_3^- term ($pH = 5.7$).

According to this method, once the concentration of H^+ ions is known, the other carbonic acid system components can be calculated using existing equations. At this point, it is possible to calculate the ionic strength and the activity coefficients that can be substituted back into the equation for $[H^+]$ using the previously calculated value for the initial evaluation. This process is, then, repeated until $[H^+]$ is constant to within a specific value (e.g. 1%). Table 3.8 contains the data calculated by Morse and Mackenzie.

Similar calculations can be carried out automatically by PHREEQC, modelling a reaction between liquid water (initial $pH = 7$) and CO_2 gas at 0.00033 atm pressure and 25°C temperature. In accordance with the instructions provided with the software,

Table 3.8.: Composition of pure water in equilibrium with atmospheric CO_2 as published by Morse and Mackenzie (1990, p.57).

Case	P_{CO_2}	pH	$[CO_2]$	A_t	A_c	$\{Ca^{2+}\}$	$\{CO_2\}$
1	3.30×10^{-4}	5.65	1.34×10^{-5}	0	2.22×10^{-6}	0	1.12×10^{-5}

Case	$\{HCO_3^-\}$	$\{CO_3^{2-}\}$	$\gamma_{Ca^{2+}}$	$\gamma_{HCO_3^-}$	$\gamma_{CO_3^{2-}}$	γ_{H^+}
1	2.23×10^{-6}	4.68×10^{-11}	0.99	1.00	0.99	1.00

Algorithm 3.4 PHREEQC script to calculate the ion activities of all carbonic acid system species dissolved in water in equilibrium with atmospheric CO_2 at 25°C.

```
SOLUTION 1

temp 25
pH 7 charge
pe 4
redox pe
units mol/kgw
density 1
-water 1 # kg
EQUILIBRIUM_PHASES 1
CO2(g) -3.487202673 1000

END
```

in order to simulate the presence of this gas an *equilibrium phase* made of gaseous CO_2 is introduced as the initial condition. For this solid phase, the log of p_{CO_2} in bar is used in the place of the saturation index and the number of moles is set to 1000 as this simulates an infinite reservoir. Script used for this calculation is reported in algorithm 3.4 and the results are reported in table 3.9. A comparison of these results with those reported in table 3.8 highlight the reliability of PHREEQC in modelling this type of solution.

Table 3.10 reports the activity of the different carbonic acid system ions at different temperature and at the pH potentially produced by portlandite dissolution at the same temperatures. Calculations were carried using out PHREEQC under the same conditions previously described. Results show that because $\left[CO_3^{2-}\right]$ is higher at high temperature, the final pH of solution tends to increase with an increase in the temperature. Increasing the temperature causes the number of CO_2 and HCO_3^- ions to slightly decrease while CO_3^{2-} ions increase.

Table 3.9.: Composition of the activity of the carbonic acid system ions in pure water in equilibrium with atmospheric CO_2 at 25°C calculated using PHREEQC.

p_{CO_2}	pH	A_t	$[CO_2]$	$\left[HCO_3^-\right]$	$\left[CO_3^{2-}\right]$
3.30×10^{-4}	5.65	2.995×10^{-17}	1.129×10^{-5}	2.238×10^{-6}	4.680×10^{-11}

Table 3.10.: Activity of the carbonic acid system ions in pure water in equilibrium with atmospheric CO_2 in the temperature range between 0 and 40°C and at the initial pH that would be produced by the portlandite dissolution at the same temperatures. Calculations carried out using PHREEQC.

Temperature [ºC]	Initial pH	Final pH	$[CO_2]$	$[HCO_3^-]$	$[CO_3^{2-}]$
0	13.424	5.58	2.49×10^{-5}	2.64×10^{-6}	2.54×10^{-11}
10	12.985	5.609	1.78×10^{-5}	2.46×10^{-6}	3.22×10^{-11}
20	12.564	5.641	1.29×10^{-5}	2.28×10^{-6}	4.04×10^{-11}
25	12.372	5.657	1.12×10^{-5}	2.20×10^{-6}	4.46×10^{-11}
30	11.91	5.673	9.82×10^{-5}	2.12×10^{-6}	4.89×10^{-11}
40	11.85	5.705	7.76×10^{-6}	1.96×10^{-6}	5.72×10^{-11}

3.4. Calcium carbonate

Six different solid $CaCO_3$ phases are known to be produced by carbonation at ambient temperature and pressure: three anhydrous crystalline polymorphs, two hydrated crystalline forms and an amorphous hydrate phase (Lopez-Arce et al., 2011; Brecevic and Kralj, 2007; Brooks et al., 1950)[10]. The anhydrous crystalline phases are: calcite, aragonite and vaterite while the two hydrated crystalline minerals are: monohydrocalcite and ikaite. The amorphous phase is simply called amophous calcium carbonate or ACC.

As a general rule it is possible to state that the hydrated forms precipitate from supersaturated solutions before the more stable anhydrous forms precipitate (Brecevic and Kralj, 2007, p.470) but to investigate processes such as precipitation and growth of $CaCO_3$ it is first necessary have a basic knowledge of their chemical and mineralogical characteristics.

3.4.1. Anhydrous calcium carbonate

Calcite

Calcite is the most stable polymorph of $CaCO_3$ at room temperature and atmospheric pressure (figure 2.1) and for this reason is the most abundant (Morse and Mackenzie, 1990, p.40). Calcite has molar weight of 100.09 g/mol and density of 2.71 g/cm^3 at 20ºC. Solubility in water at the same temperature is of about 0.00066 g/l (Chemical Rubber Company, 2013-2014, 4-54).

Calcite crystallizes in a rhombohedral structure that can be described using three different unit cells (figure 3.18).

Figure 3.19 emphasizes the alternating layers of Ca atoms and CO_3 groups in this mineral. Each CO_3 group within one layer has a common orientation which is 180°

[10] At elevated temperatures and/or pressures five other $CaCO_3$ polymorphs are known from experimental work (Tucker and Wright, 1992, p.289).

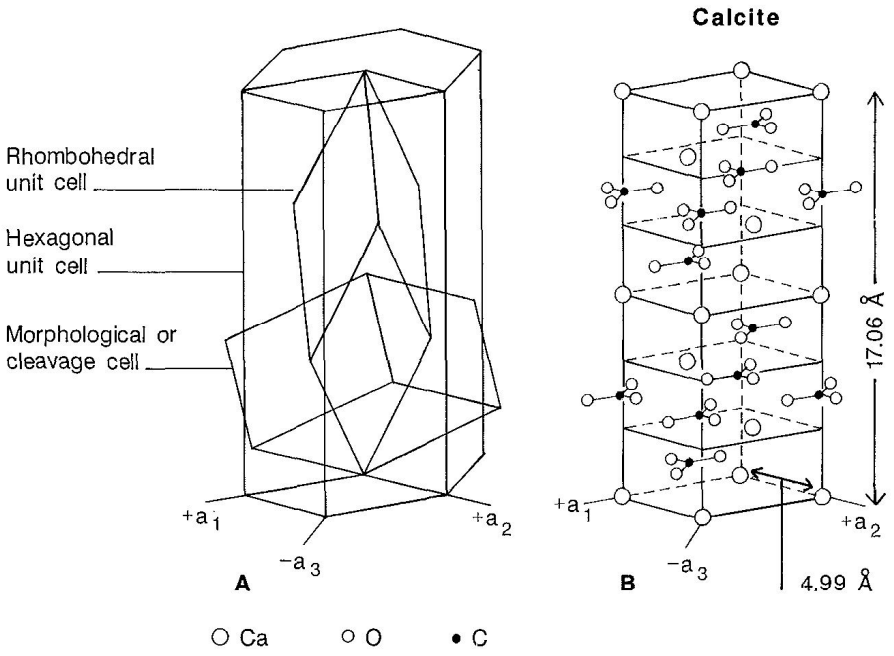

Figure 3.18.: (A): diagrammatic relationship between rhombohedral, hexagonal and morphological unit cell and the hexagonal crystallographic axes. (B): hexagonal unit cell of calcite, apparent rectilinear shape due to perspective; a_1, a_2 and $a_3 = 4.99$Å; $c = 17.06$Å (from: Tucker and Wright, 1992, p. 285).

reversed in each adjacent layer. The *Ca* atom is coordinated with six oxygen atoms from different CO_3 groups to form a slightly distorted octahedron (figure 3.20). Each oxygen in the CO_3 group is bonded to one carbon and two *Ca* atoms from the adjacent cation layers. In calcite, the $C-O$ bonds are coincident with the three a-axes (Tucker and Wright, 1992, p. 284).

Eight divalent cations are known to exist as calcite isotypes (Ca, Cd, Mn, Fe, Co, Zn, Mg and Ni) but no complete miscibility exists for rhombohedral carbonates containing calcium (figure 3.21). Only limited miscibility exist, instead, with carbonate containing Mn, Fe and Mg (Tucker and Wright, 1992, pp. 287-288, Morse and Mackenzie, 1990, p.44).

Aragonite

Sharing the same chemical formula, aragonite has the same molar weight as calcite (100.09 g/mol) but its density is 2.93 g/cm^3 at 20ºC. Aragonite is relatively abundant in nature and is 1.5 times more soluble than calcite (Morse and Mackenzie, 1990, p.40, Krauskopf, 1979, p.55, Brooks et al., 1950, p.147; slightly different values are given in Appelo and D., 2005, pp. 176, 206-207):

$$k_{calcite} = \left\{Ca^{2+}\right\}\left\{CO_3^{2-}\right\} = 10^{-8.35} = 4.5 \times 10^{-9} \tag{3.4.1}$$

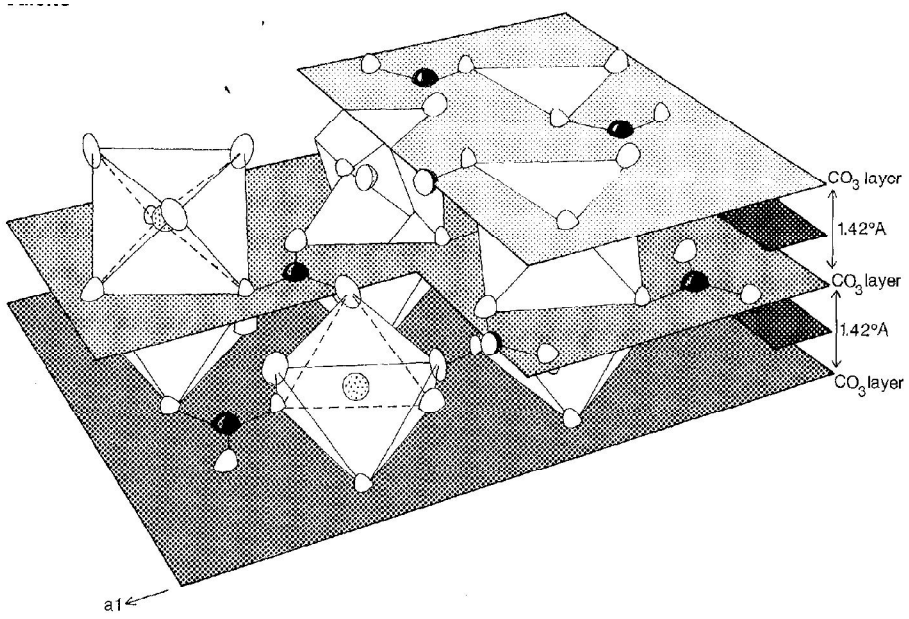

Figure 3.19.: Perspective view of calcite in which the layered structure is emphasized by shaded planes: black spheres = carbon atoms; stippled spheres = calcium atoms and unshaded ellipsoids = oxygen atoms (from: Tucker and Wright, 1992, p.286).

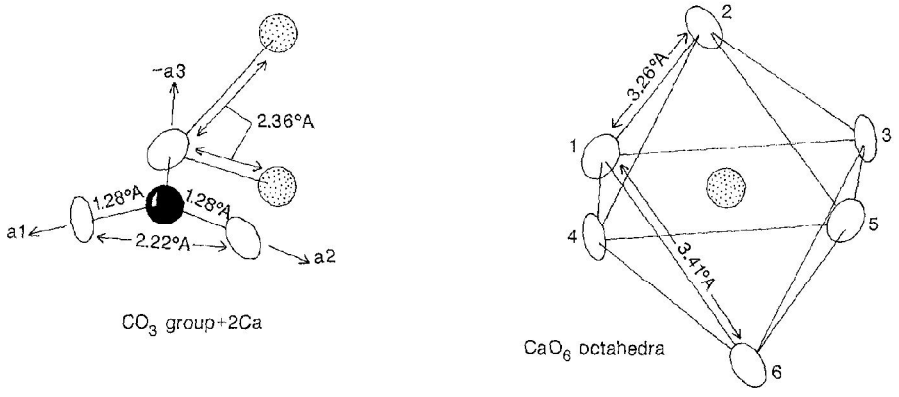

Figure 3.20.: Left hand side: CO_3 group within the calcite structure, with one oxygen showing two bonded Ca atoms. Right hand side: CaO_6 octahedron showing bond lengths. Black spheres = carbon atoms; stippled spheres = calcium atoms and unshaded ellipsoids = oxygen atoms (from: Tucker and Wright, 1992, p.286).

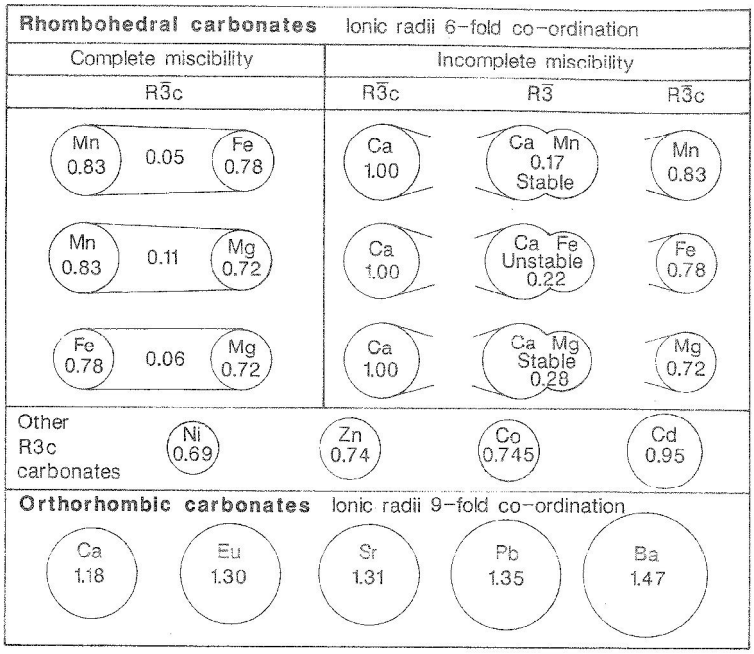

Figure 3.21.: Cationic radii and carbonate space groups. Diameters of the cation circles are proportional to their radii. Linked cations show the extent of miscibility for some rhombohedral carbonates. Central figures in these solid solutions series are differences (in Å) between end-members radii (from: Tucker and Wright, 1992, p.289).

$$k_{aragonite} = \left\{Ca^{2+}\right\}\left\{CO_3^{2-}\right\} = 10^{-8.22} = 6.0 \times 10^{-9} \tag{3.4.2}$$

Aragonite crystallizes with an orthorhombic structure, differing from the structure of calcite. It has larger cation sites compared to calcite (Morse and Mackenzie, 1990, p. 40) and the CO_3 group is virtually identical to that in the rhombohedral carbonates such as dolomite but while in dolomite the C atom is displaced from the plane of the three oxygen atoms towards the layer containing the smaller Mg (compared to Ca) atoms, in aragonite the C atom is displaced toward the nearest Ca layer. The Ca atoms are arranged in pseudo-hexagonal layers parallel to the (001) face with an ABAB sequence along the c-axes (figure 3.22). These layers are separated by two distinct layers of CO_3 groups. Overall, the Ca atoms are bonded to nine oxygen atoms. Two oxygens at the edge of three CO_3 groups and one oxygen at the apex of three CO_3 groups (Tucker and Wright, 1992, p.285). Since this arrangement is more dense compared to the calcite arrangement, aragonite is a high pressure phase (figure 2.1; Morse and Mackenzie, 1990, p.40).

Substitution for Ca in the aragonite structure is exemplified by isomorphous strontianite ($SrCO_3$), cerussite ($PbCO_3$) and witherite ($BaCO_3$). Aragonite may contain up to 14% mole $SrCO_3$ and 2.5% mole $PbCO_3$ (Tucker and Wright, 1992, p.288). The addition of Sr, though, reduces the phase boundary between calcite and aragonite (figure 2.1) to a lower pressure (but an amount greater than 50 mole % of $SrCO_3$ is required

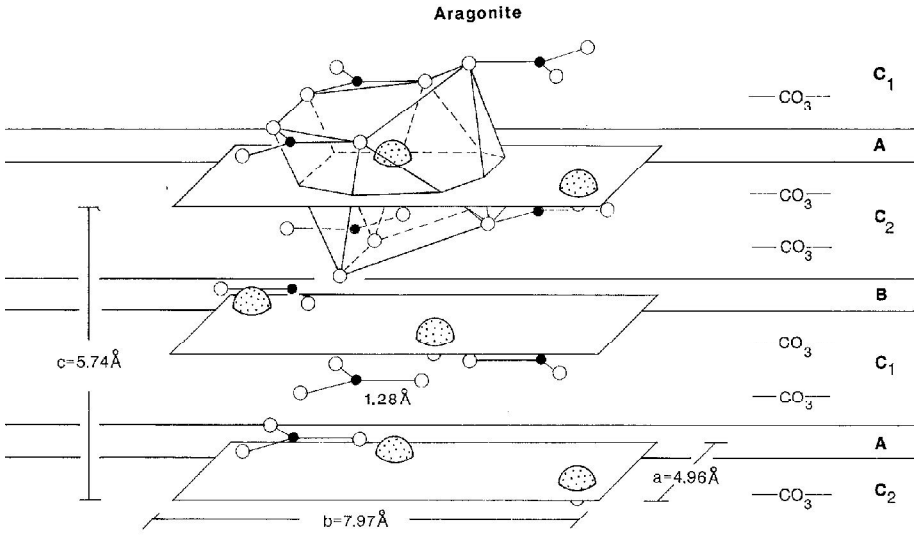

Figure 3.22.: Layered structure of aragonite against the (100) plane. Three horizontal planes intersect Ca atoms (ABAB layering). Black spheres represent carbon atoms; unshaded spheres represent oxygen atoms. The CaO_9 coordination polyhedron characteristic of the orthorhombic carbonates is outlined (from: Tucker and Wright, 1992, p.288).

to depress the boundary to 1kbar; Tucker and Wright, 1992, p.289).

Aragonite has clear advantages over calcite and vaterite when filling micropores and is less prone to cleavage (is less brittle). Aragonite crystals typically have the shape of long prisms ranging in length from several nanometres to several millimetres (Chervonnyi et al., 2003, p.386).

Vaterite

The third anhydrous polymorph of $CaCO_3$, vaterite (or μ-calcium carbonate; Brooks et al., 1950, p.146), is known to occur naturally and is frequently encountered in experimental work. Vaterite is metastable although, according to Brooks and colleagues, it remains unchanged for long periods when it is dry. It slowly transform into calcite when, instead, is left in moist conditions, especially when it is heated (Brooks et al., 1950, p.147). According to the results of several researchers, vaterite is the first solid phase formed when $CaCO_3$ spontaneously precipitates (Brecevic and Kralj, 2007, p.472).

Vaterite has the same molar weight of calcite and aragonite but a density of 2.653 g/cm^3 at 20ºC. Solubility in water at the same temperature is of about 0.0011 g/l (Chemical Rubber Company, 2013-2014, 4-54): this means that vaterite is approximately 3.7 times more soluble than calcite and 2.5 times more soluble than aragonite. Vaterite has a lower density compared to calcite and aragonite but its hexagonal structure has some similarities with the aragonite structure (Tucker and Wright, 1992, p.289).

In natural system it is metastable relative to calcite and aragonite, however, it can be produced in the laboratory under conditions that promote high precipitation rates

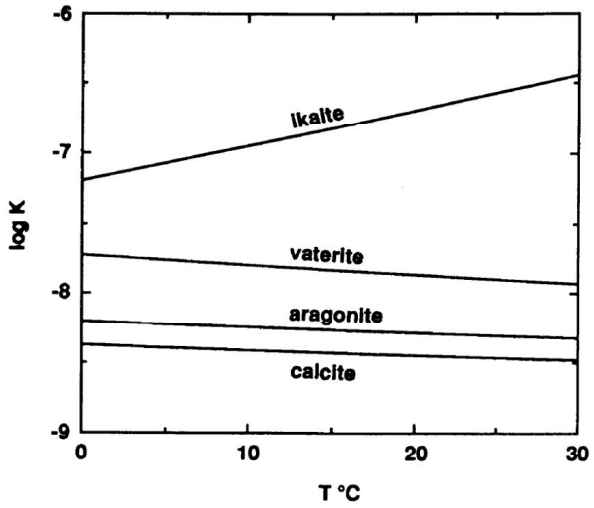

Figure 3.23.: Plot of solubility (log K) versus temperature for ikaite, vaterite, aragonite and calcite. The diagram shows that ikaite solubility has an opposite trend compared to anhydrous $CaCO_3$ but it is more soluble at all temperatures above zero (from: Bischoff et al., 1993, p.28).

(Morse and Mackenzie, 1990, p.42).

3.4.2. Hydrated calcium carbonate

Ikaite

Ikaite (sometimes described as the *hexahydrate calcium carbonate*) is a compound with chemical formula $CaCO_3 \cdot 6H_2O$, considered metastable at the Earth's surface (Brecevic and Kralj, 2007, p.470). Its density was calculated to be between 1.752 g/cm^3 at 18ºC and 1.834 g/cm^3 at 0ºC (Hume and Topley, 1926). The differences may be due to different experimental conditions since, according to Hume and Topley (1926, p.2932), the properties of this mineral may show some variations depending on the formation conditions.

This mineral has been reported by several researchers (e.g. Brooks et al., 1950, p.146 and Brecevic and Kralj, 2007, p.470) since the beginning of 19th century but its characteristics were only studied in detail in the following century.

Monoclinic ikaite forms at 0ºC (Brooks et al., 1950) or subzero temperatures. According to Brooks et al. (1950, p.147) ikaite was reported to be unstable in contact with water at all temperatures above 0ºC but in some solutions this mineral can persist in the metastable condition at much higher temperatures (up to 20ºC) and, moreover, in some experimental conditions it can be formed at temperatures higher than this limit.

In some experiments ikaite crystallized in well-defined rhombohedral crystals ranging from 10 to 40 microns that decomposed at temperatures above 6°C (Brecevic and Kralj, 2007, p.4710). In these very same experiments the water content of this compound was found to be between 5.9 and 6 water molecules per molecule of $CaCO_3$.

Table 3.11.: Solubility of ikaite (from Brecevic and Kralj, 2007, p.471, modified).

Temperature [ºC]	$-\log K_s$
10	7.245
25	7.461
40	7.711

Table 3.12.: Solubility of calcium carbonate monohydrate (from Brecevic and Kralj, 2007, p.472, modified).

Temperature [ºC]	$-\log K_s$
15	7.06
25	7.21
35	7.21

Bischoff et al. (1993) pointed out that the temperature dependence of ikaite solubility is opposite in sign to that of vaterite, aragonite and calcite, which becomes increasingly soluble at lower temperatures (figure 3.23). The strong temperature dependence of ikaite is typical of inorganic hydrates such as epsomite and bischofite because the waters of hydration are more like ice in their entropy and enthalpy than liquid water, although they have a higher density than ice. For example, ikaite occupies a volume 20% smaller than the equivalent quantity of calcite and water. The results also show that ikaite is more soluble than calcite, aragonite and vaterite in water at all temperatures at atmospheric pressure. The solubility constants calculated for this compound between 10 and 40ºC are reported in table 3.11

Monohydrocalcite

Calcium carbonate monohydrate or monohydrocalcite has the chemical formula $CaCO_3 \cdot H_2O$ and a density of 2.38 2 g/cm^3. This mineral was first discussed in the scientific literature in 1930 (Brecevic and Kralj, 2007, p.471) and is generally found in the form of spherulitic aggregates which may slowly convert to aragonite or calcite. In some laboratory experiments these spheres had a diameter ranging from 13 to 30 microns (Brecevic and Kralj, 2007, p.471). Like ikaite, monohydrocalcite formation is favoured by low temperature and high hydrostatic pressure (Morse and Mackenzie, 1990, p.43).

According to Brecevic and Kralj (2007, p.471) who summarized some recent findings, precipitaiton of monohydrocalcite is favoured by the presence of magnesium in solution and other seawater ions. The thermodynamic solubility constants calculated for this compound from 15 to 35ºC are reported in table 3.12.

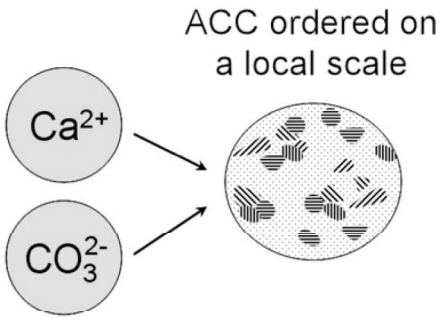

Figure 3.24.: Hypothetical evolution from $CaCO_3$ supersaturated aqueous solution to an ACC with low-range ordered domains (from: Rodriguez-Blanco et al., 2008, p.286).

Amorphous calcium carbonate

Amorphous calcium carbonate (ACC), firstly detected in 1938 (Brecevic and Kralj, 2007, p.469), is a rather unstable solid phase that rapidly transforms to one of the most stable $CaCO_3$ polymorphs (Brecevic and Kralj, 2007, p.469). ACC is, in fact, considered a precursor of the more stable $CaCO_3$ crystalline phases (Nebel et al., 2008, p.7874) and of $CaCO_3$ biomineralization in nature (Xu et al., 2008; Nebel et al., 2008).

It precipitates in spherical particles with diameters ranging from 50 to 400 nm. The water content of these particles is less than a water molecule per $CaCO_3$ molecule. According to Brecevic and Kralj (2007, p.469), the water is located in different positions inside the spherulitic structure and is characterized by different bonds.

According to other researchers, ACC has a variable composition and structure (Nebel et al., 2008, p.7874). Based on the powder diffraction data, ACC is though to be completely amorphous or with a local order reaching 15 Å (figure 3.24; Rodriguez-Blanco et al., 2008, p.283). Nebel et al. (2008, p.7874) reported that in some research it was found that the internal structure of the subsequently forming crystalline $CaCO_3$ was already *imprinted* into the structure of the initial ACC. Furthermore, this research suggested a relationship between the structure of ACC and monohydrocalcite (Nebel et al., 2008, p.7875). Regarding the kinetics of ACC transformation it is important to highlight that it can be relatively fast: in research carried out by Rodriguez-Blanco et al. (2011, p.283), it took only 1 minute at 25ºC for the calcite to form from ACC.

ACC dissolves rapidly when in under-saturated solutions (respect to ACC), producing in this manner a supersaturated solution with respect to calcite, aragonite and vaterite (Brecevic and Kralj, 2007, p.470). The thermodynamic equilibrium constants calculated for this compound are reported in table 3.13

Table 3.13.: Solubility of ACC according to Brecevic and Kralj (2007, p.470), modified.

Temperature [ºC]	$-\log K_s$
10	6.266
25	6.393
40	6.594

3.4.3. Effect of temperature and pressure on the $CaCO_3$ solubility

The solubility of anhydrous $CaCO_3$ in pure water decreases as temperature increases (figure 3.23). This behaviour is the opposite to the behaviour of many salts. In natural water this is probably due to the fact that at higher temperatures CO_2 is less soluble (see table 3.10). In general the solubility of carbonates is influenced much more by this change than by the temperature coefficient of the solubility itself (Krauskopf, 1979, p. 44).

The effect of pressure is to slightly increase the solubility of $CaCO_3$. The main reason for this is the change in the amount of dissolved CO_2 in water when the pressure of the gas in the surrounding atmosphere changes. Theoretically even the day-to-day barometric changes can have an effect on the solubility of CO_2, but circulation in the atmosphere keeps the concentration of CO_2 uniformly distributed (Krauskopf, 1979, p.44).

3.4.4. Effect of $CaCO_3$ polymorphism on solution pH

pH of solutions in equilibrium with different $CaCO_3$ polymorphs are different because of the differences in solubility.

Table 3.14 and figure 3.25 show the values of the theoretical pH of pure water in equilibrium with an infinite reservoir of $CO_{2(g)}$ at $p_{CO_2} = 350\ ppm$ and an infinite reservoir of different $CaCO_3$ solid phases. Calculations were made with PHREEQC. Initial pH of water was 7. Calculations with aragonite, calcite and monohydrocalcite were carried out using the *llnl* database, while calculations for vaterite were carried our using the *sit* database. Results show a difference of 0.27 pH at 0ºC when the solid phase in equilibrium is monohydrocalcite instead of calcite. At 40ºC this difference increases to 0.31 point of pH. Script used to simulate the effect of different solid phases on the pH of aqueous solutions is reported in algorithm 3.5

Table 3.14.: Calculated pH of pure water in equilibrium with an infinite reservoir of $CO_{2(g)}$ at $p_{CO_2} = 350\ ppm$ and with an infinite reservoir of different $CaCO_3$ solid phases in the temperature range 0-40ºC.

Solid phase	Temperature [ºC]					
	0	10	20	25	30	40
Calcite	8.284	8.269	8.257	8.251	8.247	8.239
Aragonite	8.334	8.319	8.306	8.301	8.296	8.288
Vaterite	8.502	8.482	8.461	8.451	8.442	8.424
Monohydrocalcite	8.55	8.544	8.541	8.541	8.541	8.546

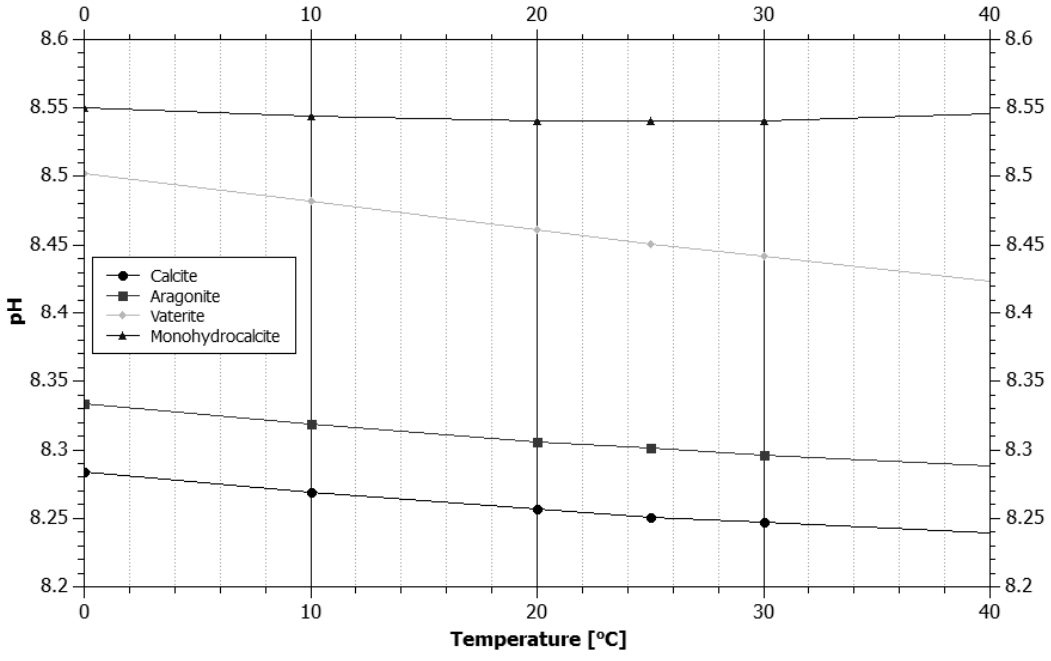

Figure 3.25.: Calculated pH of pure water in equilibrium with an infinite reservoir of $CO_{2(g)}$ at $p_{CO_2} = 350\ ppm$ and with an infinite reservoir of different $CaCO_3$ solid phases in the temperature range 0-40ºC.

Algorithm 3.5 PHREEQC script used to calculate the pH of a solution in equilibrium with different $CaCO_3$ solid phases and with an infinite reservoir of $CO_{2(g)}$ at $p_{CO_2} = 350\ ppm$.

```
SOLUTION 1

temp 25
pH 7 charge
pe 4
redox pe
units mmol/kgw
density 1
-water 1 # kg
EQUILIBRIUM_PHASES 1
CO2(g) -3.461648568 10
Aragonite 0 10
# Calcite 0 10
# Vaterite 0 10
# Monohydrocalcite 0 10

END
```

3.4.5. A comparison of the molar volumes and densities of different carbonate phases

According to the data contained in the *Crystallographic and Crystallochemical Database for Minerals and their Structural Analogues*[11], almost all the crystalline phases of $CaCO_3$ (both, anhydrous and hydrate) have a molar volume greater than $Ca(OH)_2$ (table 3.15). Only monohydrocalcite seems to have a molar volume smaller than portlandite but only one data is available in the database regarding this mineral.

Among the others minerals, it is interesting to note that the more unstable phases (ikaite and vaterite) are characterized by the highest molar volume. Ikaite, in particular, has a molar volume 3.44 times bigger than portlandite while vaterite is only slightly bigger than portlandite. The three anydrous phases of $CaCO_3$ are only slightly bigger than portlandite but among them it is possible to note a difference between aragonite (only 3.39% increase) and calcite and vaterite (more than 10% increase).

If instead of using crystallographic data, the molar volume is calculated from the molar weight and the molar volume as used by other researchers such as Putnis and Austrheim (2013, p.149), the small increase between anhydrous phases of $CaCO_3$ and portlandite is confirmed in addition to the fact that ikaite is the mineral with the largest molar volume (table 3.16). In this case, however, monohydrocalcite assumes the second largest molar volume with an increase of 49% compared to portlandite which may have an effect on the carbonation mechanism.

Considering the density, it is interesting to note that almost all the $CaCO_3$ polymorphs are more dense compared to portlandite. The exception is ikaite that is about

[11] Accessible at URL: http://database.iem.ac.ru/mincryst/index.php.

Table 3.15.: Comparison of the molar volume of different $CaCO_3$ phases with the molar volume of portlandite. Data from the *Crystallographic and Crystallochemical Database for Minerals and their Structural Analogues*. Difference in percentage, compared to portlandite. Details of data used to calculate the molar volumes are as follow: only one datum was available at the time of this calculations for monohydrocalite (contained in card n. 2951) and portlandite (contained in card n. 3739). Aragonite's molar volume is calculated as arithmetic mean between the 34.17 cm^3/mol reported in card n. 298 and the 34.19 cm^3/mol reported in card n. 6164. Calcite's molar volume is calculated as arithmetic mean among the 36.96 cm^3/mol reported in card n. 706, the 36.90 cm^3/mol reported in card n. 708, the 36.96 cm^3/mol reported in card n. 8196 and the 37.07 cm^3/mol reported in card n. 8432. Vaterite's molar volume is calculated as arithmetic mean between the 37.71 cm^3/mol reported in card n. 5094 and the 37.77 cm^3/mol reported in card n. 5093. Only one datum was available for ikaite (contained in card n. 2122).

Mineral	Molar volume (cm^3/mol)	Difference (%)
Monohydrocalcite	16.23	-50.91
Portlandite	33.06	-
Aragonite	34.18	3.39
Calcite	36.97	11.83
Vaterite	37.74	14.16
Ikaite	113.55	243.47

Table 3.16.: Comparison of the density and molar volume of different phases of $CaCO_3$ with portlandite. Data from the *Mineralogy Database* (URL: http://webmineral.com/). Difference in percentage, compared to portlandite .

Mineral	Density (g/cm^3)	Difference (%)	Molar weight (g/mol)	Molar volume (cm^3/mol)	Difference (%)
Portlandite	2.23	-	74.09	32.22	-
Aragonite	2.93	31.39	100.09	34.16	2.82
Calcite	2.71	21.53	100.09	36.93	11.17
Vaterite	2.54	13.90	100.09	39.41	18.61
Monohydrocalcite	2.38	6.73	118.1	49.62	49.36
Ikaite	1.78	-20.18	208.18	116.96	252.02

20% lighter. Monohydrocalicite has almost the same density of portlandite (almost 7% more dense). Anhydrous phases are about 14%, 22% and 31% more dense that portlandite, considering respectively vaterite, calcite and aragonite. Unfortunately no information was found for ACC.

According to these data it would be possible to point out that, if ikaite is formed at the beginning of carbonation, because of its density and molar weight, it may tend to emerge from the other solid phases, forming a crust (superficial layer) that tends to seal the beneath phases.

3.4.6. Precipitation diagram of $CaCO_3$ polymorphs

In 2009 Kawano et al. (2009) published a precipitation diagram of $CaCO_3$ polymorphs (figure 3.26) showing which phase first precipitates from a solution containing

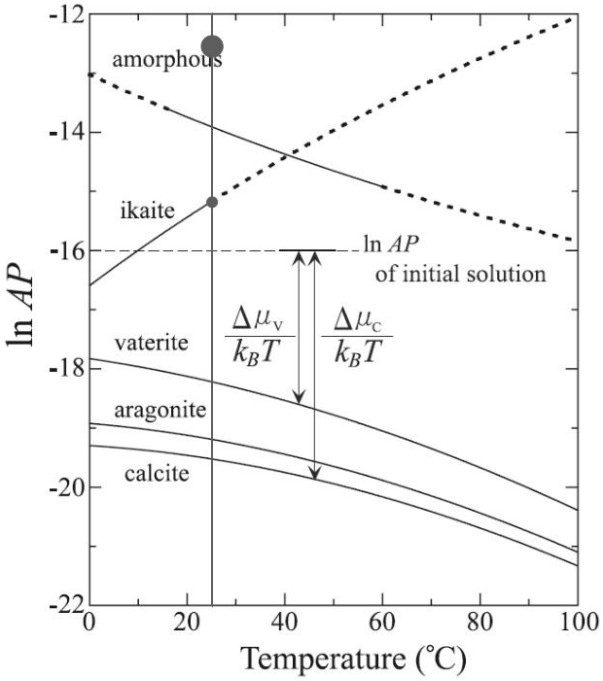

Figure 3.26.: Modified version of the precipitation diagram of $CaCO_3$ polymorphs as published by Kawano et al. (2009, p.425102). The vertical axes represents the natural logarithm of the activity product of Ca^{2+} and CO_3^{2-} ions ($\ln AP$) while in the horizontal axes is temperature. The circle on the top of represents the case of a $\ln AB$ value typical of a freshly mixed lime mortar. As soon as one of the activity values reduces, the $\ln AB$ value moves along the vertical line, towards more stable phases. At specific values (such as that highlighted by the small circle) a small temperature change can promote formation of different polymorphs.

Ca^{2+} and CO_3^{2-} ions under specific conditions. According to these authors, the diagram is based on the physical principles of these polymorphs in solution and adopts two variables: 1) the driving force for nucleation and (2) the temperature. The system where precipitation takes place is considered impurities free.

In this diagram, the nucleation's driving force for one of the $CaCO_3$ polymorphs from aqueous solutions is expressed by the following ratio:

$$\frac{\triangle\mu_i}{k_BT} \tag{3.4.3}$$

where $\triangle\mu_i$ is the chemical potential difference for the reaction that leads to the precipitation of the generic phase i, k_B is the Boltzmann constant and T is the absolute temperature.

The equilibrium constant for the generic phase i is calculated as:

$$K_i = \left[Ca^{2+^0}\right] \cdot \left[CO_3^{2-^0}\right] \tag{3.4.4}$$

where $\left[Ca^{2+^0}\right]$ and $\left[CO_3^{2-^0}\right]$ are the activities of the two ions in the saturated state. The product of the two activities is defined as AP:

$$AP = \left[Ca^{2+}\right] \cdot \left[CO_3^{2-}\right] \tag{3.4.5}$$

where $\left[Ca^{2+}\right]$ and $\left[CO_3^{2-}\right]$ are the actual activity of the two ions.
The driving force of the nucleation is, then, given as:

$$\frac{\triangle \mu_i}{k_B T} = \ln AP - \ln K_i \tag{3.4.6}$$

The equilibrium constants of all carbonate phases (k_i; both anhydrous and hydrate) have been published by several authors and, consequently, using this equation, it is possible to plot the $\ln AP$ against T.

According to Kawano and colleagues, the relative positions of the equilibrium curve in the whole temperature range considered in figure 3.26 are related to the relative stabilities of polymorphs. The lower the curve, the more stable the polymorph. The figure illustrates that the most stable phase at all temperatures is calcite. Aragonite is more stable than vaterite that, in turn, is more stable than ikaite and ACC, although starting from about 40ºC ACC becomes more stable of ikaite.

The driving force represented in equation 3.4.6 expresses the distance between the $\ln AB$ of a solution and the equilibrium curve for the i^{th} phase at a given temperature. This means that the i^{th} phase can nucleate only if $\ln AB$ is above its equilibrium curve (Kawano et al., 2009, p.425102).

Using a very simple PHREEQC script (algorithm 3.6) it is possible to calculate the $\left[Ca^{2+}\right]$ and $\left[CO_3^{2-}\right]$ under different conditions such as those of a freshly mixed lime mortar and plot them on the diagram to verify which solid phases can precipitate. For instance, a PHREEQC simulation containing a water solution at 23ºC at the same pH (12.448) and with the same concentration of Ca^{2+} ions (0.0125 $^{mol}/_{kg_{solution}}$), like that of a saturated aqueous solution of $Ca(OH)_2$ in equilibrium with atmospheric CO_2, ($p_{CO_2} = 350\ ppm$) is characterized by an ion activity of 4.13×10^{-3} and 8.48×10^{-4} for Ca^{2+} and CO_3^{2-} ions, respectively. This leads to a value of -12.5615 for the $\ln AB$. This value reported on the precipitation diagram shows that under these conditions (e.g. at the very beginning of the carbonation in a lime based mortar), all the $CaCO_3$ polymorphs can precipitate, ACC included (main circle in figure 3.26).

As soon as one of the activity values reduces (for instance when the CO_2 diffusion in the lime mortars is reduced by a reduction in the pore size or by presence of a thick layers of water) the $\ln AB$ value reduces along a vertical line, towards more stable phases.

In this path, when the $\ln AB$ reaches specific values, (e.g. when it is just below -15, that is when the $\ln AB$ is on the stability curve of ikaite), a small change in temperature (e.g. ±1ºC) can lead to the formation of a specific $CaCO_3$ solid phase rather than

Algorithm 3.6 PHREEQC script used to calculate the $\left[Ca^{2+}\right]$ and $\left[CO_3^{2-}\right]$ in a aqueous solution at 23ºC with initial pH of 12.448, in equilibrium with atmospheric CO_2 ($p_{CO_2} = 350\ ppm$).

```
SOLUTION 1

temp 23
pH 12.448 charge
pe 4
redox pe
units mmol/kgw
density 1
Ca 0.0125 portlandite 0
-water 1 # kg
EQUILIBRIUM_PHASES 1
CO2(g) -3.461648568 10

END
```

another (e.g. ikaite rather than vaterite).

In general, the diagram shows that low temperatures (e.g. 0-20ºC) favour ikaite, vaterite and calcite formation because the widening of their stability fields, while high temperatures (e.g. 20-40ºC) favour precipitation of ACC and ikaite.

Furthermore, it is noteworthy that, if the value of $\ln AB$ at the beginning of carbonation is high (e.g. -12.56 in the case previously reported) even the most unstable compounds can precipitate (e.g. ACC). Subsequently, when the Ca initially available for reaction is consumed or when the initial amount of CO_2 is reduced by a reduction in the diffusion process of this gas, only the more stable phases can nucleate and precipitate. This means that different times in the carbonation process of lime can be characterized by different polymorphs, depending on the product of the two ion activities (equation 3.4.5).

3.5. Conclusions: a short description of the carbonation reaction

Overall, the literature review and the study of the chemistry related to this reaction demonstrate that carbonation is a complex process, very sensitive to the conditions under which it takes place (e.g. temperature, solution composition, presence of foreign ions).

Carbonation can be seen as the result of a competition between three reactions occurring at the same time (Dheilly et al., 2002; Lawrence et al., 2007): the dissolution of $Ca(OH)_2$ and CO_2 in water and the reaction between $Ca^{2+}_{(aq)}$ and $CO^{2-}_{3(aq)}$ that leads to the production of a new solid phase (eventually calcite).

In the construction industry, the system where this competition takes place is initially formed from three phases in different states: a solid phase formed by the $Ca(OH)_2$, a liquid phase formed by the H_2O and a gas phase normally formed by air containing CO_2 with $p_{CO_2} \approx 340\ ppm$.

Within this system, water plays an important role because it acts as a medium in which the other two phases can dissolve and react and where the newly formed solid phases can dissolve and grow. Besides, the very basic pH of the aqueous solution produced by the dissolution of $Ca(OH)_2$, increases the CO^{2-}_3 ions, that allows precipitation of larger amounts of $CaCO_3$ [12].

For allowing the carbonation, however, the water must be in the right amount: it cannot be too much neither too little. Too much water reduces the carbonation rate due to the fact that the CO_2 diffusion in water is 10,000 times slower than that in air (Van Balen, 2005), whereas, in the absence of water the reaction cannot take place (Yang et al., 2003).

The minimum amount of water needed to initiate the reaction has been evaluated to be, at least, 4 molecular layers adsorbed on the surface of the $Ca(OH)_2$ crystals (Beruto and Botter, 2000)[13] and a relative humidity between 8 and 30% has been evaluated to be the minimum for producing detectable effects in powdered hydrated lime (Shih et al., 1999; Dheilly et al., 2002; Van Balen and Gemert, 1994).

Apart from promoting the carbonation reaction, the RH level has also an effect on the formation of different $CaCO_3$ polymorphs as well as on the reaction rate, crystallinity and crystal size of solid phases produced (Lopez-Arce et al., 2011). Summarising the results of previous researchers, it is possible to state that, overall, RHs between 75 and 95% can be considered optimal for the carbonation (Lopez-Arce et al., 2011,

[12] If the reaction was based on the dissociation constant of CO^{2-}_3 in water at neutral pH, it is likely that carbonation would be so slow that it would be almost impossible to use lime as a binder material for the construction industry.

[13] According to Cizer et al. (2012b) this corresponds to a partial pressure of water ≥ 0.7.

2010; El-Turki et al., 2007). Above this value CO_2 diffusion coefficient within the lime mortars starts to reduce reaching zero at 100% RH because of water content in the pores (Van Balen and Gemert, 1994, p.396). In such conditions, the diffusion coefficient is a hundred times smaller than at 75% RH. According to the mathematical model of the water vapour transport developed by Van Balen and Gemert, the pore surface in the lime mortars available for the carbonation reaction is maximum when the relative humidity is between 40 and 75% Van Balen and Gemert (1994, fig 3 p.396).

Calcium hydroxide dissolution is an interfacial reaction and, consequently, the specific surface area of $Ca(OH)_2$ particles (related to the particle size) and aggregation state of the particles play an important role on the amount of Ca^{2+} ions that dissolve in solution (Johannsen and Rademacher, 1999; Cizer, 2009). In addition, $Ca(OH)_2$ solubility in water changes inversely with the temperature: the lower the temperature, the higher the solubility. This means that, at the same time, small well dispersed particles at low temperatures (e.g. nano-lime used at temperatures between 0 and 10ºC) introduce more Ca^{2+} ions into solution than larger particles gathered into clusters at higher temperatures (e.g. powdered hydrated lime used at temperatures between 20 and 30ºC).

According to the Kawano's diagram (Kawano et al., 2009), this high release of Ca^{2+} ions has an effect on the formation of $CaCO_3$ solid phases because it increases the $\left[Ca^{2+}\right] \cdot [CO_2]$ product favouring formation of metastable phases (assuming fixed $\left[CO_3^{2-}\right]$ which is not dependant on the $Ca(OH)_2$ dissolution).

Contrary to the $Ca(OH)_2$, CO_2 solubility in water changes directly with temperature and with the p_{CO_2}: the lower the temperature or higher the p_{CO_2}, the higher the amount of CO_2 dissolved. In the absence of carbonate phases, however, CO_3^{2-} dissociation in water mainly depends on the solution pH: the higher the pH, the higher the CO_3^{2-} concentration so that the alkaline environment produced since the very beginning of the $Ca(OH)_2$ dissolution favours carbonation by promoting the complete dissociation of carbonic acid.

Disregarding the $Ca(OH)_2$ particle size, simple PHREEQC calculations of Ca^{2+} and CO_3^{2-} activity in aqueous solution at temperatures between 1 and 40ºC in the presence of solid phases such as monohydrocalcite, aragonite or calcite, show that the activity of Ca^{2+} ions is always 3 orders magnitude higher than the activity of CO_3^{2-} ions. This means that, theoretically, the only limiting factor of carbonation is the dissolution of CO_2 in water (until almost all of the $Ca(OH)_2$ solid phase is consumed). Furthermore, this means that the $[Ca^{2+}]/[CO_2]$ ratio produced by the dissolution of portlandite and CO_2 in water would always be >1 with a continuous production of rhombohedral calcite (Cizer et al., 2012a).

This is not confirmed by practical experience, which shows a reduction in the carbonation rate that can reach a value of zero even if the $Ca(OH)_2$ is not completely consumed (Cizer et al., 2012b; Van Balen, 2005).

This is probably due to the reaction mechanism and in particular to the formation of a (initially) discontinuous layer on the $Ca(OH)_2$ surfaces where it is likely that the carbonate phases nucleate (Yang et al., 2003; Beruto and Botter, 2000). Beruto and Botter (2000), in fact, suggested that the beginning of the reaction is characterized by the formation of a liquid-like H_2O adsorption layer entirely distributed within the initial porous particles that catalyse the $Ca(OH)_2 - CO_2$ solid–gas reaction forming a non-protective solid layer. Matsushita et al. (1993, p.727), instead, described the layer formed at the very beginning of the carbonation as an almost homogeneous amorphous phase with formula $Ca_{1+x}CO_3(OH)_{2x} \cdot yH_2O$ (with $x > 0.05$ and $y = 0.6 - 0.8$), differing from the ACC.

Although no connection has yet been proved between the layers described by Beruto and Botter, and Matsushita, it is likely that both are related to the film of solid $Ca(OH)_2$ present on the reacting surfaces of portlandite crystals in equilibrium with the Ca^{2+} and OH^- ions in solution. This layer was described by Ritchie and Xu (1990) as the cause of the diffusion controlled mechanism of $Ca(OH)_2$ dissolution reaction.

At a micro-metric scale, the very beginning of carbonation was described by Yang et al. (2003) with the formation of small scattered spots on the {001} surface of $Ca(OH)_2$ crystals, characterized by a low adhesion to the substrate[14]. Unfortunately no analysis were carried out in order to identify the mineralogical characteristics of these spots but, independently of whether those spots had or had not the same composition of the layers studied by Matsushita and Beruto, it is likely that with the formation of new phases on the portlandite faces, $Ca(OH)_2$ solubility and CO_3^{2-} diffusion are reduced (compared to the solubility and diffusion in pure water) so that the formation of this new phases may have the effect of slowing down the whole reaction.

Furthermore, despite the fact that there is no evidence that the amorphous phases described by Matsushita and Beruto act as precursor for the formation of the carbonate phases, it is likely that formation of carbonates follows the formation of these layers.

According to a number of authors (Ogino et al., 1990; Clarkson et al., 1992; Kawano et al., 2002; Carmona et al., 2004; Andreassen, 2005; Nehrke and Van Cappellen, 2006; Rodriguez-Blanco et al., 2011), the metastable carbonates (e.g. ACC, ikaite) are the first phases to be formed during the carbonation reaction, while calcite is the last one and its formation occurs by transformation of metastable phases. The basic sequence describing these transformations is reported in the following scheme, although the ikaite phase was not always identified:

[14] Similar spots were observed also at the SEM (Cizer et al., 2012b).

$$ACC \rightarrow (ikaite) \rightarrow vaterite \rightarrow calcite \tag{3.5.1}$$

According to Rodriguez-Blanco et al. (2011), the crystallization process of ACC to calcite occurs in two stages: 1) ACC particles rapidly dehydrate and crystallize forming individual particles of vaterite; 2) the vaterite dissolves and re-precipitates as calcite (the reaction rate of this transformation is controlled by the surface area of calcite[15]).

Regarding this sequence, it is interesting to note that all the phases formed have a larger molar volume compared to portlandite and, moreover, that the molar volume of solid phases produced tends to reduce during this transformation. The following scheme reports the differences in percentage of the molar volumes of different carbonates compared to that of portlandite according to the sequence in 3.5.1[16]:

$$\overset{ikaite}{243.47} \rightarrow \overset{vaterite}{14.16} \rightarrow \overset{calcite}{11.38} \tag{3.5.2}$$

The study of densities highlight that, together with a higher molar volume, ikaite is also characterized by a lower density, compared to portlandite and to the other carbonate phases. These, however, become more and more dense during the transformations described in 3.5.1. Scheme 3.5.3 reports the differences in percentage of the carbonate density compared to that of portlandite and suggests that ikaite may also float on the surface of $Ca(OH)_2$ (or on the surface of Beruto and Matsushita's layers) giving an explanation of the low adhesion of the new layer detected by Yang et al. (2003) with the tip of an AFM[17].

$$\overset{ikaite}{-20.18} \rightarrow \overset{vaterite}{13.90} \rightarrow \overset{calcite}{21.53} \tag{3.5.3}$$

Altogether, this information suggests that the formation of the first carbonate phases on the surface of $Ca(OH)_2$ crystals produces a layer that can reduce the portlandite solubility reducing the water-solid interface and this effect is even more relevant if ikaite is among the first phases formed.

Because of this layer, in fact, carbonation can proceed only where the $Ca(OH)_2$ is still exposed to the surrounding aqueous solution (e.g within the spaces among the carbonate phases) and, from this point of view, the reduction in molar volume of carbonate phases during their transformation can be considered advantageous for the progress of carbonation (although some time is needed for this transformation). Besides, since the

[15] Ogino et al. (1990) confirmed the last step also for aragonite. The second stage of the reaction was found to be approximately 10 times slower than the first one (Rodriguez-Blanco et al., 2011).

[16] No information is available for the ACC.

[17] A different explanation was given by Van Balen that hypothesized that the detachment of the layer on the portlandite crystals is due to the higher solubility of $Ca(OH)_2$ compared to that of $CaCO_3$ (Van Balen, 2005).

dissolution of even a very small amount of $Ca(OH)_2$ produces a very alkaline environment, a drop in the solution pH (that has an effect on the CO_3^{2-} dissociation) is likely to occur only when almost all the portlandite crystals are covered with this carbonate layer and this means that the carbonic ion dissociation is at its maximum until almost the very end of the reaction.

A reduction in the solid-liquid interface is likely to entail a local reduction in the Ca^{2+} ion concentration in solution and this may promote the dissolution of the newly formed metastable phases (from this point of view, it is important to note that a reduction in the portlandite dissolution at the very beginning of the reaction was experimentally detected by Cizer et al., 2012b). Because of the high solubility of these carbonates, a reduction in the $\left\{Ca^{2+}\right\}$ ions in the solution surrounding the portlandite crystals, makes the same solution under-saturated with respect to the metastable phases that necessarily dissolve allowing nucleation of new solid phases in different equilibrium conditions.

Since this dissolution takes place at the interface between the newly formed carbonate layer and the surrounding aqueous solution, the $\{Ca^{2+}\}/\{CO_3^{2-}\}$ ratio can be different compared to the beginning of the reaction, when the Ca^{2+} ion was the dominant specie. At this stage, the Ca^{2+} ions are likely to be mainly provided by the carbonate dissolution, together with the CO_3^{2-} ion. Furthermore, because of the metastable carbonate dissolution, locally, the CO_3^{2-} ion concentration becomes regulated by this reaction rather than by the CO_2 dissolution in water that, as a consequence, can be reduced.

The reduced solubility of CO_2 in water due to the dissolution of metastable phases can be the cause of the dormant period detected by Van Balen in 2005 (phase I; Van Balen, 2005) and confirmed later with new research that highlighted also formation of amorphous phases during this time (Cizer et al., 2012b).

Formation of more stable phases at this stage of the reaction would be suggested by the Kawano's precipitation diagram that highlights how at lower values of the $\ln AP$ (i.e. at lower value of the $\left[Ca^{2+}\right] \cdot \left[CO_3^{2-}\right]$ product that is at low Ca^{2+} and CO_3^{2-} ion concentrations) only the more stable phases can precipitate. The dissolution-precipitation mechanisms for this stage, instead, would be confirmed by results of Rodriguez-Blanco's researches (Rodriguez-Blanco et al., 2011).

Dissolution of metastable phases and nucleation of new more stable phases such as vaterite and calcite entail a general reduction in the molar volume of carbonate phases grown on the portlandite surfaces that, in turn, increases the portlandite-water interface (previously reduced by the formation of metastable phases) allowing dissolution of more Ca^{2+} in solution.

Availability of more Ca^{2+} ions in solution attracts more CO_3^{2-} ions that, in this manner, can no longer be provided only by the dissolution of amorphous phases. As

a consequence, dissolution of CO_2 in water starts again. This time, however, instead of taking part in the formation of amorphous phases, because of presence of calcite nuclei (initially formed by the dissolution of metastable phases), CO_3^{2-} ions take part in the growth of the more stable calcite crystals. In this manner the effect of metastable phases on the whole reaction is limited only to the very beginning of the reaction and the reactivation step found by Van Balen and his group can be explained (Cizer et al., 2012b; Van Balen, 2005).

After the initial stage involving formation of metastable phases, carbonation proceeds with nucleation and growth of more stable phases that have the effect of reducing the size of the pore where water diffuses together with the CO_2. When all the pores are closed and no more water and CO_2 can diffuse inside, carbonation stops even if not all the $Ca(OH)_2$ is consumed (e.g. Van Balen, 2005; Cizer et al., 2012b).

In this process the $\{Ca^{2+}\}/\{CO_3^{2-}\}$ ratio seems to be the main factor affecting the reaction, when in equilibrium with the surrounding environment. According to Cizer (2009) the $\{Ca^{2+}\}/\{CO_3^{2-}\}$ ratio in the pore water determines the habit and the morphology of the calcite crystals. In particular, at $\{Ca^{2+}\}/\{CO_3^{2-}\} \approx 1$ the growth of the rhombohedral calcite crystals is favoured. Excess of $\{Ca^{2+}\}$, instead, promotes formation of calcite with scalenohedral morphology that may dissolve and re-precipitate again as rhombohedral calcite upon the reduction of $\{Ca^{2+}\}$ and pH drop in pore water (Cizer et al., 2012a). An effect of $\{Ca^{2+}\}$ and $\{CO_3^{2-}\}$ on the calcite formation was found also by Spanos and Koutsoukos (1998). According to Kitamura et al. (2002) at $\{Ca\}$ near the portlandite solubility, the low CO_3^{2-} concentration favours aragonite formation. High CO_2 content, instead, is seen to favour vaterite formation (Han et al., 2005; Dickinson et al., 2002).

Looking at the precipitation diagram developed by Kawano et al. (2009), it is interesting to note that, even if at the beginning of the reaction in a freshly mixed lime mortar at about 25ºC, all the $CaCO_3$ polymorphs are likely to precipitate, with the reduction of the $\{Ca^{2+}\}$ and $\{CO_3^{2-}\}$ ions (and, consequently, with the reduction of the $\ln AB$ value), only the more stable phases can precipitate. As a consequence, the reaction product at the beginning of carbonation can be significantly different from the product reaction in the most advanced stages of the same process simply because the change in the solute composition.

Another important factor related to the ion concentrations that can affect the $CaCO_3$ polymorph precipitation is the size of the pores where the reaction takes place. According to Rodriguez-Navarro et al. (2002), because of the Laplace curvature effect, in pores with diameter $<1\mu m$, $CaCO_3$ precipitates from highly supersaturated solutions and with higher nucleation rates compared to the nucleation and precipitation process

in bigger pores. This means that in such pore types, precipitation of metastable phases such as ACC (that are more soluble), is favoured and, moreover, the local conditions may favour persistence of such a type of phase over a longer period of time.

Independently from the solid phases formed, with the growth of $CaCO_3$, the system initially formed of three phases ($Ca(OH)_{2(s)}$, $H_2O_{(l)}$ and $CO_{2(g)}$) acquires a new phase (although this is likely to change with time). The formation of a new solid phase has an effect on the pH since the CO_3^{2-} dissociation is affected by the presence of $CaCO_3$. As an example, a phase sequence is presented similar to those described above where, instead of comparing the molar volume or density of different carbonates, the equilibrium pH is calculated with PHREEQC using the code reported in algorithm 5.1 for pure water at 25ºC in equilibrium with a $p_{CO_2} = 350\ ppm$ and different $CaCO_3$ solid phases:

$$\underset{8.541}{\overset{monohydrocalcite}{}} \rightarrow \underset{8.451}{\overset{vaterite}{}} \rightarrow \underset{8.301}{\overset{aragonite}{}} \rightarrow \underset{8.251}{\overset{calcite}{}} \tag{3.5.4}$$

Results show that the final pH of the solution where carbonation takes place is different depending on the solid phase produced. According to the studies carried out by a number of researchers, the pH has an important role in the transformation phase of $CaCO_3$. In the temperature range of interest for the construction industry, pHs<10 are though to favours vaterite crystallization (Tai and Chen, 1998) and, as a consequence, pHs >10 are though to retard the transformation of vaterite in calcite (Ogino et al., 1990; Tai and Chen, 1998). pH>12 are thought to favour calcite (Tai and Chen, 1998) while pH>13.5 are thought to favour aragonite formation (Kitamura et al., 2002)[18].

Within this basic description of the chemical process of carbonation, other variables can play an important role changing the final products of the reaction. Presence of foreign ions such as Mg^{2+}, Fe^{2+} and Cu^{2+}, for instance, can favour precipitation of different crystalline phases such as aragonite (Loste et al., 2003; Wada et al., 1995). Pore water evaporation can modify the saturation state of the pore solution accelerating the precipitation of solid phases and leading to precipitation of different $CaCO_3$ polymorphs (Cizer et al., 2012a). Formation of a complete dry environment before all the $Ca(OH)_2$ is consumed can stop the reaction.

All these variables clearly show the complexity of this reaction that, as previously said, is very sensitive to the conditions under which it takes place and, for this reason, is more difficult to control in the building sites than hydration of silicate phases such as those contained in natural hydraulic limes.

[18]Tai and Cheng, instead, found that maximum yield of aragonite occurred at about pH=11 (Tai and Chen, 1998).

4. Techniques

4.1. Pd-hydride nanostructured micro-electrodes for the pH measurements

4.1.1. pH and traditional pH electrodes

One of the most important electrochemical measurements is the measure of acidity or basicity of aqueous solution.

Acidity (or basicity) is measured on a pH scale, where the pH is the negative logarithm of the activity of the hydride ion (Pankow, 1991, p.111):

$$pH = -\log[H^+] \tag{4.1.1}$$

According to this scale, pure water has a pH close to 7 while aqueous solutions of acids have pHs of less than 7 and solutions of bases have pHs above this value.

pH measurements are important in many fields including medicine, biology, chemistry, agriculture, food science, environmental science, water treatment and civil engineering. In medicine, for instance, a proper slightly alkaline pH level of the blood is an important aspect of a healthy body and for this reason monitoring the pH of blood is an important diagnostic action. In soils pH can influence plant growth by its effect on microorganisms and bacterial activity that decompose organic matter (Vimer et al., 2009, p.51).

In a similar manner to the biological systems, most deterioration processes in organic and inorganic materials used in the construction industry involve chemical reactions which are rate controlled by ionic transport and that can lead to microstructural changes potentially dangerous for the physical properties of the materials themselves. In concrete, for example, the presence of abundant $Ca(OH)_2$ as well as smaller amount of other alkaline species such as $Na(OH)$ and $K(OH)$ produces high pH levels (≈12-14) that react with acidic environments with the formation of soluble salts. The acidic environment can be produced by several factors such as bacterial activity or atmospheric CO_2 dissolved in water. At an early age, the high alkalinity in concrete causes the formation of a tightly adhering oxide layer on the surface of the embedded reinforcement steel that keeps the steel electrochemically passive and protects it from

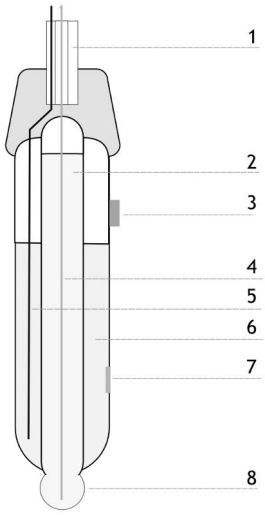

Figure 4.1.: Scheme of a combined electrode: 1) coaxial cable; 2) *AgCl* electrolyte; 3) removable cap; 4 and 5) *Ag* wire; 6) Hg_2Cl_2 solution; 7) porous membrane (salt bridge); 8) thin glass membrane where the pH is actually measured.

corrosion. With time, however, this protective film can be neutralized by the acid environment and the steel can be corroded by the most common degradation processes such as rust. Factors contributing to the destruction of such passive films include, among other things, the reduction of the pH levels of the internal pore solution and for this reason it is important to monitor the pH in the reinforced concrete (Vimer et al., 2009, p.51).

One of the most traditional methods for measuring the pH in the construction industry is the pH meter with glass electrode, which is a special type of membrane electrode (Garrels and Christ, 1965, p.293). Together with this, some chemical indicators such as phenolphthalein can be used but successful developments of new methods for monitoring pH levels or pH-dependent processes in structural materials include potentiometric measurements using embedded micro-sensors and also electrochemical impedance spectroscopy (Vimer et al., 2009, p.52).

The most common pH electrodes are made of sodium-calcium-silcate glass with a relatively low resistance. This type of device is called a *combined electrode* and its function principle is based on a two-electrode system: a working electrode and a reference electrode. The working electrode is made of a bulb of glass containing a solution of fixed H^+ activity with an electrode dipped into this solution (usually an $Ag-AgCl$ with an *Ag* wire). This inner electrode conducts electrons reversibly into and out of the contained solution. The reference electrode is external and contains an *Ag* electrode within a saturated *calomel*[1] solution (Garrels and Christ, 1965, p.293).

[1] *Calomel* is the name of a rare mineral form of Mercury(I) chloride (Hg_2Cl_2) called also Mercurous chloride: a dense white or yellowish-white, odorless solid. The Saturated Calomel Electrode (SCE) is based on the reaction between elemental mercury and Hg_2Cl_2. The aqueous phase in contact with the mercury and the *calomel* is a saturated solution of potassium chloride in water.

The sensitive part of this electrode is a thin glass membrane at the bottom where a ionic exchange occurs between the Na^+ ions of the glass and the H^+ ions of the solution in contact with it. The internal face of this membrane is in contact with a solution at known pH, isolated from the outside environment while the external face is in contact with the solution where the pH must be measured. If this solution is acid, there is an accumulation of H^+ ions along the external surface of the membrane while if the solution is basic there is a depletion of H^+ ions. The electric potential measured by the electrode is due to this mismatch between the H^+ ions on the two sides of the membrane.

Measure of this potential is sent through a coaxial cable to a pH-meter where the signal is amplified and displayed in a unit of corresponding pH.

Because of its characteristics, it would be expected that such an electrode would be sensitive to sodium ions in the external solution, but experiments show that for pH values up to about 9, the electromotive force (or *emf*; this is the voltage developed by any source of electrical energy) depends only on the activity of hydrogen ions (Garrels and Christ, 1965, p.293). The most common general purpose pH-electrodes, in fact, behave most efficiently in the pH range 0 to about 9. For pH measurements of above 9, *high pH* electrodes must be used for accurate work. In high pH solutions, such as the one produced by the dissolution of $Ca(OH)_2$, the hydrogen ion activity is so low and the activity of alkali metal (or alkaline earth) ions is usually so high, that ordinary pH electrodes begin to respond to these ions (Garrels and Christ, 1965, p.126; Morse and Mackenzie, 1990, p.28).

4.1.2. Palladium-Hydride pH microelectrodes

The difficulty in measuring high pHs led researchers to develop new types of electrodes. In 2006 Imokawa and colleagues (Imokawa et al., 2006), developed a microelectrode that was very efficient and reliable also to high pH ($\approx$12-14). They recognized that the response of most potentiometric pH microsensors made with either, glass, liquid (or polymeric) membranes or metal oxide films is far from ideal. This means that $E - pH$[2] plots (e.g. figure 4.2) may possess different slopes in different pH regions and intercepts may vary unpredictably (Imokawa et al., 2006, p.256). Antimony oxide micro disks used for measuring the pH, for instance, have a linear $E - pH$ relation, but this is unstable and the electrode requires regular preconditioning. Furthermore, stability, accuracy and reproducibility of their potentiometric response become worst when the sensor size becomes smaller (although the potentiometric properties of micro disks should not be size dependent; Imokawa et al., 2006, pp.256-257).

To address this problems, Imokawa and his group focused their attention on the

[2] E is the open circuit potential (Imokawa et al., 2006, p.270).

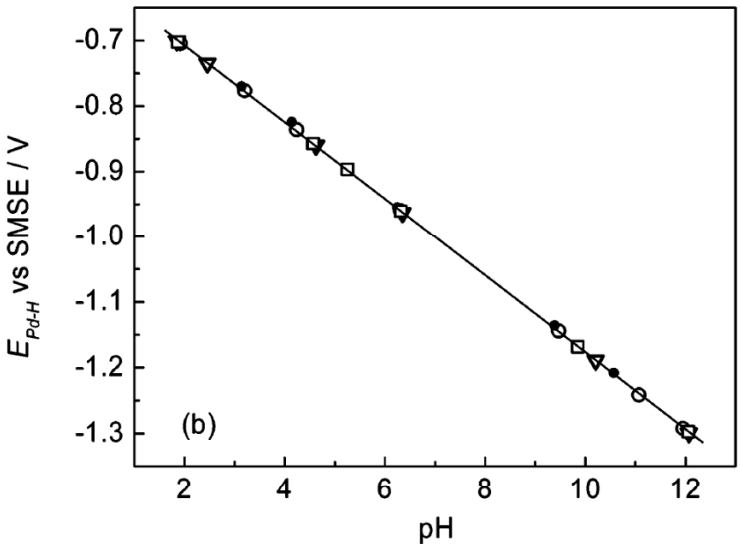

Figure 4.2.: E versus pH calibration curve obtained with different $H_1 - e$ Pd films (from: Imokawa et al., 2006, p.270).

Palladium-hydride micro disks (which was already used a as pH electrode), increasing the electroactive area retaining at the same time its geometric dimension. In particular, they modified the micro disk by electro-depositing on its surface a nano-structured palladium film from a liquid crystal template according to the procedure developed by Attard and colleagues and published by Attard et al., 1997.

The metal films produced in this manner (figure 4.3) are termed $H_1 - e$ to indicate that they were electrodeposited from the H_1 liquid crystal phase (Imokawa et al., 2006, p.257). The pore diameters of these films reflect those of the liquid crystal structure and typically range between 2 and 5 nm. The walls among the pores are between 2 and 5 nm thick and their depth is in the range of micrometers (the depth depends on the electrochemical charge passed during deposition and, consequently, can be variable). The electroactive area of the films is up to 3 orders of magnitude greater than that of the bare electrode. The surface area-to-volume ratio of the films is $10^7\ cm^2 \cdot cm^{-3}$, corresponding to a specific surface area of 91 $m^2 \cdot g^{-1}$: a value more than three time the specific area of the platinum, which is of the order of 22 $m^2 \cdot g^{-1}$ (Imokawa et al., 2006, p.257). The typical roughness factor of the film surface is around 300 (Imokawa et al., 2006, p.271)

This type of electrode is based on the fact that the nano-structured palladium film can accommodate protons in its structure becoming Palladium-hydride. The amounts of protons that can be absorbed within this film is limited and during the absorption the Pd-hydride change its crystalline structure in order to accommodate a different amount of protons. Three are the main crystalline structures (phases) identified for the Pd-hydride: α, β, $\alpha + \beta$. When the Pd hydride is in the $\alpha + \beta$ phase (that is when the H/Pd ratio is between 0.02 and 0.6; Serrapede et al., 2013, p.8341), it behaves as a

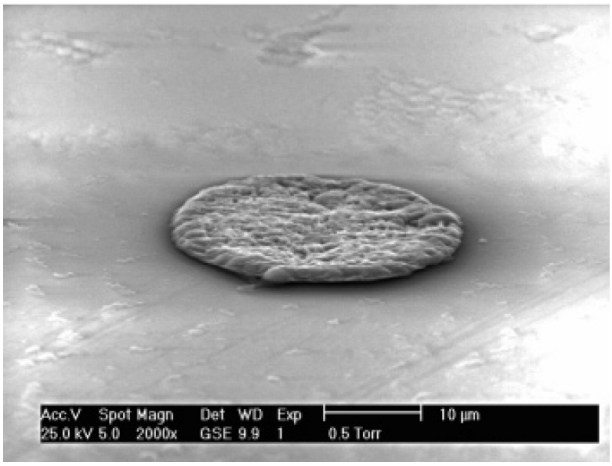

Figure 4.3.: Scanning electron micrographs of a 25μm diameter Platinum disk after deposition of Palladium films (from: Imokawa et al., 2006, p.267).

hydrogen electrode and yields a Nernstian dependence of potential on pH (figure 4.2)[3]. This is because the potential of the Pd hydride in the $\alpha + \beta$ phase is independent of the hydride composition (its hydrogen loading, i.e. the ratio Pd:H) and for any ratio Pd:H within this phase, it holds a steady value of +0.050V versus the *reversible hydrogen electrode* (RHE)[4] (Imokawa et al., 2006, p.266).

Despite this characteristic, until 2006 there was only one report of a Pd hydride micro disk pH sensor. This was probably due to several limiting factors: the potentiometric response, generally worse than that of large Pd hydride electrodes; the loading time of hydrogen into the tip that is slow; the instability of the potential (as hydrogen continually diffuses along the wire).

The nano-structure introduced by Imokawa and his colleagues avoided these problems (Imokawa et al., 2006, p.266). The nano structure, in fact, increases the hydrogen absorption rate and allows a rapid, stable, reproducible and almost theoretical potentiometric pH response in de-aerated solutions. The lifetime of micro-electrodes in the range 10-25 microns diameter is of 1-3 hours (in de-areated solution) which is not a very long time but is enough for many analytical applications. The lifetime of 250 μm diameter micro-electrodes has proved to be more than 8 hours. Furthermore, the electrode can be reloaded with hydrogen quickly, so that it is possible to perform pH measurements repeatedly (Imokawa et al., 2006, p.271).

In order to be used, the palladium film needs to be loaded with hydrogen. The loading is usually carried out in the same solution where the pH has to be measured by

[3] An electrode is said to behave *nernstially* if the equilibrium electrode potential obeys the Nernst equation when the activity of a species involved in the electrode reaction changes. The Nernst equation is an equation that relates the equilibrium reduction potential of a half-cell in an electrochemical cell (or the total voltage for a full cell) to the standard electrode potential, temperature, activity and reaction quotient of the underlying reactions and species used.

[4] The reversible hydrogen electrode is a particular type of the *standard hydrogen electrode* that differs from it by the fact that the measured potential does not change with the pH.

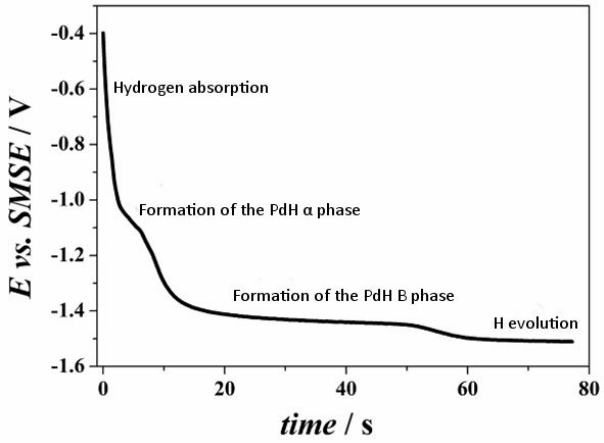

Figure 4.4.: Typical loading curve of a Pd-hydride micro-electorde. Labels highlight the following processes: hydrogen adsorption, formation of the PdH α phase, formation of the PdH β phase, hydrogen gas evolution (from: Serrapede et al., 2013, Supporting information, modified).

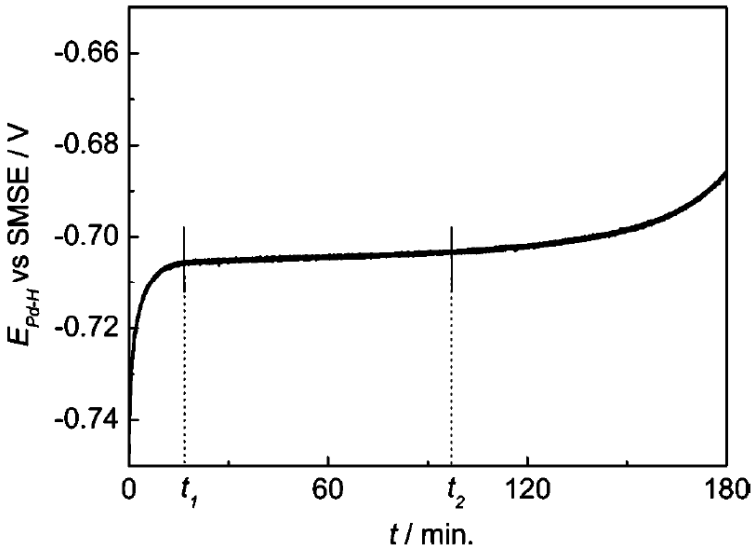

Figure 4.5.: Typical potential transient recorded with a $H_1 - e$ Pd film deposited on a 25 μm diameter Pt microdisk (from: Imokawa et al., 2006, p.270).

stepping the potential applied to the electrode from the double layer region to a value in the hydrogen region and, then, by holding this potential for a set time or until the current decays to zero (figure 4.4; Imokawa et al., 2006, p.268).

Once the formation of the β Pd hydride phase is completed and hydrogen gas starts to evolve, the load is stopped and the potential transient is recorded to evaluate the pH of the solution in contact with the electrode. The Ph hydride, in fact, naturally discharges the hydrogen electrochemically loaded (forced) in its structure and, when the Pd:H ratio is such to produce the $\alpha + \beta$ phase, the potential transient can be used as a measure of the pH of the solution.

Figure 4.5 shows the typical potential transient with the two characteristic times t_1 and t_2 corresponding to the gradual loss of hydrogen. In this figure, the three regions defined by the two times can be explained as follow:

- from time 0 to time t_1 the discharge of hydrogen from the β phase is the main event. Because the PdH film is still in the β phase, the potential is not yet related by a Nernstian dependence to the pH. The time taken to reach t_1 is dependent on hydrogen loading (Imokawa et al., 2006, p.270).

- from time t_1 to time t_2 the Pd hydride is in the $\alpha+\beta$ phase. As already said, in this phase the potential is characterized by a Nerstian dependence on the pH and, consequently, the average value that can be read on the y axis can be used to calculate the pH of the solution using a calibration curve such as the one in figure 4.2. The lifetime of the electrode (t_2-t_1) is independent from the solution pH but is roughly proportional to the geometric diameter and thickness of the Pd film. Between t_1 and t_2, the plateau potential does not vary by more than 1.2 mV (Imokawa et al., 2006, p.270).

- from t_2 to 180 minutes the potential rises significantly because the Ph hydride transforms into the α phase and the potential is no longer related to the pH by a Nernstian dependence. Consequently, the electrode cannot be used anymore for the pH measurement but the film can be loaded again for starting a new measurement.

4.2. Impedance spectroscopy

Impedance Spectroscopy (IS) or Electrochemical Impedance Spectroscopy (EIS) or, the ac Impedance method is a rapid, accurate and sensitive electrochemical technique for measuring electrochemical phenomena, particularly useful for monitoring the processes continuously. Measurements are rapid and accurate as the system under investigation is perturbed from its normal state by an external signal that changes the properties. For this reason EIS must be used with great care especially when interpreting results (Lasia, 1999, p.4).

More precisely, impedance spectroscopy studies the system response to the application of a periodic small amplitude AC signal. Measurements are carried out at different frequencies because the chemical and physical characteristics of the cell containing the specimen vary with frequency (Denuault, 2007; hence the name of spectroscopy). Analysis of the system response contains information about interfaces and the bulk system, their structures and reactions taking place there.

Contrary to the dc technique, used for corrosion rate measurement which uses a relatively large perturbation signal, ac method introduces only small perturbation signals and for this reason also low conductivity media can be investigated (Cogger and Evans, 1998, p.1).

EIS is considered a complementary technique: this means that other methods must be used together with it in order to understand the processes under evaluation (Lasia, 1999, p.4).

4.2.1. Principles of electrochemical measurements

If an electrical perturbation (potential) is applied to an electrochemical cell (electrical circuit), a current flow through the cell and its value is determined by the reactions that takes place such as the formation of new chemical species due to the ion movements through the solute. The ionic movements are caused by the applied potential and these movements constitute a flow of electrical current (Cogger and Evans, 1998, p.1). If the applied potential E, calculated as:

$$E = |E| \sin(\omega t) \tag{4.2.1}$$

is small (a small perturbation is needed because it is necessary to obtain a linear response between I and E so that $I \propto E$; Denuault, 2007) and sinusoidal, the subsequent current will also be sinusoidal (fig. 4.6):

$$I = |I| \sin(\omega t + \Phi) \tag{4.2.2}$$

In these equations $|E|$ is the absolute value of the amplitude of perturbation, $|I|$ is

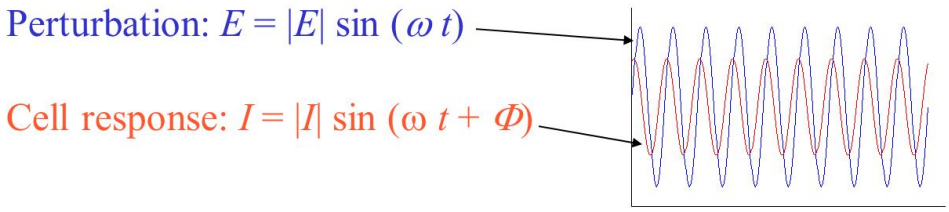

Figure 4.6.: Perturbation and cell response scheme (Denuault, 2007).

the absolute value of the amplitude of response, Φ is the phase difference between response and perturbation and ω is the angular frequency in radians, s^{-1}. Value of the angular frequency can be calculated as follow:

$$\omega = 2\pi f \tag{4.2.3}$$

where f is the frequency of perturbation in Hertz (Hz).

Impedance (Z) is the relation between the applied potential and the current flow:

$$Z = \frac{E}{I} \tag{4.2.4}$$

It has magnitude E/I and phase Φ and, consequently, it is a vector quantity and it has the unit of Ω.

If the perturbation is applied to a poorly conducting solution that behaves like a pure resistor of magnitude R, then the magnitude of the impedance is $Z = R$ and the related phase $\Phi = 0$ for all the frequencies (Cogger and Evans, 1998, p.1). The response is pure ohmic and the current is in phase with potential (Denuault, 2007). On the contrary, if the perturbation is applied to a solid-liquid interface, that is to a system that behaves as capacitor, perturbation can be calculated according to 4.2.1, while the response can be calculated according to the following equation:

$$I = C\frac{dE}{dT} = \omega C\,|E|\cos(\omega t) = \omega C\,|E|\sin\left(\omega t + \frac{\pi}{2}\right) \tag{4.2.5}$$

where C is the capacitance.

Consequently, according to the equation 4.2.4, the impedance can be calculated as follows:

$$Z = \frac{|E|\sin(\omega t)}{\omega C\,|E|\cos(\omega t)} \tag{4.2.6}$$

To facilitate dealing with impedance, very often a complex notation it is used that removes the time dependence (t). In this case, instead of considering E as a vector, it is possible to take it as a point in the complex plane $sin(\omega t) - cos(\omega t)$ (figure 4.7; Denuault, 2007) and rewrite E in form of a complex number:

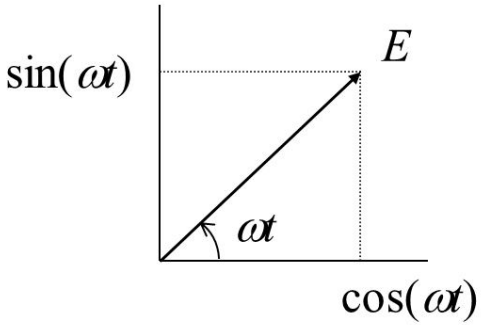

Figure 4.7.: Complex plane $sin(\omega t) - cos(\omega t)$ (from: Denuault, 2007).

$$E = |E| (\cos(\omega t) + i \sin(\omega t)) \tag{4.2.7}$$

where $i = \sqrt{-1}$.

Like E and I, also Z is a complex number made of a real (Z') and an imaginary (Z") part, both of them in Ω units:

$$Z = Z' + iZ'' \tag{4.2.8}$$

Consequently, if the system behaves like a resistor there will be no differences to the previously described case (Z is still equal to R because the real one is the only part of the complex number; Mcdonald, 1992), but if the system behaves like a capacitor, the perturbation can be rewritten as follow:

$$E = |E| (\cos(\omega t) + i \sin(\omega t)) \tag{4.2.9}$$

as well as the response:

$$I = C\frac{dE}{dT} = \omega C |E| (-\sin(\omega t) + i \cos(\omega t)) \tag{4.2.10}$$

Consequently, the impedance can be recalculated:

$$Z = \frac{E}{I} = \frac{-i}{\omega C} \tag{4.2.11}$$

Results of impedance measurements can be plotted in two ways as function of frequency (f):

- considering individually Z', Z'' or Φ in the so called Bode plots (fig. 4.8 left hand side);
- plotting the inverse of the imaginary part of impedance ($-Z''$) as function of the real part (Z'). In this case the plots are called Nyquist, Argand or Cole-Cole plots and are still frequency-dependent because both, Z' and Z" are f-dependent

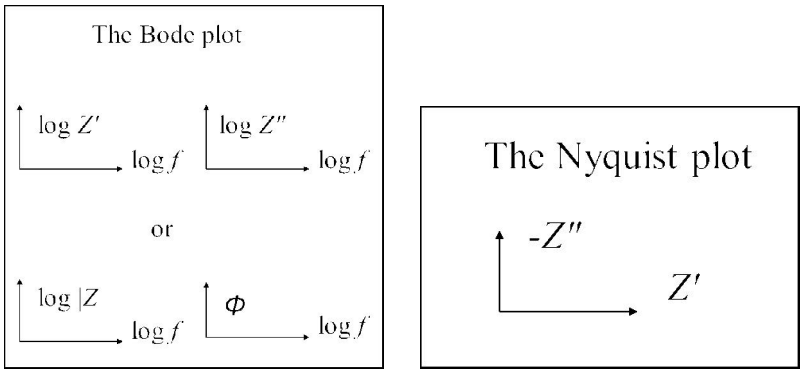

Figure 4.8.: Different types of Bode plots (left hand side) and generic Nyquist plot (right hand side; Denuault, 2007).

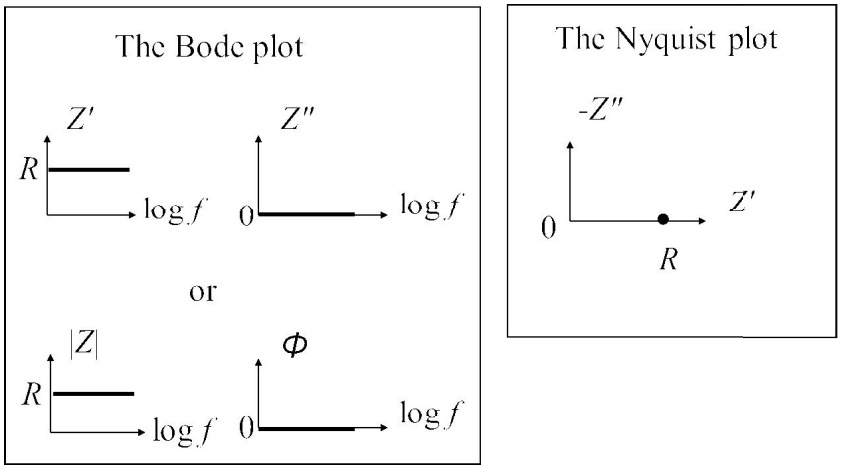

Figure 4.9.: Bode plot (left hand side) and Nyquist plot (right hand side) for a pure resistor (from: Denuault, 2007).

(fig. 4.8 right hand side).

The bode plot and the Nyquist plot for a pure resistor of magnitude R (Z' $= R$; Z" $= \Phi = |Z| = 0$) is reported in figure 4.9.

If the sinusoidal potential is, instead, applied to a system that behaves like a capacitor (this is the case of the double layer capacitance which occurs at the electrode/electrolyte interface; Cogger and Evans, 1998, p.7) values of Z, Z', Z", $|Z|$ and Φ are as follow:

$$Z = \frac{-i}{\omega C} \tag{4.2.12}$$

$$Z' = 0;\ Z'' = \frac{-i}{\omega C} \tag{4.2.13}$$

$$|Z| = \frac{1}{\omega C};\ \Phi = \frac{\pi}{2} \tag{4.2.14}$$

and the related plots are as in figure 4.10:

Combinations of these two basic circuit components (resistor and capacitor) in series

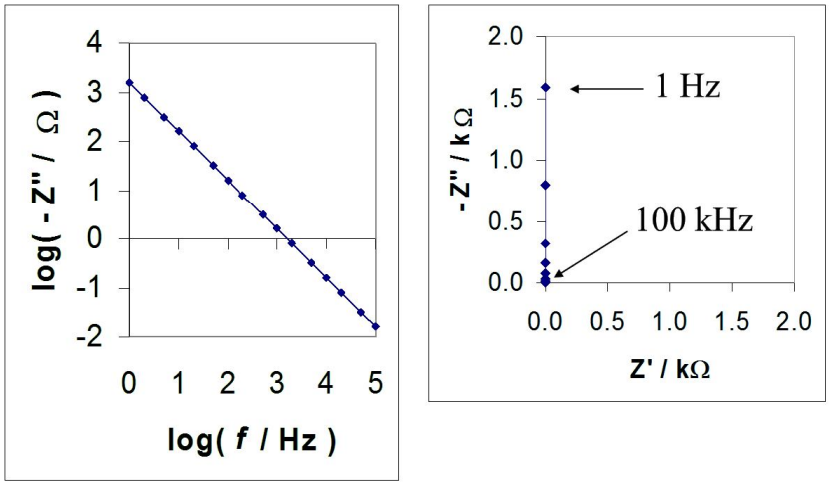

Figure 4.10.: Bode plot (left hand side) and Nyquist plot (right hand side) for a pure capacitor (Denuault, 2007).

or in parallel produce different results that can be easily deduced. For instance, a series resistance and capacitance produces the plot showed in figure 4.11 while for a parallel resistance and capacitance the plot is as in figure 4.12.

Overall, this means that an electrochemical cell can be represented by a network of resistors and capacitors, called an *equivalent circuit*. This means that from a generic impedance spectrum it is possible to deduce the equivalent circuit and determine the significance of different components (Cogger and Evans, 1998, p.7). For instance, a simple corrosion system can be represented with the diagram in figure 4.13 where the resistance of electrolytes, surface films and leads used to connect the cell to the analyzer are represented by the series resistor R_1. The parallel resistance R_2 is known as the charge transfer resistance and determines the corrosion rate in the system. The capacitance (C) is known as the double layer capacitance which occurs at the electrode/electrolyte interface (Cogger and Evans, 1998, p.7). Through the plot it is possible to evaluate that at very high frequency the capacitor conducts easily (effectively shorting out the charge transfer resistance R_2) leaving only the effect of the conduction series resistance (R_1). As the frequency decreases, the conduction of the capacitor decreases and the response due to R_2 increases. As the frequency approaches zero the capacitor ceases to conduct and the cell impedance is a function of R_1 and R_2 only.

In figure 4.14, which contains a more generic representation of the Nyquist plot, it is interesting to notice that the absolute value of Z is represented by the conjunction line between the origin of the Cartesian axes and the point considered, while the phase angle Φ is the angle between the above mentioned line and the Z' axis. R_2 is the diameter of the semicircle, whereas R_1 is the distance of the semicircle from the $-Z$" axis.

The frequency increases anticlockwise along the semicircle (arrow on the right hand side of the figure 4.14) and the double layer capacitance (C) can be obtained through

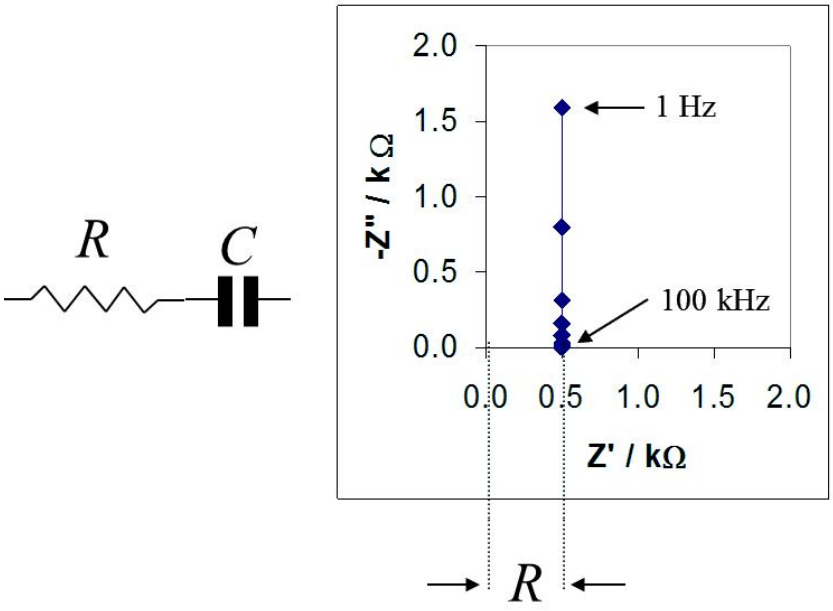

Figure 4.11.: Nyquist plot of a series resistance and capacitance (Denuault, 2007).

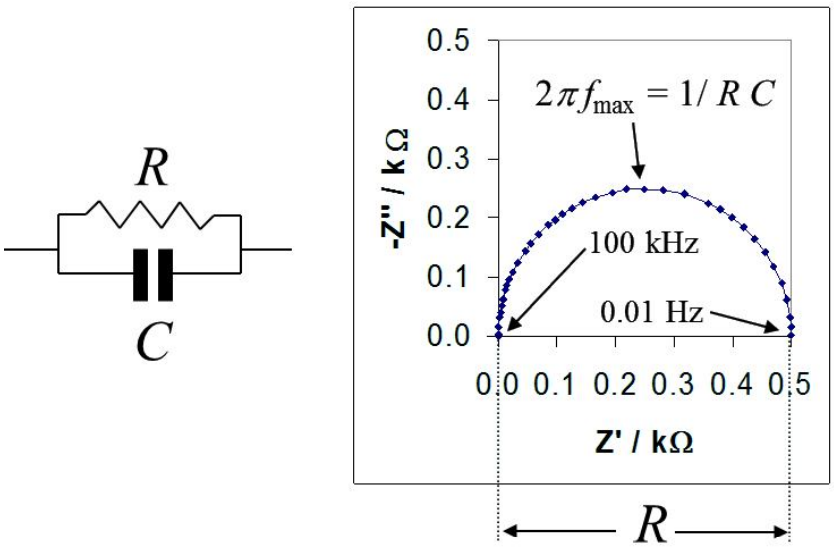

Figure 4.12.: Nyquist plot of a parallel resistance and capacitance (Denuault, 2007).

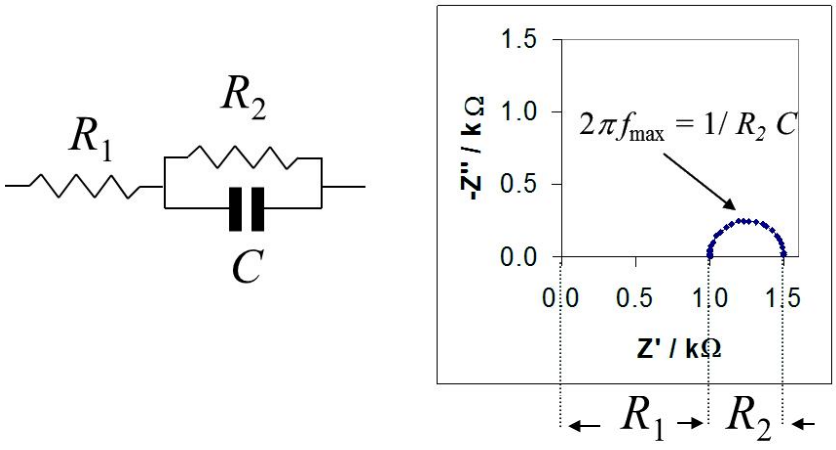

Figure 4.13.: Nyquist plot of a system with a resistance in series with a parallel resistance and capacitance (Denuault, 2007).

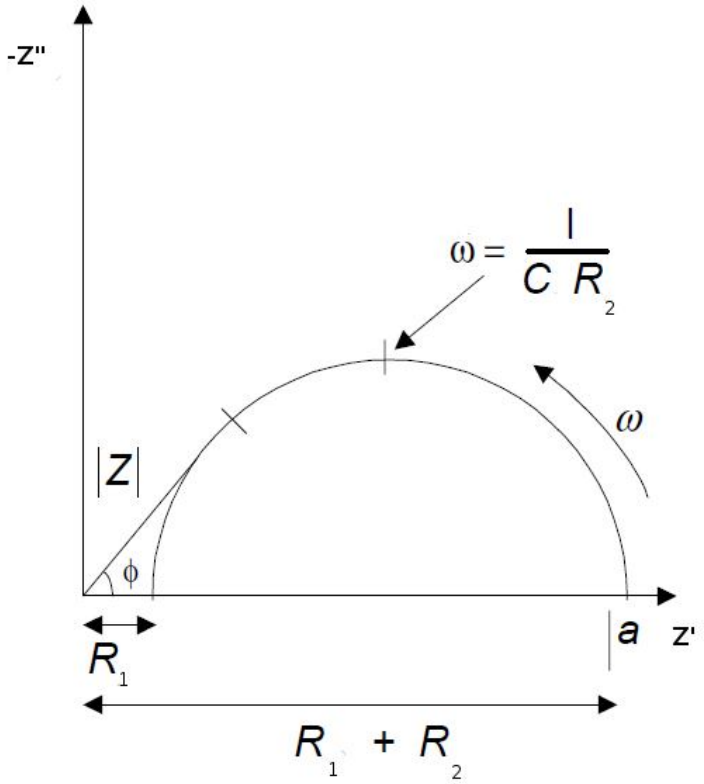

Figure 4.14.: Nyquist plot of a simple system made of a resistor in parallel with a series resistor capacitor (Cogger and Evans, 1998).

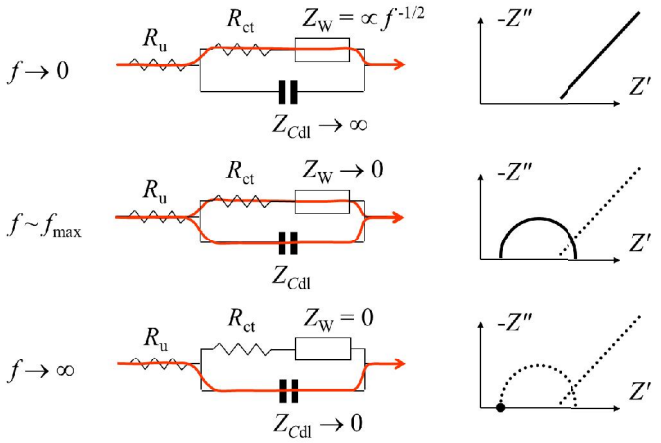

Figure 4.15.: Nyquist plot at different frequencies of a simple system containing a Randles circuit (Cogger and Evans, 1998).

ω according to the equation (Denuault, 2007):

$$\omega = \frac{1}{CR_2} \tag{4.2.15}$$

More complex systems require more complex equivalent circuits to model other natural phenomena such as the effects of diffusion of charged species. To include the mass transfer diffusion effect, for instance, a specific equivalent circuit has been developed which includes an additional element called the *Randles circuit* (figure 4.15). This is a complex quantity having a real part equal to the imaginary and the impedance is proportional to the reciprocal of the square root of the frequency ($1/\sqrt{\omega}$). This means that at high frequencies, the contribution of this element is small and the diffusion process is observed only at low frequencies. At low frequency the semicircle is distorted by the Warburg impedance with a straight line at 45° to the axis (but the diffusion layer effect can also cause a double semicircle due to the bend of the above mentioned Warburg line toward the Z' axis). A second low frequencies semicircle might also be due to adsorption phenomena, while a depressed semicircle is caused by a time constant dispersion due, for instance, to inhomogeneity in the electrode surface (Cogger and Evans, 1998, p.7).

Overall, it can be seen that the basic parameters (electrolyte resistance, double layer capacitance, corrosion reaction and diffusion effects) can be determined by empirical impedance data, provided that a sufficient frequency range is investigated. In particular, the low frequency region can provide information concerning charge transfer and diffusion phenomena, while the high frequency part defines the solution resistance (Cogger and Evans, 1998, pp.7-8).

4.2.2. The use of impedance spectroscopy in the study of lime based materials

As already stated, impedance spectroscopy is a rapid, accurate and sensitive electrochemical technique for measuring electrochemical phenomena, particularly useful for monitoring the processes continuously. It is commonly used to study processes in a range of materials including ceramics, polymers and composites.

Over the past 30 years its use in the construction industry has been mostly confined to cement hydration and rebar corrosion in concrete (McCarter et al., 1988, 2002) and only limited work has been carried out in applying this technique to lime based mixtures (Ball and Allen, 2010; Ball et al., 2011).

However, results obtained in systems containing even a small amount of lime already highlighted the usefulness of this technique in the study of lime based materials. Response of IS analyzers to the reactions that happen within the lime (e.g. hydraulic lime), for instance, can be evaluated by comparison with the results obtained for cementicius materials. Systems containing natural hydraulic lime, in fact, have common characteristics with the those containing ordinary Portland cement. For instance, researches carried out on the interaction of cement with pozzolanic materials such us rice husk ash and fly ashes (a reaction that takes places because the $Ca(OH)_2$ is contained and produced by the cement) can be used to interpret the results of lime based mixes containing pozzolanic additives.

4.3. Nuclear Magnetic Resonance

4.3.1. Nuclear spin and nuclear spin quantum number

Subatomic particles such as electrons, protons and neutrons can be imagined as spinning on their axes. Spin, in fact, is a fundamental property of nature such as the electrical charge or the mass. The spin for each individual subatomic particle assumes the value of $1/2$ and can be positive ($+1/2$) or negative ($-1/2$).

The *nuclear spin* (I) represents the total angular momentum of a single nuclide, produced by the sum of all the spins of particles contained in the nucleus (for this reason I comes in multiples of $1/2$; Hornak, 2011; Tonellato, no date).

Spin of subatomic particles can be paired or unpaired. Paired spins (i.e. with opposite sign) annul each other with the consequence that the overall spin is null. Helium-4, for instance, that contains two protons and two neutrons has a nuclear spin $I = 0$. When the particles are not paired up, the atoms are characterized by spins. Helium-3, that contains two protons and an unpaired neutron, for example, has a nuclear spin $I = \pm 1/2$.

Nuclei of many elemental isotopes have characteristic spin (almost every element in the periodic table has an isotope with a non zero nuclear spin). Some of them have integral spin (e.g. I =1, 2, 3, ...), other have fractional spin (e.g. I=$1/2$, $3/2$, $5/2$, ...) and a few have no spin ($I = 0$; e.g.^{12}C, ^{16}O, ^{32}S, ...). Rules for determining the net spin of a nucleus are the following:

- if the number of neutrons *and* protons are both even, then the nucleus has *no* spin (I=0). Examples are ^{12}C and ^{16}O (that, consequently, cannot be observed with nuclear magnetic resonance);
- if the number of neutrons *plus* the number of protons is odd, then the nucleus has an half-integer spin (e.g. I=$1/2$, $3/2$, $5/2$, ...);
- if the number of neutrons and the number of protons are both odd, then the nucleus has an integer spin (e.g. I=1, 2, 3, ...; Hornak, 2011; Tonellato, no date).

4.3.2. Magnetic moment

As well as a charge in motion along a straight line, also a spinning charge generates a magnetic field. It is possible to think of the spin as a magnetic moment vector causing the charged nuclear particle to behave like a tiny magnet with a north and a south pole like a compass needle. For this reason a spinning charge such as a proton is (also) characterized by a *magnetic moment* (μ) proportional to the spin and described by the following equation:

$$\mu = \gamma I \frac{h}{2\pi} \tag{4.3.1}$$

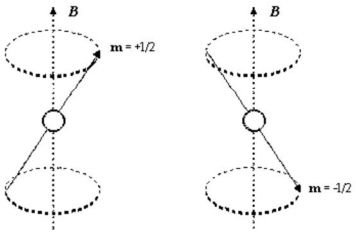

Figure 4.16.: Representation of the magnetic quantum number (from: Tonellato, no date, p.1, modified).

or by the equation:

$$\mu = \gamma I \bar{h} \tag{4.3.2}$$

where:

$$\bar{h} = \frac{h}{2\pi} \tag{4.3.3}$$

In the these equations, h is the Plank's constant, I is the nuclear spin previously described and γ is the gyromagnetic (or magnetogyric) ratio: a fundamental nuclear constant that is different for each nucleus. In NMR, γ can be used to determine the sensitivity of a nuclide to detection. Nuclides with large values of γ are easy to observe while nuclides with small values are difficult to detect (Edwards, 2009; Tonellato, no date; Hornak, 2011).

4.3.3. Magnetic quantum number, energy states and transition energy

When a charged particle is placed in an external magnetic field, its magnetic moment tends to align the spin vector with the external field, just like a magnet would do. Because of the spin is governed by quantum mechanics, only certain discrete orientations of the magnetic moment are allowed. These discrete values are integral or half integral multiplies of I called the *magnetic quantum number* (m). The *magnetic quantum number*, assumes the values $-I$, $(-I+1)$, $(I-1)$, I (Hornak, 2011; Tonellato, no date).

For instance, if $I = 3/2$, then $m = -3/2, -1/2, 1/2, 3/2$. Each nucleus with spin I has, therefore, $2I+1$ possible orientations. In the case of hydrogen, $I = 1/2$ and, consequently, the allowed spin states of the nucleus are 2: -1/2 and +1/2 (figure 4.16).

In a similar manner, a nuclide with a magnetic moment within an external magnetic field (B) has a potential energy (E) that also takes only certain discrete values. For a nucleus with $2I+1$ orientations, for instance, there are also $2I+1$ energy states called *Zeeman levels*, given by the following equation:

$$E = -\gamma \bar{h} m B \tag{4.3.4}$$

For a proton, $m = \pm 1/2$ and, therefore, there are two possible energy states:

$$E_1 = -\frac{1}{2}\gamma\bar{h}B \tag{4.3.5}$$

$$E_2 = +\frac{1}{2}\gamma\bar{h}B \tag{4.3.6}$$

where B is the external magnetic field and $\bar{h}$ is calculated according to equation 4.3.3.

When $m = 1/2$, μ is parallel to the direction of the external magnetic field that is the preferred orientation, characterized by low energy level. On the contrary, when $m = -1/2$, μ is anti-parallel to the direction of the field and, consequently, is associated with a high energy level.

The difference in energy between the two levels, called *transition energy*, can be evaluated as:

$$\Delta E = E_2 - E_1$$

The selection rule for NMR transition states that m can only change by one unit. This means that the transition can only occurs between adjacent energy levels so that the previous equation leads to the following evaluation of the transition energy:

$$\Delta E = +\frac{1}{2}\gamma\bar{h}B - (-\frac{1}{2}\gamma\bar{h}B) = \gamma\bar{h}B \tag{4.3.7}$$

Equation 4.3.7 states that a transition between two adjacent energy levels requires only a specific transition energy ΔE, that depends on the type of nuclide (γ) and the external magnetic field (B) (Hornak, 2011; Tonellato, no date).

4.3.4. Population in the different energy levels

Because the energy difference between the two energy states is very small (about $9 \cdot 10^{-6} kcal \cdot mol^{-1}$), nucleus population in the two states is very similar with a slight predominance of particles in the low energy state (that is aligned to the magnetic field; Hornak, 2011; Tonellato, no date).

Considering a macroscopic sample, it is possible to calculate the population of nuclei for each energy level. For instance, for nuclides with $I = 1/2$, if the number of nuclei in the higher energy level is called N_β and the number of nuclei in the lower energy level is called N_α, the ratio between these two populations can be evaluated by the following equation:

$$\frac{N_\beta}{N_\alpha} = e^{-\frac{\Delta E}{KT}} \approx 1 - \frac{\Delta E}{KT} = 1 - \frac{\gamma\bar{h}B}{KT} \tag{4.3.8}$$

where: K is the Boltzmann's constant and T is the absolute temperature.

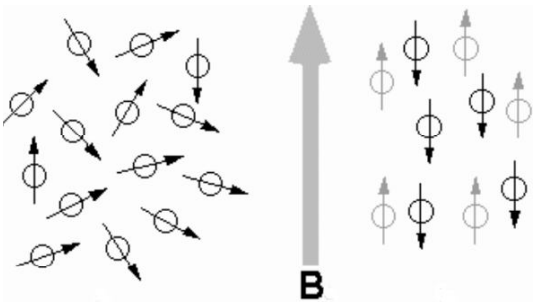

Figure 4.17.: Schematic representation of the orientations within a magnetic field (right hand side) and without the magnetic field (left hand side; from: Tonellato, no date, p.2, modified).

Since in this equation the energy difference (numerator) is very small compared to the product KT (that represents the average energy of particles), it is clear that the difference in the populations of the nuclei in the two energy levels is very small. From equation 4.3.8 it appears that there is an excess of nuclei in the low energy level and this excess can be evaluated in parts per million (ppm; Hornak, 2011; Tonellato, no date).

For instance, in the case of protons (^1H) at room temperature in a magnetic field of 1.41 T ($\nu_{(^1H)} = 60MHz$) there is just one nucleus more in the low energy state every 200000 nuclei than nuclei with high energy levels. In a magnetic field of 7.05T ($\nu = 300MHz$) there are 5 nuclei more in the low energy state every 200000 nuclei.

Despite its magnitude, it is this number of nuclei aligned with the external field that generates the signal for the nuclear magnetic resonance. Of course, the more intense is the magnetic field (B) the higher is the number of nuclei aligned. In other words, a higher external magnetic field increases the sensitivity in the NMR (Hornak, 2011; Tonellato, no date).

4.3.5. Energy absorption

A nuclide with a net spin $\neq 0$ placed in a magnetic field of strength B, can absorb a photon. Absorption of a photon produces a transition between the two energy states. For this reason a particle such as a proton in the lower energy state that can absorb the photon can end up with the upper energy state (Hornak, 2011; Tonellato, no date).

In order to produce this transition, the energy of the photon must match the difference of energy between the two states described by equation 4.3.7.

Because the energy of a photon (E_F) is related to its frequency (ν) by the Plank's constant h ($h = 6.626 \times 10^{-34}$Js) according to equation 4.3.9, it is possible to calculate the frequency of the photon causing a transition between the two spin states by the combination of equation 4.3.7 and equation 4.3.9 as described in equation 4.3.10.

$$E_F = h\nu \tag{4.3.9}$$

$$\nu = \left|\frac{\gamma}{2\pi}\right| B \tag{4.3.10}$$

This equation, in particular, shows the *Larmor's frequency* (ν) that depends only on the characteristics of the nuclide (γ) and of the external magnetic field (B). When B increases, the Larmor's frequency increases and vice-versa.

In classical mechanics, the Larmor's frequency represents the procession frequency of the magnetic spin around the z axis which is assumed to be the direction of the external magnetic field. This precession occurs at specific angles due to a directional quantization. For protons this angle is 54°44', known as the *magic angle* and the NMR technique is known as Magic Angle Spinning (MAS; Edwards, 2009, p.147).

In the NMR experiment, the role of photon is replaced by a radio frequency pulse in a specific range. For hydrogen nuclei (protons), for instance, ν is between 60 and 800MHz (Hornak, 2011; Tonellato, no date).

4.3.6. NMR signal

The two possible transitions of nuclei in a system with $I = 1/2$ are either: absorption or emission of energy. In NMR the coefficient of absorption and emission are equal and, therefore, if both energy states were equally populated, there would be no net transfer of energy from the radiation to the sample and no NMR signal to detect when the pulse of radiation finishes (Hornak, 2011; Tonellato, no date).

However, as already stated, there is a difference in the number of nuclides in the two energy levels (although very small) that produces an absorption of energy when the nuclides are irradiated and an emission of energy when the radiation finishes (the NMR signal). Both, absorption and emission are proportional to the population difference.

The excitation signal to evaluate the energy absorption or emission is constituted by a radio frequency pulse in a specific frequency range. In this manner all nuclides of the same specie are excited at the same time by the same pulse containing all the frequencies needed. Data are analyzed with the Fourier transform method.

To understand how this pulse interacts with the nucleus it is necessary to introduce a vector called magnetization (M) which is the resultant of all nuclear magnetic moments.

Because of the existence of a small difference in the nucleus aligned with the magnetic field (B), the M vector is small and aligned with the external field, along the z axes (figure 4.18; Hornak, 2011; Tonellato, no date).

When the sample is irradiated along the x axes (orthogonal to the z axis; figure 4.18) with a radio frequency pulse containing the Larmor frequency for the examined nuclide, the nucleus absorbs energy and undergos a spin transition. Under these conditions, the M vector moved away from the z axis and approaches the xy plane, with a

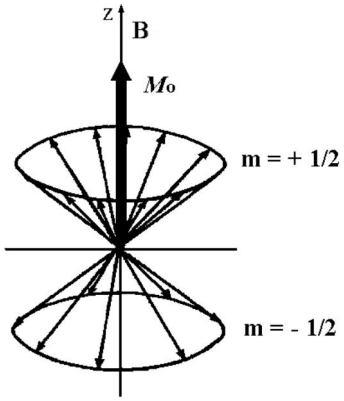

Figure 4.18.: Schematic representation of the macroscopic magnetization vector (M_0) of a nucleus immersed in a magnetic field (B) parallel to the z axes (from: Tonellato, no date, p.3, modified).

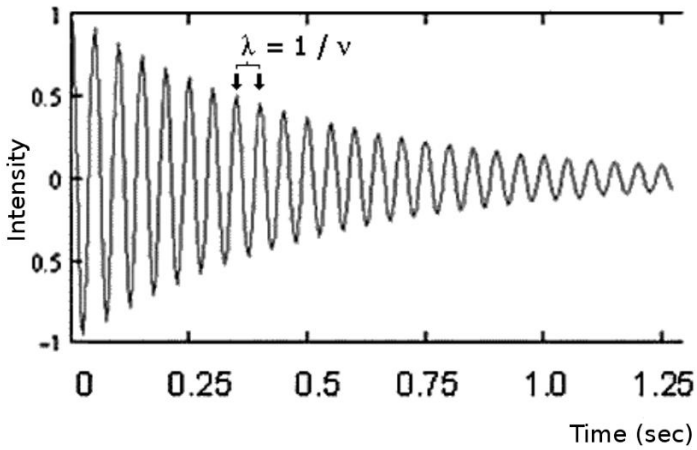

Figure 4.19.: Free induction decay of methyl iodide (CH_3I) for the hydrogen atom. Because in CH_3I hydrogen atoms are equivalent of each other, all of them have the same resonance frequency. In the graph the frequency can be calculated by evaluating the period (distance between two consecutive crests) and using the equation: $\nu = 1/\lambda$ (from: Tonellato, no date, p.4, modified).

precessional motion around the z axis.

When the radio frequency pulse is stopped, the excited nucleus continues to emit a weak signal that expires with the time. The absorbed energy is slowly given away to the nearby atoms because of the spin lattice and the spin-spin relaxation effects (Hornak, 2011; Tonellato, no date).

Because of this energy dissipation, the M vector comes back to the initial position, through an inverse precessional motion.

This dissipated energy can be recorded to characterize the nucleus under examination. In order to record this weak signal and in particular the M component of the signal along the y axis, a detector is located along the y axes (in these conditions, obviously, $M_y = 0$ is the initial position).

The signal recorded is an oscillating signal with the Larmor frequency of the examined nucleus. This signal decays over the time and is called *free induction decay* (FID; figure 4.19).

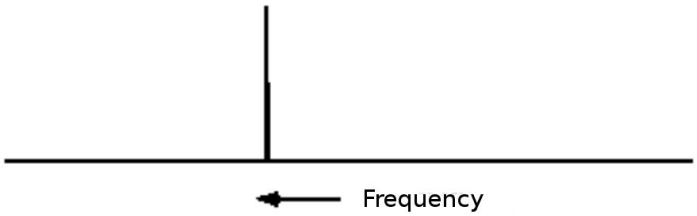

Figure 4.20.: Basic NMR spectrum that shows the frequency absorbed by the hydrogen atoms in the CH_3I molecule (from: Tonellato, no date, p.5, modified).

Starting from a FID plot it is possible to produce a plot as a function of the frequencies that shows which frequencies are absorbed by a particular nucleus, called an NMR spectrum (figure 4.20).

If the sample contains nuclei with a different resonance frequency, all these nuclei are excited at the same time by the radio frequency pulse and, consequently, the recorded FID signal is a complex curve called an interferogram produced by the combination of several simple FID (one for each absorbed frequency). Application of the Fourier transform allows the extraction of the information needed and production of the NMR spectrum (Hornak, 2011; Tonellato, no date).

4.3.7. Chemical shift

Because the magnetic dipole (μ) of a particular nuclide is a constant, it would be possible to expect that all nuclides of a same specie (such as ^1H) within a specific magnetic field (B) resonate exactly at the same frequency. Fortunately this does not happen because otherwise there would be a single signal for the same nuclides in a single molecule and it would be impossible to differentiate among them (Hornak, 2011; Tonellato, no date).

In realty the NMR signal of each nucleus is shifted in the frequency spectrum to higher or lower frequencies because of its chemical surrounding.

This happens because electrons are charged particles and when they are immersed in a magnetic field, they move and generate a small induced magnetic field $-\beta_i$ which is opposite to the applied magnetic field B. This induced magnetic field shields the nucleus from the externally applied magnetic field. The magnetic field felt by the nucleus is, then:

$$B_0 = B - \beta_i \tag{4.3.11}$$

Bonding electrons, in particular, can be closer or further away from the nucleus of the examined atom depending on the electronegativity of bonded atoms. For instance, if a hydrogen atom is bonded to low atomic number electronegative atoms such as carbon, the magnetic field generated by the electron $-\beta_i$ is closer to the hydrogen so

that the atom experiences a slightly lower external magnetic field. Consequently, this atom undergoes a transition to a lower frequency compared to the ^1H atoms bonded to more electronegative atoms such as oxygen (Hornak, 2011; Tonellato, no date).

By convention, the reference point of the chemical shift for ^1H-NMR and $^{13}C-NMR$ are assumed to be those of tetramethylsilane (TMS) where hydrogen and carbons are more strongly shielded compared to other organic molecules that, consequently, have all positive shifts:

$$Chemical\,shift = Hz_{H\,measured} - Hz_{H_{TMS}} \tag{4.3.12}$$

Absolute chemical shift is, however, dependent on the external magnetic field and, consequently, instruments that generate higher magnetic fields, produce higher shifts. For this reason the relative chemical shift (δ) is defined according to equation 4.3.13.

$$\delta = \frac{Hz_{H_{measured}} - Hz_{H_{TMS}}}{MHz_{H_{TMS}}} \tag{4.3.13}$$

In this manner the chemical shift δ (measured in ppm: $^{Hz}/_{MHz}$) is not dependent on the magnetic field applied and, consequently, is the same for all instruments.

For the ^1H-NMR, the δ scale is usually between 0 and 12 ppm, while for the $^{13}C-NMR$ is much bigger and goes from 0 to 220 ppm. In general, hydrogen or carbon atoms bonded to more electronegative atoms are less shielded and, consequently, are subject to a more intense magnetic field. This produces a shift toward higher frequencies and within the spectrum their signal is towards the left where it is possible to find the higher chemical shifts.

Another characteristic of ^1H-NMR is that the intensity of the signal is proportional to the number of hydrogen atoms. In particular, the area enclosed below a specific peak is proportional to the number of atoms of a specific type of nucleides contained in the molecule.

For instance, the ^1H-NMR signal of acetic acid (CH_3COOH) has two peaks: a peak at $\delta = 2$ with area =3 and a peak at $\delta = 12$ with area =1 (Hornak, 2011; Tonellato, no date).

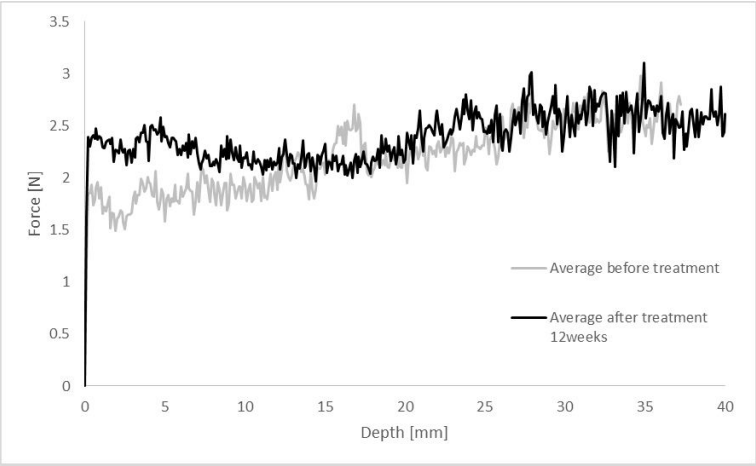

Figure 4.21.: Drilling resistance profile of a piece of Clunch stone before (gray line) and after (black line) a consolidation treatment with nano-lime. Each line represent an average of three measurements.

4.4. Drilling Resistance Measurements

4.4.1. Drilling resistance technique

Drilling resistance is a technique in which the resistance of a sample to be drilled is measured continuously, from the surface of the sample itself (where the drill bit starts to penetrate) to its most inner parts. Such a test provides a resistance profile of the sample under investigation that is a valuable tool for evaluating some of the mechanical and physical properties of the material. A typical plot produced with a DRMS, is shown in figure 4.21.

In 2007 Pamplona and colleagues published a paper (Pamplona et al., 2007) that provided an overview of the technique with references to its development during the last century and its function principle. The same researchers also highlighted the main advantages and limits of the technique together with the existence of a linear relation between the results of the drilling resistance and the results of the uniaxial compressive strength test.

Overall, the technique is mainly directed towards building materials and materials used in conservation and restoration of architectural heritage. Its current application varies from the *in situ* assessment of stone quality (both at the quarry or at the building site), to the determination of the extent of weathering in ancient and modern buildings, to the evaluation of the effects of consolidant treatments.

Reliability and sensitivity are among the advantages of the technique that is also considered micro-destructive and can be used both *in situ* and in the laboratory (Pamplona et al., 2007, p.675).

Among the method drawbacks, drill bit variability, cutting tool wear, dust transport problems, the lack of comparison between drilling resistance, strength and hardness, and the fact that for natural materials the absolute values of the drilling force have to be

considered as indicative and cannot be used as a reference for other samples (Pamplona et al., 2007, p.668).

Wear effect of the drill bits

The wear effect is one of the main problems when abrasive materials are measured. In these cases, in fact, the drilling resistance increases during the drill bit working life even when a more or less homogeneous material is drilled. Attempts to correct this effect are based on the assumption that the wear is constant and, consequently, a hypothetical abrasion rate can be estimated. Alternatively, calibration materials can be used at the beginning and at regular intervals during the tests for monitoring the wear (correction formulas can be applied to the measured drilling forces, based on the drilled length and resistance value of the first hole; Pamplona et al., 2007).

Dust accumulation in the drill hole

The dust accumulation in the drill hole is another major problem. According to some researchers (Pamplona et al., 2007, p.671), the obstacle formed by the drill dust increases with depth and seems to be dependent on the pore structure and moisture content of the sample under investigation. Other researchers pointed out that in some tests it is possible to identify a zone where the force applied is relatively constant whereas after this zone an increase in the resistance becomes evident. According to these researchers, the constant zone should be used to calculate the average drilling force value in order to avoid the dust transport effect.

Drill bit variability

In the context of the EC Hardrock Project, some commercial drill bits for masonry were tested using the ARS as reference material[5]. It was found that these drill bits are characterized by a high variability of the measured forces. The variation coefficient, in fact, was found to be 16% in 190 specimens and was supposed to be due to small differences either in the hardness or in the geometry (Pamplona et al., 2007, p.668) .

Similarly, some specially constructed diamond drill bits were tested and the data indicate less scatter in the results (variation coefficient of 7% in 10 specimens).

Since then, diamond drill bits are usually preferred. Although a better control exists on the production of the specially manufactured drill bits, it is still advisable to evaluate scatter before making use of them. Other tests where the drilling resistance values (maximum and minimum forces) obtained by drilling holes in a calibration material,

[5] ARS stands for Artificial Reference Stone. ARS is one of the reference materials used in the drilling resistance measurements. More information about this material is reported in the following paragraph.

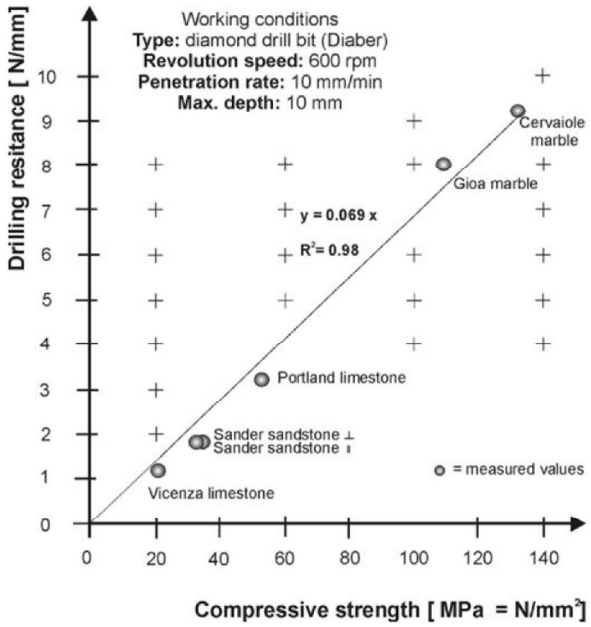

Figure 4.22.: Correlation between drilling resistance measurements (DR) and uni-axial compressive strength (UCS) for different types of stones (from: Pamplona et al., 2007, p.673).

showed that the calculated average value of the maximum and minimum force bits coincided with the measured value of the force bit (Pamplona et al., 2007, p.668).

4.4.2. Comparison of drilling resistance to uniaxial compressive strength

During the McDUR European project, a comparison between the data obtained with the drilling resistance (DR) measurements system and with uni-axial compressive strength (UCS) tests made according to EN 1926 (1999) were carried out.

Figure 4.22 shows the correlation found for different types of stone (limestones, sandstone and marbles) using a 5 mm drill bit.

Another correlation is presented in figure 4.23 of experimental data collected for siliceous limestone (Tuffeau) and limestones (Monks Park and Ança).

Overall, it is possible to state that, although these series of measurements were carried out with different drill bits and different working conditions, results show a good linear correlation between DR and UCS. Even if this correlation is not completely demonstrated the measurements carried out to date indicate that drilling resistance measurements can be used to obtain information on the ultimate compressive strength of the materials (Pamplona et al., 2007, p.674).

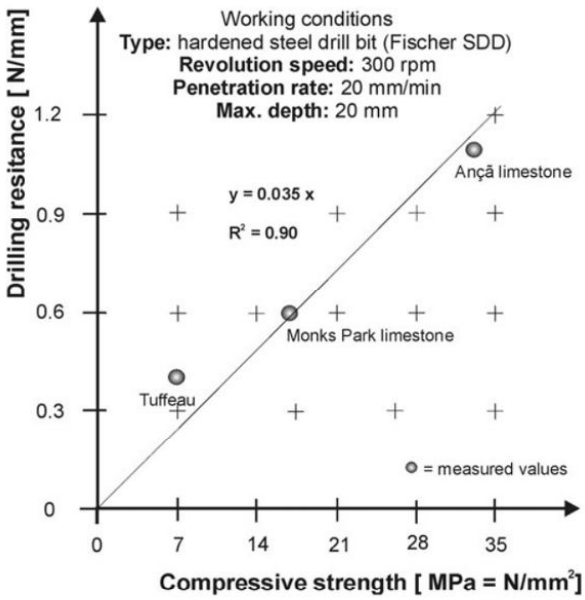

Figure 4.23.: Correlation between DR measurements and UCS in limestone and silicious limestone (from Pamplona et al., 2007, p.674).

4.4.3. The Drilling Resistance Measurement System

The Drilling Resistance Measurement System or DRMS is a system patented, produced and developed by an Italian company (SINT Technology s.r.l.), capable of measuring the drilling resistance in natural and artificial stones such as marble and mortars.

The system was developed within the European project SM&T HARDROCK (Delgado Rodriguez et al., 2002; Pamplona et al., 2007) and thanks to the improvements made over the past ten years, it is particularly suitable for *in-situ* tests where only a few methods are available for measuring strength parameters (Delgado Rodriguez et al., 2002; SINT Technology, 2014).

The system comprises a laptop, an electronic unit and a portable drilling machine equipped with two motors: one controls the rotational speed of the drill bit and the other the advance of the drill bit. A load cell measures the force applied. The position of the drill bit is simultaneously recorded. Software specifically developed allows continuous recording and monitoring of force in relation to the advancement of the bit. During the test rotational speed and penetration rate are kept constant.

Rotational speed, penetration rate and maximum depth of penetration are set by the operator at the beginning of the test through the laptop which is connected by a USB cable to the electronic unit located on the top the drilling machine itself (figure 4.24; SINT Technology, 2014). The data is collected and immediately displayed on the laptop screen and saved in the laptop hard drive, ready to be exported and replotted with software such as Microsoft Excel (Delgado Rodriguez et al., 2002).

The rotational speed can be varied between 20 and 1000 rpm to obtain optimum results for the material under investigation, while the penetration rate can be selected

Figure 4.24.: Drilling Resistance Measurement System (top PC used to collect data, bottom drilling machine).

between 1 and 80mm/min. Measurable forces range from 1 to 100 N.

Drill bits that can be used with this equipment are both the common tungsten drill bits with triangular tip or the more precise diamond flat drill bits. The diameter of the drill bits suitable for the chuck is between 3 and 10 mm. Maximum depth attainable with a 5 mm diameter drill bit is about 37 mm.

Drill bit wear can be monitored during the tests using several calibration materials such as the Artificial Reference Stone (ARS) provided by the same SINT Technology. ARS is made of porcelain with 28.4% accessible water porosity and 61.3 MPa uniaxial compressive strength (Pamplona et al., 2007, p.667).

The portability and light weight of the instrument (approx. 5 kg.) make it possible to carry out measurements in various directions. This system has already been used in several studies involving professional works such as those on at the Parthenon (Greece), Pisa tower (Italy), Trondheim Cathedral (Norway) and Florence Cathedral (Italy; SINT Technology, 2014).

4.5. Modeling software

4.5.1. Application of PHREEQC to model construction materials

PHREEQC (an acronym that stands for pH-REdox-EQuilibrium) is a computer program for simulating chemical reactions in natural water in both laboratory experiments and in industrial processes.

The program is based on equilibrium chemistry of aqueous solutions interacting with several phases such as minerals, gases and solid solutions. Furthermore, the program includes the capability to model kinetic reactions and one-dimensional transport.

The software has already been used in several scientific fields such as geochemistry, hydrology, environmental pollution, vulcanology, water treatment but also in other fields such as the construction industry. In this field, in particular, PHREEQC has been used to simulate several scenarios including the ion–ion and the ion–solid interactions in the multi-ionic transport in concrete (e.g. Elakneswaran et al., 2010, Brown and Doerr, 2000), to model the chemical degradation of concrete (e.g. Jacques et al., 2010, Sugiyama, 2008, Moranville et al., 2004), to model the dissolution processes of CSH (e.g. Walker et al., 2007, Blanc et al., 2010), to compare test methods to assess pozzolanic activity (e.g. Donatello et al., 2010) to study the evaporation process of saline solutions within porous building rocks (e.g. Benavente et al., 2003) as well as the role of evaporation for the thaumasite formation and sulphate attack (Mittermayr et al., 2013).

Among these uses PHREEQC was also used to study the carbonation reaction in lime based materials and, in particular the phase and morphology evolution of $CaCO_3$ precipitated by carbonation of hydrated lime (Cizer et al., 2012a).

4.5.2. A short history of PHREEQC

PHREEQC derived from the Fortran program PHREEQE released in 1980, that was capable of simulating a variety of geochemical reactions including mixing of waters, phase dissolution and precipitation to achieve equilibrium with the aqueous phase and effects of changing temperature. PHREEQE was able to calculate several parameters such as concentrations of elements, molalities and activities of aqueous species, pH and pe (negative log of the conventional activity of the electron).

PHREEQC version 1, released in 1999 was different, compared to PHREEQE. It was written in the C programming language and implemented all of the capabilities of PHREEQE adding many other capabilities such as the ion-exchange equilibria, surface-complexation equilibria and fixed-pressure gas-phase equilibria.

PHREEQC version 2, instead, was a modification of version 1. All of the capabilities and most of the code from the previous version were retained but in this variant other capabilities were added, including kinetically controlled reactions, solid-solution equilibria and fixed-volume gas-phase equilibria. The numerical method was modified to use several sets of convergence parameters in order to avoid convergence problems. User-defined quantities could be written to the primary output file and to a file suitable for importation into a spreadsheet. Solution compositions could be written in a format compatible with spreadsheet programs.

PHREEQC 3 (the current version, published in 2013), extends the capability of version 2 with new features. The code was re-written (IPhreeqc) to facilitate its use by other software programs that need to calculate chemical reactions or the distribution of chemicals in various phases (Parkhurst and Appelo, 2013, pp.1-4).

4.5.3. Capability of PHREEQC

PHREEQC can be used to calculate several characteristics of solutions such as saturation indexes, distribution of aqueous species, density and specific conductance of a specified solution.

For calculating solute activities, PHREEQC uses ion-association equations (Pitzer or SIT-Specific ion Interaction Theory) to account for the non-ideality of aqueous solutions.

It allows the concentration of an element to be adjusted to obtain equilibrium (or a specified saturation index or gas partial pressure) with a specified phase, to obtain charge balance. Solution compositions can be specified with a number of concentration units.

The input to PHREEQC is just a text file, based on chemical symbolism. Balanced equations written in chemical symbols are used to define several parameters such as aqueous species and solid solutions without using index numbers to identify elements or species.

In batch-reaction calculations, PHREEQC is oriented toward system equilibrium rather than just aqueous equilibrium. Batch reactions allow any combination of solution (or mixture of solutions), gas phase, and assemblages to be brought together. For an equilibrium calculation, all of the moles of each element in the system are distributed among all the phases involved in the reactions. Non-equilibrium reactions can also be modeled.

If kinetic reactions are defined, then the kinetic reactions are integrated with an automatic time-stepping algorithm while system equilibrium is maintained for the equilibrium reactions that are defined. Kinetically controlled reactions can be defined using an embedded Basic interpreter. These can be included in the input file and the program

is able to use the Basic interpreter to calculate rates.

Temperature effects can be modeled with the reaction enthalpy or with a polynomial for the equilibrium constant. Pressure effects can be simulated by defining molar volumes of solids and parameters for the specific volume of aqueous species as a function of temperature, pressure, and ionic strength.

The PHREEQC graphical user interface is called PhreeqcI and provides input screens for all of the features contained in version 2 and most of the features of version 3 (Parkhurst and Appelo, 2013, pp.5-10).

4.5.4. Limitations

Apart from the above mentioned capability, this software contains some limitations that must be consiedered. Among these, the aqueous model, the ion-exchange formulation and the inverse modeling are thought to be the most important to be considered in this research.

The aqueous model presents a lack of internal consistency in the data within the databases. The database *pitzer.dat* defines the most consistent aqueous model; however, this database includes only a limited number of elements. All of the other databases are a collection of logarithms of equilibrium constants ($logK_s$) and enthalpies of reaction that have been taken from various literature sources. No systematic attempt has been made to determine the aqueous model that was used to develop the individual log K_s. For this reason the database included in the program should be considered to be preliminary.

The default ion-exchange formulation assumes that the thermodynamic activity of an exchange species is equal to its equivalent fraction. Optionally, the equivalent fraction can be multiplied by a Debye-Hückel activity coefficient and (or) an *active fraction* coefficient to define the activity of an exchange species.

Despite the fact that the new version includes uncertainties in the process of identifying inverse models, the numerical method used by the software has shown some inconsistencies in results due to the way the solver handles small numbers.

5. *In situ* monitoring pH changes in porous media

One of the most important electrochemical measurements is the measure of acidity or basicity of aqueous solutions. Numerous chemical reactions involve pH changes that can highlight processes otherwise difficult to monitor such as the corrosion of steel reinforcement in reinforced concrete.

The steel reinforcement in concrete is normally in a passive state with respect to corrosion due to a thin iron oxide layer produced by the highly alkaline environment (pH>12) of the concrete pore solution. This alkaline environment is mainly produced by the $Ca(OH)_2$ contained in the cement as well as by the smaller amount of other alkaline species such as $Na(OH)$ and $K(OH)$ (Garcia-Alonso et al., 2007).

Because of the reduced porosity of concrete, these hydroxides do not fully carbonate during the hardening process and this guarantees an almost constant alkaline environment that maintains the protective layer around the steel reinforcement preventing corrosion (Bertolini et al., 2013).

However, if over time CO_2 penetrates within the concrete, it may cause carbonation of alkali and alkaline-earth elements, that lead toward a more acidic environment. As a consequence, the passivated layer of iron oxides can be reduced with the risk of corrosion. For this reason monitoring the pH in steel reinforced concrete structures is an important key to evaluate the state of the structures themselves (Pu et al., 2012).

Despite its importance, however, pH remains a difficult parameter to determine in many cases, including those in the construction industry. In this specific case, two of the main factors affecting the pH measurements are:

- pHs above 9 cannot be measured reliably with most of the pH sensitive devices including the conventional glass electrode, because of the alkaline error;
- pH is hard to measure in confined places.

The alkaline error is due to the fact that in high pH solutions (>9) the hydrogen ion activity is so low and the activity of alkali or alkaline-earth metal ions (mainly contained in the glass of the membrane of the electrode itself) is so high that the ordinary

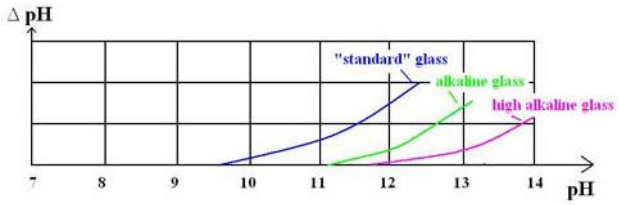

Figure 5.1.: Alkaline error as a deviation from the linear pH dependence (from: http://www.all-about-ph.com/acid-and-alkaline.html).

pH electrode begins to respond to these latter ions rather than to the hydrogen ions[1].

To take this effect into account correction tables are available as well as special electrodes (preferable to the correction tables; Garrels and Christ, 1965, p.126). These special electrodes use special alkali-glass membranes that are less sensitive to ions such as Na^+ and Li^+. However, no type of glass membranes currently available has zero alkaline error (Ives and Janz, 1961). For instance, the Sentek P11-PB (PH0043) combination type electrode, sold as suitable for measurements within the pH range 0-14[2] and, in particular, for measuring the pH in cement[3], measured a pH of 12.8 in a pure $Ca(OH)_2$ aqueous solution whose pH at 20ºC, according to theoretical calculations and to some measurements carried out with a solid state electrode (see further on in this chapter), was calculated to be 12.56.

This chapter describes how nano-structured Pd hydride microelectrodes (these electrodes are described in paragraph 4.1.2) can be exploited to monitor pH variations in a carbonation reaction confined to a porous substrate that mimics the porous materials used in the construction industry such as concrete, lime mortars and stones.

Through calibrations it is first demonstrated that the Nernstian response of the microelectrodes extended to strong alkaline conditions (up to pH=14). Then, the electrodes are employed to record pH transients during the carbonation of lime within a humid fibrous mesh. To control the carbonation the experiments are carried out at different partial pressures of CO_2 and in each case the experimental results were compared to theoretical calculations using PHREEQC. SEM observations and XRD analysis of the $CaCO_3$ particles deposited on the fibrous mesh were used to evaluate characteristics of the solid phases precipitated during the carbonation.

The ultimate aim of this research is the development of micro-sensors for monitoring the pH in structural elements such as beams, pillars or walls that do no need to be periodically calibrated and can be reloaded with H^+ *in situ*. Potentially, an array of these electrodes could provide information on the carbonation mechanism within the

[1] At high pH, in fact, the sodium ions replace the hydrogen ions in the outer gel layer of the glass membrane. Under extreme conditions the glass membrane responds only to sodium ions (Mettler Toledo AG, 2013, p.53-54).

[2] http://www.sentek.co.uk/spec_sheets/P11-Protected-Bulb.jpg

[3] http://www.appletonwoods.co.uk/tables/Sentek-electrodes.pdf

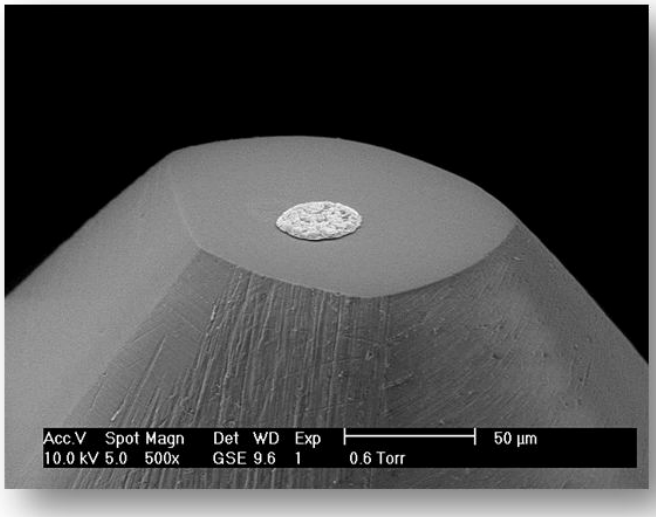

Figure 5.2.: Tip of a 25 µm diameter micro-electrodes consisting of nanostructured palladium discs electrodeposited on the end of a normal microdisc electrode (from: Serrapede et al., 2013).

structural elements in which it is incorporated, from their surface to the most internal parts. This type of device will be useful in preventing and monitoring problems such as the corrosion in the steel reinforcement of concrete.

5.1. Materials

5.1.1. Electrodes

Working electrode (pH micro-electrode)

The pH microelectrodes were fabricated and characterized as reported previously (Imokawa et al., 2006; Bartlett et al., 2002). The nanostructured palladium films were electrodeposited under potentiostatic control at 0.1 V vs. SMSE, on Pt microdisks from a plating mixture consisting of $(NH_4)_2PdCl_4$ 12% wt (Alfa Aesar, premion-99.998%), $C_{16}EO_8$ 48% wt (octaethylene glycol monohexadecyl ether, Fluka), heptane 2% wt (Lancaster, 99%) and water 40% wt (18 $M\Omega$ cm, Pur1te, Burkert). These conditions were chosen to use the hexagonal phase of $C_{16}EO_8$, a non-ionic surfactant known to form liquid crystal phases (Attard et al., 1997), as a molecular template to direct the deposition of the Pd and produce the desired nanostructure.

The films were deposited on micro-disks with diameters ranging from 25 to 250 µm with a charge $Q_{dep} = 4\ {}^{C}/_{cm^2}$ such that the film thickness was typically 1 to 2 µm (figure 5.2). The electrodes were then soaked in water for at least 24 hours to remove the surfactant and the Pd films were activated by cyclic voltammetry in sulfuric acid until stable voltammograms were obtained.

The Pd films were, then, galvanostatically loaded with hydrogen (-80 nA for the 25 µm diameter disks up to -60 µA for the 250 µm diameter disks) until a $^{H}/_{Pd}$ ratio circa 0.6 corresponding to the beginning of the β PdH phase. Loading was stopped when the potential dropped below the plateau for the α to β phase transition.

Hydrogen loading was generally performed in the solution of interest at regular intervals or whenever H needed replenishing. Sensitivity to pH was obtained by recording the electrode potential while the PdH was in its $\beta - \alpha$ transition phase. The microelectrodes were used as pH sensors by recording their open circuit potential ($OCP_{\beta\rightarrow\alpha}$) until the natural discharge of hydrogen had caused the hydride to transform into its α phase.

Reference electrodes

In all the experiments the reference electrode was a mercury sulphate electrode (SMSE; Hg/Hg_2SO_4, K_2SO_4 saturated) with an Agar salt gel bridge obtained with a saturated solution of K_2SO_4 + 1% of Agar. The salt bridge was soaked into a capillary and bound to the working electrode with PTFE.

Counter electrodes

The counter electrode used in the experiments was a platinum grid onto which the tissue paper used to mimic the porous medium could be rolled.

5.1.2. $Ca(OH)_2$ saturated solution

The $Ca(OH)_2$ saturated solution used during the tests was prepared by calcination in air of a ReagentPlus $CaCO_3$ by Sigma Aldrich (product code: C6763), $\geq$99.0% pure. Twenty grams of powder were heated inside a furnace at 1000°C for 7 hours and then cooled to a temperature of about 80°C. Eleven grams of CaO removed from the furnace was, then, immediately slaked in a litre of double distilled water degassed by boiling for 2 hours before cooling to room temperature in a sealed conical flask. The flask was subsequently agitated (sealed) for several minutes in order to facilitate hydration of quicklime and then left steady on a bench for at least 12 hours to allow precipitation of floating particles. Once the solution was clear, the pH was measured with a soil pH meter (Digital Instrument model PH-220S) and with a Mettler ToledoFE20 FiveEasy pH-meter connected to a Sentek P11 (PH0043) glass combination electrode to check the pH that was found to be 12.7 and 12.8 respectively (including the alkaline error). Both the pH-meters were previously calibrated using buffer solutions of pH 7 and 10.

In order to produce a clear solution before each test solid phases were removed filtering the solution with a syringe filter (0.1 µm Puradisc 25 TF) produced by Whatman.

5.1.3. Cells

Two cells were used during the experiments:

- a classic water-jacketed glass cell of 15 ml volume with three fits to insert the electrodes into the solution. This cell was used to check the reliability of the Pd mesoporous film by cyclic voltammetry in 1 M solution of H_2SO_4 in water;
- a specifically constructed cell made of poly-methyl methacrylate (PMMA) was used for the experiments with the $Ca(OH)_2$ solution (figure 5.3; schematic representation of the cross section within the inset in figure 5.4). The cell was open on the top and had a removable lid to allow cleaning. The two large sides were manufactured from glass in order to allow easy inspection inside the reactor. Its use required the introduction of the counter electrode at the bottom of the cell before closure of the lid. The lid itself was designed to clamp the counter electrode at the bottom of the reactor in order to prevent any movement during the tests. The working electrode and the salt bridge connected to the reference electrode were, instead, introduced into the cell after the closure of the lid, by the circular opening in the lid itself. In order to guarantee the minimum distance between the two electrodes and to prevent any movement during the tests, the working electrode and the salt bridge were held together using PTFE tape. The same opening in the lid allowed the introduction of different gases by means of a small tube such as the end of a glass pipette. At the bottom of the reactor a capillary tube a few centimetres length was connected to a syringe that allowed removal of the solution. The reactor contained up to 5 ml of solution. The cell was used for both bulk measurements and measurement on a thin film of solution. The former case required flooding of the reactor with solution and positioning the reference and working electrode a few millimetres above the cell bottom. The latter case, instead, required the use of a piece of paper wrapped around the counter electrode, that could absorb a small amount of solution. The working and the reference electrodes were moved toward the bottom of the cell until contact was made with the tissue paper. The cell was then flooded to wet the paper. When the paper had absorbed the solution, it was removed using the capillary tube at the bottom of the reactor. During the test the cell was maintained at a constant temperature using a brass base located underneath the cell and a thermostatic bath.

5.1.4. Paper

The paper wrapped around the counter electrode for the measurements on thin films was a lens cleaning tissue grade n. 105 produced by Whatman International Ltd and

Figure 5.3.: PMMA cell used for the experiments with the $Ca(OH)_2$ solution.

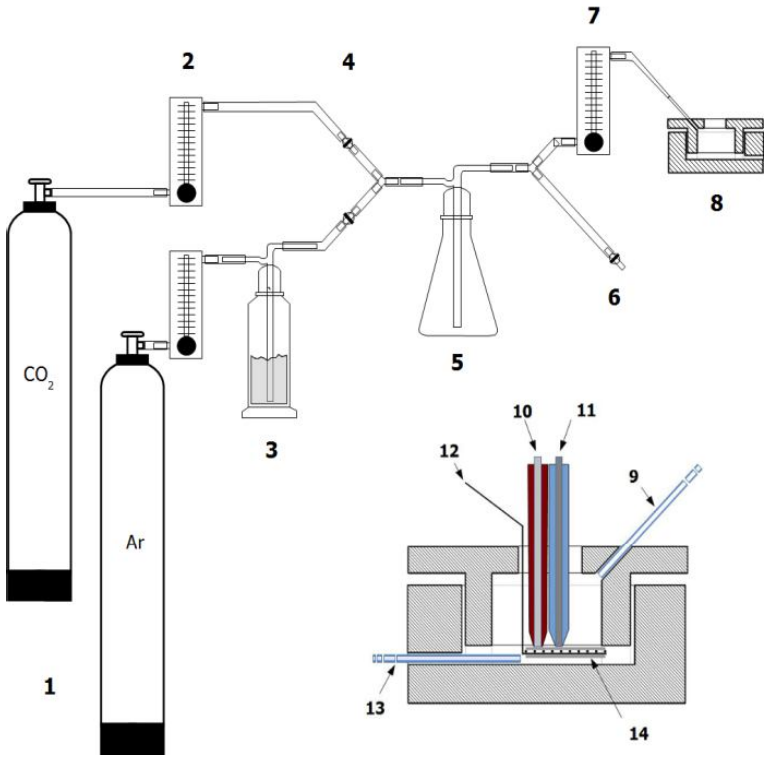

Figure 5.4.: Schematic of the experimental assembly. (1) gas cylinders, (2) gas flow meters, (3) humidifier, (4) valves, (5) mixing chamber, (6) exhaust line and valve, (7) flow meter and regulator, (8) cell (detailed in the inset at the bottom-right), (9) gas mixture injector, (10) reference electrode salt bridge, (11) pH sensing electrode, (12) counter electrode, (13) capillary to remove the solution, (14) cotton mesh.

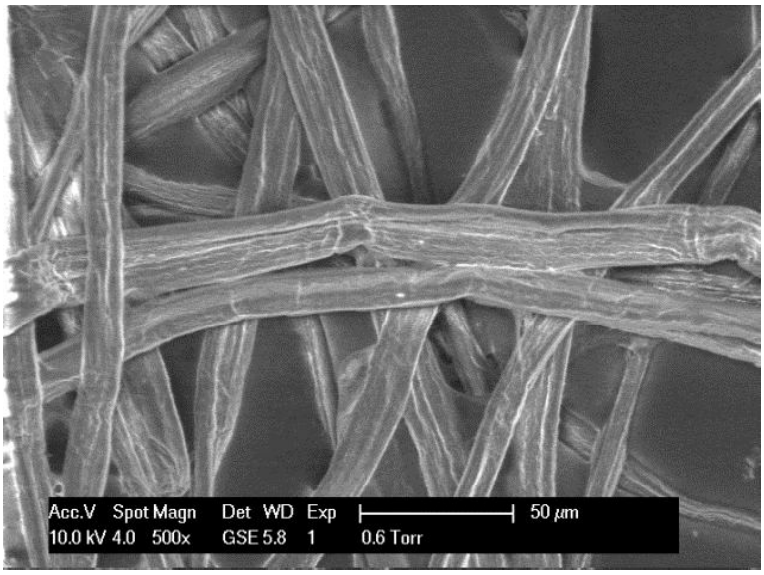

Figure 5.5.: ESEM image at low magnification of the cotton fibres contained in a piece of lens cleaning tissue grade n.105 produced by Whatman International Ltd.

supplied by both Fisher Scientific and Sigma Aldrich. The tissue is made of a pure cotton lint (figure 5.5), free from silicones and other additives.

5.1.5. Apparatus

Faraday cage

During the tests, cell, electrodes, syringe for removing the solution and tube for introducing the gas were enclosed in a grounded Faraday cage to minimise electromagnetic interferences.

Translation stage

Working and reference electrodes were held and positioned using a translation stage model M-605, supplied by Physik Instrumente GmbH & Co.

Potentiostat/Galvanostat

Electrochemical experiments were carried out using a Galvanostat/Potentiostat Autolab PGSTAT101 controlled by the software NOVA version 1.9. Algorithms for measurements, chronopotentiograms and cyclic voltammograms were written by Ms. Mara Serrapede, PhD student at the Department of Chemistry of the University of Southampton.

Gases

Specific p_{CO_2} were obtained by adjusting the valves and flow meters detailed in figure 5.4. Each cylinder was connected to a flow meter that allowed a specific flow for each gas and, consequently, a specific volume or partial pressure. The gas blend was homogenized in a mixing chamber and the stream was split between an exhaust line and a feed line regulated by a flow meter constantly set at $0.25\ ^{l}/_{min}$. The exhaust valve was adjusted to avoid gas overpressure within the system.

A CO_2 cylinder together with a Pureshield Argon cylinder both from BOC were used to produce the gas mixtures with different $Ar : CO_2$ ratios required for the tests and for producing the inert environment needed at the beginning and the end of the experiments.

To prevent water evaporation from the solution during the experiments, Ar was humidified in a gas-washing bottle containing water. In order to prevent condensation of water inside the cell, the gas-washing bottle was kept inside the thermostatic bath used to control the cell temperature.

5.2. Method

Calibration curves useful to correlate the potential measured by the working electrode with the pH of the solution in contact with the same electrode were obtained by recording the electrode potential for a range of pHs prepared using home-made buffers[4] and during the titration of 1 M $NaOH$ and 50 mM Na_3PO_4 (Sigma Aldrich, > 99%) solutions with 5, 1 and 0.1 M diluted solutions of H_2SO_4 (Fisher Scientific). Potentials were measured in the water-jacketed glass cell.

Experiments to investigate the carbonation of lime were carried out in the specifically constructed PMMA cell under thermostatic conditions (23°C) with different $Ar : CO_2$ gas mixtures. A saturated solution of $Ca(OH)_2$ was absorbed onto small strips of cotton lint (3 mm wide × 1 cm long) and wrapped around the reference electrode. The cotton mesh was used for the three following reasons:

- to trap a thin film of solution that simulated carbonation in the confinement of a porous medium;
- to provide an ionic path between the electrodes
- to capture the solid phases formed during the carbonation for subsequent analysis (figure 5.6).

[4]Produced using $H_2NaO_4P \cdot 2H_2O$ (Fisher Scientific, 99.2%) and Na_2HPO_4 (BDH, AnalaR grade), during neutralization of 1 M $NaOH$ (Fisher Scientific, 97%).

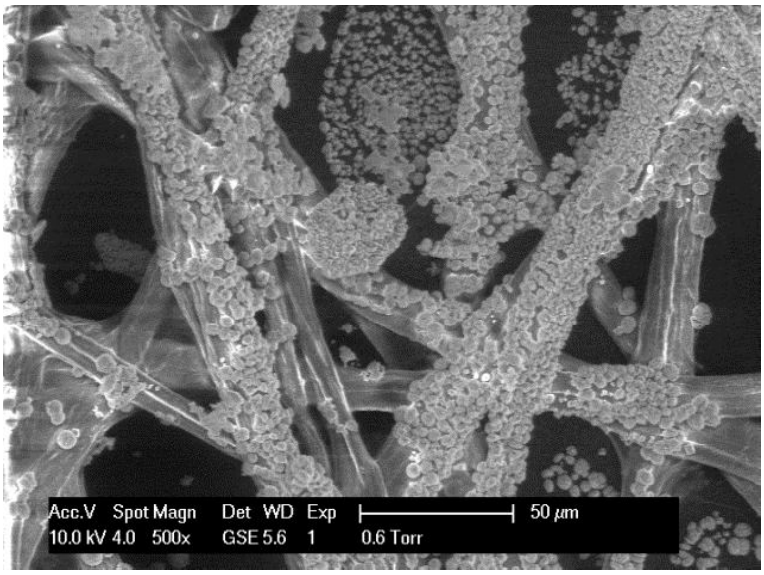

Figure 5.6.: ESEM image at low magnification showing a piece of lens cleaning tissue at the end of a test.

The reference electrode was clamped outside the cell and connected to the solution by means of a salt bridge (Agar saturated with K_2SO_4, Difco) attached to the body of the working electrode and terminated by a capillary tip that was locked very close to that of the micro-electrode. This configuration was implemented to guarantee a constant distance between the pH sensing tip and the reference electrode and, thus, to avoid Ohmic distortion while galvanostatically loading the microelectrodes with hydrogen. The two long side walls of the cell facilitated inspection of the mesh, tissue and electrodes positions.

A typical experiment was conducted according to the following steps:

1. the cotton lint strip was wrapped around the counter electrode;

2. the counter electrode was positioned inside the cell and clamped at the bottom with the lid.

3. The working and the reference electrodes were clamped to the translation stage and positioned with their tip inside the reactor through the hole in the cell lid.

4. A stream of wet Ar was passed into the cell for approximately 10 minutes in order to avoid the presence of atmospheric CO_2.

5. The cell was injected with approximately 3 ml of saturated $Ca(OH)_2$ solution using a syringe fitted with a disposable needle and filter (to avoid introducing solid phases) through the main opening in the lid.

6. Cyclic voltammograms were recorded to establish the cleanliness of the Pd nanostructure and to check the stability of the solution.

7. A chronopotentiogram was recorded while loading the palladium film galvanostatically with hydrogen to a $H : Pd$ ratio of about 0.6 corresponding to the beginning of the β phase of the hydride.

8. The micro-electrode was set to open circuit and its potential was recorded to measure the pH in the bulk of the solution.

9. While continuously recording its potential the micro-electrode was moved downwards until its tip touched the cotton mesh.

10. After checking for signal stability, the solution was removed from the cell using the capillary tube (connected to a syringe) at the bottom of the cell thereby leaving some solution absorbed in the cellulose mesh.

11. The baseline pH for the thin film of solution was recorded for a few minutes (up to 30 minutes).

12. The gas mixture was modified to allow a chosen partial pressure of humid CO_2 flux in the cell.

13. The electrode potential was recorded continuously while carbonation occurred until a stable plateau was reached.

The solid phases precipitated on the cotton lint were subsequently observed with a field emission scanning electron microscope (model FESEM6301F from JEOL) and analysed with an X-ray diffractometer (Rigaku Smartlab with a 9 kW source and Cu k-alpha X-rays).

5.3. PHREEQC modeling

pHs obtained from the microelectrode potentials during the carbonation were compared with the theoretical values calculated using PHREEQC version 3.0. Simulations followed previously reported PHREEQC protocols (Appelo and D., 2005) with an initial condition consisting of one solution in equilibrium with two phases. The solution consisting of 1 kg of pure water (set by default to pH=7 and pe=4, i.e. to a redox potential of 0.237 V) as a solvent with the addition of calcium to simulate the saturated lime. pH was set as an adjustable parameter to achieve charge balance and calculations were carried out for three temperatures: 20, 23 and 25°C.

The equilibrium phases considered in the simulations were gaseous CO_2 and one of the solid polymorphs of $CaCO_3$. In accordance with the instructions provided with the software, the log of p_{CO_2} (in bar) was set to simulate carbonation under different atmospheres. The number of moles of CO_2 was set to 1000 to model the equilibrium

Algorithm 5.1 PHREEQC script used to model the final pH of solutions.

```
SOLUTION 1

temp 23
pH 7 charge
pe 4
redox pe
units mol/kgw
density 1
Ca 0.01552 Mol/kgw
-water 1 # kg
EQUILIBRIUM_PHASES 1
Vaterite 0 1000
CO2(g) -1.3279359 1000

END
```

with an infinite reservoir of $CO_{2(g)}$. Solid $CaCO_3$ phases introduced in the simulation were: monohydrocalcite, vaterite, aragonite and calcite. These phases were modelled using a saturation index of 0 and an infinite number of moles but similar results were obtained in simulations where the number of moles of solid phase introduced was not set.

Simulations were performed with the thermodynamic data contained in the Lawrence Livermore National Laboratory database (the *llnl* database built in PHREEQC) which was modified by adding data for vaterite taken from the *sit* database, developed for the French National Radioactive Waste Management Agency. The PHREEQC input files used in the simulations are shown in algorithm 5.1 and 3.1.

5.4. Results

5.4.1. Potential – pH calibrations

Figure 5.7 shows a typical calibration curve recorded with a 25 µm diameter pH probe for the neutralization of a range of solutions. The open circuit potential for the $\beta \rightarrow \alpha$ transition of the hydride is found to be linearly related to the pH of the solution over the pH range considered and the slope of the linear fit, 58.7±0.5 mV/pH, is in good agreement with that recorded by Imokawa and colleagues (Imokawa et al., 2006).

Figure 5.7 clearly shows that the Nernstian response of the nanostructured PdH microelectrodes extends to very alkaline conditions and that the reproducibility is not affected by high pHs (error bars are comparable to or smaller than the symbols on the curve).

Interestingly the probes produced a stable response over at least 2 hours of continuous monitoring. After this time, hydrogen had to be reloaded to produce once again

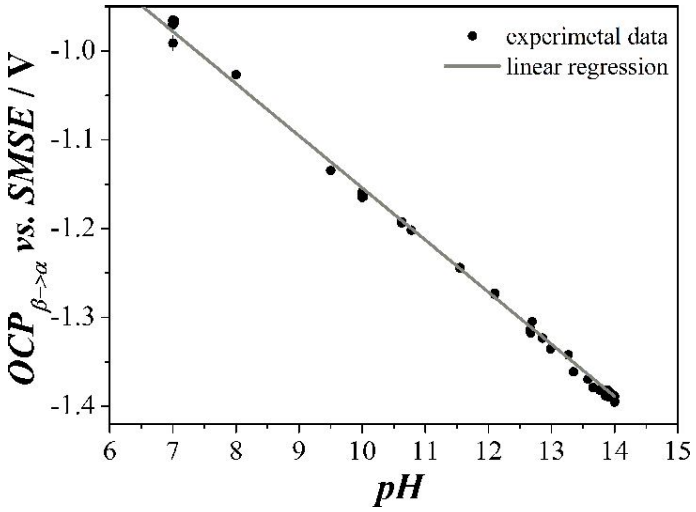

Figure 5.7.: Potential-pH calibration for a 25 µm diameter nanostructured PdH-pH probe. Each potential is the average of at least three recordings. Each pH was prepared with different buffers or though titration of NaOH as described in the experimental section.

the β phase. The electrode could be used for 14 consecutive days before renewing its nano-structure.

5.4.2. PHREEQC calculations

Results of PHREEQC calculations are reported in tables 5.1, 5.2, 5.3 and 5.4. According to these results, the initial pH of saturated $Ca(OH)_2$ solutions at 20, 23 and 25°C is 12.56, 12.45 and 12.37 respectively (calculated using the algorithm 3.1).

After carbonation, the final pH varies from a minimum of 6.08 for a solution in equilibrium with calcite at 25 °C and p_{CO_2} = 0.75 atm, to a maximum of 7.21 for a solution in equilibrium with monohydrocalcite at 23°C and p_{CO_2} = 0.038 atm.

At 23°C (the temperature at which the experiments were carried out) the final pH of the solution in equilibrium with calcite varied from 6.08 to 6.92, depending on p_{CO_2}.

Simulations show that the pH is more acidic in the presence of calcite compared to other solid phases and that it takes more neutral values with the less stable phases (respectively, aragonite, vaterite and monohydrocalcite). Aragonite produces pH values similar to those obtained with calcite while monohydrocalcite produces pH values closer to those obtained with vaterite.

The simulations show that between 20 and 25°C temperature has little effect on the final pH of the solutions. The smallest difference was found between the pH of two solutions at 20 and 25°C containing monohydrocalcite (0.001 pH) while the largest difference was found between the solutions containing vaterite (0.011 pH).

Table 5.1.: Theoretical pH values calculated with PHREEQC for the initial pH at different temperatures.

Temperature (ºC)	pH
20	12.56
23	12.45
25	12.37

Table 5.2.: Theoretical pH values calculated with PHREEQC for the carbonation of saturated $Ca(OH)_2$ solutions at 20ºC and different p_{CO_2}. Initial pH=12.56.

p_{CO_2} (atm)	Monohydrocalcite	Vaterite	Aragonite	Calcite
0.750	6.389	6.317	6.139	6.087
0.167	6.805	6.734	6.559	6.508
0.039	7.215	7.154	6.972	6.921

Table 5.3.: Theoretical pH values calculated with PHREEQC for the carbonation of saturated $Ca(OH)_2$ solutions at 23ºC and different p_{CO_2}. Initial pH=12.45.

p_{CO_2} (atm)	Monohydrocalcite	Vaterite	Aragonite	Calcite
0.750	6.338	6.310	6.135	6.083
0.167	6.805	6.728	6.555	6.504
0.039	7.214	7.139	6.968	6.917

Table 5.4.: Theoretical pH values calculated with PHREEQC for the carbonation of saturated $Ca(OH)_2$ solutions at 25ºC and different p_{CO_2}. Initial pH=12.37.

p_{CO_2} (atm)	Monohydrocalcite	Vaterite	Aragonite	Calcite
0.750	6.388	6.306	6.132	6.080
0.167	6.805	6.724	6.553	6.501
0.039	7.214	7.135	6.996	6.915

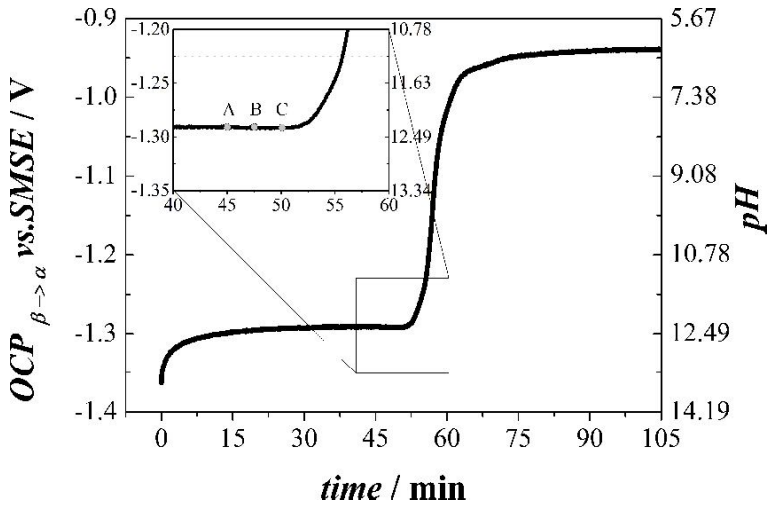

Figure 5.8.: Potential transient recorded with a 250 μm diameter nanostructured PdH disk during the carbonation of a saturated $Ca(OH)_2$ solution trapped inside a cotton lint. The pH axis was calculated from the OCP axis on the left and the calibration curve shown in figure 5.7. The insert shows the same data with A, B and C respectively indicating when the working electrode touched the surface of the porous medium, the removal of the solution and the insertion of the CO_2 in the gas stream.

5.4.3. Potential transient

Figure 5.8 shows a potential transient recorded from the formation of the β phase (just after the Pd electrode was loaded with hydrogen), until the carbonation inside the reactor was complete. The first 30 minutes of the chronopotentiogram show a rise in potential that reflects the loss of hydrogen from the hydride β phase. The plateau appears when the α phase begins to nucleate and lasts for the time when the two phases (α and β) coexist. Under this condition the electrode potential is determined only by the pH.

At point A (shown in the insert), about 45 minutes from the beginning of the experiment, the micro-electrode was moved downwards until touching the cotton lint. As it can be seen, this operation did not affect the potentiometric response. At point B (about 47 minutes since the beginning of the experiment) the solution was removed from the cell using the capillary tube at the bottom of the cell. The chronopotentiogram shows that this has had no effect on the micro-electrode potential and clearly indicated that the micro-electrode was able to monitor the pH of the saturated $Ca(OH)_2$ solution trapped within the mesh. At that stage the solution was still saturated with Ar and its pH was therefore defined by the $Ca(OH)_2$ saturation.

According to the calibration curve shown in Figure 5.7, the pH at point B is 12.45 ($OCP_{\beta\rightarrow\alpha}$= -1.295 V). This value is quite different from the values (12.7 and 12.8) measured with the glass electrodes but is in perfect agreement with the results of the PHREEQC calculation (pH 12.45; Table 5.1).

At point C (about 50 minutes after the beginning of the test) CO_2 was added to the Ar stream so that the partial pressure of CO_2 in the cell atmosphere was 0.167 atm. A

Table 5.5.: Experimental pH values recorded at the end of the carbonation of saturated $Ca(OH)_2$ solutions confined in the cellulose mesh for different p_{CO_2} at 23°C. The initial pH was consistently found to be 12.45.

p_{CO_2}(atm)	1^{st} test	2^{nd} test	3^{rd} test	average	st. error
0.750	6.13	6.06	6.17	6.12	0.03
0.167	6.34	6.56	6.47	6.46	0.06
0.039	6.95	6.78	6.85	6.86	0.05

few seconds later the potential began to rise steeply until it reached a second plateau. Since the electrode was well within its lifetime (the plateau for the $\beta \rightarrow \alpha$ transition typically lasted 2 hours for a 25 µm diameter tip, the smallest electrode used in this study) this potential shift reflected a change in the local pH. The potential rise therefore corresponded to the acidification of the solution resulting from the neutralization of the OH^- ions from the lime and the new plateau reflected the stabilization of the solution composition when all the Ca^{2+} ions had been consumed by the carbonation process as described by equilibria 2.1.1-2.1.4 and 2.1.6.

Once all the Ca^{2+} ions were consumed by reaction 2.1.6, the concentrations of all species from the carbonic acid system reached an equilibrium that depended on the partial pressure of CO_2 in the atmosphere outside the porous mesh and on the solid phases produced by the carbonation (e.g. calcite, vaterite).

According to the calibration curve, the pH of the new plateau in figure 5.8 is 6.34 (table 5.5). The theoretical pH of a similar system as calculated by PHREEQC assuming formation of calcite is 6.50 (table 5.3).

Repetitions of the same test (table 5.5) led to a mean experimental value of 6.46±0.06. The difference between this mean and the theoretical value, -0.04, therefore suggests that calcite is the most likely phase formed.

To ascertain which phase had precipitated, the mesh was observed using an SEM (to avoid further exposure to CO_2, the samples were initially dried in an Ar stream then in a drying oven under an Ar atmosphere and subsequently kept immersed in acetone; to avoid phase changed due to the thermodynamic instability of some phases, all SEM analysis were carried out within 1 week from the tests).

Figure 5.9 shows the morphologies of the two solid phases found on the cotton lint. The rhombohedral crystals are characteristic of calcite formations while the spherical crystals are characteristic of vaterite formations (Hou and Feng, 2006; Ren et al., 2011; Kitamura, 2002; Andreassen et al., 2012).

The SEM analysis was confirmed by X-ray diffraction as shown by the spectrum in figure 5.10.

The results of similar tests carried out with two other CO_2 partial pressures (0.039 and 0.750 atm), are reported in table 5.5. All tests were repeated three times and in

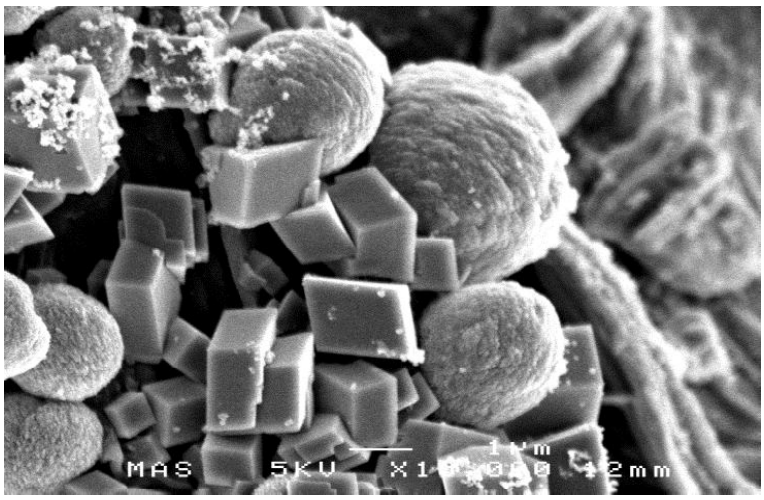

Figure 5.9.: FE-SEM images of the cellulose mesh with calcite (rhombohedral) and vaterite (spherulites) crystals. The sample was previously coated with chromium to avoid charging in the SEM chamber.

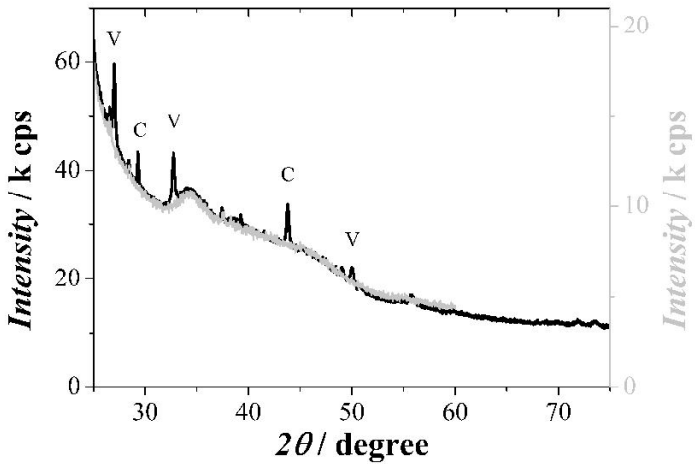

Figure 5.10.: Typical XRD spectrum recorded on the cotton lint before (grey) and after (black) carbonation. The peaks confirm the presence of calcite (C) and vaterite (V) crystals on the cotton fibres.

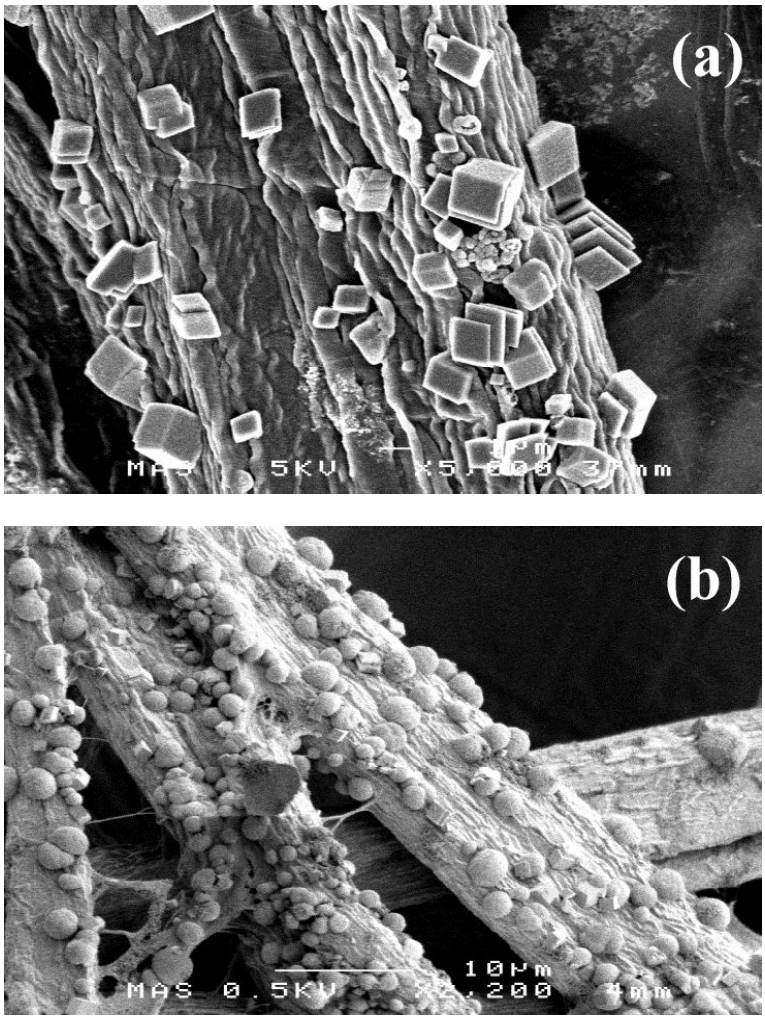

Figure 5.11.: FE-SEM images of the sample fibers with prevalent calcite crystals (a) and vaterite formations (b).

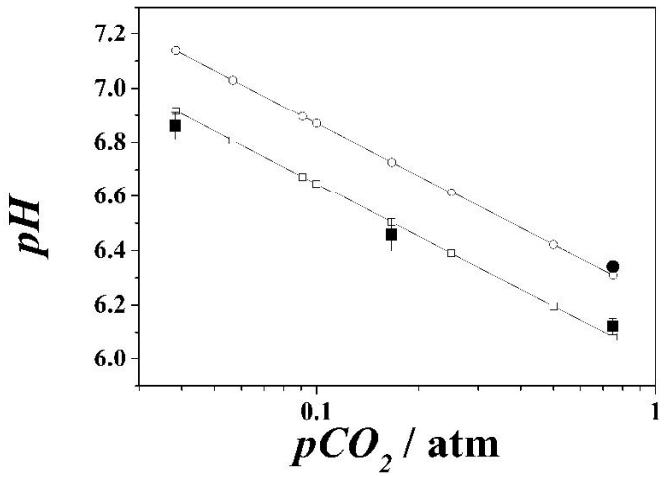

Figure 5.12.: Dependence of the solution pH on the partial pressure of CO_2 in the cell atmosphere. Theoretical (□) and experimental (■) results for calcite and theoretical (○) and experimental (●) results for vaterite.

almost all cases SEM analysis indicated that calcite was the main solid phase produced by the carbonation (figure 5.11a) however, in one case the main solid phase formed was vaterite (figure 5.11b).

The crystallization of almost pure vaterite is related to the reaction kinetics because it was obtained in an experiment where the pH variation after the introduction of CO_2 was unexpectedly fast compared with the other measurements (the second plateau was reached within a few minutes compared to the over 30 minutes needed for experiments leading to calcite).

Figure 5.12 shows a comparison of the experimental (filled symbols) and theoretical (empty symbols) results that demonstrates the dependence of the solution pH on the p_{CO_2} in the cell atmosphere. PHREEQC calculations were performed assuming the solution was in equilibrium with calcite (square symbols) and with vaterite (round symbols). In both cases the pH decreases linearly with the logarithm of p_{CO_2}.

All pH values determined from the micro-electrode potentials are in very good agreement with the theoretical values calculated with PHREEQC. When calcite was found crystallized on the mesh fibres the experimental pH values agreed with the theoretical pH values obtained when the solution was in equilibrium with calcite. When vaterite was found crystallized on the fibres the experimental pH was again in very good agreement with the theoretical pH for that phase.

Remarkably the experimental errors ($\leq$0.06 pH based on the three replicates shown in table 5.5) are smaller than the difference between the theoretical pHs obtained when the solution is in equilibrium with vaterite and with calcite (0.22 pH). Consequently it is clear that it is possible to unequivocally assign the phase produced during carbonation from the micro-electrode potential.

5.4.4. $CaCO_3$ habit and ion concentrations

According to Cizer (2009), the presence of rhombohedral calcite crystals in all the SEM images taken for the different samples (excluding those in which vaterite was found) suggests that the $[Ca^{2+}]/[CO_3^{2-}]$ was always ≥ 1.

On the basis of very simple PHREEQC calculations it is possible to verify that the concentration of Ca^{2+} in the tested solutions at 23ºC was 1.249×10^{-2} $moles/Kg_{H_2O}$ while the concentration of CO_3^{2-} in the same solution (pH=12.44) in equilibrium with calcite and at a partial pressure of 0.750 atm was 4.423×10^{-6} $moles/Kg_{H_2O}$[5]. Thus, in some of the experiments, the $\left[Ca^{2+}\right]$ was 4000 times higher that the $\left[CO_3^{2-}\right]$[6]. A consequence of this is that at the beginning and for most of the experiments the $[Ca^{2+}]/[CO_3^{2-}]$ was always $\gg 1$. Since the carbonation took place in a saturated solution of $Ca(OH)_2$ (containing a limited number of Ca^{2+} ions) and the tests were carried out at high p_{CO_2}[7] it is clear that $[Ca^{2+}]/[CO_3^{2-}]$ could only have been ≤ 1 at the end of each experiment when almost all the Ca^{2+} ions were consumed by the carbonation.

Furthermore, because of the high p_{CO_2} used in all the experiments and the use of an aqueous solution of $Ca(OH)_2$ (rather than a solid phase that could have involved a dissolution process), it is clear that the main limiting factor of the carbonation in these experiments was the solubility of CO_2 in water.

5.5. Conclusions

The study demonstrates that the pH micro-sensors made with nanostructured palladium hydride can operate reliably in very alkaline environments such as those produced by the dissolution of $Ca(OH)_2$. The potentiometric response of these electrodes, in fact, was found to be Nernstian up to pH 14.

The electrodes were successfully employed to monitor the pH changes during the carbonation in a porous substrate exposed to different p_{CO_2} and the pH detected *in situ* was found to be in perfect agreement with the theoretical calculations made with PHREEQC. Besides, the electrode response proved to be sufficiently sensitive and reproducible to differentiate, on the basis of pH, between the formation of calcite and vaterite, inside the substrate.

It is likely that these nanostructured pH microelectrodes are currently the only analytical tools capable of monitoring high pH in confined places and, for this reason, they can be considered highly valuable for the study of chemical processes involving very alkaline waters and for monitoring electrochemical processes in building materials.

[5] At $p_{CO_2} = 0.038$ atm, $\left[CO_3^{2-}\right] = 6.135 \times 10^{-5}$.

[6] 210 times, considering a $p_{CO_2} = 0.038$ atm

[7] A p_{CO_2} =0.750 atm is more than 2000 time higher than the p_{CO_2} in the air while a p_{CO_2} =0.039 atm is about 100 times the the p_{CO_2} in the air.

The main limiting factor of carbonation was found to be the solubility of CO_2 in water. The driving force for the precipitation of vaterite instead of calcite was found to be the reaction rate.

6. Carbonation in porous media

pH measurements with nano-structured Pd-hydride microelectrodes prove that carbonation reduces the pH levels of pore-water in porous materials such as concrete by transforming $Ca(OH)_2$ into $CaCO_3$. As a consequence of this process, carbonation also reduces permeability of porous matrices (Cook and Batchelor, 1996; Arandigoyen et al., 2006, p.342). This is due to the reduction in the pore size caused by formation of mineralogical phases with larger molar volume than portlandite. The molar volume of portlandite, in fact, is smaller than the molar volume of all $CaCO_3$ phases (see paragraph 3.4.5) and, if at the beginning of the carbonation, minerals such as ikaite and monohydrocalcite are formed rather than aragonite or calcite, the pore size reduction can be quite significant.

A reduction in the pore size of a porous matrix such as concrete or lime mortars, has as a consequence a reduction in the penetration of atmospheric CO_2 inside the pores and this is an important factor in the hardening process of lime and cement.

According to Cook and Batchelor (1996, p.343), gaseous CO_2 does not penetrate more than 100 mm in cementitious matrices even after a long period of exposure. The same authors report that research carried out by Parrot and Killoh showed that after 36 years exposure, atmospheric CO_2 penetrated inside a concrete column no more than 65 mm and that $Ca(OH)_2$ was completely converted to $CaCO_3$ only at depths less than approximately 25 millimeters (Cook and Batchelor, 1996, p.343). In 1980 Marchese published a paper where he described the discovery of amorphous $Ca(OH)_2$ in the setting bed carrying tesserae of a mosaic at the Museum of the Salerno Cathedral, built in the 12^{th} century (Marchese, 1980; the bed was no thicker than 12 millimetres). Moropoulou and colleagues (Moropoulou and Bakolas, 1995) found portlandite in ancient Byzantine, post-Byzantine and later historic mortars from Greece.

This limited penetration of CO_2 is believed to be caused by a low permeability carbonated region that develops near the surface of the porous matrices and hinders further diffusion of gaseous CO_2 and aqueous inorganic carbon species such as CO_3^{2-} (Cook and Batchelor, 1996, p.344).

Limiting factors of this hindering effect caused by the low permeability region are the cracks caused by carbonation shrinkage (Arizzi and Cultrone, 2014). Through the cracks in this surface layer gaseous CO_2 can penetrate deeper inside the porous matrix and react with the remaining $Ca(OH)_2$ (Cook and Batchelor, 1996, p.344).

In order to investigate carbonation within the pores, this chapter investigates the carbonation of *nano-lime* in porous media.

Nano-lime is the term used to describe a commercially available suspension of nano crystals of $Ca(OH)_2$ in alcohol that is absorbed by porous media such as lime plasters or stones and acts as a consolidant through carbonation within the pores themselves. This material was introduced about 10 years ago in the field of conservation of built heritage in order to provide a compatible consolidant for lime mortars and frescos but its application immediately showed some limitations.

Nano-lime has the potential to provide chemically compatible treatments with carbonatic materials and to produce improved consolidation compared to that achieved with traditional methods such as limewater and milk of lime. However, the exact behaviour of nano-lime is currently uncertain and widely debated. Some recent research, for instance, highlighted that different environmental conditions can affect the carbonation mechanism of nano-lime producing less stable phases such as vaterite or a recrystallisation of portlandite (Lopez-Arce et al., 2010, 2011) with a clear effect on the consolidation treatment.

6.1. Characteristics of nano-lime

In 2005 a new material named *nano-lime* was patented by Piero Baglioni and Luigi Dei (Baglioni et al., 2005). Consisting of a colloidal suspension of nano-sized particles of $Ca(OH)_2$ in an organic solvent, it was originally developed for use as a consolidant in the restoration of frescos, although its potential for strengthening deteriorating stone rapidly raised interest within the cultural heritage industry.

Macroscopically, nano-lime is a white liquid marketed in bottled form with capacities from half a litre to 10 litres. Its opacity is dependent on the particle concentration which typically ranges between 5 and 50 g/l. Currently it is manufactured by German and Italian companies: IBZ-Freiberg and CTS Europe respectively (figure 6.1; IBZ-Salzchemie GmbH (no date), CTS Europe, 2008).

Building lime is traditionally produced through the calcination of limestone (mainly made of $CaCO_3$) in a furnace around 900°C to produce quicklime which is subsequently slaked forming $Ca(OH)_2$ (a more detailed description is reported in 3.1). In comparison nano-lime production is based on a precipitation process in supersaturated aqueous solutions of calcium chloride ($CaCl_2$) and sodium hydroxide ($NaOH$). Following precipitation, water is substituted with an alcohol such as ethanol, isopropanol or n-propanol to improve crystal stability by reducing coagulation and dissolution/re-precipitation processes (Daniele and Taglieri, 2010). The manufacturing process is engineered to produce hexagonal plate-like crystals of thickness approximately 20 nm.

Figure 6.1.: One litre bottle of CaLoSil® E25: suspension of nanoparticles of $Ca(OH)_2$ in ethanol, concentration 25 g/l.

Average particle diameter is 150 nm IBZ-Salzchemie GmbH (no date) although crystals can range from a few tens to several hundred of nanometres (Daniele et al., 2008; figure 6.2).

To give a better comprehension of this size it is useful to compare to the thickness of something familiar such as the diameter of a human hair. In this case a typical nano-lime crystal is between 500 and 1000 times smaller. In the context of building stone, figure 6.3 illustrates how this compares to a typical pore size distribution in a common limestone. It is notable that the nano-lime crystals are in the range of the smaller pore sizes.

Its use as a consolidant stems from the ability of the $Ca(OH)_2$ crystals deposited following evaporation of the solvent carrier to transform, through carbonation, into $CaCO_3$. This is in fact the same chemical process responsible for the hardening of traditional lime based materials. Because $CaCO_3$ is the final product of this reaction, nano-lime is perfectly compatible with all carbonate-based surfaces including limestone, old plasters, renders and frescos (Daniele and Taglieri, 2012).

The smaller particle size of nano-lime, when compared to traditional lime products used by the construction industry allows more effective penetration into the very small pores in limestone structures. The use of alcohol is particularly important in fields such as the conservation of cultural heritage, because it can prevent any further degradation of the object where the nano-lime is applied. Before nano-lime, only *milk of lime* or *lime water* were available (see paragraph 3.1) but the aqueous solvent contained in

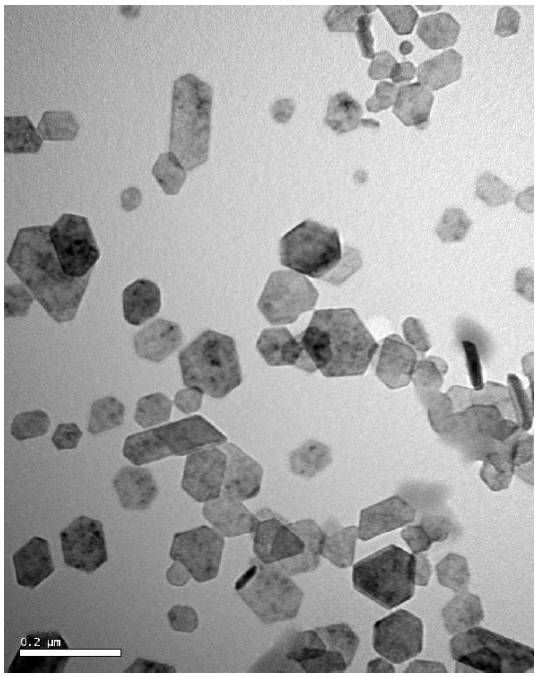

Figure 6.2.: TEM image of diluted CaLoSil® E25. The picure shows the hexagonal shape of the crystals and the wide range of sizes.

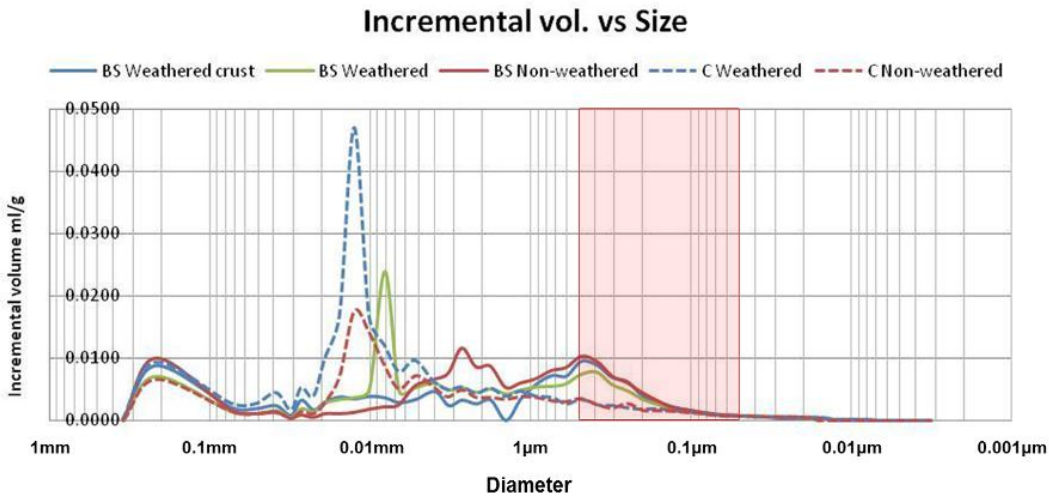

Figure 6.3.: Comparison of the nano-lime crystal size (shaded area) with the typical pore size distribution of Bath and Chilmark limestones. Pore size distribution is provided for both conditions, weathered and non-weathered (for the Bath stone also a pore size distribution of the crust is provided).

these materials often led to the dissolution of soluble salts contained in the treated stone (e.g. sulphates and chlorides) and their subsequent mobilisation. Upon recrystallization, following evaporation of water, a greater degree of damage was caused resulting in no advantage from the treatment.

Nano-lime technology was developed at the beginning of the new millennium with scientific papers emerging between 2000 and 2001 (Giorgi et al., 2000; Salvadori and L., 2001; Ambrosi et al., 2001), and the first patent slightly later in 2005 (Baglioni et al., 2005). Nano-lime development is still active, considering the most recent scientific papers (e.g. Roy and Bhattacharya, 2010) and the fact that one of the latest patents was required in 2012 (Volpe et al., 2012).

At the beginning of its development, nano-lime was mainly used as a consolidant for frescos (Giorgi et al., 2000; Baglioni and Giorgi, 2006) and for the de-acidification treatment of paper and canvas (Giorgi et al., 2002). Later, however, its use was extended to several types of stone for consolidating degraded surfaces (Daniele and Taglieri, 2010; Lopez-Arce et al., 2011).

Between 2009 and 2011 the European project *Stonecore*, focused on the development and application of nano-materials in the field of conservation of natural and artificial stone. This yielded some interesting results (for the most part) on the use of nano-lime for the consolidation of non-weathered stone, and stone powders, in a laboratory environment. However the use of these results as a means of predicting the benefits of applying nano-lime to weathered stone is controversial due to important material and environmental differences (Ghaffari and Musiela, no date).

6.1.1. Choice of the porous medium

Many of the historic buildings of England use limestone as the basic building stone or for carved ornamental features. Limestone decays through a variety of mechanisms which mostly involve weakening of the stone matrix through the dissolution of stone by reaction with atmospheric agent and pollutants. This is followed by subsequent formation of soluble salts which are then mobilised through changes in moisture content driven by changes in relative humidity and temperature. These and additional mechanisms such as freeze-thaw cycling usually manifest themselves as discolouration, powdering and spalling of the stone surface.

Although consolidation of some decayed external stone has been carried out using the lime method and, in a few cases consolidants based on silica or ethyl silicate, the effective consolidation of external limestone has remained one of the greatest challenges facing the conservation of historic stonework. A significant disadvantage of many methods is an associated reduction in vapour permeability.

The development of nano-lime in recent years has provided a promising approach

which yields a highly compatible carbonate phase by which effective consolidation of mortar, plaster and limestone is theoretically possible. This has been partially supported by trials such as those carried out during the Stonecore project.

Despite only a limited number of studies on exterior stonework there has been a significant increase in the use of nano-lime for consolidation of stone in the UK and Europe. Similarities between the calcite phases in stone and the $CaCO_3$ phases formed when nano-lime carbonates provide reassurance of compatibility to practitioners. This has however entailed a higher risk of improper treatments and increased the need for usage guidelines based on rigorous scientific investigations of weathered stones under realistic exposure conditions.

To address these important issues, in 2011 an independent programme of work was carried out by English Heritage, Odgers Conservation Ltd and the Department of Architecture and Civil Engineering, University of Bath. Work undertaken aimed to extend the current understanding of how the morphology of the stone, the moisture content of stone, the environmental conditions (relative humidity, temperature and wind speed) at the time of application and during curing, affect the depth of penetration, speed and depth of carbonation of nano-lime and the degree of consolidation of deteriorated stone.

6.2. Materials

6.2.1. Nano-lime

CaLoSiL E25 and IP25, both produced by IBZ-Freiberg and supplied by Hirst Conservation were used. E25 contains 25 g/l $Ca(OH)_2$ in ethanol and IP25 contains 25 g/l $Ca(OH)_2$ in isopropanol. The products were used in the *as received* condition from the producer with no dilution.

The particle size of E25 was previously evaluated by TEM and found to be in the range 50 and 300 nm (IBZ-Salzchemie GmbH, no date). As IP25 only differs from E25 by the carrier solvent, which is added after the crystals are formed, it is reasonable to assume that the particle sizes of these two products are similar.

6.2.2. Stones

Chilmark and Bath limestones were used in this test. Chilmark limestone is a fine-grained, dense glauconitic stone from the Portlandian formation (Jurassic; Gauri and Bandyopadhyay, 1999; Geddes, 2003). It is easy to carve and is often used in masonry buildings although it is susceptible to erosion by weathering. Bath stone is an Oolitic limestone formed during the Jurassic period, when the area where Bath now stands was

under a shallow sea. It is comprised mainly of ooliths which are formed from spherical grains of concentric layers of $CaCO_3$ called ooids, formed as they rolled around the sea bed. In addition to the ooliths minute fragments of shell, rock and decayed skeletons of marine life are also commonly observed together with the ooliths all bonded by a sparry calcite (Gauri and Bandyopadhyay, 1999; Geddes, 2003). Although both stone types studied are classed as limestones, Chilmark stone has a higher silica content when compared with Bath stone. This is an important factor to consider as it may alter how the materials weather.

The Chilmark stone used in the tests was originally a corbel removed from the Chapter House at Salisbury Cathedral during recent conservation work between 2009 and 2012. The exposed surface was very friable around the edges of the carved areas and the surface was powdery to touch.

Samples and measurements were taken from the front exposed surface (weathered) and from the back of the stone (non-weathered). The back surface, in fact, had not been exposed until its removal from the building facade after which the stone was stored in the laboratory at a temperature of 20°C and relative humidity of 53%. Sampling locations were selected which exhibited visually similar weathering and stone surface texture.

The stone sample obtained from Bath Abbey was part of a sculpture removed from the West Front in 1991 and stored since then in an external environment (during which time a layer of biological material had grown on the surface) until being moved into the laboratory where it was kept under the same conditions as the Chilmark stone. Samples and measurements were taken from the exposed surface (weathered) and from the inner part accessed through a fresh fracture (nonweathered).

6.3. Characterisation methods

Specimens before and after treatment were characterised using a variety of analysis techniques such as optical microscopy, electron microscopy, drilling resistance measurement and mercury intrusion porosimetry. Here a more detailed description of the tests carried out.

6.3.1. Karsten tube penetration test

This is a simple method of measuring the rate of water penetration into (and hence permeability of) building materials such as concrete, stone and plaster. The test was performed using a clear plastic open-ended tube marked with a volumetric scale (the so called *Karsten tube*). The base of the tube was placed on the surface of the material to be tested and the joint made watertight using plasticine. The tube was filled with dis-

tilled water and the volume of water absorbed into the surface was recorded at various time intervals. The data was used to plot curves to compare the absorption behaviour of the materials before and after the treatment, from the different stone areas.

6.3.2. Optical microscopy

Optical microscopy was performed on polished sections of representative stone fragments no more than 25 mm in length and 15 mm in depth. Samples were embedded in low-viscosity resin by vacuum impregnation before being subjected to a pressure of 0.34 MPa for 12 h during the curing period. The surface of each sample was subsequently ground using progressively finer silicon carbide papers to a 1200 grit size before polishing with, 6, 3 and 1 mm diamond paste. A final polish was achieved using colloidal silica suspension. Images of the polished sections were taken using a Zeiss ICM 405 metallurgical microscope.

6.3.3. Scanning Electron Microscopy

Micro-structural and chemical information of the stones was obtained from surface fractures using a JEOL JSM6480LV scanning electron microscope (SEM) coupled with an Oxford INCA X-ray analyser. Samples were fixed on the holder with carbon tape before application of a 30 nm thick layer of gold using an Edward Sputter S150B coater to reduce charging. Energy-dispersive X-ray (EDX) analysis data was collected and analysed using INCA Energy 350 software from Oxford Instruments.

6.3.4. Mercury intrusion porosimetry

Mercury intrusion porosimetry (MIP) was performed using a Micrometrics Auto-Pore III utilising ports for both low and high pressure. WIN9400 series (version 2.00) software from Micrometrics Instruments Corporation allowed analysis of data downloaded from the Micrometrics Interface Controllers. Penetrometers (pen and stem) for solid samples with 5 ml volume from Micrometrics were used.

6.3.5. Drilling resistance measurements

These were obtained using a SINT Technology s.r.l. drilling machine (details of this technique are given in paragraph 4.4). All tests were undertaken using a rotational speed of 600 rpm and penetration rate of 10 mm/min. The force required to maintain these rates (i.e., the drilling resistance of the material) was plotted against depth of penetration, up to a maximum depth of 40 mm. A 5 mm diameter polycrystalline diamond-coated, flat-ended drill bit was used. Drill bit wear was monitored throughout

the testing schedule using SINT Technology s.r.l. artificial reference stone (ARS) as a reference material.

Initial tests on the stones highlighted the inhomogeneity of these natural materials. For this reason absolute values of drilling resistance must be considered with caution. In this case, the results were of greater significance when the shapes of the curve produced by plotting force against depth were considered, rather than the absolute values. The DRMS results presented in this chapter were plotted using an average of three tests on an arbitrary force scale. The force curves of the treated stones were aligned to correspond with the resistance at a depth unaffected by the treatment, typically 30 to 40 mm. This allowed a meaningful comparison between weathered, non-weathered and treated samples to be made.

In some cases the geometry of the stones dictated the location and direction of the drill holes used during drilling resistance measurements.

6.4. Application method and carbonation of nano-lime

Nano-limes of both types, E25 and IP25, were applied to the Chilmark stone (weathered and non-weathered samples) to compare the effects of the different products.

Only E25 was applied to the Bath stone (weathered and non-weathered samples) to compare with the Chilmark E25 test and to evaluate the effect that different physical and chemical characteristics of the stone had on the response to treatment.

For each sample three applications of consolidant were carried out with a brush until saturation was achieved. After the treatment, a white bloom formed on the surface of the stone due to accumulation of excess nano-lime. Even though it is a common practice to remove the white bloom, in this case it was not sponged off in order to maintain an accurate record of the amount of consolidant applied each time. The applications were applied at 3 hourly intervals under laboratory conditions. To allow carbonation of the $Ca(OH)_2$ nanoparticles, the samples were stored, after treatment, for 2 weeks in the laboratory before characterisation.

6.4.1. Post-treatment characterisation tests

The tests used to characterise the stones were repeated to determine the effects of consolidation treatment. MIP analyses were performed 3 weeks after treatment. The Karsten tube test was carried out after 4 weeks. DRMS measurements were taken after 2, 4 and 24 weeks and the SEM imaging was performed at 5 weeks from the application of treatments. The MIP, Karsten tube and SEM were carried out at different times

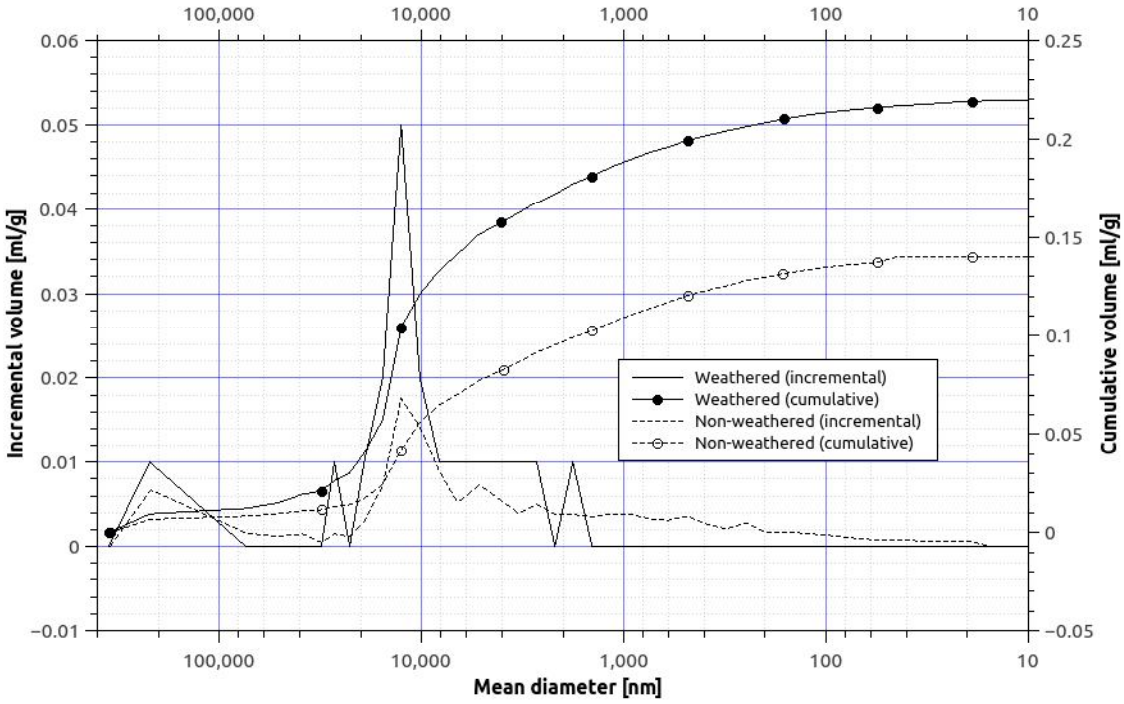

Figure 6.4.: Pore size distribution of weathered and non-weathered Chilmark stone.

as a consequence of equipment availability and scheduling of the experimental programme. A minimum period of 3 weeks was allowed before commencing these tests to ensure a significant proportion of the nano-lime had carbonated, therefore giving representative changes. Where possible, the tests were repeated to improve statistical accuracy and average values are reported. When removing samples for characterisation and identifying areas for drilling, similar positions were selected when the sample geometry allowed.

6.5. Characterisation of stones before treatment

6.5.1. Chilmark stone

Pore size distribution in Chilmark limestone is shown in Figure 6.4. Results indicated that weathering increased the total open porosity by 56% compared with non-weathered stone. Results show also that the majority of the additional pores were around 12.5 microns in diameter. However there was a smaller increase in all the pore volumes especially for those with diameters greater than 1.2 microns.

The SEM images of the samples shown in Figure 6.5a and b revealed silica grains bonded within a $CaCO_3$ matrix. The comparison of the images of weathered (Figure 6.5a) and non-weathered (Figure 6.5b) specimens suggests that the $CaCO_3$ component was more compact in the non-weathered sample.

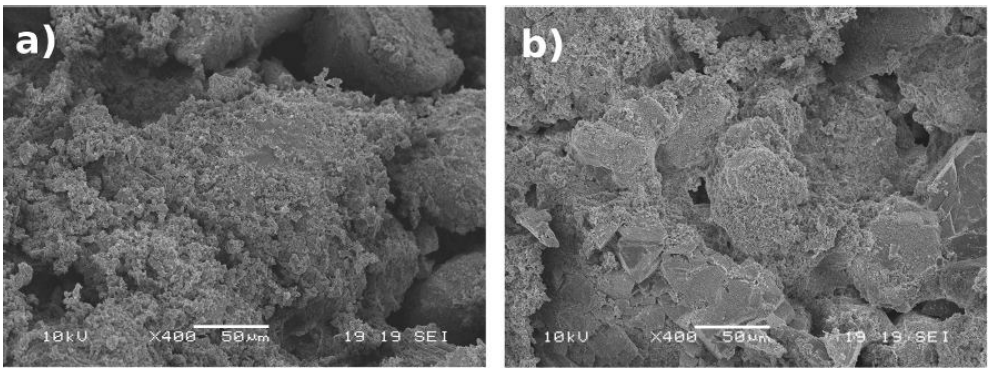

Figure 6.5.: SEM images of untreated Chilmark stone: (a) weathered, (b) non-weathered.

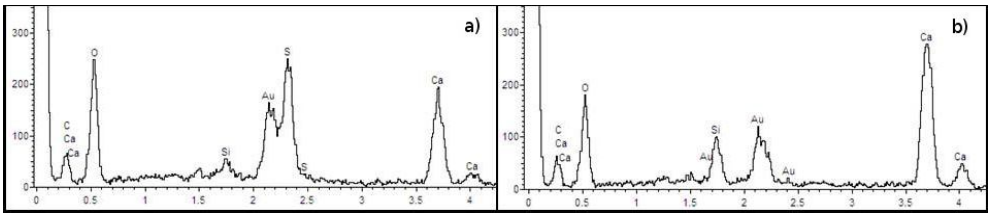

Figure 6.6.: EDX analysis of untreated Chilmark stone. a) weathered; b) non-weathered.

Figure 6.6 shows EDX spectra of untreated Chilmark stone both in the weathered (figure 6.6a) and non-weathered (figure 6.6b) condition. The presence of a sulphur peak on the analysis taken from the weathered surface (figure 6.6a) can be attributed to the reaction of the stone with atmospheric sulphur dioxide (SO_2). In comparison, the sulphur peak was not present on the spectra of the non-weathered stone (Figure 6.6b).

Water absorption characteristics determined using the Karsten tube test showed that the weathered stone surface absorbed water around seven times faster in comparison with the non-weathered surface.

Drilling resistance force was lower for the weathered surface for almost the entire depth of the hole in comparison with the non-weathered stone (figure 6.7). The non-weathered stone showed a relatively stable and constant resistance while the weathered stone exhibited a gradual increase in resistance with depth. The weathered resistance was closest to the non-weathered resistance at a depth of 30 mm after which the resistances for both stones were constant.

6.5.2. Bath stone

The structure of the Bath stone was characterised by examination of a polished cross-section taken from the surface to a depth of 19 mm. The section showed a layer of denser material located adjacent to the surface which was also visible with the naked eye as a whitened area. A 1.3 mm thickness of the outer stone edge is shown in figure 6.8 with the outer crust identified as densely packed finer grained particles on the left hand side of the image. Figure 6.8b shows a cross-section of the weathered stone at a

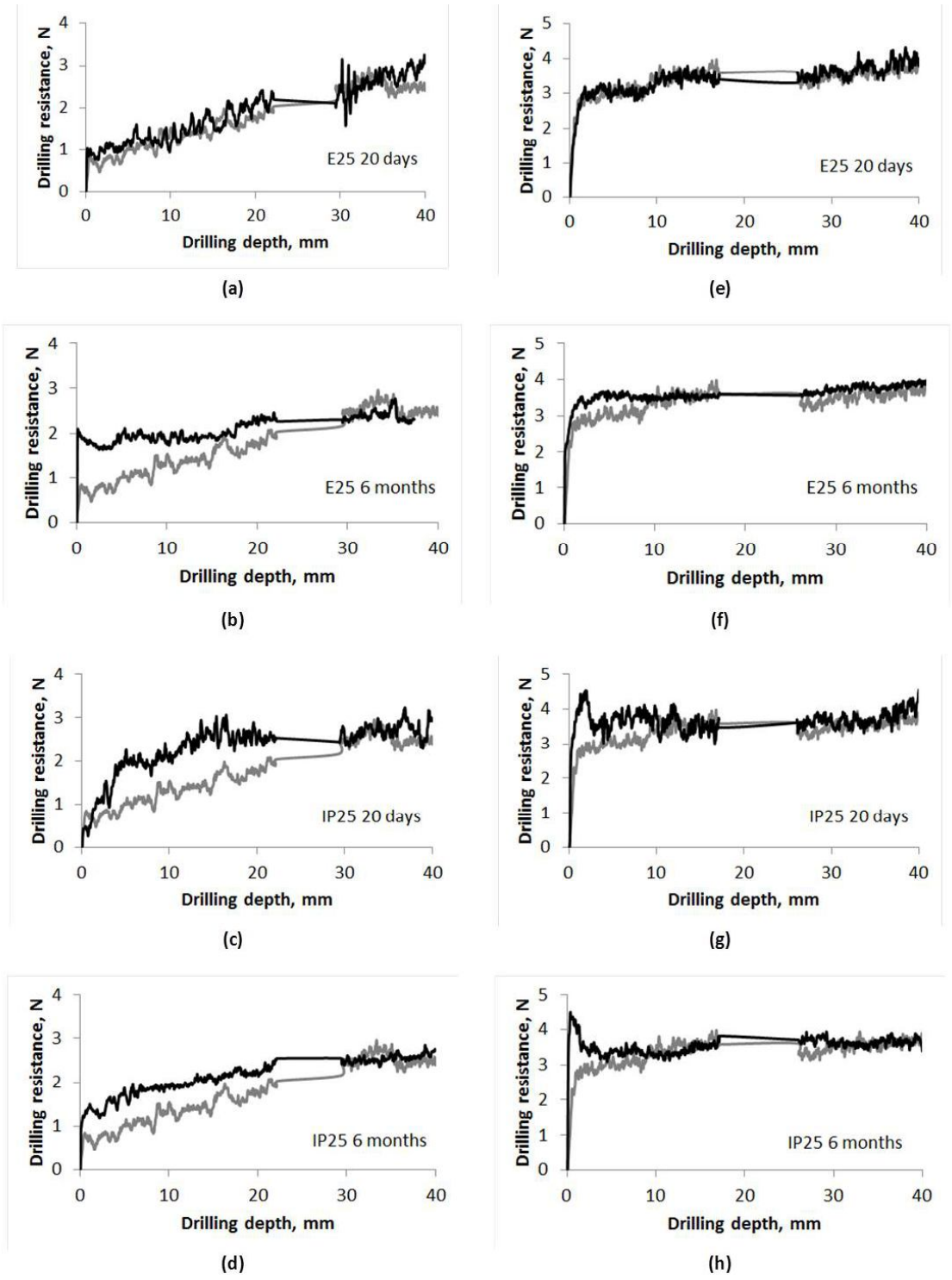

Figure 6.7.: Drilling resistance measurements of Chilmark stone. Response of untreated stone shown by grey line and treated stone by black line. Figures a, b, c, d are related to the weathered stone, while figures e, f, g, h are related to the non-weathered stone. The DRMS data between 17 and 26 mm has been omitted due to high variability.

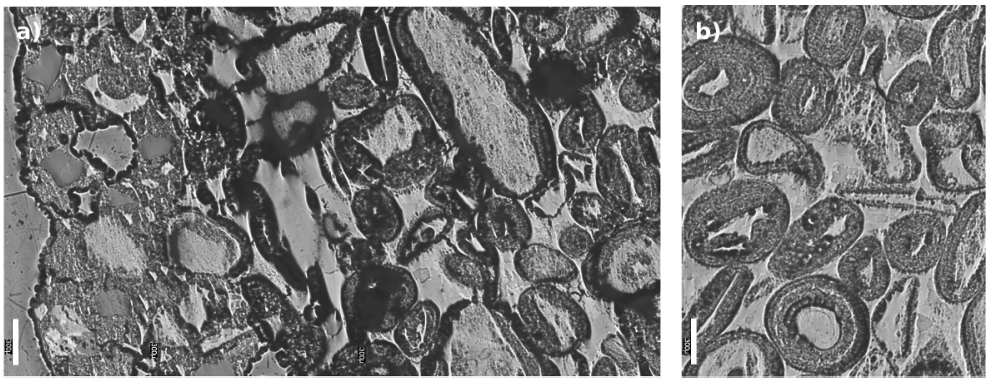

Figure 6.8.: Polished section of the Bath stone. Magnification 50x, scale bar on the left hand side 30 microns. Image on the left hand side (a) is related to the weathered stone with, on the left, the superficial crust. Image on the right hand side (b) is related to the non-weathered stone.

depth of approximately 4 mm.

The porosity of each of these samples was determined using MIP analysis on samples taken from the crust, from below the crust (still in the weathered zone, no more than 1 cm from the surface) and from a non-weathered area. Results are presented in Figure 6.9 and show that total porosity was reduced in the weathered crust by around 6% while just below the crust the total porosity was virtually the same as the non-weathered stone, albeit with different pore size distributions. The most apparent difference in pore diameter range was between 0.1 and 10 microns. In this range the weathered stone had significantly fewer pores with diameter between 1 and 6 microns. Beneath the weathered crust a distinct peak was observed corresponding to pores of 8 microns diameter, whereas in non-weathered stone the peak corresponded to pores of 2 microns diameter.

The SEM image in Figure 6.10a shows that the crust of the weathered stone consisted of smaller particles which were more densely packed together.

Absorption tests showed no significant difference in absorption rate in the first 2 seconds of weathered and non-weathered stone, although, following the initial absorption, an increase in rate was observed for the non-weathered stone. The absorption rate in the weathered zone below the crust was approximately half that of the non-weathered stone.

Drilling resistance of the non-weathered specimen in figure 6.11 showed a relatively steady resistance which was independent of the depth. However, a crust on the weathered surface was clearly observed as a distinct peak at the surface which was followed by a rapid decline in force as the drill penetrated the crust into the weaker underlying stone. A gradual increase in resistance was then observed to a depth of 20 mm where the average non-weathered resistance value was reached.

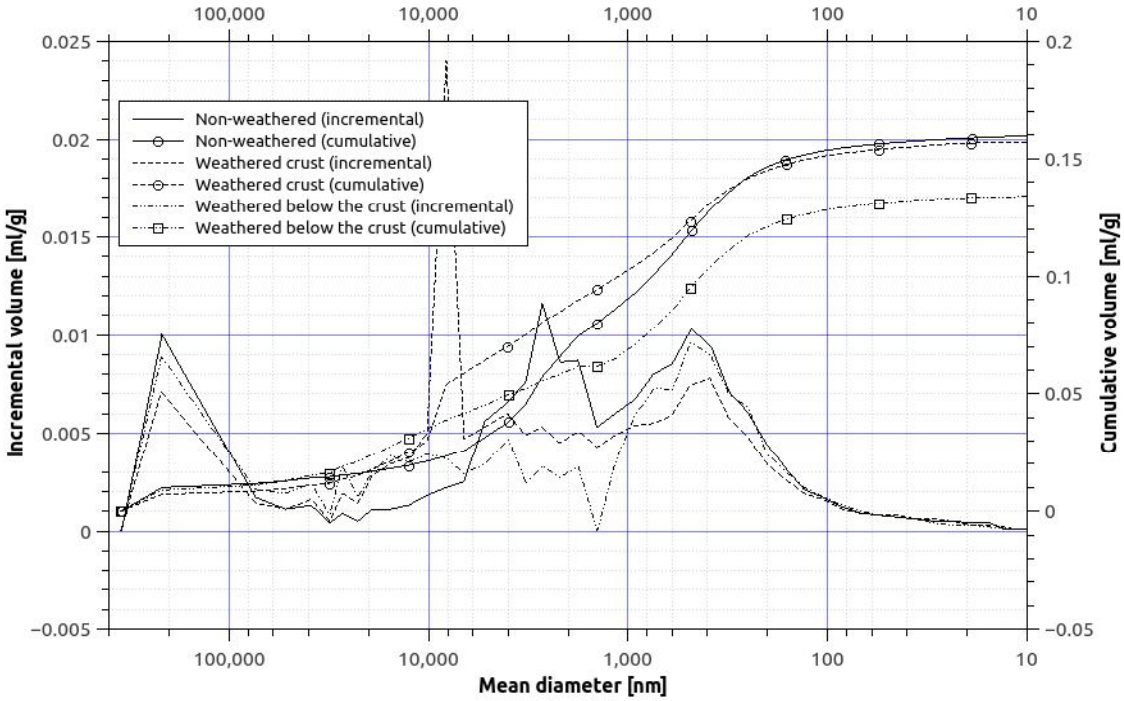

Figure 6.9.: Pore size distribution of weathered (crust and below the crust) and non-weathered Bath stone.

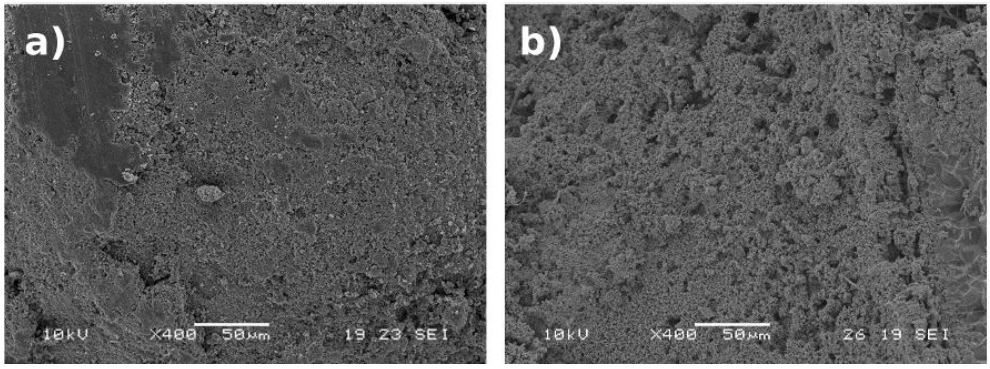

Figure 6.10.: SEM images of untreated Bath stone: (a) weathered, (b) non-weathered.

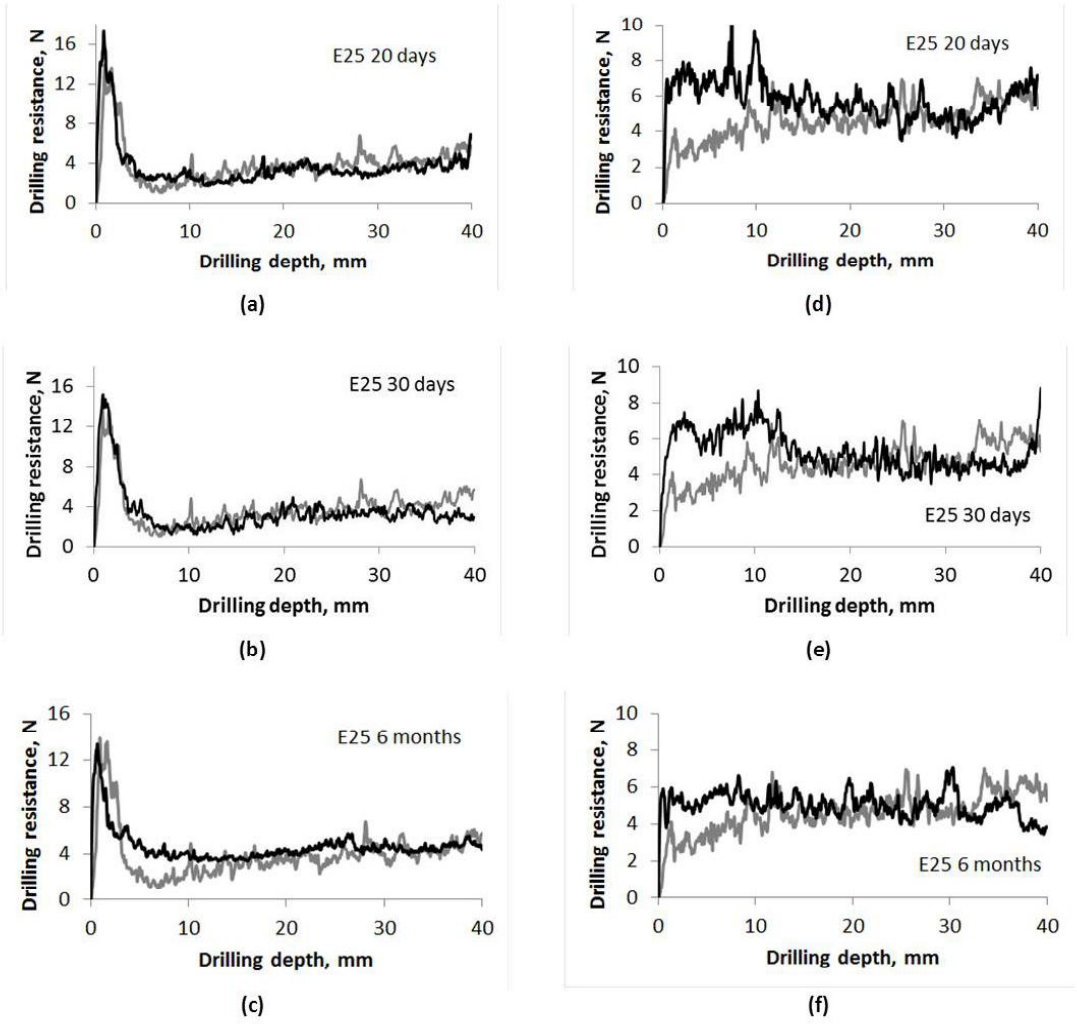

Figure 6.11.: Drilling resistance measurements of Bath stone. Response of untreated stone shown by grey line and treated stone by black line. Figures a, b, c are related to the weathered stone, while figures d, e, f are related to the non-weathered stone.

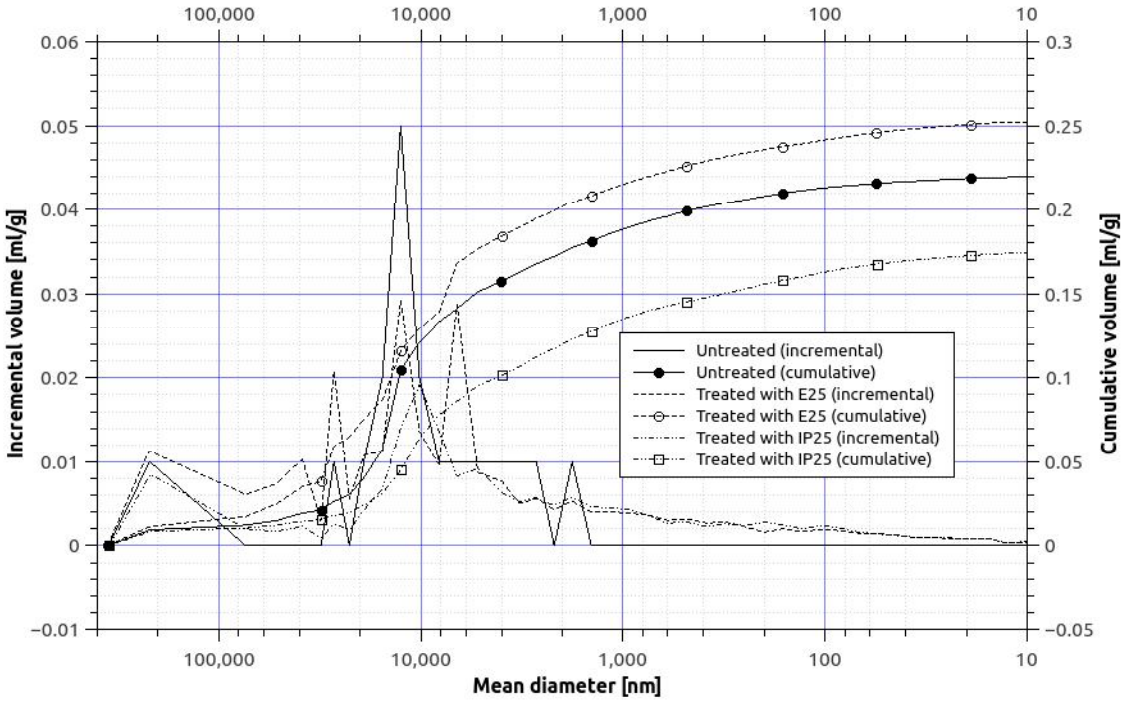

Figure 6.12.: Pore size distribution of the weathered Chilmark stone before and after the treatment with E25 (circles) and IP25 (squares).

6.6. Characterisation of stones following consolidation with nano-lime

6.6.1. Weathered Chilmark limestone

Results from MIP after treatment clearly showed a modification of the pore size distribution greater than 3 microns for the weathered sample treated with E25 (figure 6.12). Most notably the number of pores with a diameter of 12.5 microns had decreased by 38% (largest peak) and there had also been an increase in the number of pores of diameter 6.6 microns.

The effect of the white bloom can be clearly observed by comparing the SEM images of the stone before (figure 6.13a) and after treatment (figure 6.13b). The MIP results for the IP25 treatment showed a different response (figure 6.12). Whereas the E25 treatment did not affect all the pores at 12.5 microns, the IP25 produced a new peak at a pore diameter of 10 microns resulting in a total porosity decrease of 20%.

The SEM images of the surface suggest a blooming effect similar to that produced by the E25 treatment.

The DRMS results for the E25 suggest that the treatment did not add additional resistance to drilling after 20 days from the treatment whereas a clear increase was noticeable after 6 months. Use of IP25, on the contrary, allowed an increase in the

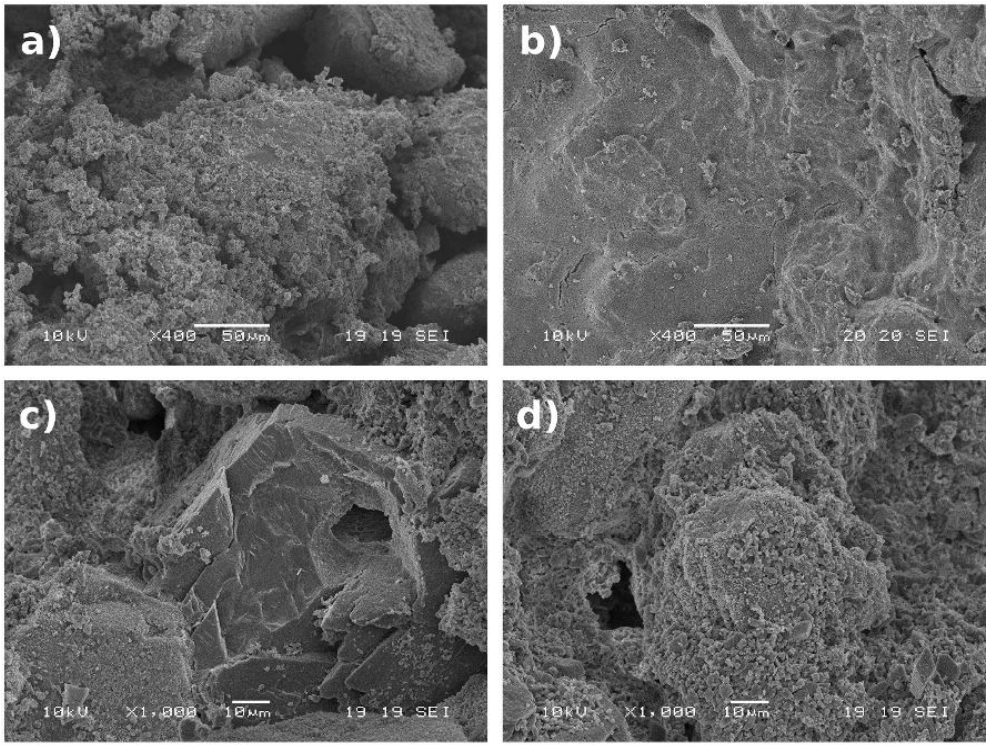

Figure 6.13.: SEM images of the surface of the weathered and non-weathered Chilmark stone before and after the treatment with E25: (a) weathered Chilmark stone before the treatment, (b) weathered Chilmark stone after the treatment with E25, (c) non-weathered Chilmark stone before the treatment and (d) non-weathered Chilmark stone after the treatment.

resistance starting from 20 days but no further increases were noticeable at 6 months after the treatment (figure 6.7).

6.6.2. Non-weathered Chilmark limestone

The MIP plot of the Chilmark stone treated with E25 suggests that the consolidant affected pores with diameter ranging between 0.9 and 3.0 microns and not larger pores of 12.5 microns (figure 6.14). MIP results also showed that treatment of the stone with IP25 shifted the modal pore diameter from 12.5 to 10 microns. The graph of the non-weathered specimen treated with IP25 (figure 6.14) showed similar results to that of the weathered stone treated with the same consolidant.

An SEM image of the untreated stone is shown in figure 6.13c. The DRMS results shown in figure 6.7 for the non-weathered samples indicate that the E25 treatment had no effect on the drilling resistance of the stone after 20 days and only a small effect after 6 months.

Results of the absorption test are given in table 6.1. $\triangle Q$ is the percentage difference in water absorption rate before and after treatment and was calculated considering the absorption rate of the untreated stone as a reference. The weathered samples exhibited a greater reduction in comparison with the non-weathered samples. For weathered

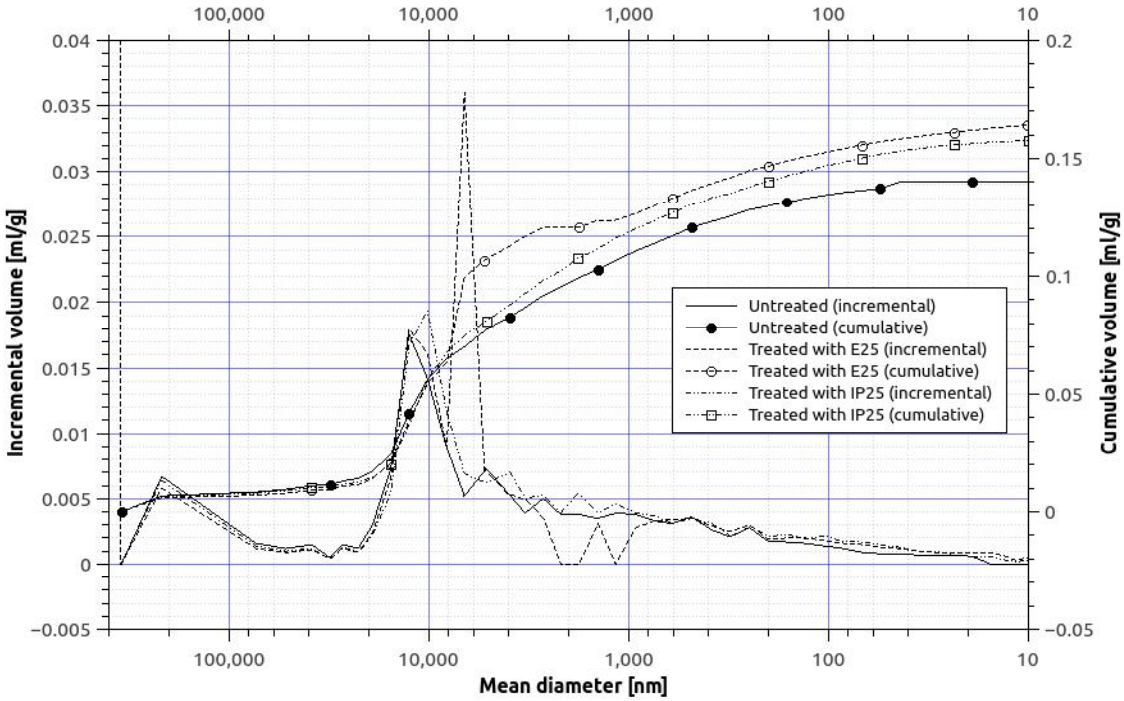

Figure 6.14.: Pore size distribution of non-weathered Chilmark stone before and after the treatment with E25 and IP25.

stone, IP25 appears to have been more effective at reducing the absorption rate than E25. Absorption curves for the Chilmark weathered and non-weathered stones, both treated and non-treated, are given in figure 6.15. In the weathered stone both IP25 and E25 behaved in the same manner whereas in the non-weathered stone E25 exhibited a greater effect than IP25.

6.6.3. Weathered Bath limestone

The pore size distribution after treatment in the crust of the weathered Bath stone showed changes in the range 0.1 to 0.6 microns (figure 6.16). The pores at 8.0 microns were reduced by 75% and there was no increase in percentage of pores with

Table 6.1.: Absorption test results for the Chilmark and the Bath stones before and after the treatment.

Stone	Conditions	Product	Q [ml/sec] untreated material	Q [ml/sec] treated material	$\triangle Q$[%]
Chilmark	Weathered	E25	0.0113	0.036	-68
		IP25	0.0113	0.032	-72
	Non-weathered	E25	0.016	0.008	-50
		IP25	0.016	0.011	-31
Bath	Weathered crust	E35	0.023	0.014	-39
	Weathered	E25	0.013	0.007	-46
	Non-weathered	E25	0.028	0.005	-82

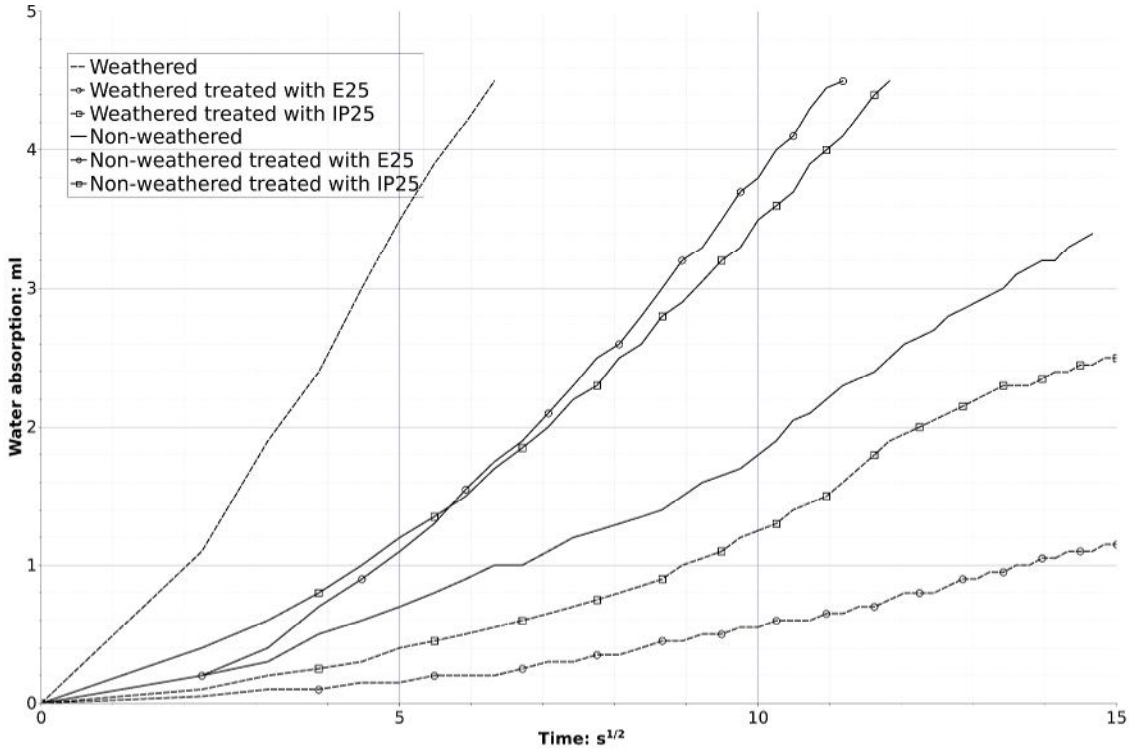

Figure 6.15.: Absorption rate for the Chilmark stone before and after treatment with E25 and IP25; weathered and non-weathered samples.

diameters less than this. The SEM images shown in figure 6.17 show a penetration of the consolidant through the material from the surface. This figure in particular, shows the deposit of nano-particles on the surface that created a layer of very dense material 15 mm thick. The DRMS results in figure 6.11 suggest that after 6 months from the treatment E25 affected only the weak stone behind the crust whereas after 20 days no significant change in resistance could be detected.

6.6.4. Non-weathered Bath limestone

The consolidation treatment showed very little effect on the pore size distribution of non-weathered stone as shown in figure 6.18. There were a few reductions in pore numbers: the graph suggests that treatment affected pores at diameter 0.4, 3.0 and 200 microns. According to the previous findings, the SEM images of the weathered Bath stone showed the fine particle surface coating formed on the exposed surface of the stone, while tests with the DRMS showed the most distinctive result of the treatment applications. Resistance of the stone appears to have been increased to a depth of 11.5 mm above the untreated average (figure 6.11), while maximum resistance showed a decrease between the test at 30 days and the test at 6 months.

All the absorption test results indicate a reduction in absorption after the treatment (table 6.1). The reduction in absorption rate for the non-weathered Bath stone after

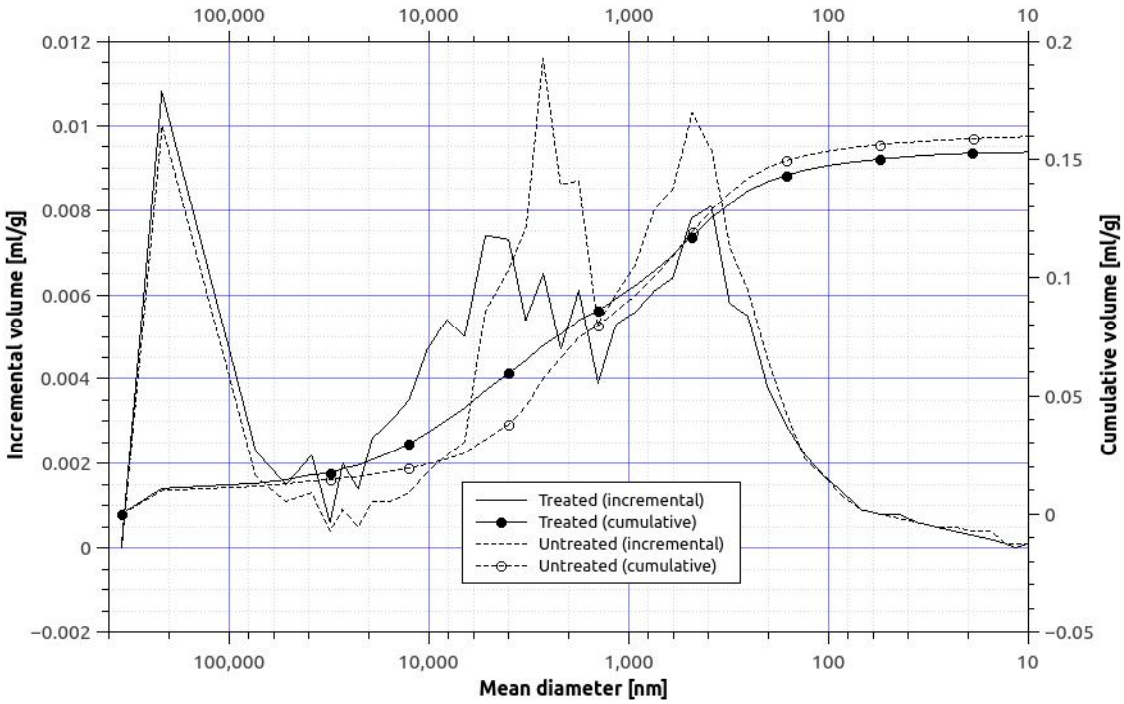

Figure 6.16.: Pore size distribution for the crust in the weathered Bath stone before and after the treatment with E25.

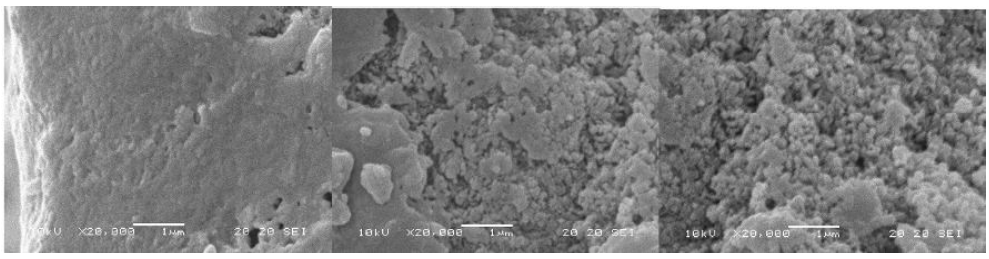

Figure 6.17.: SEM image of weathered Bath stone with visible surface layer (left hand side).

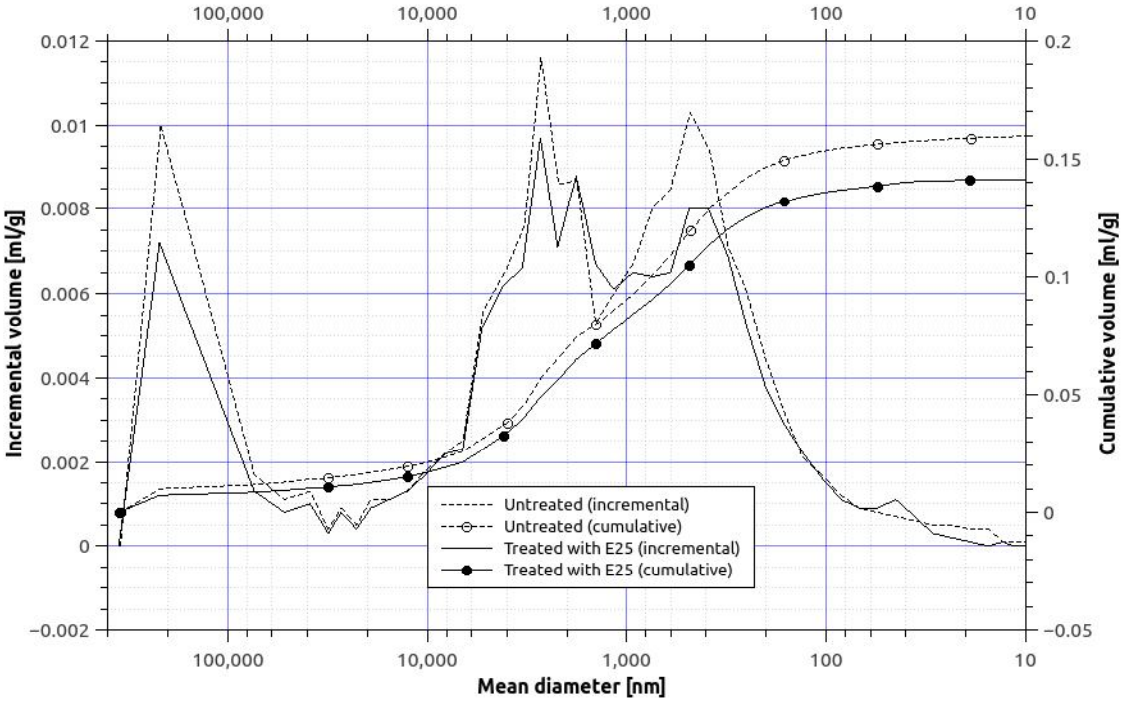

Figure 6.18.: Pore size distribution for non-weathered Bath stone before and after the treatment with E25.

consolidation was 82%.

6.7. Discussion

6.7.1. Effect of weathering on the tested stones

From characterisation of the two limestones some of their similarities and differences can be highlighted. The effect of weathering on the Chilmark stone was an increase in total open porosity (nearly double) and in particular in the pore size around 12.5 microns diameter, thus producing a material with reduced mechanical properties, greater absorbencies and with less cohesion. The depth of affected stone was estimated to be as much as 37.5 mm from the exposed surface. Results suggest that in the Chilmark stone tested, weathering had dissolved the carbonatic binder surrounding the glauconite particles, increasing the porosity and in some cases allowing attack from sulphates with a general reduction of mechanical properties.

The degradation process of the Bath stone resulted in the formation of a superficial crust with different physical and mechanical characteristics compared with the zone beneath. SEM images, MIP and DRMS results suggest that some of the carbonatic binder contained in the area just beneath the crust was dissolved by acidic rainwater and re-precipitated close to the surface to form a crust. The crust depth was between

2 and 7 mm, while below the crust where the binder had been dissolved a weak zone between 15 and 20 mm from the surface was identified. The crust was, then, characterised by a lower porosity compared with the other parts of the stone and higher drilling resistance. The stone just beneath the crust was characterised by a higher porosity (in particular in the region around 8 mm pore diameter) and lower mechanical resistance.

It is probably for this reason that the degradation process often involves the detachment (and falling) of large stone laminations from the surface of worked stone used in historic buildings. The crust itself seems to be the limiting factor of the degradation process which slows down when the crust is formed but starts again when, for some reason such as freeze–thaw or thermal cycling, the crust detaches and exposes new, non-weathered stone to the weathering processes.

6.7.2. Effect of nano-lime on the stones

Nano-lime tends to form a white dense layer on the surface of the stones that can be sponged off immediately following application. This action prevents any change in the natural colour of the stone that can adversely affect the appearance of the building after the treatment.

MIP results suggest that the porosity of the non-treated Chilmark stones was affected in different ways by the two products (E25 and IP25) but in both cases a slight shift in the position of the main peak in the pore size was observed. E25, in particular, tended to change the porosity of the stones reducing the volume of bigger pores with a consequential increase in the volume of smaller pores (non-weathered Chilmark stone, weathered Bath stone).

Differences caused by the degradation process led to variations in the results of the absorption test between the Bath stone and Chilmark stone. The most significant changes in Chilmark stone were observed in the weathered stone which was more porous in comparison with the non-weathered surface, while in the Bath stone the main changes in absorption were found in the non-weathered stone, probably because of the role played by the crust in the weathered stone.

In the Bath stone, it is interesting to note that the three parts (crust, weathered and non-weathered part) showed an absorption capacity that increased from the external surface to the inner part. According to the MIP results, this suggests that the main limiting factor in the absorption was the crust.

The absorption rate of the Chilmark stone (both treated and non-treated) showed that, even when the weathered stone was treated, it tended to absorb water faster than the non-weathered stone. As already suggested by other researchers, the absorption rate is related to the porosity (Lopez-Arce et al., 2010).

In the case of Bath stone, the nano-lime appeared to be more effective for the con-

solidation of higher porosity non-weathered stone. The IP25 exhibited a better performance than E25 for non-weathered stone. However, this was not observed for the weathered stone.

DRMS results on weathered and non-weathered Bath stone (figure 6.11), show a clear reduction in the maximum penetration resistance from 20 days to 6 months after the treatment. A reduction in the force applied is detectable even from 20 to 30 days from the treatment in the weathered stones. Opposite results were obtained for the Chilmark stone where in almost all the tests it is possible to identify an increase from 20 days to 6 months from the application of nano-lime.

This different behaviour could be explained by the formation of metastable phases in the Bath stones that, over the time, transformed into more stable phases without, however, filling all the volume initially occupied by the un-stable compounds.

Bath stone differs from Chilmark in that it has a larger volume of pores with radii $\leq 1\ \mu m$ and this, as discussed in section 2.2.1 and 3.5 promotes precipitation of metastable phases rather than the more stable calcite. Because of the Laplace effect of curvature (Rodriguez-Navarro et al., 2002), inside pores with radius $<1\mu m$, $CaCO_3$ precipitates from highly supersaturated solutions. This promotes the formation of metastable phases that, because of their higher solubility compared to the other $CaCO_3$ polymorphs, are more stable in solution with high Ca^{2+} concentration. Furthermore, according to the calculations carried out in chapter 3, because of their particle size, nano-lime dissolves rapidly, introducing high amount of Ca^{2+} ions into the solution from the very beginning of the reaction. This has an effect on the $\left[Ca^{2+}\right] \cdot [CO_2]$ product that immediately reaches values that fall within the precipitation field of metastable $CaCO_3$ in the Kawano's precipitation diagram (see section 3.4.6).

Finally, due to its porosity, Bath stone can maintain a higher humidity levels within the porous structure compared to Chilmark so that carbonation inside the pore structure of stones can differ between the specimens. Over time, transformation of metastable $CaCO_3$ phases into more stable compounds may improve the effect of treatment but the molar volume reduction associated with this phase change must be compensated by the formation of new $CaCO_3$ in order to provide the necessary strength increase.

6.8. Conclusions

Nano-lime brings a host of benefits when compared to other methods currently available to the conservator or restorer. The ability to deliver a high quantity of lime into a stone without the dangers of inadvertently mobilising soluble salts is in particular appealing. The advantages and disadvantages of this techniques compared to the other available techniques, however, must be carefully considered so as to avoid causing permanent damage or accelerating an already present degradation process.

The research carried out within the European project Stonecore on individual stones has already highlighted that effective consolidation is possible. However due to the wide diversity of stones used in the United Kingdom and Europe it is extremely difficult to use these laboratory based results to gain an accurate and reliable prediction of how nano-lime will behave in the field. This is particularly relevant to weathered stone where influencing characteristics such as presence of crust, sorptivity and pore structure continuously change with time as degradation progresses. Climatic changes and variations in pollutants such as NO_x and SO_2 all add to the complexity of the degradation process over years and decades.

In order to minimise the risk of subsequent spalling, a consolidant must penetrate through the entire thickness of degraded stone. The investigations discussed in this chapter have shown that penetration depth is often a few millimetres. This is often far less than the thickness of a typically degraded stone surface.

A reduction in the maximum drilling resistance over a long period of time (6 months) showed that nano-lime behaviour is not always as expected and this suggest that the setting process of this new material can be different from the setting process of traditional lime. Conditions where carbonation takes place (such as the humidity level inside the stones and the pore size distribution), in particular, seems to be relevant for a successful treatment.

DRMS has proved to be a powerful and useful test for *on site* and laboratory based experiment.

7. Role of pore-water in the hardening process of formulated lime

For lime based protective layers or structural elements, monitoring of the setting reactions can serve as a method of checking the quality. Quality monitoring during construction is a practice useful to both the principal subjects involved in the construction process: the builder and their clients. The builder can benefit from monitoring the early-stage hardening processes because this allows the identification of defects early and allows them to be eliminated immediately without incurring additional costs. Monitoring the setting in lime also ensures high construction quality because it alerts those involved in the construction project to possible errors and deviations. Furthermore, quality monitoring during construction allows the company to produce the necessary documentation to assure the client of the quality of the work carried out during each construction phase. Furthermore, data collected during monitoring could be used in legal disputes if a conflict between the builder and the client arises.

Monitoring the hardening process of lime is therefore an important activity of the building process and among the data that should be collected (such as pH), the water content is one of the most important (El-Turki et al., 2007; Cano-Barrita et al., 2009). Water is requested for the two main reactions that allow lime to become hard: carbonation and hydration. In carbonation water promotes the reaction between $Ca(OH)_{2(s)}$ and $CO_{2(g)}$ allowing the dissolution of the solid and the gaseous phases and subsequent nucleation of $CaCO_3$ solid phases (see paragraph 3.5). In hydration, water allows dissolution of solid phases such as $Ca(OH)_2$ and SiO_2 and also takes part in the reaction that leads to the precipitation of CSH (El-Turki et al., 2010; Karatasios et al., 2010; Ince et al., 2011; see paragraph 2.3.2).

From practical experience it is well known that, if the lime mixtures (mortars or renders) dry too rapidly the binding properties of the lime are lost and the mortars or renders are of high risk of failure (El-Turki et al., 2010).

The role of the water in the setting reactions of lime is so important that the practice of wetting and drying lime based elements is relatively common in the building industry and, despite the fact that this operation has been used for centuries in the

construction industry, it is still now a subject of research (El-Turki et al., 2010, 2007; Morgan and Ball, 2013; Ball et al., 2012a).

Even though monitoring the water content in lime mortars if of great importance, in practice it is not possible to measure *on site* the amount of water contained within the lime mixtures in a non-destructive way (El-Turki et al., 2010).

Standard methods have been set up to measure the moisture condition in concrete (e.g. relative humidity probes; ASTM Standard, 2011; Cano-Barrita et al., 2009), but obtaining *on site* accurate measurements of the relative humidity still remains difficult, mainly because of its temperature dependence (Craig and G., 2006).

A common method used as an indicator of the water content in floors is based on the use of calcium chloride ($CaCl_2$). The *Calcium Chloride Vapour Emission Test*, is a test that quantifies the moisture vapour emission rate (MVER) of a concrete subfloor (Cano-Barrita et al., 2009). It involves placing anhydrous $CaCl_2$ crystals beneath a plastic dome for 60 to 72 hours. The crystals absorb vapour in the air inside the dome and the difference between the initial and final weight of the crystals is used to determine the MVER in weight of water per surface area in 24 hours (Cano-Barrita et al., 2009).

An alternative way to monitoring water content in concrete is by embedding NMR sensors. According to Cano-Barrita and colleagues (Cano-Barrita et al., 2009) NMR is the most effective, non-destructive and non-invasive technique that has been used to undertake studies of hydrating cement based materials. Furthermore, with this technique it is possible to study the moisture distribution during drying and the capillary water absorption as well as the effects of drying and freeze-thaw cycling. The technique is based on embedding specifically produced coils in the concrete and placing these in the stray field of a superconducting magnet to obtain one-dimensional profiles of the mortar samples. Recently, miniaturized NMR sensors (figure 7.1) have been used to monitor moisture changes in Portland cement mortar caused by hydration and drying, and to measure the pore size refinement.

Impedance spectroscopy is another non-destructive technique used to study processes in a range of materials including ceramics, polymers and composites. Over the past 30 years its use in the construction industry has been mostly confined to cement hydration and rebar corrosion in concrete (McCarter et al., 1988, 2002) but recently some works have been carried out in applying this technique to lime binders (Ball and Allen, 2010; Ball et al., 2011, 2012b).

In this research the role of water in the setting reactions of formulated lime is investigated by studying the dissolution process of $Ca(OH)_2$ and the formation of hydraulic compounds in lime-metakaolin mixes. Spectroscopic techniques such as Electrochemical Impedance Spectroscopy (EIS) and Nuclear Magnetic Resonance Spectroscopy

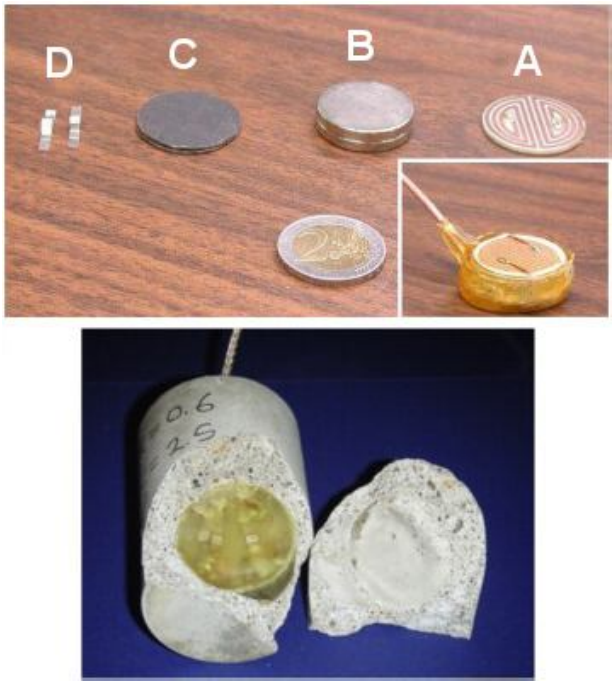

Figure 7.1.: Above: Miniature NMR sensor construction (A) RF coil; B) stack of disk magnets; C) iron disks D) small capacitors fed through a thin coaxial cable. A 2 Euro coin shows the scale). Below: NMR sensor embedded in a Portland cement mortar specimen of 40 millimetre diameter (from: Cano-Barrita et al., 2009 modified).

(NMR) are used to evaluate their use in the daily practice. A detailed description of the two techniques is given in paragraph 4.2 and 4.3, respectively.

Formulated lime is among the most commonly used lime based binder in the modern construction industry. These binders, are simpler to use compared to air lime. They have a quicker setting time and allow the use of low energy fillers and industrial wastes as a source of silica.

Tests implemented in this research were carried out at 20, 25 and 30°C on lime-MK pastes with a 10:1 w/w ratio. Tests over 28 days allowed identification of relevant changes in the EIS signals that were correlated to physical, chemical and mechanical changes through characterization of pastes using Thermal Analyses (TGA/DSC), Scanning Electron Microscopy (SEM), Mercury Intrusion Porosimetry (MIP) and uniaxial compressive tests. Tests over shorter periods of time (up to 42 hours) allowed more detailed studies of the reaction at the very beginning of the hardening process.

7.1. Lime and metakaolin mixtures in the scientific literature

7.1.1. Hydraulic reactions in lime-metakaolin mixtures

Metakaolin (MK) has been used for centuries as a hydraulic additive in the construction industry (Pesce and Ricci, 2008; Pesce, 2006). Currently it is mainly used for the production of high performance, high strength and lightweight concrete, in fiber-cement products or in glass fiber reinforced concrete. In addition to these products, MK is also used in smaller productions used in the conservation of built heritage (such as *Albaria allettamento*: a lime based material produced by BASF Construction Chemicals Italy) and in several research projects aimed to develop new eco-sustainable lime based materials (e.g. Morsy et al., 2012).

Cold mixtures of air lime and MK[1] are important binders for conservation, restoration and new build applications. Elasticity, vapor permeability and the eco-sustainability of the mortars produced with these binders are the most important attributes that can be ascribed to the precipitation of calcium silicate and aluminate hydrate and, in the long term, to carbonation (Ball et al., 2012b).

Despite these interesting properties, however, little work to date has been carried out on the evolution of hydraulic phases in pure MK-lime mixtures. The existing scientific literature, in fact, is mainly focused on MK-cement blends but unfortunately these systems cannot be easily used in the study of lime based materials containing air lime. Differences in chemistry of cement and lime are the main limitations. In cement, mineralogical phases such as tricalcium aluminate (C_3A) or tricalcium silicate (C_3S) that do not exist in pastes of air lime and MK, form specific hydraulic compounds which create highly complex systems that do not allow an easy transmission of knowledge between materials with different binder phases (Frias et al., 2013, p.2306).

Despite these limitations, however, some general knowledge has already been agreed among researchers interested in lime based building materials. It is agreed, for instance, that the times at which different hydration products are formed, their stability and the mineralogical transformations that occur with the hydration time depend on several factors such as MK-lime ratio, temperature and presence of activators (Cabrera and Rojas, 2001, p.180). In 2001 Cabrera and Rojas detected CSH as hydration products after six hours in a 1:1 lime-MK paste cured at 60°C. After 12 hours other hydration products such as stratlingite (C_2ASH_8) and tetra calcium aluminate hydrate (C_4AH_{13}) were also clearly detected. Hydrogarnet appeared after 21 hours hydration and this suggested that this compound can be produced not only by transformation of metastable phases but also by a direct reaction between MK and lime (Cabrera and

[1] *Cold mixtures* are those mixtures that, as mixes, do not undergo to a thermal treatment.

Rojas, 2001, pp.180, 182).

7.1.2. Techniques for the study of lime-metakaolin mixtures

Until a few years ago results like these were mainly obtained using traditional techniques such as thermo-gravimetry, differential thermal analyses (TG/DTA) and X-ray diffraction (XRD; Frias et al., 2013, p.2036). Most recently, however, an insight into the hydraulic reaction between air lime and MK was provided by less traditional techniques including Raman spectroscopy (Martinez-Ramirez and Frias, 2011) and Nuclear Magnetic Resonance spectroscopy (NMR; Frias et al., 2013). In 2011, in particular, Martinez-Ramirez and Frias analyzed the hydration compounds of a 1:1 w/w $Ca(OH)_2$:MK blend with a 2:37 water solid ratio, cured at 60ºC in plastic airtight containers. After two hours from the mix, the researchers found the typical Raman bands of portlandite and a small signal of carbonate, probably due to carbonation during handling and storage of the sample. Three more bands were attributed to O-H stretching vibrations of water molecules (one of these was attributed to unreacted MK) and a small band was attributed to Si-O-Si symmetrical bending vibration in CSH gel (Martinez-Ramirez and Frias, 2011, p.284). After six hours of curing, the portlandite bands were still detected together with the first signal due to the OH bonded into C_4AH_{13} phase and in calcium aluminum hydrate phases (C_4AH_{19}, C_2ASH_8). The broadness of this signal suggested presence of different AlO_4^{-5} environments. At 21 hours, portlandite, stratlingite and calcium aluminum hydrate (C_2ASH_8 and C_4AH_{13}) could be identified. Unusually, no CSH bands were detected at this stage but a new previously unknown broad band was detected. This band was attributed to several intermediate compounds with metastable hexagonal aluminate phases (Martinez-Ramirez and Frias, 2011, p.285). At 30 hours the broad band attributed to the presence of AlO_6 groups increased. Over a longer period of time (34 days), the portlandite bands disappeared as well as the broad band attributed to the metastable compounds containing hexagonal aluminate phases. In place of these bands, a new band appeared, attributed to a C_3ASH_6-type phase, probably formed from the metastable AlO_6 phases (Martinez-Ramirez and Frias, 2011, p.285). This band was found to increase over a longer period of time (up to 123 days curing).

The first paper on the evolution of hydraulic compounds in lime based materials using ^{27}Al and ^{29}Si NMR was published in 2013 by Frias and colleagues (Frias et al., 2013). In this paper, the same MK-lime system analyzed in 2011 by Raman spectroscopy was studied with up to 123 days of curing. Results showed that within the first 30 hours, the 6-coordinated Al represented by the NMR peak at 9.6 ppm started to appear due to the metastable phases C_4AH_{13} and C_2ASH_8 and that this peak increased over time. In the meantime, the 5-coordinated Al peak reduced and the peak of the

4-coordinated Al shifted from 56 to 60 ppm. This shift was attributed to the formation of a stable cubic phase with tetrahedral Al (e.g. C_3ASH_6) or to the incorporation of Al in CSH gel (Frias et al., 2013, p.2307). Interestingly, according to these authors, within the first 6 hours there were no signs of CSH gel or stratlingite in the ^{29}Si or ^{27}Al NMR signals but only the presence of 6-coordinated Al which was attributed to metastable phases. This suggested a new mechanism in the reaction kinetics (Frias et al., 2013, p.2309).

Early signals from ^{29}Si were difficult to analyse because of a peak broadness at -100 ppm, although it was noticed that the peak intensity decreased with the reaction time during the first hours and shifted toward less negative values (-93 ppm) indicating that the MK was becoming less polymerized (Frias et al., 2013, p. 2308). At 21 hours, a peak at -86 ppm assigned to Q_2 units[2] was clearly visible and two signals at -76 and -81 ppm began to develop. These three resonance peaks increased with hydration time until 30 hours. The peaks at -76 and -81 ppm were difficult to attribute but Frias and colleagues pointed out that peaks at 79.9 ppm were attributed by other researchers to Q_0 units (part of amorphous or crystalline structures) and peaks at -81 ppm were attributed to Q_1 units of the CSH gel (Frias et al., 2013, p. 2309). In summary, Frias and colleagues highlighted that at the early stage of the curing time (up to 30 hours) the metastable phases predominate over the most stable cubic phase and that the evolution they were able to reconstruct suggests that the three hydrated phases (metastable and cubic ones) were generated directly from the reaction between lime and MK rather than by a conversion reaction (Frias et al., 2013, p.2307).

As previously stated, other than for acquiring ^{27}Al and ^{29}Si spectra, NMR has also been used to study the moisture distribution in cement based materials during the drying, the capillary water absorption or, again, the effect of drying and freeze-thaw cycling (Cano-Barrita et al., 2009, p.324). These results were obtained by measuring the T_2 relaxation time: a physical parameter related to the degree of confinement of the water molecules within the cement (Boguszynska et al., 2005, p.2034). The NMR relaxation times are known to be sensitive to pore structure and reduction in pore size. A number of theories have been developed to explain why the relaxation time of water in porous materials is influenced by the pore size. It is generally agreed that collisions and/or interactions of water molecules with pore walls control the relaxation behaviour and, in particular, that the relaxation rate increases with the surface/volume ratio in pores (Beyea et al., 1998, p.454).

In 2009 Cano-Barrita and colleagues used the Carr–Purcell–Meiboom–Gill (CPMG) technique to monitor moisture changes in Portland cement mortar caused by hydration, drying and by pore size refinement. The technique they used was based on obtaining experimentally the Effective Transverse Relaxation Time (T_{2eff}) decay envelope

[2]Definition of Q_x units is reported in: Zendri et al., 2004, p.2

(figure 3 in Cano-Barrita et al., 2009, p.325) which was used to calculate the T_{2eff} relaxation time. This value was then used to determine the signal amplitude $M_{(0)}$ in equation 7.1.1 which is proportional to the amount of water in fresh cement paste and in hardened mortar specimens (Cano-Barrita et al., 2009, p.325 and Boguszynska et al., 2005, p.2035; a more detailed description of the theory connected with this technique is available in Apih et al., 2001).

$$M_{(t)} = M_{(0)}.e^{-\frac{t}{T_{2eff}}} \tag{7.1.1}$$

As a result of their experiment Cano-Barrita and colleagues found a decrease in NMR signal due to the hydration of the cement that reduced with the amount of evaporable water in the sample (Cano-Barrita et al., 2009, p.327). Although similar results were found by other groups (e.g. Boguszynska et al., 2005) this chapter presents the first attempt to apply this technique to lime based materials.

7.1.3. NMR spectra of metakaolin in the scientific literature

MK is produced from kaolinite: a hydrous layer silicate clay mineral. Its structural unit consists of a Si-O tetrahedral sheet and an Al-O(OH) octahedral sheet connected by O atoms (Liu et al., 2001). In this structure, silicon shares three oxygens with three silicate tetrahedra and an oxygen with two 6-coordinated Al atoms (Rocha and Klinowski, 1990a).

When kaolinite is fired at temperatures between 550 and 950°C (Rocha and Klinowski, 1990a; Edwards, 2009)[3], some of the OH^- anions within the Al octahedral layer are driven off the structure and some of the Si-O bonds in the Si layer are broken so that the long distance arrangement of the crystalline structure is interrupted and a compound with low distance order called metakaolinite is formed (Liu et al., 2001).

This transformation is highlighted by ^{29}Si and ^{27}Al Magic Angle Spinning Nuclear Magnetic Resonance (MAS NMR) spectra. Liu and colleagues reported that the ^{29}Si MAS NMR spectrum of kaolinite consists of a single resonance at -91 ppm, which is characteristic of layer silicates and assigned to silicon linked to three other silicon atoms and one aluminium atom via oxygens (Q_3 sites; Liu et al., 2001). Rocha and Klinowski instead, reported that highly crystalline kaolinite gives 2 very close ^{29}Si peaks when the spectrum is recorded decoupling the ^1H (Rocha and Klinowski, 1990b, p.568). The chemical shift of ^{29}Si for metakaolinite is instead at -106 ppm which is characteristic of a distribution of sites where the silicon can also be linked to four other silicon atoms and suggests the presence of amorphous silica (Rocha and Klinowski,

[3]Rocha and Klinowski found that the reactivity of MK is greatest at temperatures between 750 and 800ºC, while Edward found a temperature of 500°C; a general overview on the studies of the dehydroxilation process of kaolinite has been described in Rashad (2013).

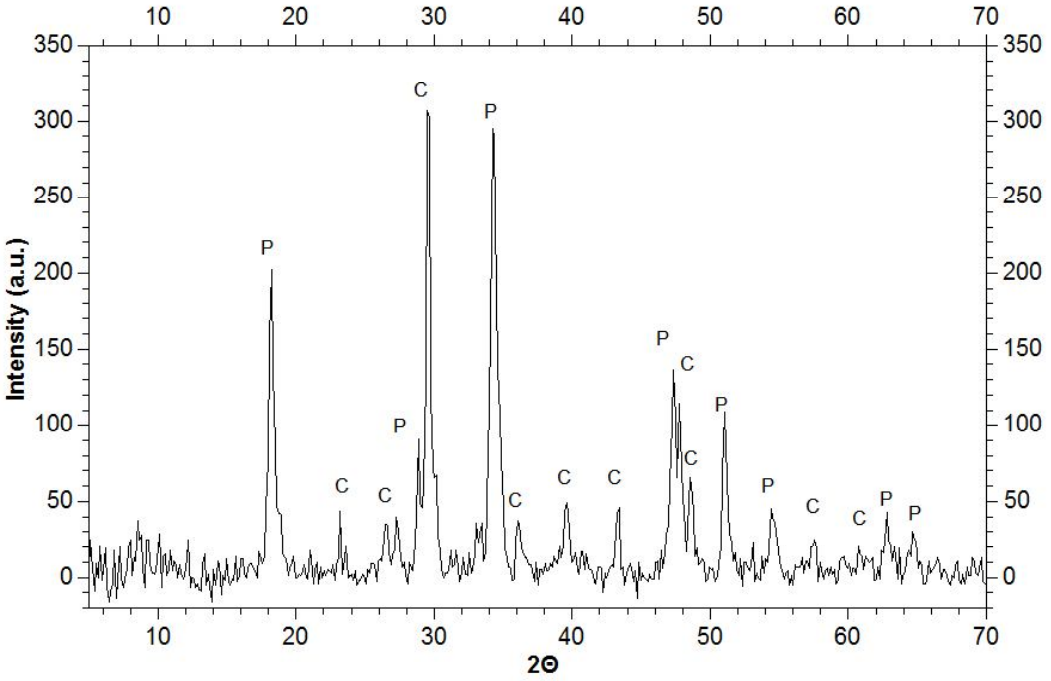

Figure 7.2.: XRD pattern of the CL90 lime used in the tests. Peaks of portlandite are identified by the letter 'P' and calcite peaks are identified by the letter 'C'.

1990a; Liu et al., 2001).

The ^{27}Al MAS NMR spectrum of kaolinite, in turn, contains a single peak at -2 ppm which is assigned to 6-coordinated Al. After calcination at 950°C, metakaolinite exhibits two other resonances at 0-2 ppm assigned to 6-coordinated Al and another at 56-59 ppm attributed to 4-coordinated Al. The broader and asymmetrical peak shapes of metakaolinite show its disordered structure (Rocha and Klinowski, 1990a).

7.2. Materials

The hydraulic reactions between lime and MK were studied using a commercially available dry hydrated lime (commercial name *Ultralime*) classified as CL 90 according to the BS EN 459-1 (2010) and produced by Singleton Birch Ltd. Figure 7.2 shows the XRD pattern of the lime where it is possible to identify peaks of portlandite and calcite (a small amount of $CaCO_3$ is always detected in commercial hydrated lime).

The MK used in the experiments was manufactured by Imerys Minerals Ltd. Its oxide composition, determined by X-ray fluorescence analysis (XRF), is shown in table 7.1. An Energy Dispersive X-ray analysis carried out by Edwards (2009) identified the elements Si, Al, O, K and Fe in the order of decreasing peak intensity.

Figure 7.3 shows the ^{27}Al NMR spectrum of MK (continuous line) with three broad resonances peaks at 0.6, 27.4 and 56.8 ppm attributed, respectively, to octahedral (usu-

Table 7.1.: Oxide composition of the MK used in the tests (results in mass %; L.O.I. = loss on ignition; data from: Moropoulou et al., 2004).

Oxide	SiO_2	Al_2O_3	Fe_2O_3	CaO	MgO	K_2O	Na_2O	SO_3	L.O.I.
Mass [%]	51.70	40.60	0.64	0.71	0.69	2.00	0.31	0.11	1.19

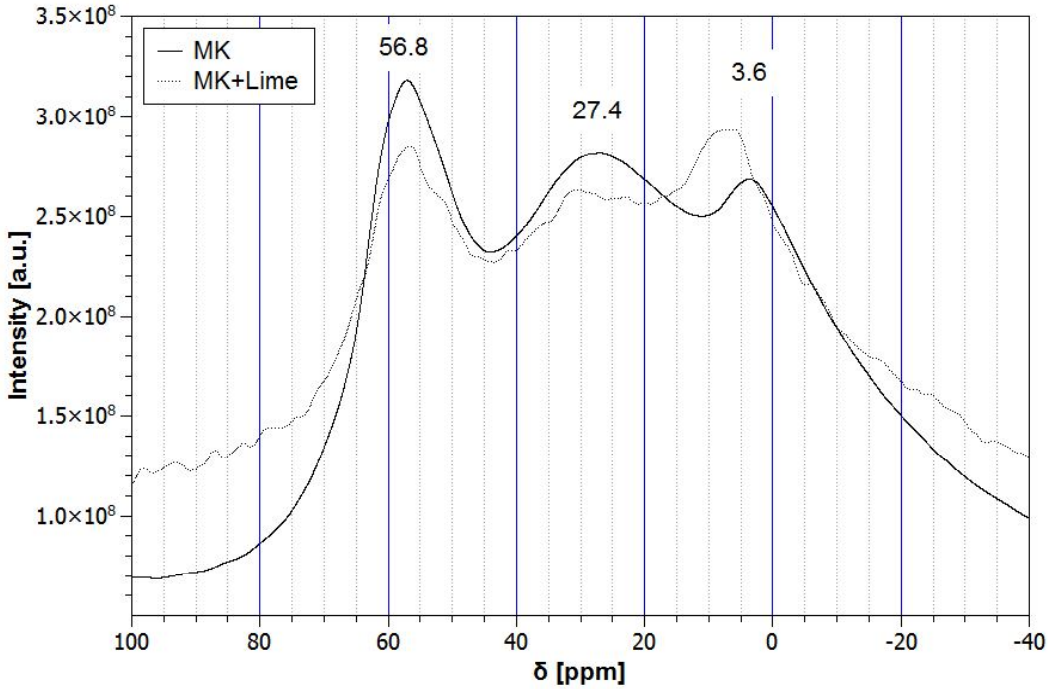

Figure 7.3.: ^{27}Al NMR spectra of MK before (continuous line) and after mixing with lime (dashed line).

ally in the range 20 to -10 ppm; Rocha and Klinowski, 1990a; Andersen et al., 2003), penthaedral and 4-coordinated Al (Rocha and Klinowski, 1990a; Frias et al., 2013; Andersen et al., 2003).

For comparison, the continuous line in figure 7.4 , depicts the ^{29}Si NMR spectrum of MK which displays a broad band characteristic of disordered Si environments (tetrahedral coordination) at about 100 ppm. This peak is characteristic of the dehydroxilated kaolin (Frias et al., 2013, p.2308).

7.3. Method

According to previous research (e.g. Edwards, 2009; Aggelakopoulou et al., 2011), optimum mechanical properties are obtained from a 10:1 mixture of lime to MK w/w ratio, therefore a similar mix ratio has been adopted in this study. Initial tests were carried out over 28 days at 20 and 25±1ºC in order to evaluate changes in EIS response. To investigate the very beginning of the reactions tests over shorter periods of time (up to 42 hours) and at 30±1ºC temperatures were subsequently carried out. In both

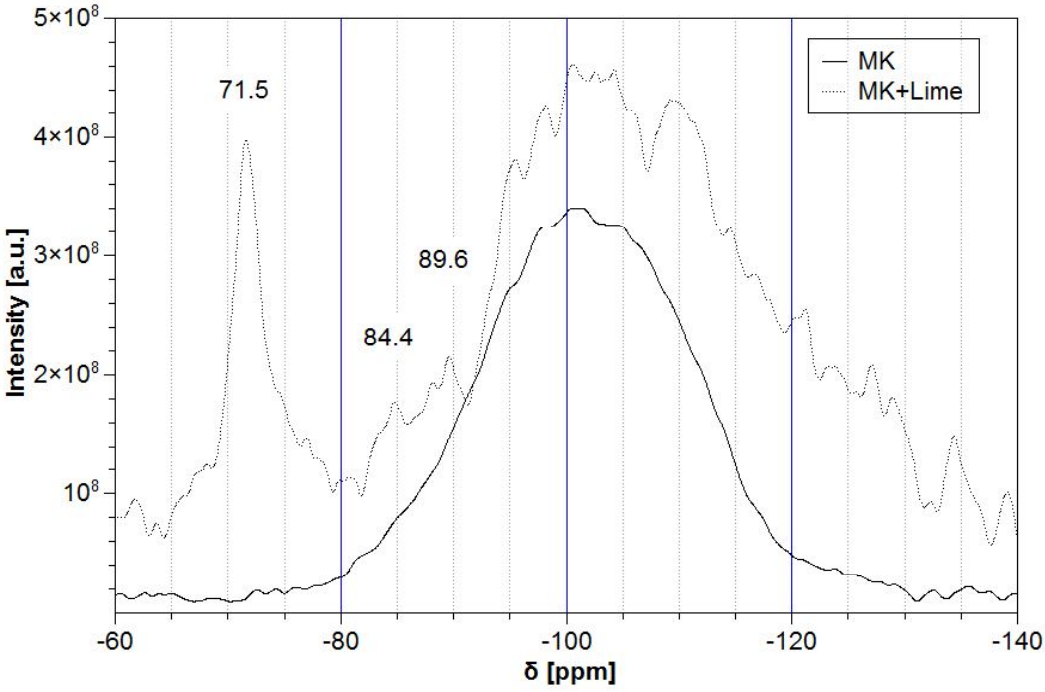

Figure 7.4.: ^{29}Si NMR spectra of MK before (continuous line) and after mixing with lime (dashed line).

cases, EIS was used to continuously monitor the impedance response of the pastes and identify changes in the signal that could be related to changes in the chemical, physical and/or mechanical properties of the samples. Chemical physical and mechanical characterization of pastes was carried out at the end of each week in the long term tests using thermal analyses (TGA/DSC), Scanning Electron Microscopy (SEM), Mercury Intrusion Porosimetry (MIP) and uni-axial compressive strength. In order to study the chemical changes in the short term tests, NMR spectroscopy was used in association with the data already collected during the first week of the long term tests.

7.3.1. Sample manufacture and EIS

Pastes for the EIS tests were cast in an open top polycarbonate reaction cell of internal dimensions 50 x 50 x 50 mm containing two 50 x 50 x 3 mm stainless steel electrodes on opposing faces. A number of additional samples were cast into stainless steel molds for the chemical, physical and mechanical tests. Due to the small quantities of material, the required mixing was performed by hand in a plastic container. A mixing time of approximately eight minutes was considered adequate to obtain a homogeneous mixture using a water-lime ratio of 1.2:1.

Water evaporation and carbonation within the cell and the molds were minimized by covering the top surfaces that were open to air with a thin layer of plastic. In order to reduce the above mentioned processes during curing, the molds were inserted into a polystyrene box where the temperature was controlled by a thermostatic bath.

Inside the box a beaker of water maintained humidity at near 100% while a petri dish containing lime putty was used to adsorb excess CO_2. Before sealing the box, the plexiglass cell was connected to the impedance analyzer and the EIS test was initiated. Long term tests were carried out at 20 and 25±1ºC, while short term tests were carried out at 30±1ºC over a period of 50 hours. In all cases the first measurement was recorded one hour after the initial mix.

EIS measurements were performed using a Solartron SI 1260 Impedance/Gain-Phase Analyzer. Measurement acquisition was controlled with SMaRT (Solartron Materials Research and Test; Solartron Mobrey Ltd) software version 2.7.0. Impedance sweeps were taken in the frequency range 1MHz to 10Hz. The sample impedance, $Z_{(f)}$ at a frequency, *f*, is described in equation 7.3.1 while calculations of the relative permittivity ($\varepsilon_r^{'}$) and *ac* conductivity (σ) of the sample at a given frequency are reported in equation 7.3.2 and 7.3.3, respectively (Ball et al., 2011).

$$Z_{(f)} = Z_{(f)}^{'} - iZ_{(f)}^{"} \tag{7.3.1}$$

$$\sigma_{(f)} = \frac{Z_{(f)}^{'}}{Z_{(f)}^{'2} + Z_{(f)}^{"2}} \tag{7.3.2}$$

$$\varepsilon_{r(f)}^{'} = \frac{Z_{(f)}^{"}}{\varepsilon_0 \omega \left(Z_{(f)}^{'2} + Z_{(f)}^{"2} \right)} \tag{7.3.3}$$

In these equations, *Z*' is the real part of impedance, *Z*" the imaginary part, ω is the angular frequency and ε_0 is the permittivity of the vacuum (see section 4.2).

In order to evaluate the response of EIS to the hydraulic reactions, a similar test with only air lime was performed simultaneously with the test on the hydration to evaluate behaviour of air lime itself.

Uni-axial compressive strength Compressive strengths of the samples were determined using a Instron Fastrack 8800 digitally controlled servo hydraulic system with 100 kN load cell at a loading speed of 0.2 mm/min. Tests were performed at the end of each week of the long term test using cubic samples of 40 x 40 x 40 mm.

Scanning Electron Microscopy Microstructural information relating to phases within the hardened samples was obtained from fresh surface fractures using a JEOL JSM6480LV Scanning Electron Microscope. Samples were attached to the holder with a carbon tape and, then, covered with a 30 nm thin layer of gold using an Edward

Sputter S150B Coater. Images were taken using the secondary electron detector with a gun tension of 15kV, high vacuum mode. Analysis were carried out on samples collected at the end of each compression test.

Thermal analyses Thermal analyses were performed using a SETARAM thermo gravimetric/differential scanning calorimetry (TG/DSC) thermal balance model TGA 92-1750 with a 1600°C module. Analyses were carried out on samples of weight between 13.5-14.5 mg using a dynamic regime, with a temperature rate of 10°C/min up to 950°C, starting from 20°C. During the test, nitrogen gas was fluxed inside the furnace in order to prevent any reaction between the samples and atmospheric oxygen or CO_2. Samples for the thermal analyses were collected after having crushed the cubic samples in the compression tests. In order to have a sample with an average content of moisture, fragments from the inner and the outer regions of the cubic samples were crushed with a pestle and mortar prior to particles greater than 250 μm being removed with a sieve.

Mercury Intrusion Porosimetry Mercury intrusion porosimetry was performed using a Micrometrics AutoPore III utilizing ports for both low and high pressure. A WIN9400 series version 2.00 software developed by the Micrometrics Instruments Corporation allowed analysis of data downloaded from the Micrometrics Interface Controllers. Penetrometers (pen and stem) for solid samples with 5 ml volume from Micrometrics where used. MIP analyses were carried out on samples collected after having crushed cubic specimens in the compression tests.

Nuclear Magnetic Resonance Due to the small amount of material needed for this analysis (5 g of lime and 0.5 g of MK), the required mixing was carried out by hand in a 50 ml glass beaker. A mixing time of approximately three minutes was considered adequate to obtain a homogeneous dry mixture of powders ready to be mixed with water. Then, 5 ml of distilled water was gradually added to the powder and continuously mixed for approximately three minutes inside the beaker in order to produce a paste suitable for insertion into the rotor. Once a suitable quantity of paste was put inside, the rotor was sealed thus preventing any carbonation.

^{29}Si, ^{27}Al and ^{1}H 1D MAS NMR spectra were acquired on a Bruker Avance III 400 spectrometer operating at a B_0 field of 9.4 T with ^{29}Si, ^{27}Al and ^{1}H Larmor frequencies of 79.5, 104.3 and 400.1 MHz, respectively. All spectra were acquired starting from 30 minutes after initial mixing, at 30ºC (rotor temperature). Compressed air was used as the driving gas for spinning the rotors. ^{29}Si MAS NMR spectra were recorded using a 7 mm probe employing a rotation speed of 5 kHz, using a 4.5 μs radio-frequency (RF) excitation pulse length with a RF field strength of 56 kHz ($\pi/2$ flip angle) and 60

seconds recycle delay. ^{27}Al MAS NMR spectra were recorded using a 4 mm probe with a spinning rate of 12 kHz, 1s recycle delay, 0.78 μs RF excitation pulse (equivalent to a $\pi/12$ flip angle). The flip angle pulse for ^{27}Al was optimized using an aqueous solution of $Al(NO_3)_3$.

The T_2 relaxation time of protons was recorded using the Carr-Purcell-Meiboom-Gill (CPMG) technique according to the method described in Cano-Barrita et al. (2009). For this analysis, a 4 mm probe with static rotor was used. Acquisition parameters were as follows: 5 s recycle delay, 3.25 μs and 6.5 μs RF pulse length, using a RF field strength of 77 kHz, for the $\pi/2$ and π flip angles, respectively. The acquisition time for each experiment was 30 minutes. Chemical shifts are quoted in ppm from TMS for ^{1}H and ^{29}Si (using Q_8M_8 as standard 109.68 ppm, for the farthest downfield frequency peak). Aqueous solution of $Al(NO_3)_3$ was used as standard for ^{27}Al.

7.4. Results and discussion

Results have been divided into two sections. The first addresses long term studies over 28 days, whereas the second describes a more detailed study using NMR over the initial hours of hydration.

7.4.1. Long term test at 20 and 25 ºC

Electrochemical Impedance Spectroscopy (EIS) Figure 7.5 shows changes in conductivity and relative permittivity, with frequency, from the 6th to the 28th day during the test at 20ºC (similar results were obtained during the test at 25ºC). The plot shows a decrease in dielectric constant (that describes the electric polarizability) with frequency and a relatively small increase in ac conductivity. The sum of all polarization processes operating within the lime-MK structure contribute to this value at a given frequency of applied field. These processes, which may be superimposed, each have a characteristic relaxation frequency defining the polarization behaviour. The permittivity exists across the entire frequency range under study and is indicative of a spread of relaxation frequencies. At the lower frequencies the dielectric constant rises to anomalously high values of around 108. This behaviour is attributed to the dominating influence of electrode polarization below this frequency. Previous work suggests polarization is a combination of electric double-layer polarization and an interfacial polarization processes (Ball et al., 2011). The presence of conductive species, such as water can also lead to very high relative permittivity (Almond and Bowen, 2004). With hardening time, a decrease is recorded both, in conductivity and in relative permittivity. A more detailed study of changes in dielectric constant and conductivity over the first two weeks shows a clear difference between 0 to 7 days and 7 to 14 days.

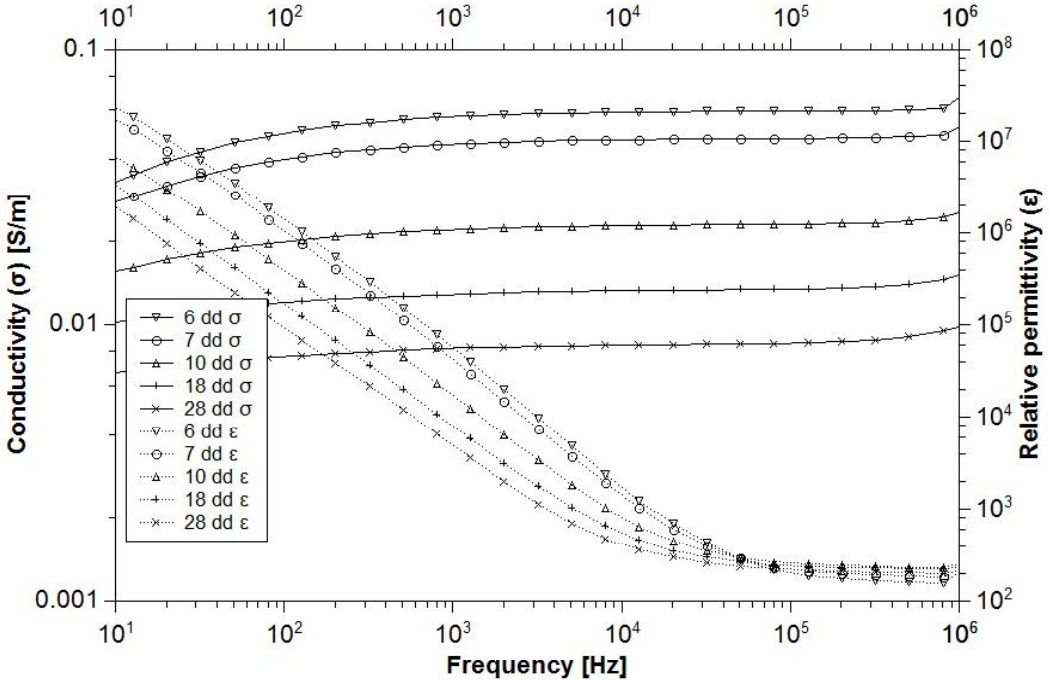

Figure 7.5.: Conductivity and relative permittivity as function of frequency at 6, 7, 10, 18 and 28 days from the initial mixing, for the test at 20°C.

Figure 7.6 shows that the decrease in conductivity and permittivity is more pronounced during the first 8 days compared to the following days.

Figure 7.7 shows changes in the real impedance (Z') as a function of time for the tests at 20 and 25ºC. During the test at 20ºC, the impedance was measured at a frequency of 3.2 kHz, while during the test at 25ºC the impedance was measured at 12.7 kHz. These frequencies corresponded to the minimum real impedance when plotted as a Nyquist plot, which is equivalent to the bulk resistance. A dramatic increase in resistance is shown after approximately 80 hours from the initial mix. Impedance data of the following weeks indicates a further continuous increase in resistance following a levelling of the real part of the impedance. Results of the test carried out on a paste of air lime without MK prove that changes in the impedance are due to the hydraulic reactions (figure 7.7a).

Compressive testing Results from compression tests performed on the samples cured at 20°C are shown in figure 7.8. The one week old sample clearly demonstrates a maximum resistance of about 0.30 MPa and a low slope of the curve (E=557 MPa). After two weeks the slope increases to about 800 MPa and the maximum load reaches 0.40 MPa. At the end of the third week the maximum load rises again to 0.44 MPa but little change is recorded in the slope of the curve (E=845 MPa). At the end of fourth week the maximum load rises to 0.55 MPa and the slope of the curve remains almost constant. In all samples the maximum value is followed by a gradual reduction

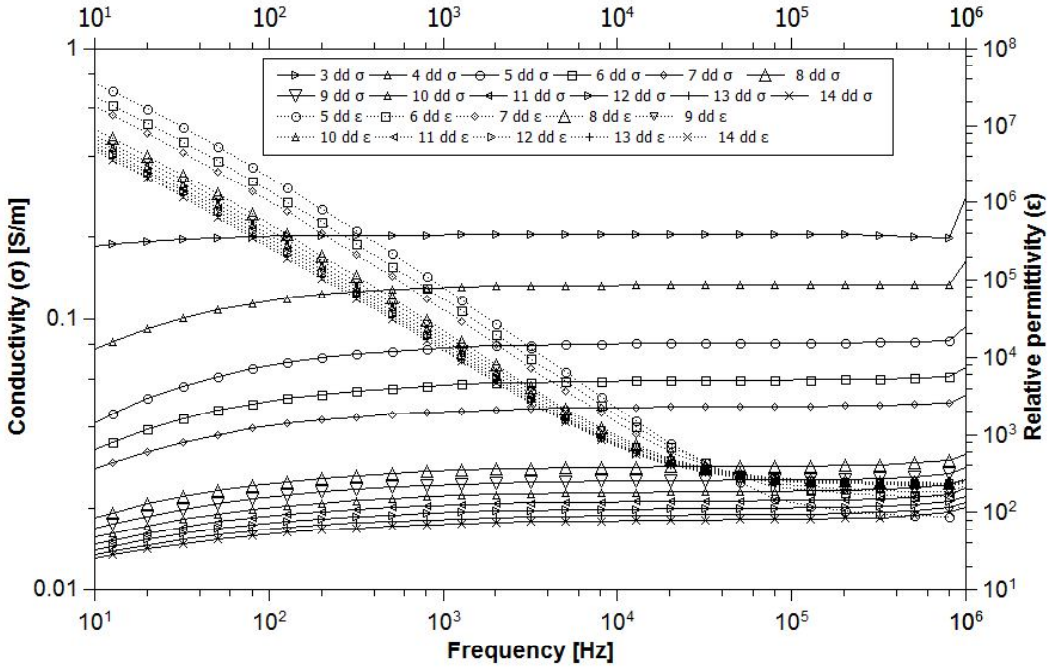

Figure 7.6.: Conductivity and relative permittivity as function of frequency from the 3rd to the 14th days, for the test at 20°C.

of resistance without breaking of the sample. Similar results were found during the test at 25°C temperature.

Micro-structural analysis The micro-structure of a clean fracture surface is characterized by the presence of MK plates randomly distributed throughout the porous matrix. Plates can be single or grouped in packs of 2-8 plates and it is often possible to recognize plate fragments intimately mixed and incorporated into the lime matrix. In the sample cured for one week it is possible to observe bridges of amorphous phases between two plates and the growth of amorphous structures on the edge of the plates. MK plates were readily identifiable in the one week old sample (figure 7.9). However it is noteworthy that, due to the progress of the reaction of MK with lime, the plates became covered and harder to identify in the two three and four week old pastes. SEM microstructure of the four week old sample shows a higher compactness compared with the microstructure of the one week old sample.

Thermal Analysis Figure 7.10 shows the results of the DTA carried out on samples cured at 20ºC. It is already known that the endothermic reaction and weight loss due to dehydration of CSH occurs in the temperature range 110-140°C (Rojas and de Roja, 2003; Moropoulou et al., 2004; Bakolas et al., 2006). Calculations using the TG data within this temperature range (table 7.2) show an increase in the formation of CSH between the first and the second week and a similar decrease between the second and

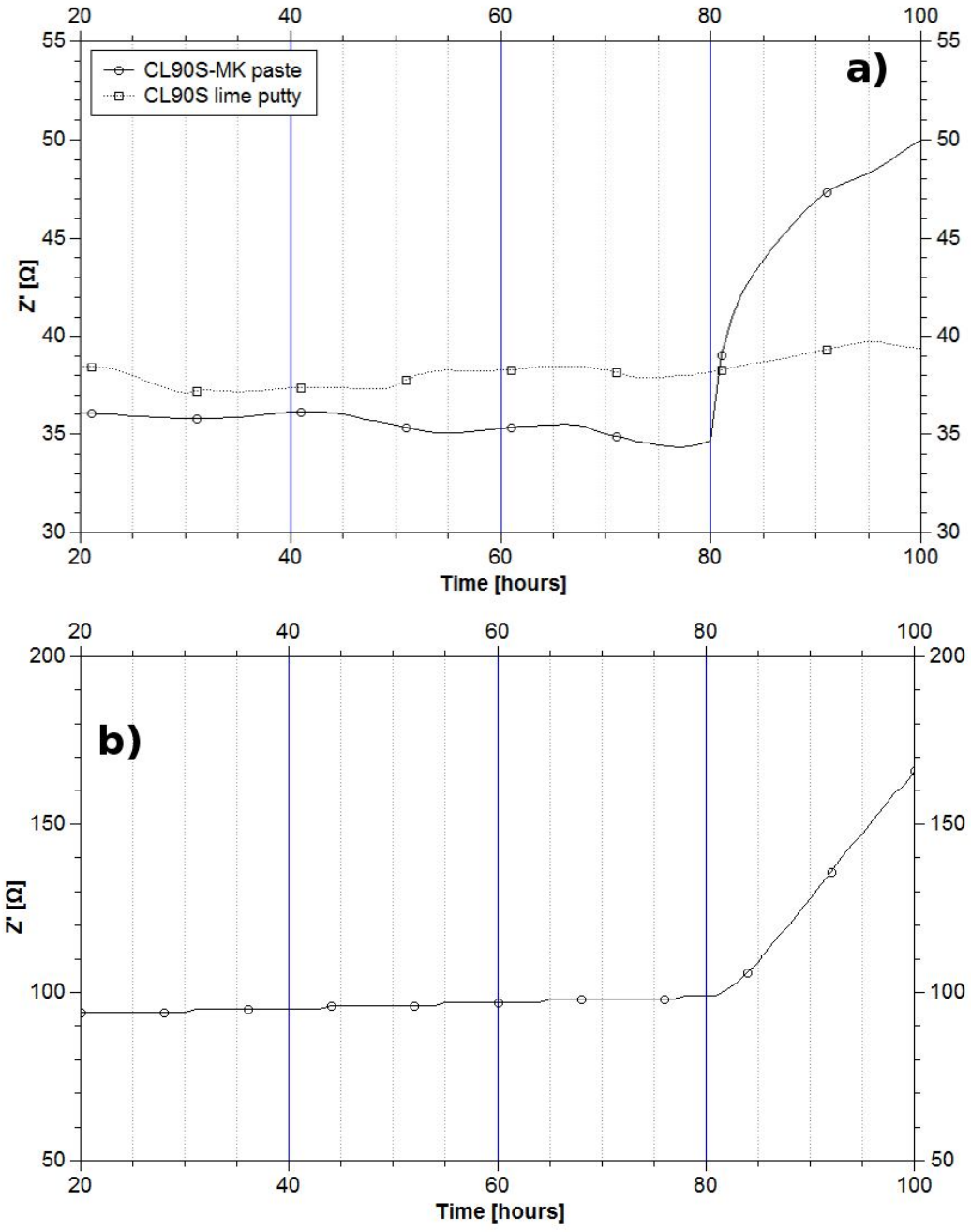

Figure 7.7.: Bulk resistance as function of time for the test at 25°C (a) and 20°C (b). A lime putty without addition of MK was tested a 20°C and its EIS signal is shown together with the signal from the lime-MK mixture .

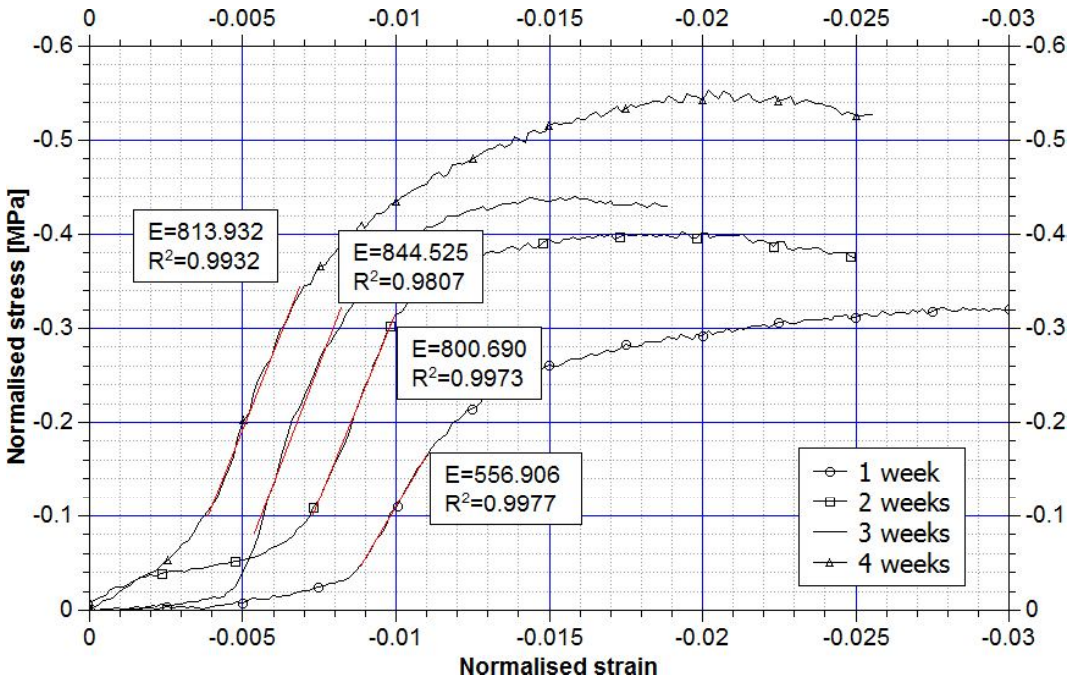

Figure 7.8.: Stress-strain plot for lime-MK paste cured at 20°C for one to four weeks.

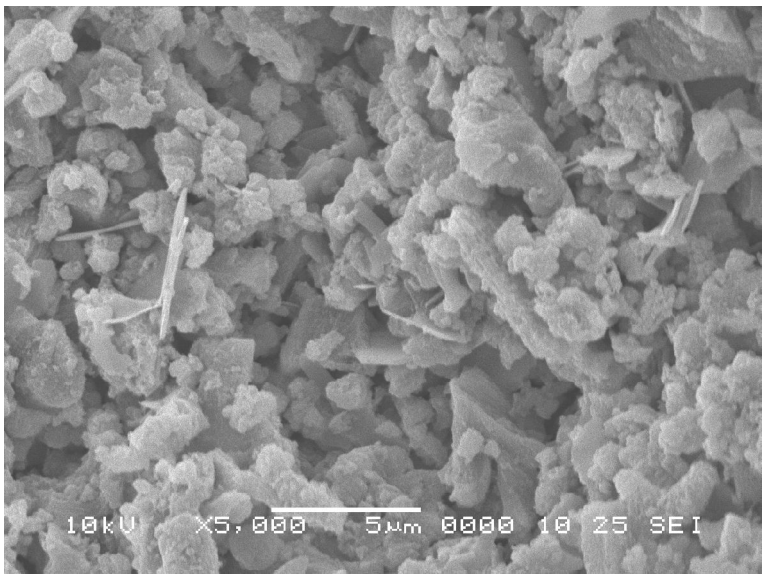

Figure 7.9.: SEM image of the lime-MK paste at one week cured at 20°C.

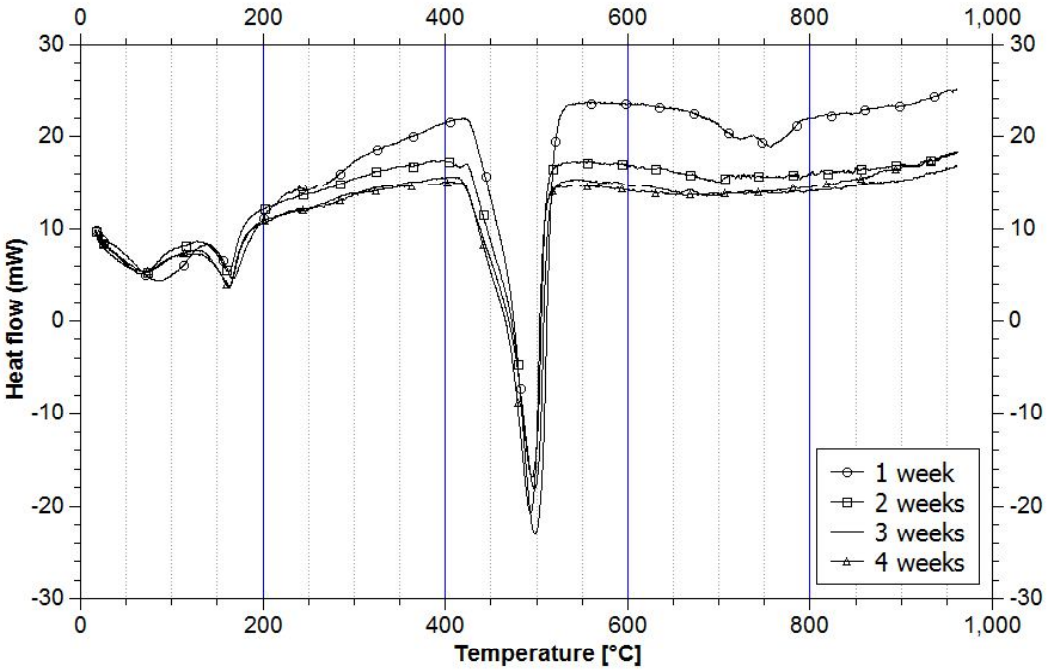

Figure 7.10.: DSC of lime-MK paste cured at 20°C up to 4 weeks.

Table 7.2.: Weight loss in percentage calculated for the different hydraulic compounds formed at 20ºC temperature from the data of the thermo-gravimetric analysis.

Sample	CSH	C_2ASH_8	C_4AH_{13}	C_3ASH_6	$Ca(OH)_2$	Total mass sample [mg]
1 week	0.58	1.88	0.80	0.80	14.49	13.8
2 week	0.67	2.43	1.01	1.08	15.03	14.84
3 week	0.54	2.38	1.09	1.02	15.34	14.73
4 week	0.57	2.55	0.92	1.13	15.04	14.1

the third week (figure 7.11). The DSC curves show a peak between 140-200°C attributed to the dehydration of the hydraulic compound stratlingite (C_2ASH_8; Cabrera and Rojas, 2001). Calculations show a clear increase for this compound between the first and the second week and a less pronounced increase after the second week. A second less clear peak which is visible by close inspection of the one week old sample between 200-270°C, is attributed to hydrogarnet C_4AH_{13} (Bakolas et al., 2006; Moropoulou et al., 2004; Cabrera and Rojas, 2001). Calculation for this compound show a clear increase between the first and the second week that continues in the third week. Decomposition of C_3ASH_6 occurs between 270 and 380ºC. Between first and the second week, a pronounced increase in the amount of this compound was detected while after the second week the increase was less pronounced. The large endothermic peak around 500°C is due to the dehydration of $Ca(OH)_2$.

Tests at 25ºC confirm the results obtained at lower temperature and allows a better evaluation of the phase formation and evolution (Ball et al., 2012b). According to these

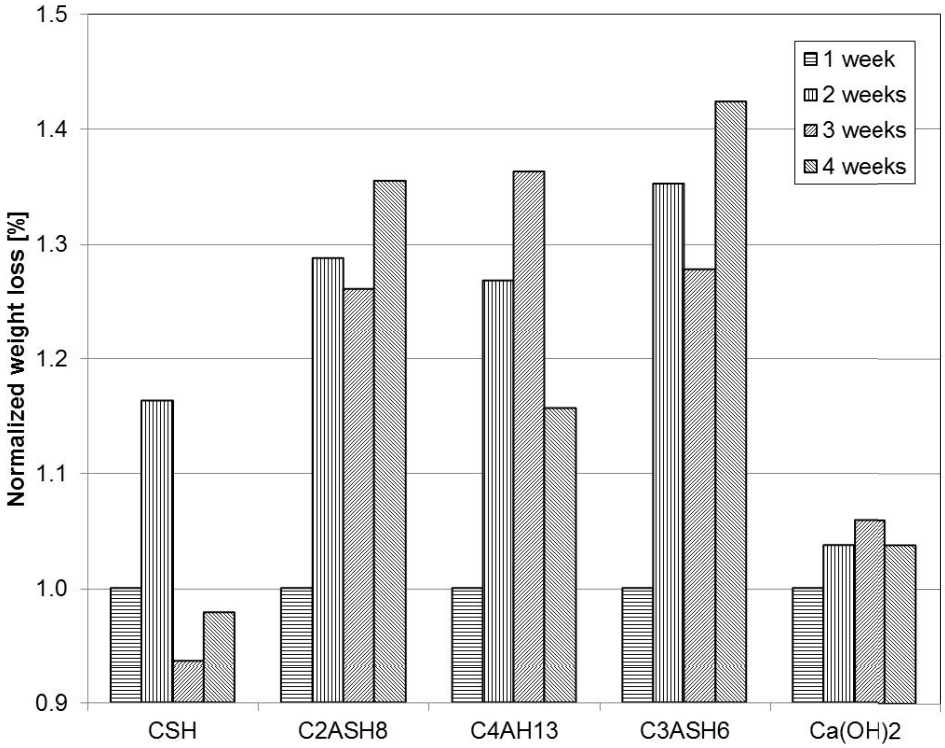

Figure 7.11.: Change in the amount of different hydraulic compounds formed at 20ºC. Calculation in percentage from the thermo-gravimetric analysis, normalized to the value of the first week.

Table 7.3.: Weight loss in percentage calculated from the thermo-gravimetric analysis at different temperature ranges for the test at 25ºC.

Sample	CSH	C_2ASH_8	C_4AH_{13}	C_3ASH_6	$Ca(OH)_2$	Total mass sample [mg]
1 week	11.13	1.34	0.89	0.34	6.98	20.68
2 week	6.25	1.77	0.94	1.12	6.84	16.92
3 week	6.68	2.14	1.09	1.15	7.12	18.18

results (table 7.3 and figure 7.12), CSH phases are clearly identified at the end of the first week and their abundance decreases at the end of the second remaining almost constant at the end of the third week. Stratlingite increases over the following two weeks as well as calcium aluminate hydrate C_4AH_{13} and the C_3ASH_6 while $Ca(OH)_2$ remains almost constant over the three weeks.

Mercury intrusion porosimetry Mercury intrusion porosimetry (MIP) of lime-MK paste aged up to four weeks is shown in figure 7.13. Results of the one week old sample shows that pores are mainly in the 400-1200 nm diameter range but a small quantity of smaller pores in the range between 4 and 200 nm are also detected (peaks at 8 and 12 nm). Results on the two week old samples show a slight reduction in the pore range between 20 and 600 nm diameter while an increase is visible in the pores of 800 nm diameter. This small increase is shown also in the total intrusion volume of

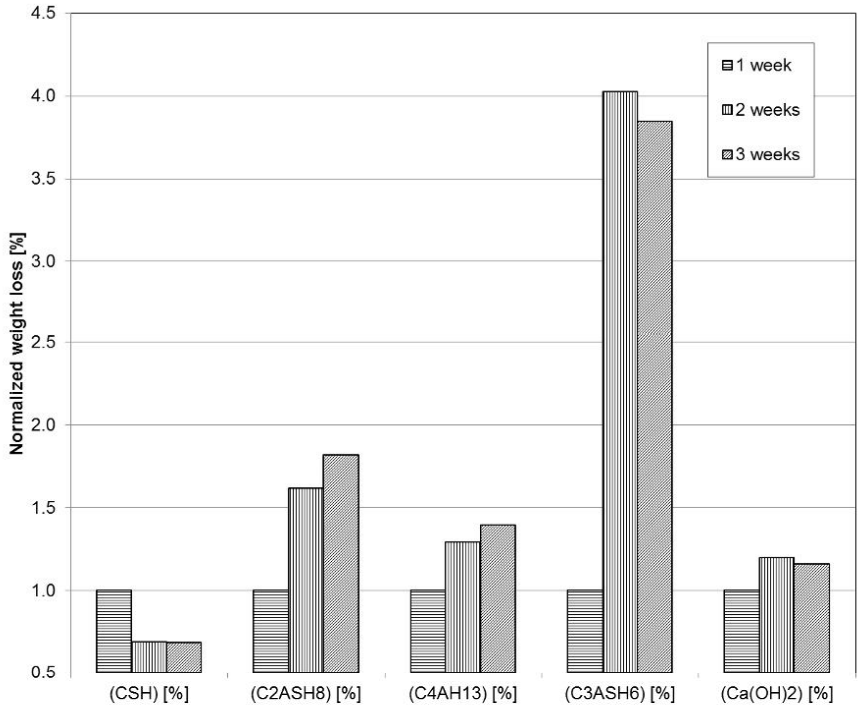

Figure 7.12.: Change in the amount of different hydraulic compounds formed at 25ºC. Calculation in percentage from the thermo-gravimetric analysis, normalized to the value of the first week.

mercury and the reduction in volume of median pore diameter. In contrast to week one and three, a significant pore reduction in the porosity is detected in week four (Khatib and Wild, 1996; Frias and Cabrera, 2000).

7.4.2. Short term test at 30 ℃

Electrochemical Impedance Spectroscopy (EIS) EIS tests at 30°C were carried out 50 hours after the initial mix to investigate the initial stages of the hydraulic reactions and, in particular, the increase in bulk resistance found at about 80 hours in the tests at 20 and 25ºC (respectively figure 7.7b and 7.7a).

Figure 7.14b shows changes in the real part of the impedance during the test at 30ºC. As already noted for the tests at 20 and 25°C, after an initial stability, the bulk resistance suddenly increases but, differently from the tests at lower temperature, this increase is clearly detected after about 35 hours from the initial mixing.

By examining the changes in conductivity and dielectric constant within the first 42 hours (figure 7.14a) a decrease in conductivity until 26 hours is visible from the beginning of the test and a sharper decrease after this time. An almost symmetrical behaviour is recognizable in the dielectric constant that slowly rises during the first 26 hours and, then, exhibits a rapid increase.

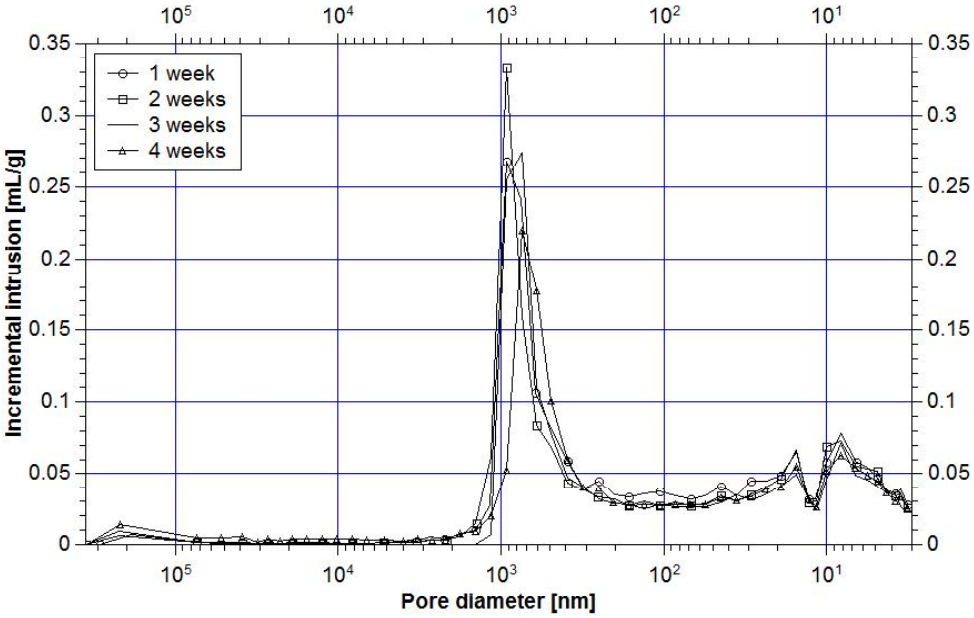

Figure 7.13.: Mercury intrusion porosimetry results of lime-MK pastes cured at 20°C and aged up to four weeks.

7.4.3. Nuclear Magnetic Resonence (NMR)

NMR analysis was used to investigate changes in bulk resistance highlighted by EIS during the very early stages of hydration. Tests were carried out at 30°C to allow comparison with the EIS results.

^{27}Al and ^{29}Si MAS NMR spectra The dashed line in figure 7.3 shows the ^{27}Al NMR spectrum of MK about 30 minutes after the initial mix. Comparison of this spectrum with the spectrum of non-reacted MK (in the same figure) highlights a reduction in the 4 and 5-coordinated Al peak and an increase in the peak of 6-coordinated Al suggesting a reaction between lime and MK at least 30 minutes after the initial mix.

Figure 7.15 shows changes in the coordination number of Al over a longer period of time (up to 42.5h). Measurements taken every 3.5 hours show an initial increase in the peak of 6-coordinated Al and a later reduction, followed by another increase and reduction cycle. Peaks of 5- and 4- coordinated Al, instead, show a continuous decrease until disappearance of the 5-coordinated Al and an almost complete disappearance of the 4-coordinated Al. A plot of the normalized 6-coordinated Al using the 4-coordinated peak as a reference is shown in figure 7.14b. This highlights the initial increase and the subsequent stabilization or decrease in the number of sites of octahedral Al.

The dashed line in figure 7.4 represents the ^{29}Si MAS NMR spectrum, about 8 hours after the MK was mixed with lime. In this spectrum a new sharp peak at 71.5 ppm is

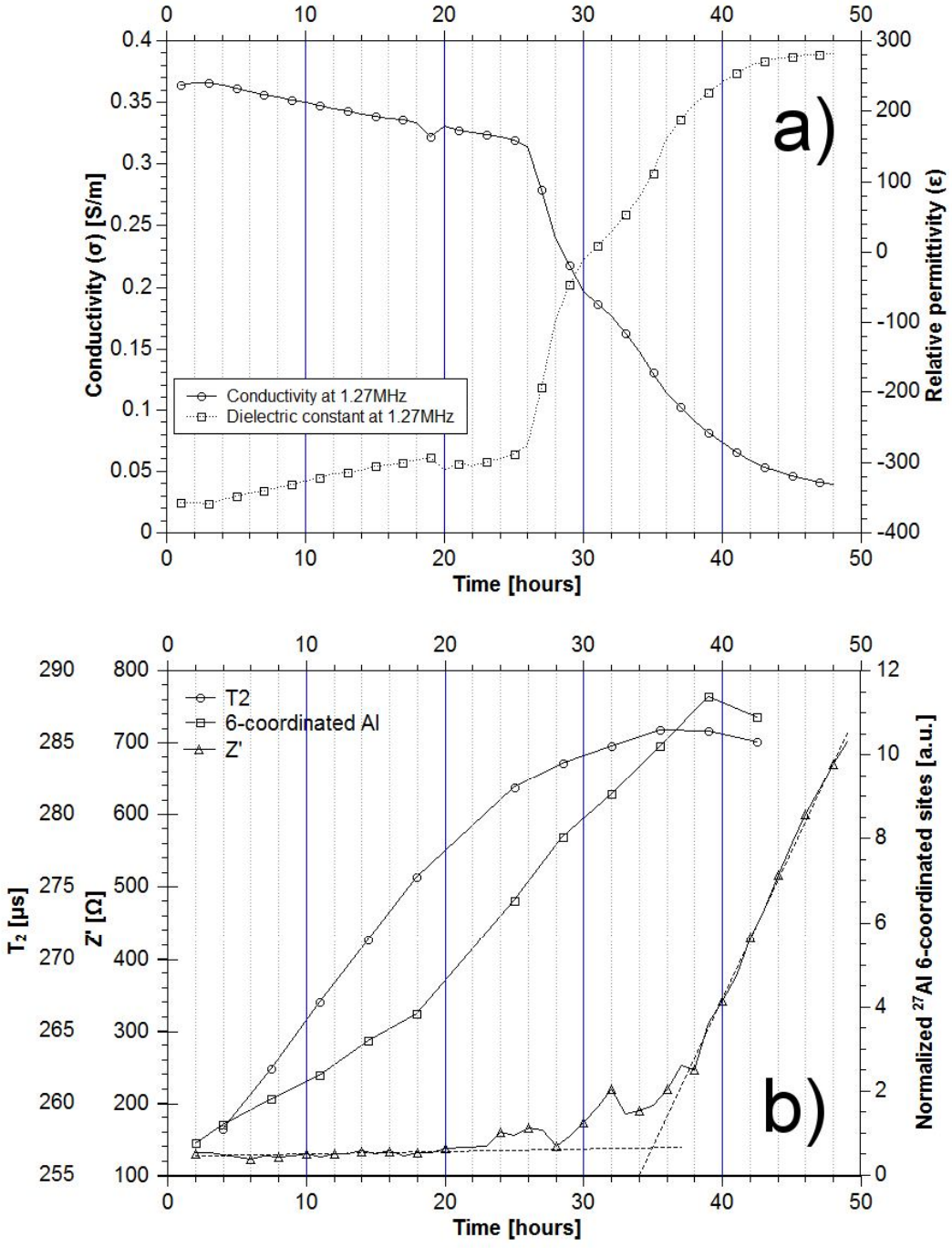

Figure 7.14.: a) Changes in conductivity and dielectric constant during the first 48 hours of the test at 30ºC temperature. Measurement were taken at 1.27MHz frequency; b) Comparison of the T_2 relaxation time, ^{27}Al MAS NMR spectrum and Z' EIS spectrum during the first 42.5 hours test.

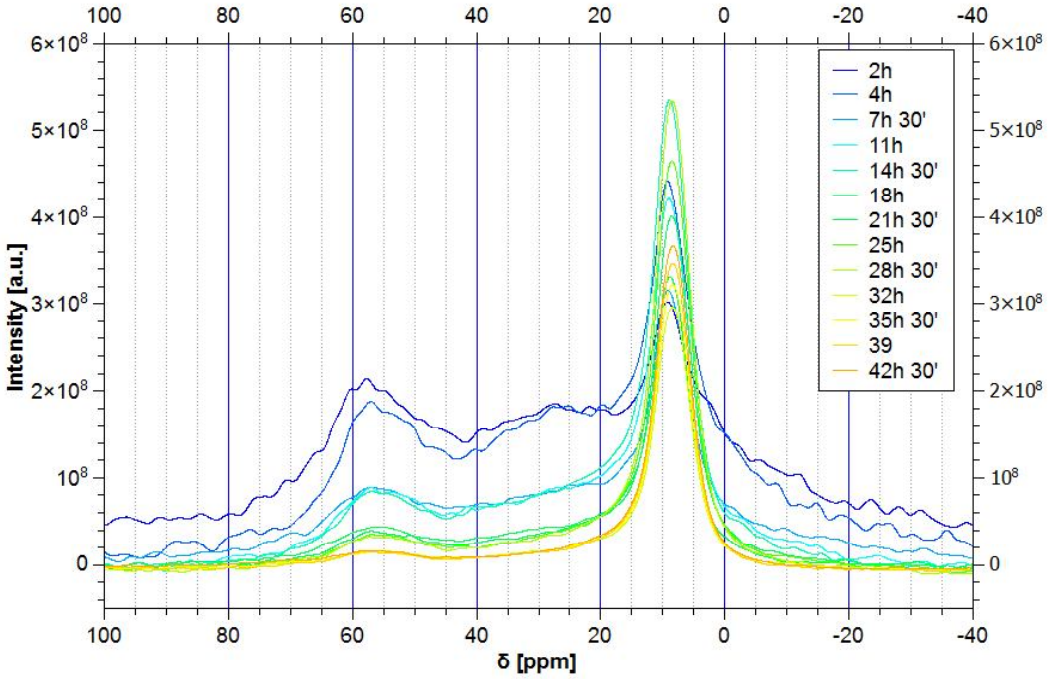

Figure 7.15.: ^{27}Al NMR spectra of MK mixed with lime over a period of time of 42h and 30 minutes at 30ºC temperature.

recognizable as well as two smaller peaks at 84.8 and 89.6 ppm. Despite the fact that in some cases these peaks could be considered noise, for some authors, the first peak can also be attributed to Q_0 sites (isolated tetrahedra; Cong and Kirkpatrick, 1996, p.142, Frias et al., 2013, p.2306) while the last two peaks can be attributed to the Q_2 (84.8 ppm) or Q_3 (89.6 ppm) units formation. Liu and colleagues highlight that chemical shifts in the range -85 to -90 in the ^{29}Si MAS NMR spectra correspond to Si with one nearest Al neighbour (Liu et al., 2001, p.90) while the peak at 84.8 corresponds to CSH gel that, according to other researchers, is the first hydrated phase formed in this type of mix (Frias et al., 2013, p.2308; Cong and Kirkpatrick, 1996, p.134).

T_2 spectrum Figure 7.14b also shows the relaxation time T_2 as a function of cure time. Contrary to observations by other researchers for cement based mixtures, the T_2 time in MK-lime pastes shows an initial regular increase that reaches a maximum at about 35 hours. Comparison of these data with the increase in 6-coordinated Al and with the changes of the real part of the impedance over the time highlights a correspondence among the data that suggests that EIS is able to detect specific chemical changes within the paste useful for monitoring the hardening process of lime-MK mixtures.

7.5. Discussion

Despite the fact that spins >1/2 (quadrupolar nuclei) give asymmetric lines even if the material is very ordered[4] the broad and asymmetrical shape of the NMR signal of ^{27}Al produced by the MK used for the mixes (figure 7.3), can be considered as suggesting of the existence of a disordered structure (Frias et al., 2013; Rocha and Klinowski, 1990a). According to the results of other researchers the reactivity of MK is greater when the population of 6-coordinated Al is minimal and the 4- and 5-coordinated Al populations are at a maximum (Frias et al., 2013; Edwards, 2009). In agreement with these data is also the ^{29}Si NMR spectrum of MK where a broad band representative of a range of environments, including some with at least an Al atom in the second coordination with Q_4 type Si bonds, is visible (figure 7.4; Frias et al., 2013, p.2308). All these data suggest that the MK used in the tests has lost its order along the axes perpendicular to the plates (ab plane) and, consequently, can be considered suitable for studying the hydraulic reactions with lime.

Results of thermo-gravimetric analysis suggest that all the samples contained a certain amount of water even after four weeks and that negligible carbonation had taken place. This observation is also supported by the absence of angular $CaCO_3$ crystals in the SEM micrograph. Consequently, the only reaction that can be considered as cause for the mechanical and physical characteristics acquired by the hardened samples at 20 and 25°C, is the hydration process of silicon and aluminium. The same process can be considered also for the sample at 30°C.

The results of thermal analysis highlight that at the end of the first week, all the hydraulic compounds already found by other researchers in similar mixes (CSH, C_2ASH_8, C_4AH_{13} and C_3ASH_6) were formed. The only difference between the tests at 20 and 25ºC is the amount of CSH produced at the end of the first week and the time needed to detect the reduction in the same compound. This difference can be explained by the temperature (higher in the second test) that accelerated the formation of CSH.

Among all the hydraulic compounds detected, CSH is the only one that reduces drastically after one/two weeks. C_2ASH_8, C_4AH_{13} and C_3ASH_6 grow substantially between the beginning and the end of the tests (although in the test at 20ºC C_4AH_{13} showed a decrease between the third and the forth week). Because C_3ASH_6 is detected after the end of the first week, it is difficult to determine if its formation is from metastable phases (Moropoulou et al., 2004; Cabrera and Rojas, 2001) or by direct reaction between lime and MK (Cabrera and Rojas, 2001, pp.180, 182) but in the test at 25ºC the increase in C_3ASH_6 corresponds to a decrease in CSH and this suggests that the transformation mechanism may have taken place.

[4]Depending on the local symmetry of the electronic cloud around the nuclei; in practice a lot of local disorder may result in more symmetrical lines because of distribution of local environments.

The near constant amount of $Ca(OH)_2$ detected over the four week monitoring period suggests that all the calcium needed for the reactions with the MK reacted during the first week. This is in agreement with the results of other researchers that found lime is consumed rapidly in the initial period of reaction (up to 50 hours in a 1:1 lime:MK ratio; Cabrera and Rojas, 2001, p.182).

Results of the MIP suggest that formation of metastable and stable hydraulic phases between the first and the second week (test at 20ºC) caused changes in the pore size distribution between 20 and 800 nm diameter. Changes between the first two weeks are also evident in the slope of the strain-stress curve. Increases in the maximum load, instead, does not seem to be influenced by CSH formation.

Formation of solid phases between the first and the second week is reflected by the conductivity and the relative permittivity that show a pronounced reduction in the measurements recorded during the second week. A reduction in freely rotational water molecules associated with the formation of the hydraulic phases is consistent with the results.

Considering the results of ^{29}Si MAS NMR, it is possible to deduce that during the first 8 hours of reaction, CSH (resonance at -84.8 ppm) and a compound containing Si and Al (resonance peak at -89.3 ppm, which is likely to be C_2ASH_8) are formed (Frias et al., 2013, p.2307). According to the results of Cong and Kirkpatric (Cong and Kirkpatrick, 1996, p.134) and to the phase diagram developed by Damidot and Glasser for the CaO–Al_2O_3–SiO_2–H_2O system (Damidot and Glasser, 1995, p.26), the CSH formed in these experiments is likely to be CSH(I) with a tobermorite-like structure.

Within the same first 8 hours, another part of the Si contained in the original MK dissolved to form Q_0 tetrahedra (peak at -71.5 ppm) and the rest of the MK remained within a short distance order as documented by the broad resonance peak around 100 ppm and by the MK plates still visible at the end of the first week in the SEM image (figure 7.9).

Looking in detail at the initial stages of the reaction, it is possible to deduce that results of the ^{27}Al MAS NMR analysis show an increase in the 6-coordinated Al peak during the first 42 hours, that can be interpreted as formation of the metastable phase C_4AH_{13} and, as previously noted, of C_3ASH_6. According to Cabrera and Rojas formation of C_4AH_{13} can be promoted by the presence of a supersaturated aqueous solution of $Ca(OH)_2$ in particular during the early stages of hydration. High concentrations of Ca^{2+} and OH^- in the pore solution (i.e. a very alkaline pH) maintain a pore fluid composition that allows precipitation of C_4AH_{13} (Cabrera and Rojas, 2001, p.180).

The normalized plot of the 6-coordinated Al sites (figure 7.14b) demonstrate that formation of hydraulic compounds with the capture of ions from the solution to the solid phases, starts at the very beginning of the test. Furthermore, at about 18 hours the formation of 6-coordinated Al sites starts to increase, reaching a maximum (or a

relative maximum) at about 39 hours.

Interestingly, at the same time, the T_2 relaxation time (figure 7.14b) increases due to the dissolution of $Ca(OH)_2$ promoted by the capture of Ca^{2+} ions in the newly formed solid phases. The increase in the relaxation time is regular until around 36 hours, when it starts to decrease or stabilize. At this time all the Ca^{2+} needed for the formation of hydraulic compounds seems to be acquired and it is likely that from this time on no more ions are introduced in the solution. Consequently, starting from 18 hours from the initial mix, the collisions and/or interactions of water molecules with pore walls control the relaxation time according to the results already found by other researchers for cement based materials (Beyea et al., 1998, p.454). It is possible that until about 18 hours T_2 is determined by other processes and, then, when the pores reach a certain size the interaction with inner surfaces determines T_2 and the gradient of the curve (derivative) decreases.

The increase of 6-coordinated Al sites being coincidental with a decrease of the relaxation time suggests that the decrease in the relaxation time can only be partially due to the formation of hydrated compounds containing aluminum. Formation of CSH could be the other reason for the T_2 reduction.

The results of the EIS bulk resistance measurements (figure 7.14b) show that the end of the initial stability coincides with the increase in the 6-coordinated Al sites and with the decrease in the T_2 relaxation time. The plot of conductivity and relative permittivity highlights this time by a relative minimum (conductivity) and maximum (dielectric constant; figure 7.14a). The maximum in the T_2 curve coincides with the theoretical change in gradient of the bulk resistance curve. Overall, the results suggest that the bulk measurement obtained with the EIS method is able to detect the end of the dissolution of $Ca(OH)_2$ by measuring the effect of the reduction in the amount of OH^- ions introduced in the solution by the dissolution process.

7.6. Conclusions

The research has demonstrated the potential of EIS as a non-destructive technique for real time *in situ* monitoring and study of the the reaction between lime and MK.

Changes of impedance response with time are shown to be associated with reaction kinetics. Changes in bulk measurements at the very beginning of the tests have been associated with the end of $Ca(OH)_2$ dissolution. Changes in conductivity and relative permittivity over a longer period of time (1-2 weeks) have been demonstrated to be related to the formation of hydraulic compounds that are likely to be the cause of porosity reduction.

The research has also demonstrated the importance of NMR spectroscopy for the study of hydraulic reactions in lime based materials and, in particular, the importance

of ^{1}H-NMR that can provides a detailed insight in the moisture changes in lime based building materials. ^{27}Al NMR spectra have proved to be relevant to the study of the formulated hydraulic limes (when the hydraulic additives contain aluminium are used).

8. Conclusions

This research has provided (chapters 2 and 3) a detailed insight into the chemistry and reaction mechanism of carbonation and has demonstrated the complexity of this process, which is very sensitive to the conditions under which it takes place. Carbonation is the only reaction common to all types of lime based materials used by the construction industry, from the simplest calcium lime to the most complex mixtures of natural hydraulic lime and hydraulic additives containing silica and alumina. Carbonation can be influenced by a large number of different factors such as presence of foreign ions and evaporation rate of water and can be in competition with other reactions such as formation of hydraulic compounds when hydraulic additives are present in the lime.

Formation of metastable phases such as ikaite with high molar volume is suggested to be the main limiting factor at the very beginning of this chemical process whereas, later, the main limiting factor is suggested to be the carbonate ion dissociation, dependent on the partial pressure of carbon dioxide and on pH.

The innovative approach to pH measurements in building materials introduced by this research in chapter 5 demonstrated the reliability and precision of Pd-hydride micro-electrodes. Within this study, in particular:

- the nano-structured Pd-hydride electrodes were successfully employed to precisely monitor the pH changes during the carbonation in porous media.

- The pH detected *in situ* was always found to be in good agreement with the theoretical calculations and the electrode response proved to be so sensitive and reproducible to differentiate, on the basis of pH, between the formation of calcite and vaterite.

- PHREEQC has proved to be a powerful tool that can be successfully used in the study of lime based building materials.

- Calculations made with PHREEQC were in very good agreement with the experimental results and to our knowledge this is the first time that this type of test has been successfully carried out for construction materials.

Overall it is possible to state that this type of pH electrode is currently the only analytical tool capable of monitoring reliably high pHs in confined spaces and, for this reason, they can be considered highly valuable for the study of chemical processes involving very alkaline waters and for monitoring electrochemical processes in building materials.

The role of pore size on the solid phases formed by carbonation of lime was proved to be relevant not only to the mineralogical characteristics of calcium carbonate but also to the general performances of lime used in the construction industry.

Use of nano-lime discussed in chapter 6, in particular, has proved that this is a material that brings a host of benefits when compared to other consolidation methods currently available. The ability to deliver a high quantity of lime into a stone without the dangers of inadvertently mobilising soluble salts is particularly appealing. However, little research has been carried out to date to verify short and long term performance on weathered stones historically used in the United Kingdom.

The studies described in this thesis allow the following conclusions to be drawn:

- changes in the characteristics of stones attributed to weathering can substantially modify physical properties such as porosity and in turn the effect of the consolidation treatment.
- Different stones weather in different manners even if they belong to the same type (e.g. limestone). As a consequence, if treatments with nano-lime have to be applied on stones that were never treated with this consolidant before, tests should be carried out in order to verify the effects of treatment, even if other similar stones were previously treated successfully .
- Insufficient penetration inside the stones was found to be a performance limiting factor.
- Decreases in drilling resistance over time for nano-lime treated stones was found to be consistent and are postulated to be due to the initial formation of metastable phases that over the time re-precipitate forming more stable compounds.
- the DRMS proved to be a useful tool for the on site and laboratory based experiments on the aplications of nanolime as a consolidant.

Studies of the influence of pore-water on the hardening process of lime described in chapter 7 has widely proved the possibilities of using the electrochemical impedance spectroscopy as a non-destructive technique for real time *in situ* monitoring and study of the hydraulic reaction in lime based building materials. In this research, in particular:

- for the first time a dramatic increase in real impedance at the beginning of the reaction was found and studied using EIS results obtained for lime-metakaolin mixes.
- change in IS bulk measurements at the very beginning of the reaction between lime and metakaolin has been proved to be associated with the end of $Ca(OH)_2$ uptake from the silicate and aluminate phases.
- Changes of impedance response with time are shown to be associated with reaction kinetics.
- Changes in conductivity and relative permittivity over a longer period of time have been demonstrated to be related to the formation of hydraulic compounds that are considered the cause of a reduction in porosity.

The research has also demonstrated the importance of NMR spectroscopy for the study of hydraulic reactions in lime based materials and, in particular:

- the importance of ^{1}H NMR spectroscopy for monitoring moisture changes in building materials. To our knowledge this is the first time that this technique has been used in lime based materials, highlighting the different behaviour compared to cement.
- the importance of ^{27}Al NMR spectra for studying the formation of hydraulic compounds in lime-metakaolin mixes.

In this respect, it is important to highlight that in this thesis for the first time a combined EIS/NMR study was carried out and proved to provide useful information in the investigation of formulated lime.

Overall, this thesis has demonstrated that the on site non-destructive monitoring of hardening process of lime is actually possible. In particular, this research has demonstrated that it is possible to precisely measure the pH and the amount of water (two of the most important parameters) during the hardening process of lime mixtures daily used on building sites.

This result can lead in a relatively short time, to the design and development of reasonably inexpensive small devices that can be embedded in lime and cement mortars for the continuous monitoring of these two parameters. These devices could be connected to small external analyzer for collecting and recording data when requested. The data can be used for a number of purposes such as the early identification of defects or possible errors in the hardening process of mortars, the evaluation of the safety of the construction work or, again, in legal disputes if conflicts between builders and the clients arise.

8.1. Future work

One of the most important key points in the study of the carbonation mechanism and process in the next a few years will be the study of layers formed on the surface of $Ca(OH)_2$ particles before the formation of $CaCO_3$ solid phases.

Following this, a more detailed insight into the factors affecting the formation of metastable phases will be necessary to understand and improve the first steps of the whole process. It is likely that, by controlling the formation of metastable phases with the production of minerals with the smaller molar volume, it will be possible to favour dissolution of a higher amount of calcium hydroxide from the beginning of the reaction with a consequential increase in the amount of calcium carbonate produced.

The set up used for monitoring the pH with Pd-H micro-electrodes during carbonation, can be developed in order to study the reaction kinetics. The latest results obtained, in fact, suggest that this target is achievable but in order to do this a new gas system more responsive to the gas changes is required.

The same system can also be used to study the effect of different ions such as magnesium and silicon on the carbonation process and in a similar manner, different solutions produced from commercially available limes can be tested to investigate the effect of other impurities on the precipitation of calcium carbonate.

Regarding the nano-lime, more research is needed to investigate the role of pore size and humidity of the stones on the carbonation reaction. In a similar manner, the role of atmospheric conditions (in particular temperature, wind speed and RH) on the carbonation process of these nano sized crystals could be investigated as well as the role of water content in the nano-lime suspension that can have an effect on the crystal size and shape and, consequently, on the effect of treatments.

EIS tests should be carried out on high calcium lime (overcoming the shrinkage problem that lead to the electrode detachment from the mortar) in order to acquire the typical response of carbonation to EIS perturbation and, then, the results of all reactions should be studied in a mix where both, hydration and carbonation take place.

Development of the smart devices previously mentioned should be pursued in order to provide the construction industry with tools that suit a modern construction industry.

References

Abdel-Aal, N., Satoh, K., Sawada, K., Nov. 2002. Study of the adhesion mechanism of $CaCO_3$ using a combined bulk chemistry/qcm technique. Journal of Crystal Growth 245 (1-2), 87–100.
URL http://www.sciencedirect.com/science/article/pii/S0022024802016573

Adam, J.-P., 1999. Roman building: materials and techniques. Routledge.

Aggelakopoulou, E., Bakolas, A., Moropoulou, A., 2011. Properties of lime-metakolin mortars for the restoration of historic masonries. Applied Clay Science 53 (1), 15–19.
URL http://www.sciencedirect.com/science/article/pii/S0169131711001372

Allen, G., Allen, J., Elton, N., Farey, M., Holmes, S., Livesey, P., Radonjic, M., 2003. Hydraulic lime mortar for stone, brick and block masonry: A best practice guide. Donhead.

Almond, D. P., Bowen, C. R., 2004. Anomalous power law dispersions in ac conductivity and permittivity shown to be characteristics of microstructural electrical networks. Phys. Rev. Lett. 92, 157601.

Altay, E., Shahwan, T., Tanoglu, M., 2007. Morphosynthesis of $CaCO_3$ at different reaction temperatures and the effects of PDDA, CTAB, and EDTA on the particle morphology and polymorph stability. Powder Technology 178 (3), 194–202.
URL http://www.sciencedirect.com/science/article/pii/S0032591007002513

Ambrosi, M., Dei, L., Giorgi, R., Neto, C., Baglioni, P., 2001. Stable dispersions of $Ca(OH)_2$ in aliphatic alcohols: properties and application in cultural heritage conservation. In: Koutsoukos, P. (Ed.), Trends in Colloid and Interface Science XV. Vol. 118 of Progress in Colloid and Polymer Science. Springer Berlin Heidelberg, pp. 68–72.

Andersen, M. D., Jakobsen, H. J., Skibsted, J., 2003. Incorporation of aluminum in the calcium silicate hydrate (C-S-H) of hydrated portland cements: A high-fieldield

^{27}Al and ^{29}Si mas nmr investigation. Inorganic Chemistry 42 (7), 2280–2287, pMID: 12665361.

Andreassen, J.-P., Jan. 2005. Formation mechanism and morphology in precipitation of vaterite–nano-aggregation or crystal growth? Journal of Crystal Growth 274 (1-2), 256–264.
URL http://www.sciencedirect.com/science/article/pii/S0022024804012345

Andreassen, J.-P., Beck, R., Nergaard, M., 2012. Biomimetic type morphologies of calcium carbonate grown in absence of additives. Faraday Discuss. 159, 247–261.

Apih, T., Lahajnar, G., Sepe, A., Blinc, R., Milia, F., Cvelbar, R., Emri, I., Gusev, B., Titova, L., 2001. Proton spin-lattice relaxation study of the hydration of self-stressed expansive cement. Cement and Concrete Research 31 (2), 263–269.
URL http://www.sciencedirect.com/science/article/pii/S0008884600004609

Appelo, C. A. J., D., P., 2005. Geochemistry, groundwater and pollution. Taylor & Francis.

Arandigoyen, M., Bicer-Simsir, B., Alvarez, J., Lange, D., 2006. Variation of microstructure with carbonation in lime and blended pastes. Applied Surface Science 252 (20), 7562–7571.
URL http://www.sciencedirect.com/science/article/pii/S0169433205012705

Arcolao, C., 1998. Le ricette del restauro. Malte, intonaci, stucchi dal XV al XIX secolo.

Arizzi, A., Cultrone, G., 2014. The water transfer properties and drying shrinkage of aerial lime-based mortars: an assessment of their quality as repair rendering materials. Environmental Earth Sciences 71 (4), 1699–1710.

ASTM Standard, 2011. Standard test method for determining relative humidity in concrete floor slabs using in situ probes.

Attard, G. S., Bartlett, P. N., Coleman, N. R. B., Elliott, J. M., Owen, J. R., Wang, J. H., Oct. 1997. Mesoporous platinum films from lyotropic liquid crystalline phases. Science 278 (5339), 838–849.

Atzeni, C., Farci, A., Floris, D., Meloni, P., 2004. Effect of aging on rheological properties of lime putty. Journal of American Ceramic Society 87 (9), 1764–1766.

Baglioni, P., Dei, L., Fratoni, L., Lo Nosotro, P., Moroni, M., 2005. Process for the preparation of nano-and micro-particles of group ii and transition metals oxides and hydroxides, the nano-and micro-particles thus obtained and their use in the ceramic, textile and paper industries.

Baglioni, P., Giorgi, R., 2006. Soft and hard nanomaterials for restoration and conservation of cultural heritage. Soft Matter 2, 293–303.

Bakolas, A., Aggelakopoulou, E., Moropoulou, A., Anagnostopoulou, S., 2006. Evaluation of pozzolanic activity and physicomechanical characteristics in metakaolin-lime pastes. Journal of Thermal Analysis and Calorimetry 84 (1), 157–163.

Bakolas, A., Biscontin, G., Moropoulou, A., Zendri, E., 1995. Characterization of the lumps in the mortars of historic masonry. Thermochimica Acta 269270 (0), 809–816, recent Advances in Thermal Analysis and Calorimetry.
URL http://www.sciencedirect.com/science/article/pii/0040603195025731

Ball, R., Allen, G., 2010. The measurement of water transport in porous materials using impedance spectroscopy. Journal of Physics D: Applied Physics 43 (10), 105503.
URL http://stacks.iop.org/0022-3727/43/i=10/a=105503

Ball, R., Allen, G., Carter, M., Wilson, M., Ince, C., El-Turki, A., 2012a. The application of electrical resistance measurements to water transport in lime-masonry systems. Applied Physics A 106 (3), 669–677.

Ball, R., Allen, G., Starrs, G., McCarter, W., 2011. Impedance spectroscopy measurements to study physio-chemical processes in lime-based composites. Applied Physics A 105 (3), 739–751.

Ball, R., Pesce, G., Bowen, C. R., Allen, G., 2012b. Characterisation of lime/metakaolin paste using impedance spectroscopy. In: Xiao, Y., Li, Z., Wang, R., Shan, B., Ghavami, K. (Eds.), Novel and Non-Conventional Materials and Technologies for Sustainability. Vol. Key Engineering Materials. pp. 487–494.

Baronio, G., Binda, L., Lombardini, N., 1997. The role of brick pebbles and dust in conglomerates based on hydrated lime and crushed bricks. Construction and Building Materials 11 (1), 33–40.
URL http://www.sciencedirect.com/science/article/pii/S0950061896000311

Bartlett, P. N., Gollas, B., Guerin, S., Marwan, J., 2002. The preparation and characterisation of H^{1-e} palladium films with a regular hexagonal nanostructure formed

by electrochemical deposition from lyotropic liquid crystalline phases. Phys. Chem. Chem. Phys. 4, 3835–3842.

Bates, R. G., Bower, V. E., Canham, R. G., Prue, J. E., 1959. The dissociation constant of $CaOH^+$ from 0 to 40^oC. Trans. Faraday Soc. 55, 2062–2068.

Benavente, D., del Cura, M. G., Ordonez, S., 2003. Salt influence on evaporation from porous building rocks. Construction and Building Materials 17 (2), 113–122.
URL http://www.sciencedirect.com/science/article/pii/S0950061802001009

Berger, R., 1992. ^{14}C dating mortar in ireland. Radiocarbon 34 (3), 880–889.

Bertolini, L., Elsener, B., P. P., Redaelli, E., R.B., P., 2013. Corrosion of steel in concrete. Prevention, diagnosis, repair., 2nd Edition. Wiley-VCN Verlag GmbH and Co.

Beruto, D. T., Barberis, F., Botter, R., 2005. Calcium carbonate binding mechanisms in the setting of calcium and calcium-magnesium putty-limes. Journal of Cultural Heritage 6 (3), 253–260.

Beruto, D. T., Botter, R., Apr. 2000. Liquid-like H_2O adsorption layers to catalyze the $Ca(OH)_2/CO_2$ solid-gas reaction and to form a non-protective solid product layer at 20^oC. Journal of the European Ceramic Society 20 (4), 497–503.
URL http://www.sciencedirect.com/science/article/pii/S0955221999001855

Beyea, S., Balcom, B., Bremner, T., Prado, P., Green, D., Armstrong, R., Grattan-Bellew, P., 1998. Magnetic resonance imaging and moisture content profiles of drying concrete. Cement and Concrete Research 28 (3), 453–463.
URL http://www.sciencedirect.com/science/article/pii/S000888469800009X

Bischoff, J. L., Fitzpatrick, J. A., Rosenbauer, R. J., Jan. 1993. The solubility and stabilization of ikaite from 0 to 25^oC: Environmental and paleoclimatic implications for thinolite tufa. The Journal of Geology 101 (1), 21–33.

Blanc, P., Bourbon, X., Lassin, A., Gaucher, E., 2010. Chemical model for cement-based materials: Thermodynamic data assessment for phases other than C-S-H. Cement and Concrete Research 40 (9), 1360–1374.
URL http://www.sciencedirect.com/science/article/pii/S0008884610001031

Blandamer, M. J., Engberts, J. B. F. N., Gleeson, P. T., Reis, J. C. R., 2005. Activity of water in aqueous systems. a frequently neglected property. Chem. Soc. Rev. 34, 440–458.

Boguszynska, J., Brown, M. C., McDonald, P. J., Mitchell, J., Mulheron, M., Tritt-Goc, J., Verganelakis, D. A., 2005. Magnetic resonance studies of cement based materials in inhomogeneous magnetic fields. Cement and Concrete Research 35 (10), 2033–2040.
URL http://www.sciencedirect.com/science/article/pii/S0008884605001742

Bowman, S., 1990. Radiocarbon dating. University of California Press/British Museum.

Boynton, R. S., 1966. Chemistry and technology of lime and limestone, 1st Edition. Wiley and Sons.

Brecevic, L., Kralj, D., 2007. On calcium carbonates: from fundamental research to application. Croatica Chemica Acta 80 (3-4), 467–484.

British Lime Association, 2013. Lime. the versatile mineral that supports our vital industries. Tech. rep., British Lime Association.
URL http://www.britishlime.org/documents/BLA-Lime-the-versatile-material-021013.pdf

Brooks, R., Clark, L. M., Thurston, E. F., December 1950. Calcium carbonate and its hydrates. Philosophical Transactions of the Royal Society of London. Series A, Mathematical and Physical Sciences 243 (861), 145–167.

Brown, P., Doerr, A., 2000. Chemical changes in concrete due to the ingress of aggressive species. Cement and Concrete Research 30 (3), 411–418.
URL http://www.sciencedirect.com/science/article/pii/S0008884699002665

Brown, T., Highley, D., Lusty, P., Cameron, D., Bate, R., Rayner, D., February 2008. Cement. Facsheet, Brisith Geological Survey.

Bruni, S., Cariati, F., Fermo, P., Cariati, P., G., A., L., T., 1997. White lumps in fifth to seventeenth century ad mortars from northern Italy. Archaeometry 39 (1), 1–7.

BS EN 459-1, 2010. Building lime. part 1: Definition, specifications and conformity criteria.

Bugini, R., Toniolo, L., 1990. La presenza di grumi bianchi nelle malte antiche: ipotesi sull'origine. Arkos Notizie GOR 12, 4–8.

Cabrera, J., Rojas, M. F., 2001. Mechanism of hydration of the metakaolin-lime-water system. Cement and Concrete Research 31 (2), 177–182.
URL http://www.sciencedirect.com/science/article/pii/S0008884600004567

Callebaut, K., Elsen, J., Balen, K. V., Viaene, W., 2001. Nineteenth century hydraulic restoration mortars in the Saint Michael's church (Leuven, Belgium): natural hydraulic lime or cement? Cement and Concrete Research 31 (3), 397–403.
URL http://www.sciencedirect.com/science/article/pii/S0008884600004993

Cano-Barrita, P. d. J., Marble, A., Balcom, B., Garcia, J., Masthikin, I., Thomas, M., Bremner, T., 2009. Embedded nmr sensors to monitor evaporable water loss caused by hydration and drying in portland cement mortar. Cement and Concrete Research 39 (4), 324–328.
URL http://www.sciencedirect.com/science/article/pii/S0008884609000210

Carmona, J. G., Morales, J. G., Sainz, J. F., Loste, E., Clemente, R. R., 2004. The mechanism of precipitation of chain-like calcite. Journal of Crystal Growth 262 (1-4), 479–489.
URL http://www.sciencedirect.com/science/article/pii/S0022024803018645

Cazalla, O., Rodriguez-Navarro, C., Sebastian, E., Cultrone, G., 2000. Agin of lime putty: Effect on traditional lime mortar carbonation. Journal of American Ceramic Society 83 (5), 1070–1076.

CEDAD, 2011. Sample preparation for AMS radiocarbon dating. Internet site of CEDAD.
URL http://cedad.unisalento.it/en/clams.php

Chemical Rubber Company, 2013-2014. CRC handbook of chemistry and physics, 94th Edition. Taylor & Francis.

Chen, J., Xiang, L., 2009. Controllable synthesis of calcium carbonate polymorphs at different temperatures. Powder Technology 189 (1), 64–69.

Chen, J. J., Thomas, J. J., Taylor, H. F., Jennings, H. M., 2004. Solubility and structure of calcium silicate hydrate. Cement and Concrete Research 34 (9), 1499–1519, h. F. W. Taylor Commemorative Issue.
URL http://www.sciencedirect.com/science/article/pii/S000888460400211X

Chen, T., Neville, A., Yuan, M., 2005. Assessing the effect of Mg^{2+} on $CaCO_3$ scale formation-bulk precipitation and surface deposition. Journal of Crystal Growth 275 (1-2), e1341–e1347.
URL http://www.sciencedirect.com/science/article/pii/S0022024804016616

Chervonnyi, A., Chervonnaya, N., Chukanov, N., 2003. Effect of $CaCO_3$ polymorphs on the strength of a calcium aluminosilicate composite. Inorganic Materials 39 (4), 386–391.

Cizer, O., 2009. Competition between carbonation and hydration on the hardening of calcium hydroxide and calcium silicate binders. Phd thesis, Catholic University of Leuven.

Cizer, O., Rodriguez-Navarro, C., Ruiz-Agudo, E., Elsen, J., Gemert, D., Balen, K., 2012a. Phase and morphology evolution of calcium carbonate precipitated by carbonation of hydrated lime. Journal of Materials Science 47 (16), 6151–6165.

Cizer, O., Van Balen, K., Elsen, J., Van Gemert, D., Oct. 2012b. Real-time investigation of reaction rate and mineral phase modifications of lime carbonation. Construction and Building Materials 35 (0), 741–751.
URL http://www.sciencedirect.com/science/article/pii/S0950061812002383

Clarkson, J. R., Price, T. J., Adams, C. J., 1992. Role of metastable phases in the spontaneous precipitation of calcium carbonate. J. Chem. Soc., Faraday Trans. 88, 243–249.

Cogger, N., Evans, N., 1998. An introduction to electrochemical impedance measurement. Technical Report 006, ed. Solartron.
URL http://www.korozja.pl/html/eis/technote06.pdf

Cong, X., Kirkpatrick, R., 1996. ^{29}Si and ^{17}O nmr investigation of the structure of some crystalline calcium silicate hydrates. Advanced Cement Based Materials 3 (3-4), 133–143.
URL http://www.sciencedirect.com/science/article/pii/S1065735596900450

Cook, E. R., Batchelor, B., 1996. Chapter 4 - stabilization/solidification of hazardous wastes in soil matrices. Vol. 3 of Advances in Porous Media. Elsevier, pp. 307–359.
URL http://www.sciencedirect.com/science/article/pii/S1873975X96800060

Coutelas, A., Godard, G., Blanc, P., Person, A., 2004. Les mortiers hydrauliques: synthèse bibliographique et premiers rèsultats sur les mortiers de gaule romaine. Revue d'Archèomètrie, 127–139.

Craig, P., G., D., 2006. Moisture testing of concrete slabs. when 3 lbs is not 3 lbs. Concrete International, 23.27.

CTS Europe, 2008. Nanorestore. dispersione di nanocalce in alcool isopropilico denaturato. brevetto italiano consorzio csgi-universita' degli studi di firenze.

Damidot, D., Glasser, F., 1995. Investigation of the CaO-Al_2O_3-SiO_2-H_2O system at 25^oC by thermodynamic calculations. Cement and Concrete Research 25 (1), 22–28.
URL http://www.sciencedirect.com/science/article/pii/000888469400108B

Daniele, V., Taglieri, G., 2010. Nanolime suspensions applied on natural lithotypes: The influence of concentration and residual water content on carbonatation process and on treatment effectiveness. Journal of Cultural Heritage 11 (1), 102–106.
URL http://www.sciencedirect.com/science/article/pii/S1296207409000946

Daniele, V., Taglieri, G., 2012. Synthesis of $Ca(OH)_2$ nanoparticles with the addition of triton x-100. protective treatments on natural stones: Preliminary results. Journal of Cultural Heritage 13 (1), 40–46.
URL http://www.sciencedirect.com/science/article/pii/S1296207411000562

Daniele, V., Taglieri, G., Quaresima, R., 2008. The nanolimes in cultural heritage conservation: Characterisation and analysis of the carbonatation process. Journal of Cultural Heritage 9 (3), 294–301.
URL http://www.sciencedirect.com/science/article/pii/S1296207408000538

Datta, N., Chatterji, S., , Jeffrey, J. W., Mackay, A. L., June 1969. On the oriented transformation of Ca(OH) to CaO. Mineralogical Magazine 37 (286), 250–252.

De Silva, P., Bucea, L., Moorehead, D., Sirivivatnanon, V., Aug. 2006. Carbonate binders: reaction kinetics, strength and microstructure. Cement and Concrete Composites 28 (7), 613–620.
URL http://www.sciencedirect.com/science/article/pii/S0958946506000527

Delgado Rodriguez, J., Ferreira Pinto, A., Rodrigues da Costa, D., 2002. Tracing of decay profiles and evaluation of stones tratments by means of microdrilling techniques. Journal of Cultural Heritage 3 (3), 117–125.

Denuault, G., 2007. Instrumental methods in electrochemistry. complex impedance i and ii., slides of the lectures. Southampton Electrochemistry Group, unpublished.

Dheilly, R., Tudo, J., Sebaibi, Y., Queneudec, M., 2002. Influence of storage conditions on the carbonation of powdered $Ca(OH)_2$. Construction and Building Materials 16 (3), 155–161.
URL http://www.sciencedirect.com/science/article/pii/S0950061802000120

Dickinson, S. R., Henderson, G., McGrath, K., Oct. 2002. Controlling the kinetic versus thermodynamic crystallisation of calcium carbonate. Journal of Crystal Growth 244 (3-4), 369–378.
URL http://www.sciencedirect.com/science/article/pii/S0022024802017001

Domingo, C., Garcia-Carmona, J., Loste, E., Fanovich, A., Fraile, J., Gomez-Morales, J., Oct. 2004. Control of calcium carbonate morphology by precipitation in compressed and supercritical carbon dioxide media. Journal of Crystal Growth 271 (1-2), 268–273.
URL http://www.sciencedirect.com/science/article/pii/S0022024804009054

Donatello, S., Tyrer, M., Cheeseman, C., 2010. Comparison of test methods to assess pozzolanic activity. Cement and Concrete Composites 32 (2), 121–127.
URL http://www.sciencedirect.com/science/article/pii/S0958946509001644

Dutkiewicz, E., Jakubowska, A., 2002. Water activity in aqueous solutions of homogeneous electrolytes. the effect of ions on the structure of water. ChemPhysChem 3 (2), 221–224.

Edwards, D., 2009. Sustainable lime mortars. Ph.D. thesis, Interface Analysis Centre, University of Bristol.

El-Turki, A., Ball, R., Allen, G., 2007. The influence of relative humidity on structural and chemical changes during carbonation of hydraulic lime. Cement and Concrete Research 37 (8), 1233–1240.
URL http://www.sciencedirect.com/science/article/pii/S0008884607001196

El-Turki, A., Ball, R. J., Holmes, S., Allen, W. J., Allen, G. C., 2010. Environmental cycling and laboratory testing to evaluate the significance of moisture control for lime mortars. Construction and Building Materials 24 (8), 1392–1397.

Elakneswaran, Y., Iwasa, A., Nawa, T., Sato, T., Kurumisawa, K., 2010. Ion-cement hydrate interactions govern multi-ionic transport model for cementitious materials. Cement and Concrete Research 40 (12), 1756–1765.
URL http://www.sciencedirect.com/science/article/pii/S0008884610002048

Elsen, J., 2006. Microscopy of historic mortars: a review. Cement and Concrete Research 36 (8), 1416–1424, 10th EUROSEMINAR on microscopy applied to building materials, University of Paisley, June 21-25, 2005.
URL http://www.sciencedirect.com/science/article/pii/S0008884605003145

Elsen, J., Brutsaert, A., Deckers, M., Brulet, R., 2004. Microscopical study of ancient mortars from Turnay (Belgium). Materials Characterization 53, 289–294.

Euvrard, M., Membrey, F., Filiatre, C., Foissy, A., Apr. 2004. Crystallization of calcium carbonate at a solid/liquid interface examined by reflection of a laser beam. Journal of Crystal Growth 265 (1-2), 322–330.
URL http://www.sciencedirect.com/science/article/pii/S002202480400079X

Fieni, L., 2002. La basilica di San Lorenzo Maggiore a Milano tra etá tardoantica e medioevo: metodologie di indagine archeometrica per lo studio dell'elevato. Archeologia della Architettura 7, 51–98.

Folk, R., Valastro, S. J., 1976. Successful technique for dating of lime mortar by carbon-14. Journal of Field Archaeology 3, 203–208.

Franzini, M., Leoni, L., Lezzerini, M., Sartori, F., 1990. On the binder of some ancient mortars. Mineralogy and Petrology 67, 59–69.

Frias, M., Cabrera, J., 2000. Pore size distribution and degree of hydration of metakaolin-cement pastes. Cement and Concrete Research 30 (4), 561–569.
URL http://www.sciencedirect.com/science/article/pii/S0008884600002039

Frias, M., Martinez-Ramirez, S., Blasco, T., Rodriguez, M. F., 2013. Evolution of mineralogical phases by ^{27}Al and ^{29}Si NMR in $MK - Ca(OH)_2$ system cured at 60^oC. Journal of the American Ceramic Society 96 (7), 2306–2310.

Gabrielli, C., Maurin, G., Poindessous, G., Rosset, R., Apr. 1999. Nucleation and growth of calcium carbonate by an electrochemical scaling process. Journal of Crystal Growth 200 (1-2), 236–250.
URL http://www.sciencedirect.com/science/article/pii/S0022024898012615

Gallo, N., 2001. ^{14}C e archeologia del costruito: il caso di castello Aghinolfi (MS). Archeologia dellÁrchitettura 4, 31–36.

Gallo, N., Fieni, L., Martini, M., Sibilia, E., 6-10 Avril 1998. Archéologie du bati, ^{14}C et thermolumiscence: deux exemples en comparaison. In: Actes du 3eme Congrés International 14C et Archéologie. Lyon.

Garcia-Alonso, M., Escudero, M., Miranda, J., Vega, M., Capilla, F., Correia, M., Salta, M., Bennani, A., Gonzalez, J., 2007. Corrosion behaviour of new stainless steels reinforcing bars embedded in concrete. Cement and Concrete Research 37 (10), 1463–1471.
URL http://www.sciencedirect.com/science/article/pii/S0008884607001305

Garcia Carmona, J., Gomez Morales, J., Rodriquez Clemente, R., 2003. Rhombohedral-scalenohedral calcite transition produced by adjusting the solution electrical conductivity in the system $Ca(OH)_2$-CO_2-H_2O. Journal of Colloid and Interface Science 261 (2), 434–440.

Garrels, R. M., Christ, C. L., 1965. Solutions, minerals, and equilibria. Freeman, Cooper & Company.

Gauri, K. L., Bandyopadhyay, J. K., 1999. Carbonate stone: chemical behavior, durability, and conservation. Wiley, Chichester, iSBN: 978-0-471-17977-1.

Geddes, I., 2003. Hidden depths. Wiltshire's geology and landscape. Libris Press, Bradford-on-Avon, UK.

Ghaffari, E., Musiela, M., no date. Consolidation with CaLoSiL and combined systems to bind aggregates in laboratory made samples. assessment of their distribution by methods of SEM. Presentation at the stone conservation for the refurbishment of buildings project.

Giles, D., Ritchie, I., Xu, B.-A., 1993. The kinetics of dissolution of slaked lime. Hydrometallurgy 32 (1), 119–128.
URL http://www.sciencedirect.com/science/article/pii/0304386X9390061H

Giorgi, R., Dei, L., Ceccato, M., Schettino, C., P., B., 2002. Nanotechnologies for conservation of cultural heritage: paper and canvas deacidification. Langmuir 18, 8198–8203.

Giorgi, R., Dei, L., P., B., 2000. A new method for consolidating wall paintings based on dispersion of lime in alcohol. Study in Conservation (45), 154–161.

Gliozzo, E., Memmi Turbanti, I., Feb. 2006. La catodoluminescenza e l'analisi di immagine per lo studio delle malte. In: Proceedings of the IV Congresso Nazionale di Archeometria - Scienza e Beni Culturali. Pise.

Gomez-Morales, J., Torrent-Burgues, J., Lopez-Macipe, A., Rodriguez-Clemente, R., Sep. 1996. Precipitation of calcium carbonate from solutions with varying Ca^{2+}:carbonate ratios. Journal of Crystal Growth 166 (1-4), 1020–1026.
URL http://www.sciencedirect.com/science/article/pii/0022024896000838

Goren, Y., Goring-Morris, A., 2008. Early pyrotechnology in the near east: experimental lime-plaster production at the pre-pottery neolithic B site of Kfar HaHoresh, Israel. Geoarchaeology: An International Journal 23 (6), 779–798.

Greppi, P., 2013. La cattedrale di Alba. Archeologia di un cantiere dall'eta' paleocristiana al XV secolo. All'Insegna del Giglio, Ch. Murature medievali in laterizi dalla cattedrale di S. Lorenzo.

Griffiths, G., 2011. Single crystal deposition of portlandite. Phd thesis, University of Bristol.

Hale, J., Heinemeier, J., Lancaster, L., Lindroos, A., Ringbom, A., 2003. Dating ancient mortar. American Scientist 91, 130–137.

Han, Y. S., Hadiko, G., Fuji, M., Takahashi, M., Apr. 2005. Effect of flow rate and CO_2 content on the phase and morphology of $CaCO_3$ prepared by bubbling method. Journal of Crystal Growth 276 (3-4), 541–548.
URL http://www.sciencedirect.com/science/article/pii/S0022024804019165

Hansen, E. F., Tagle, A., Erder, E., Baron, S., Connell, S., Rodriguez-Navarro, Carlos andVan Balen, K., 1999. Effects of ageing on lime putty. In: Bartos, P., Groot, C., Hughes, J. J. (Eds.), International RILEM Workshop on Historic Mortars: Characteristics and Tests. RILEM Publications SARL, pp. 197–206.

Haslam, R., Calingaert, G., Taylor, C., 1924. The hydrates of lime. Journal of American Chemical Society (46), 308–311.

Heinemeier, J., Ringbom, A., Lindroos, A., Sveinbjornsdottir, A. E., 2010. Successful AMS ^{14}C dating of non-hydraulic lime mortars from the medieval chchurch of the Aland island, Finalnd. Radiocarbon 52 (1), 171–204.

Hewlett, P., 2004. Lea's Chemistry of Cement and Concrete. Elsevier.

Hornak, J. P., 2011. The basic of NMR. Internet site.
URL http://www.cis.rit.edu/htbooks/nmr/

Hou, W., Feng, Q., 2006. Morphology and formation mechanism of vaterite particles grown in glycine-containing aqueous solutions. Materials Science and Engineering: C 26 (4), 644–647, second Asian Symposium on Biomineralization (ASB-2).
URL http://www.sciencedirect.com/science/article/pii/S0928493105003449

Hughen, K., Baillie, M., Bard, E., Bayliss, A., Beck, J., Bertrand, C., Blackwell, P., Buck, C., Burr, G., Cutler, K., Damon, P., Edwards, R., Fairbanks, R., Friedrich, M., Guilderson, T., Kromer, B., McCormac, G., Manning, S., Bronk Ramsey, C., Reimer, P., Reimer, R., Remmele, S., Southon, J., Stuiver, M., Talamo, S., Taylor, F., van der Plicht, J., Weyhenmeyer, C., 2004. Marine04 marine radiocarbon age calibration, 0-26 cal kyr BP. Radiocarbon 46 (3), 1059–1086.

Hume, J., Topley, B., 1926. CCCXC -the density of calcium carbonate hexahydrate. J. Chem. Soc. 129, 2932–2934.
URL http://dx.doi.org/10.1039/JR9262902932

IBZ-Salzchemie GmbH, . C. K., no date. CaLoSiL - Colloidal nano-particles of lime for stone and plaster consolidation. Technical leaflet, IBZ-Salzchemie GmbH & Co. KG.
URL http://www.ibz-freiberg.de/download/pdf/nanomaterialien/CaLoSiL_EN.pdf

Imokawa, T., Williams, K.-J., Denuault, G., 2006. Fabrication and characterization of nanostructured Pd hydride pH microelectrodes. Analytical Chemistry 78 (1), 265–271.

Ince, C., Carter, M., Wilson, M., Collier, N., El-Turki, A., Ball, R., Allen, G., 2011. Factors affecting the water retaining characteristics of lime and cement mortars in the freshly-mixed state. Materials and Structures 44 (2), 509–516.

Ingham, J., Jun. 2005. Investigation of traditional lime mortars - the role of optical microscopy. In: Proceedings of the 10th Euroseminar on Microscopy Applied to Building Materials. Paisley, Glasgow, pp. 1–18.

Ives, D. J. G., Janz, G. J., 1961. Reference electrodes: theory and practice. Academic Press, New York-London.

Jacques, D., Wang, L., Martens, E., Mallants, D., 2010. Modelling chemical degradation of concrete during leaching with rain and soil water types. Cement and Concrete Research 40 (8), 1306–1313.
URL http://www.sciencedirect.com/science/article/pii/S0008884610000451

Johannsen, K., Rademacher, S., 1999. Modelling the kinetics of calcium hydroxide dissolution in water. Acta Hydrochimica Hydrobiologica 27 (2), 72–78.

Karatasios, I., Amenta, M., Tziotziou, M., Kilikoglou, V., 2010. The effect of relative humidity on the performance of lime-pozzolan mortars. In: VÃ¡lek, J., Groot, C., Hughes, J. (Eds.), 2nd Conference on Historic Mortars - HMC 2010 and RILEM TC 203-RHM final workshop. RILEM Publications SARL.

Karkanas, P., 2007. Identification of lime plaster in prehistory using petrographic methods: a review and reconsideration of the data on the basis of experimental and case studies. Geoarchaeology: An international journal 22 (7), 775–796.

Kawano, J., Shimobayashi, N., Kitamura, M., Shinoda, K., Aikawa, N., Apr. 2002. Formation process of calcium carbonate from highly supersaturated solution. Journal of Crystal Growth 237-239, Part 1 (0), 419–423.
URL http://www.sciencedirect.com/science/article/pii/S0022024801018668

Kawano, J., Shimobayashi, N., Miyake, A., Kitamura, M., 2009. Precipitation diagram of calcium carbonate polymorphs: its construction and significance. Journal of physics: condensed matter 21 (42), 425102–425108.

Khatib, J., Wild, S., 1996. Pore size distribution of metakaolin paste. Cement and Concrete Research 26 (10), 1545–1553.
URL http://www.sciencedirect.com/science/article/pii/0008884696001470

Kitamura, M., 2002. Controlling factor of polymorphism in crystallization process. Journal of Crystal Growth 237-239 (0), 2205–2214, the thirteenth international conference on Crystal Growth in conjunction with the eleventh international conference on Vapor Growth and Epitaxy.
URL http://www.sciencedirect.com/science/article/pii/S0022024801022771

Kitamura, M., Konno, H., Yasui, A., Masuoka, H., 2002. Controlling factors and mechanism of reactive crystallization of calcium carbonate polymorphs from calcium hydroxide suspensions. Journal of Crystal Growth 236 (1-3), 323–332.
URL http://www.sciencedirect.com/science/article/pii/S0022024801020826

Klein, R. T., Walter, L. M., Sep. 1995. Interactions between dissolved silica and carbonate minerals: an experimental study at $25 - 50^{o}C$. Chemical Geology 125 (1-2), 29–43.
URL http://www.sciencedirect.com/science/article/pii/0009254195000806

Kralj, D., Brecevic, L., Kontrec, J., Jun. 1997. Vaterite growth and dissolution in aqueous solution III. kinetics of transformation. Journal of Crystal Growth 177 (3=4), 248–257.
URL http://www.sciencedirect.com/science/article/pii/S0022024896011281

Krauskopf, K. B., 1979. Introduction to geochemistry, 2nd Edition. International series in the earth and planetary sciences. McGraw-Hill Book Company.

Labeyrie, J., Delibrias, G., Feb. 1964. Dating of old mortars by the carbon-14 method. Nature 201 (4920), 742–742.

Lakshtanov, L., Stipp, S., 2010. Interaction between dissolved silica and calcium carbonate: 1. spontaneous precipitation of calcium carbonate in the presence of dissolved silica. Geochimica et Cosmochimica Acta 74 (9), 2655–2664.
URL http://www.sciencedirect.com/science/article/pii/S0016703710000694

Lasia, A., 1999. Electrochemical impedance spectroscopy and its applications. In: Conway, B. E., Bockris, J., White, R. (Eds.), Modern Aspects of Electrochemistry. Vol. 32. Kluwer Academic/Plenum Publishers, pp. 143–248.
URL http://pirg.ch.pw.edu.pl/instrukcje/eis_extensive_introduction.pdf

Lawrence, R. M., Mays, T. J., Rigby, S. P., Walker, P., D'Ayala, D., Jul. 2007. Effects of carbonation on the pore structure of non-hydraulic lime mortars. Cement and Concrete Research 37 (7), 1059–1069.
URL http://www.sciencedirect.com/science/article/pii/S0008884607001020

Leslie, A., Hughes, J., 2002. Binder microstructure in lime mortars: implications for the interpretation of analysis results. Quarterly Journal of Engineering Geology and Hydrogeology 35, 257–263.

Lin, Y.-P., Singer, P. C., 2009. Effect of Mg^{2+} on the kinetics of calcite crystal growth. Journal of Crystal Growth 312 (1), 136–140.
URL http://www.sciencedirect.com/science/article/pii/S0022024809008781

Liu, Q., Spears, D., Liu, Q., 2001. MAS NMR study of surface-modified calcined kaolin. Applied Clay Science 19 (1-6), 89–94.
URL http://www.sciencedirect.com/science/article/pii/S0169131701000576

Loewenthal, R., Marais, G., 1978. Carbonate chemistry of aquatic systems. Theory and application. Vol. 1. Ann Arbor Science.

Lopez-Arce, P., Gomez-Villalba, L., Martinez-Ramirez, S., de Buergo, M. A., Fort, R., 2011. Influence of relative humidity on the carbonation of calcium hydroxide nanoparticles and the formation of calcium carbonate polymorphs. Powder Technology 205 (1-3), 263–269.
URL http://www.sciencedirect.com/science/article/pii/S0032591010005127

Lopez-Arce, P., Gomez-Villalba, L., Pinho, L., Fernandez-Valle, M., de Buergo, M. A., Fort, R., 2010. Influence of porosity and relative humidity on consolidation of dolostone with calcium hydroxide nanoparticles: effectiveness assessment with non-destructive techniques. Materials Characterization 61 (2), 168–184.
URL http://www.sciencedirect.com/science/article/pii/S1044580309003532

Loste, E., Wilson, R. M., Seshadri, R., Meldrum, F. C., 2003. The role of magnesium in stabilising amorphous calcium carbonate and controlling calcite morphologies. Journal of Crystal Growth 254 (1-2), 206–218.
URL http://www.sciencedirect.com/science/article/pii/S0022024803011539

Lower, S. K., 1999. Carbonate equilibria in natural waters. A Chem1 Reference Text.
URL http://www.chem1.com/acad/webtext/pdf/c3carb.pdf

Lurio, J. L. D., Frakes, L., 1999. Glendonites as a paleoenvironmental tool: implications for early cretaceous high latitude climates in Australia. Geochimica et Cosmochimica Acta 63 (6-7), 1039–1048.

URL http://www.sciencedirect.com/science/article/pii/S0016703799000198

Ma, Y., Gao, Y., Feng, Q., Oct. 2010. Effects of pH and temperature on $CaCO_3$ crystallization in aqueous solution with water soluble matrix of pearls. Journal of Crystal Growth 312 (21), 3165–3170.
URL http://www.sciencedirect.com/science/article/pii/S002202481000504X

Manahan, S. E., 2000. Chimica dell'ambiente, italian Edition. Piccin.

Mannoni, T., Giannichedda, E., 2003. Archeologia della produzione.

Marchese, B., 1980. Non-crystalline $Ca(OH)_2$ in ancient non-hydraulic lime mortars. Cement and Concrete Research 10 (6), 861–864.
URL http://www.sciencedirect.com/science/article/pii/0008884680900149

Margalha, M. G., Silva, A. S., Veiga, M. d. R. V., de Brito, J., Ball, R. J., Allen, G. C., 2012. Microstructural changes of lime putty during ageing. Journal of Materials in Civil Engineering 10 (1061).

Martinez-Ramirez, S., Frias, M., 2011. Micro-raman study of stable and metastable phases in metakaolin/$Ca(OH)_2$ system cured at 60^oC. Applied Clay Science 51 (3), 283–286.
URL http://www.sciencedirect.com/science/article/pii/S0169131710004151

Marzaioli, F., Lubritto, C., Nonni, S., Passariello, S., Capano, M., Terrasi, F., 2011. Mortar radiocarbon dating: preliminary accuracy evaluation of a novel methodology. Analytical Chemistry 83 (6), 2038–2045.

Mascolo, G., Mascolo, M. C., Vitale, A., Marino, O., 2010. Microstructure evolution of lime putty upon aging. Journal of Crystal Growth 312 (16-17), 2363–2368.
URL http://www.sciencedirect.com/science/article/pii/S0022024810003465

Matsushita, I., Suzuki, T., Moriga, T., Ashida, T., 1993. XPS study on the carbonation process of $Ca(OH)_2$. Journal of the Ceramic Society of Japan 101 (6), 725–727.

McCarter, W., Garvin, S., Bouzid, N., 1988. Impedance measurements on cement paste. Journal of Materials Science Letters 7 (10), 1056–1057.

McCarter, W., Starrs, G., Chrisp, T., 2002. Structure and performance of cements. SPON, London, Ch. Electrical monitoring methods in cement science.

McCormac, F., Hogg, A., Blackwell, P., Buck, C., Higham, T., Reimer, P., 2004. Shcal04 southern hemisphere calibration 0 - 1000 cal BP. Radiocarbon 46, 1087–1092.

Mcdonald, J., 1992. Impedance spectroscopy. Annals of Biomedical Engineering 20, 298–305.
URL http://jrossmacdonald.com/jrmpubs/187ImpSpectroscopy.pdf

Meldrum, F. C., Hyde, S. T., 2001. Morphological influence of magnesium and organic additives on the precipitation of calcite. Journal of Crystal Growth 231 (4), 544–558.
URL http://www.sciencedirect.com/science/article/pii/S0022024801015196

Mettler Toledo AG, Apr. 2013. A guide to pH measurement. theory and practice of laboratory pH applications. Printed in Switzerland, Schwerzenbach, Switzerland.

Micheletto, E., 2013. La cattedrale di Alba. Archeologia di un cantiere dall'eta' paleocristiana al XV secolo. All'Insegna del Giglio, Florence.

Mittermayr, F., Baldermann, A., Kurta, C., Rinder, T., Klammer, D., Leis, A., Tritthart, J., Dietzel, M., 2013. Evaporation - a key mechanism for the thaumasite form of sulfate attack. Cement and Concrete Research 49 (0), 55–64.
URL http://www.sciencedirect.com/science/article/pii/S0008884613000574

Montes-Hernandez, G., Fernandez-MartÃnez, A., Charlet, L., Tisserand, D., Renard, F., May 2008. Textural properties of synthetic nano-calcite produced by hydrothermal carbonation of calcium hydroxide. Journal of Crystal Growth 310 (11), 2946–2953.
URL http://www.sciencedirect.com/science/article/pii/S0022024808001425

Moorehead, D., 1986. Cementation by the carbonation of hydrated lime. Cement and Concrete Research 16 (5), 700–708.
URL http://www.sciencedirect.com/science/article/pii/000888468690044X

Moranville, M., Kamali, S., Guillon, E., 2004. Physicochemical equilibria of cement-based materials in aggressive environments-experiment and modeling. Cement and Concrete Research 34 (9), 1569–1578, <ce:title>H. F. W. Taylor Commemorative Issue</ce:title>.

URL http://www.sciencedirect.com/science/article/pii/S0008884604002091

Morgan, R., Ball, R. J., Oct. 2013. Environmental (wet and dry) cycling of hydraulic lime mortars. Journal of the Building Limes Forum 20, 21–31.

Moropoulou, A., Bakolas, A., 1995. Characterization of ancient, byzantine and later historic mortars by thermal and X-ray diffraction techniques. Thermochimica Acta 269/270 (0), 779–795.
URL http://www.sciencedirect.com/science/article/pii/0040603195025715

Moropoulou, A., Bakolas, A., 2000. Physico-chemical adhesion and cohesion bonds in joint mortars imparting durability to the historic structures. Construction and Building Materials 14 (1), 35–46.
URL http://www.sciencedirect.com/science/article/pii/S0950061899000458

Moropoulou, A., Bakolas, A., Aggelakopoulou, E., 2004. Evaluation of pozzolanic activity of natural and artificial pozzolans by thermal analysis. Thermochimica Acta 420 (1-2), 135–140, a collection of papers from the 6th Mediterranean Conference on Calorimetry and Thermal Analysis.
URL http://www.sciencedirect.com/science/article/pii/S0040603104002369

Morse, J., Mackenzie, F., 1990. Geochemestry of sedimentary carbonates. No. 48 in Developments in Sedimentology. Elsevier Science Publisher B.V.

Morsy, M., Alsayed, S., Salloum, Y., 2012. Development of eco-friendly binder using metakaolin-fly ash-lime-anhydrous gypsum. Construction and Building Materials 35, 772–777.
URL http://www.sciencedirect.com/science/article/pii/S0950061812003467

National Lime Association, no date. Properties of typical commerical lime products. [Accessed: 06 June 2013]. Available at: $http://www.lime.org/documents/lime_basics/lime-physical-chemical.pdf$.

Nawrocka, D. M., 2012. Radiometric Dating. InTech, Prague.

Nebel, H., Neumann, M., Mayer, C., Epple, M., 2008. On the structure of amorphous calcium carbonates. a detailed study by solid-state NMR spectroscopy. Inorganic Chemistry 47 (17), 7874–7879, pMID: 18665585.
URL http://pubs.acs.org/doi/abs/10.1021/ic8007409

Nehrke, G., Van Cappellen, P., Jan. 2006. Framboidal vaterite aggregates and their transformation into calcite: a morphological study. Journal of Crystal Growth 287 (2), 528–530.
URL http://www.sciencedirect.com/science/article/pii/S0022024805014016

Norman, D., 1961. A history of building materials. Phoenix House, London.

Oates, J., 1998. Lime and limestone: chemistry and technology, production and uses. Wiley-VCH, Weinheim.

Ogino, T., Suzuki, T., Sawada, K., 1990. The rate and mechanism of polymorphic transformation of calcium carbonate in water. Journal of Crystal Growth 100 (1-2), 159–167.
URL http://www.sciencedirect.com/science/article/pii/002202489090618U

Ottonello, G., 1996. Principi di geochimica. Zanichelli Editore S.p.A.

Pachiaudi, C., Marechal, J., Van Strydonck, M., Dupas, M., Dauchot-Dehon, M., 1986. Isotopic fractionation of carbon during CO_2 absorption by mortar. Radiocarbon 28 (2A), 691–697.

Pamplona, M., Kocher, M., Snethlage, R., Barros, L. A., Sep. 2007. Drilling resistance: overview and outlook. Zeitschrift der Deutschen Gesellschaft fur Geowissenschaften 158 (3), 665–679.

Pankow, J. K., 1991. Aquatic chemistry concepts. Lewis Publisheds.

Park, W. K., Ko, S.-J., Lee, S. W., Cho, K.-H., Ahn, J.-W., Han, C., May 2008. Effects of magnesium chloride and organic additives on the synthesis of aragonite precipitated calcium carbonate. Journal of Crystal Growth 310 (10), 2593–2601.
URL http://www.sciencedirect.com/science/article/pii/S0022024808000754

Parkhurst, D., Appelo, C., 2013. Description of input and examples for PHREEQC version 3A computer program for speciation, batch-reaction, one-dimensional transport, and inverse geochemical calculations: U.S. Geological Survey Techniques and Methods. Vol. 6. Ch. A43, p. 497.
URL http://pubs.usgs.gov/tm/06/a43/

Pesce, G., 2006. Optimization of the thermal activation of kaolin used as hydraulic additive for air lime. influence of partial pressure of water on the reactivity of metaka-

olin. Phd thesis, Department of Construction, Town planning and Materials Engineering of the University of Genoa (Italy).

Pesce, G., Sep. 2010. Radiocarbon dating of lumps of no completely mixed lime in old constructions: the sampling problem. In: Proceedings of 2nd Historic Mortar Conference. InTech, Prague.

Pesce, G., Ball, R., Quarta, G., Calcagnile, L., 2012. Identification, extraction and preparation of reliable lime sample for the C^{14} dating of plasters and mortars with the method of pure lime lumps. Radiocarbon 54 (3-4), 933–942.

Pesce, G., Quarta, G., Calcagnile, L., D'Elia, M., Cavaciocchi, P., Lastrico, C., Guastella, R., 2009. Radiocarbon dating of lumps from aerial lime mortars and plasters: methodological issues and results from the S. Nicoló of Capodimonte church (Camogli, Genoa - Italy). Radiocarbon 51 (2), 867–872.

Pesce, G., Ricci, R., 2008. The use of metakaolinite as a hydraulic agent of aerial lime plasters and mortars. the case study of Genoa (Italy). In: Proceedings of the 1st Historical Mortars Conference - HMC08 - Characterization, Diagnosis, Conservation, Repair and Compatibility.

Pokrovsky, O., Mar. 1998. Precipitation of calcium and magnesium carbonates from homogeneous supersaturated solutions. Journal of Crystal Growth 186 (1-2), 233–239.
URL http://www.sciencedirect.com/science/article/pii/S0022024897004624

Pu, Q., Jiang, L., Xu, J., Chu, H., Xu, Y., Zhang, Y., 2012. Evolution of pH and chemical composition of pore solution in carbonated concrete. Construction and Building Materials 28 (1), 519–524.
URL http://www.sciencedirect.com/science/article/pii/S0950061811005265

Putnis, A., Austrheim, H., 2013. Mechanisms of metasomatism and metamorphism on the local mineral scale: the role of dissolution-reprecipitation during mineral re-equilibration. In: Metasomatism and the Chemical Transformation of Rock. Lecture Notes in Earth System Sciences. Springer Berlin Heidelberg, pp. 141–170.

Rashad, A. M., 2013. Metakaolin as cementitious material: History, scours, production and composition. a comprehensive overview. Construction and Building Materials 41 (0), 303–318.
URL http://www.sciencedirect.com/science/article/pii/S0950061812009543

Rattazzi, A., 2007. Conosci il grassello di calce? Origine, produzione, impiego del grassello di calce in architettura, nell'arte e nel restauro. Edicom Edizioni, Monfalcone.

Reddy, M., Nancollas, G., Aug. 1976. The crystallization of calcium carbonate: IV. the effect of magnesium, strontium and sulfate ions. Journal of Crystal Growth 35 (1), 33–38.
URL http://www.sciencedirect.com/science/article/pii/0022024876902402

Reimer, P., Baillie, M., Bard, E., Bayliss, A., Beck, J., Bertrand, C., Blackwell, P., Buck, C., Burr, G., Cutler, K., Damon, P., Edwards, R., Fairbanks, R., Friedrich, M., Guilderson, T., Hogg, A., Hughen, K., Kromer, B., McCormac, G., Manning, S., Bronk Ramsey, C., Reimer, R., Remmele, S., Southon, J., Stuiver, M., Talamo, S., Taylor, F., Van der Plicht, J., Weyhenmeyer, C., 2004. Intcal04 terrestrial radiocarbon age calibration, 0-26 cal kyr BP. Radiocarbon 46 (3), 1029–1058.

Reimer, P. J., Baillie, M. G. L., Bard, E., Bayliss, A., Beck, J. W., Blackwell, P. G., Bronk Ramsey, C., Buck, C. E., Burr, G. S., Edwards, R. L., Friedrich, M., Grootes, P. M., Guilderson, T. P., Hajdas, I., Heaton, T. J., Hogg, A. G., Hughen, K. A., Kaiser, K. F., Kromer, B., McCormac, F. G., Manning, S. W., Reimer, R. W., Richards, D. A., Southon, J. R., Talamo, S., Turney, C. S. M., van der Plicht, J., Weyhenmeyer, C. E., 2009. Intcal09 and marine09 radiocarbon age calibration curves, 0-50,000 years cal BP. Radiocarbon 51 (4), 1111–1150.

Ren, D., Feng, Q., Bourrat, X., 2011. Effects of additives and templates on calcium carbonate mineralization in vitro. Micron 42 (3), 228–245.
URL http://www.sciencedirect.com/science/article/pii/S0968432810002192

Ritchie, I. m., Xu, B.-A., 1990. The kinetics of lime slaking. Hydrometallurgy 23, 377–396.

Rocha, J., Klinowski, J., 1990a. ^{29}Si and ^{27}Al magic-angle-spinning NMR studies of the thermal transformation of kaolinite. Physics and Chemistry of Minerals 17 (2), 179–186.

Rocha, J., Klinowski, J., 1990b. Kaolinite as a convenient standard for setting the hartmann-hahn match for ^{29}Si MAS NMR of silicates. Journal of Magnetic Resonance (1969) 90 (3), 567–568.
URL http://www.sciencedirect.com/science/article/pii/002223649090062E

Rodriguez-Blanco, J. D., Shaw, S., Benning, L. G., 2008. How to make 'stable' ACC: protocol and preliminary structural characterization. Mineralogical Magazine 72 (1), 283–286.

Rodriguez-Blanco, J. D., Shaw, S., Benning, L. G., 2011. The kinetics and mechanisms of amorphous calcium carbonate (ACC) crystallization to calcite, viavaterite. Nanoscale 3, 265–271.

Rodriguez-Navarro, C., Cazalla, O., Elert, K., Sebastian, E., 2002. Liesegang pattern development in carbonating traditional lime mortars. Proceedings of the Royal Society of London. Series A: Mathematical, Physical and Engineering Sciences 458 (2025), 2261–2273.
URL http://rspa.royalsocietypublishing.org/content/458/2025/2261.abstract

Rodriguez-Navarro, C., Hansen, E., Ginell, W. S., 1998. Calcium hydroxide crystal evolution upon aging of lime putty. Journal of American Ceramic Society 81 (11), 3032–3034.

Rojas, M. F., de Roja, M. S., 2003. The effect of high curing temperature on the reaction kinetics in MK/lime and MK-blended cement matrices at 60^oC. Cement and Concrete Research 33 (5), 643–649.
URL http://www.sciencedirect.com/science/article/pii/S0008884602010402

Roy, A., Bhattacharya, J., 2010. Synthesis of $Ca(OH)_2$ nanoparticles by wet chemical method. Micro and Nano Letters 5 (2), 131–134.

Salvadori, B., L., D., 2001. Synthesis of $Ca(OH)_2$ nanoparticles from diols. Langmuir 17, 2371–2374.

Serrapede, M., Denuault, G., Sosna, M., Pesce, G. L., Ball, R. J., 2013. Scanning electrochemical microscopy: Using the potentiometric mode of SECM to study the mixed potential arising from two independent redox processes. Analytical Chemistry 85 (17), 8341–8346.

Sheng Han, Y., Hadiko, G., Fuji, M., Takahashi, M., Mar. 2006. Crystallization and transformation of vaterite at controlled pH. Journal of Crystal Growth 289 (1), 269–274.
URL http://www.sciencedirect.com/science/article/pii/S0022024805012893

Shih, S.-M., Ho, C.-S., Song, Y.-S., Lin, J.-P., 1999. Kinetics of the reaction of $Ca(OH)_2$ with CO_2 at low temperature. Industrial & Engineering Chemistry Research 38 (4), 1316–1322.

Sibilia, E., 2010. Analisi di termoluminescenza, (TL) cattedrale di alba. Tech. rep., Dating Centre of the University Milano Bicocca, Laboratory of Archaeometry, Milan.

SINT Technology, s., Jan. 2014. DRMs - drilling resistance measurement system. Checked in January 2014.
URL http://www.sint-technology.com/drilling_resistance_measurement_system.asp

Sonninen, E., Junger, H., 2001. An improvement in preparation of mortar for radiocarbon dating. Radiocarbon 43 (2A), 271–273.

Spanos, N., Koutsoukos, P. G., Aug. 1998. The transformation of vaterite to calcite: effect of the conditions of the solutions in contact with the mineral phase. Journal of Crystal Growth 191 (4), 783–790.
URL http://www.sciencedirect.com/science/article/pii/S0022024898003856

Stuiver, van der Plicht, 1998. Calibration issue. Radiocarbon 40 (3).

Stuiver, M., Kra, R. e., 1986. Calibration issue. proceedings of the 12^{th} international ^{14}C conference. No. 28(2B) in Radiocarbon. pp. 805–1030.

Stuiver, M. A., Long, A., Kra, R., 1993. Calibration issue. Radiocarbon 35 (1).

Subbrizio, M., 2013. La cattedrale di Alba. Archeologia di un cantiere dall'eta' paleocristiana al XV secolo. All'Insegna del Giglio, Ch. Lo scavo archeologico.

Sugiyama, D., 2008. Chemical alteration of calcium silicate hydrate (C-S-H) in sodium chloride solution. Cement and Concrete Research 38 (11), 1270–1275.
URL http://www.sciencedirect.com/science/article/pii/S0008884608001373

Tai, C. Y., Chen, F.-B., 1998. Polymorphism of $CaCO_3$, precipitated in a constant-composition environment. AIChE Journal 44 (8), 1790–1798.

Tonellato, M., no date. Introduzione alla spettroscopia NMR, last access: September 2013.
URL http://www.pianetachimica.it/NMR

Tracy, S., Francois, C., Jennings, H., Oct. 1998a. The growth of calcite spherulites from solution: I. experimental design techniques. Journal of Crystal Growth 193 (3), 374–381.
URL http://www.sciencedirect.com/science/article/pii/S002202489800520X

Tracy, S., Williams, D., Jennings, H., Oct. 1998b. The growth of calcite spherulites from solution: II. kinetics of formation. Journal of Crystal Growth 193 (3), 382–388.
URL http://www.sciencedirect.com/science/article/pii/S0022024898005211

Tucker, M. E., Wright, V. P., 1992. Carbonate sedimentology. Blackwell Scientific Publications.

Ugge', S., 2013. La cattedrale di Alba. Archeologia di un cantiere dall'eta' paleocristiana al XV secolo. All'Insegna del Giglio, Ch. Il fonte battesimale.

Van Balen, K., 2005. Carbonation reaction of lime, kinetics at ambient temperature. Cement and Concrete Research 35 (4), 647–657.
URL http://www.sciencedirect.com/science/article/pii/S0008884604002753

Van Balen, K., Gemert, D., 1994. Modelling lime mortar carbonation. Materials and Structures 27 (7), 393–398.

van der Weijden, R., van der Heijden, A., Witkamp, G., van Rosmalen, G., Jan. 1997. The influence of total calcium and total carbonate on the growth rate of calcite. Journal of Crystal Growth 171 (1-2), 190–196.
URL http://www.sciencedirect.com/science/article/pii/S0022024896004873

Van Strydonck, M., Dupas, M., Dauchot-Dehon, M., Pachiaudi, C., Marechal, J., 1986. The influence of contaminating (fossil) carbonate and the variations of $\delta^{13}C$ in mortar dating. Radiocarbon 28 (2A), 702–710.

Van Strydonck, M., Van der Borg, A., De Jong, E., 1992. Radiocarbon dating of lime fractions and organic material from buildings. Radiocarbon 34 (3), 873–879.

Vecchiattini, R., 2010. La civilta' della calce. Storia, scienza e restauro. De Ferrari, Genova.

Vimer, C., Yu, S., Ghandehari, M., Feb. 2009. Probing pH levels in civil engineering materials. Journal of Materials in Civil Engineering 21 (2), 51–57.

Visser, J., no date. Influence of the carbon dioxide concentration on the resistance to carbonation of concrete. Construction and Building Materials (0).
URL http://www.sciencedirect.com/science/article/pii/S095006181301026X

Volpe, R., Taglieri, G., Daniele, V., Del Re, G., 2012. Procedimento per la sintesi di nanoparticelle di ca(oh)2 mediante processo a scambio ionico.

Vucak, M., Peric, J., Pons, M., Chanel, S., Jan. 1999. Morphological development in calcium carbonate precipitation by the ethanolamine process. Powder Technology 101 (1), 1–6.

Wada, N., Yamashita, K., Umegaki, T., Mar. 1995. Effects of divalent cations upon nucleation, growth and transformation of calcium carbonate polymorphs under conditions of double diffusion. Journal of Crystal Growth 148 (3), 297–304.
URL http://www.sciencedirect.com/science/article/pii/0022024894008809

Walker, C. S., Savage, D., Tyrer, M., Ragnarsdottir, K. V., 2007. Non-ideal solid solution aqueous solution modeling of synthetic calcium silicate hydrate. Cement and Concrete Research 37 (4), 502–511.
URL http://www.sciencedirect.com/science/article/pii/S0008884606003140

Wang, Y., Babchin, J., Chernyi, L., Chow, R., Sawatzky, R., Feb. 1997. Rapid onset of calcium carbonate crystallization under the influence of a magnetic field. Water Research 31 (2), 346–350.
URL http://www.sciencedirect.com/science/article/pii/S0043135496002436

Watanabe, J., Akashi, M., Jul. 2009. Formation of various polymorphs of calcium carbonate on porous membrane by electrochemical approach. Journal of Crystal Growth 311 (14), 3697–3701.
URL http://www.sciencedirect.com/science/article/pii/S002202480900596X

Wei, H., Shen, Q., Zhao, Y., Wang, D., Xu, D., 2004. Crystallization habit of calcium carbonate in the presence of sodium dodecyl sulfate and/or polypyrrolidone. Journal of Crystal Growth 260 (3-4), 511–516.

Xu, X.-R., Cai, A.-H., Liu, R., Pan, H.-H., Tang, R.-K., Cho, K., Aug. 2008. The roles of water and polyelectrolytes in the phase transformation of amorphous calcium carbonate. Journal of Crystal Growth 310 (16), 3779–3787.

URL http://www.sciencedirect.com/science/article/pii/S002202480800403X

Yang, T., Keller, B., Magyari, E., Hametner, K., Gunther, D., 2003. Direct observation of the carbonation process on the surface of calcium hydroxide crystals in hardened cement paste using an atomic force microscope. Journal of Materials Science 38 (9), 1909–1916.

Zendri, E., Lucchini, V., Biscontin, G., Morabito, Z. M., 2004. Interaction between clay and lime in cocciopesto mortars: a study by ^{29}Si MAS spectroscopy. Applied Clay Science 25 (1-2), 1–7.
URL http://www.sciencedirect.com/science/article/pii/S0169131703001558

Part I.

Appendix

A. Radiocarbon dating of carbonated lime in historic mortars

A.1. Introduction

A.1.1. Radiocarbon and radiocarbon dating method

Radiocarbon dating is a measurement of the age of matter based on the comparison of the current radioactive carbon ^{14}C content with the initial amount of ^{14}C (Bowman, 1990).

Radioactive carbon ^{14}C (or, more simply, *radiocarbon*) is one of the three principal isotopes of carbon together with ^{13}C and ^{12}C [1]. Compared to the ^{13}C and ^{12}C stable isotopes, radiocarbon is unstable due to the excess of neutrons. Its instability results in a decay to nitrogen-14 (^{14}N). The decay produces emission of a weak β particle (an electron) due to the conversion of a neutron (n) into a proton (p), an electron (e^-; the particle emitted that is cause of the radioactivity) and an electron-type antineutrino ($\bar{\nu}_e$), as described by the following general equation of the β^- decay:

$$n \rightarrow p + e^- + \bar{\nu}_e \tag{A.1.1}$$

The decay of the radioactive carbon ^{14}C to ^{14}N is described by equation A.1.2 and on the right hand side of figure A.1[2]:

$$^{14}_{6}C \rightarrow ^{14}_{7}N + e^- + \bar{\nu}_e \tag{A.1.2}$$

In nuclear physics and nuclear chemistry, the time required on a probabilistic base for half of the unstable atoms to undergo radioactive decay is called *half-life*. The half-life of radiocarbon is 5730 years. This means that every 5730 years about half of of

[1] Carbon has 15 known isotopes, from ^{8}C to ^{22}C. Among these isotopes, only 2, ^{12}C and ^{13}C, are stable.

[2] Image taken from: http://en.wikipedia.org/wiki/File:Carbon_14_formation_and_decay.svg, modified.

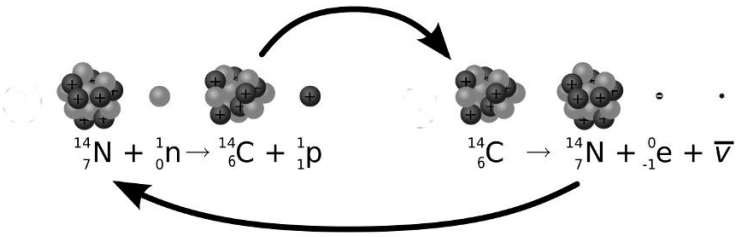

Figure A.1.: Formation and decay of radiocarbon.

the initial ^{14}C contained in a specimen decays into ^{14}N. In 11460 years, for instance, the amount of ^{14}C contained in a specimen is a quarter of the initial amount.

Radiocarbon is produced in the high atmosphere (upper layers of the troposphere and stratosphere) by the effect of cosmic rays on the ^{14}N. When the cosmic rays enter the atmosphere, they undergo various transformations, including the production of neutrons. These neutrons (^{1}n) take part in the reaction that convert the ^{14}N in ^{14}C, as described by equation A.1.3 and on the left hand side of figure A.1.

$$^{14}_{7}N + {}^{1}n \rightarrow {}^{14}_{6}C + {}^{1}p \tag{A.1.3}$$

Compared to the other isotopes, the amount of radiocarbon produced by the cosmic rays is relatively small. It has been calculated that 98.89% of the total carbon existing in the Earth's atmosphere is ^{12}C, 1.11% is ^{13}C and only 0.0000000001% is ^{14}C. This means that only one ^{14}C atom exists in nature for every 1,000,000,000,000 of ^{12}C atoms (1 in a trillion).

The ^{14}C formed in the atmosphere is rapidly oxidized to CO_2 so that through this molecule it easily enters in the normal chemical processes active on the Earth. For instance, plants continuously absorb atmospheric CO_2 through photosynthesis fixing the radiocarbon in their cells. Animals feed on plants and absorb in turn the radiocarbon. Humans eat animal meat absorbing themselves the radioactive carbon.

Despite the natural decay of radiocarbon that would lead to a reduction in the total amount of ^{14}C contained in living organisms, continuous absorption of CO_2 from the atmosphere allow them to constantly maintain the same level of ^{14}C in their structure. At their death, though, the assimilation process stops and the radioactive decay loss is no longer compensated by the intake of food. As a consequence, since its death, a living organism starts to lose radiocarbon atoms. Because the ^{14}C decays at a known rate, it is possible to know the age of the death of the organism by measuring its ^{14}C content and comparing this with the initial content (supposed corresponding to the ^{14}C contained in the atmosphere).

This method is called *radiocarbon dating* or simply *carbon dating*. The basic principle underlying it was first suggested by Professor Willar Libby who in the mid-1940

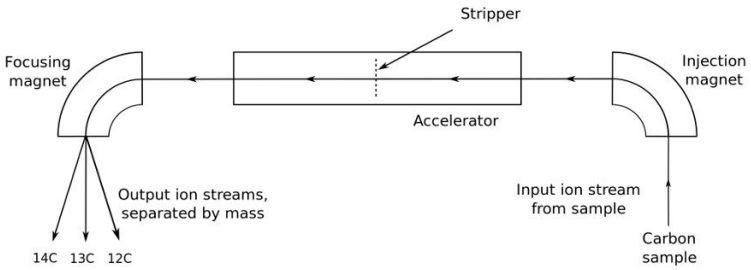

Figure A.2.: Simplified layout of an accelerator mass spectrometer.

realized that the decay of radioactive carbon could lead to a method for dating organic matter. In 1960 he received the Nobel Prize for his work in developing radiocarbon dating.

The equation governing the decay is reported in A.1.4 where N_0 is the number of radioactive atoms in the sample at time $t = 0$ and N_t is the number of atoms remained after time t. Lambda is a constant that depends on the isotope and is equal to the reciprocal of its mean-life[3].

$$N_t = N_0 \cdot e^{-\lambda t} \tag{A.1.4}$$

For the radioactive carbon this constant is 8267[4] so that the time t can be calculated as follows:

$$t = 8267 \cdot \ln \frac{N_0}{N_t} \tag{A.1.5}$$

A.1.2. Technique for measuring radiocarbon

At the beginning, the only way to measure the amount of ^{14}C contained in a sample was to detect the radioactive decay of individual carbon atoms (i.e. the electrons emitted). The technique was known as *beta counting* because what was detected was the number of β particles emitted by the decaying of ^{14}C.

In the late 1970s, however, an alternative technique became available thanks to the introduction of the Accelerator Mass Spectrometry (AMS). The AMS allowed the number of ^{14}C and ^{12}C atoms in a sample to be determined. For its use, the sample has to be in graphitic form which it is made to emit negatively charged C^- ions, which are subsequently injected into an accelerator (figure A.2[5]).

The accelerated ions are passed through a stripper which removes several electrons, so that only positive charged ions emerge. The C^{3+} ions are then passed through a

[3]The *mean-life* is the average time that a given atom survives before undergoing the radioactive decay.

[4]Mean-life and half-life of radiocarbon are related by the following equation: $T_{\frac{1}{2}} = \tau \cdot \ln 2$ where $T_{\frac{1}{2}}$ is the half-life and τ the mean-life.

[5]Image taken from: http://en.wikipedia.org/wiki/File:Accelerator_mass_spectrometer_schematic_for_radiocarbon.svg

magnet that curves their path: the heavier ions are curved less than the lighter ones so that different isotopes emerge as separate streams of ions.

Particle detectors measuring the electric current created in a Faraday cup are located at the end of the magnetic path to count and record the number of ions in the ^{14}C, ^{13}C and ^{12}C stream.

The method allows dating samples containing only a few milligrams of carbon, such as individual seeds but despite this sensitivity it is not yet possible to date materials older than about 50,000 years (approximately nine half-lives). The amount of radiocarbon still contained in the samples after such a long time is too small to be reliably measured with currently availalbe instruments (Bowman, 1990).

A.1.3. Calibration curve

Using equation A.1.5 it is assumed that the number of ^{14}C atoms at time 0 (that is N_0) is known and equal to the number of the ^{14}C atoms contained in the biosphere. It is also assumed that the number of ^{14}C atoms contained in the biosphere has been constant over time so that measuring the number of ^{14}C atoms in the sample at time t, easily allows calculation of the sample's age.

Unfortunately, the level of ^{14}C in the biosphere has varied significantly over time and, consequently, the results obtainable with the equation A.1.5, have to be corrected using a calibration curve.

Several sources can affect the radiocarbon content in the biosphere such as natural atmospheric variation, the impact of climatic cycles, the effect of human activity, fractionation of carbon isotopes and volcanoes. Effects of all these sources must be considered in the calibration curve (Bowman, 1990).

The main calibration curves that have been used to date are reported in table A.1[6] but for most applications with terrestrial material the IntCal04 curve should be used. Figure A.3[7] allows verification of the effect of radiocarbon calibration on the radiocarbon age. For instance, considering an object from 1300 A.D. (on the x axis), the calibrated range is likely to be between the 1290 A.D. and the 1400 A.D. (on the y axis).

A.2. Basic principles of radiocarbon dating of lime

A number of studies carried out over the last forty years describe the application of radiocarbon dating of lime mixtures such as mortars, plasters and renders (Labeyrie and Delibrias, 1964; Folk and Valastro, 1976; Pachiaudi et al., 1986; Van Strydonck

[6]Data from https://c14.arch.ox.ac.uk/embed.php?File=calibration.html

[7]This figure is published on Internet at URL: https://c14.arch.ox.ac.uk/embed.php?File=typical_cal.html

Table A.1.: List of calibration curves currently available.

Name	Reference
1986	Stuiver and Kra, 1986
1993	Stuiver et al., 1993
IntCal98	Stuiver and van der Plicht, 1998
Marine98	Stuiver and van der Plicht, 1998
IntCal04	Reimer et al., 2004
Marine04	Hughen et al., 2004
ShCal04	McCormac et al., 2004
IntCal09	Reimer et al., 2009
Marine09	Reimer et al., 2009

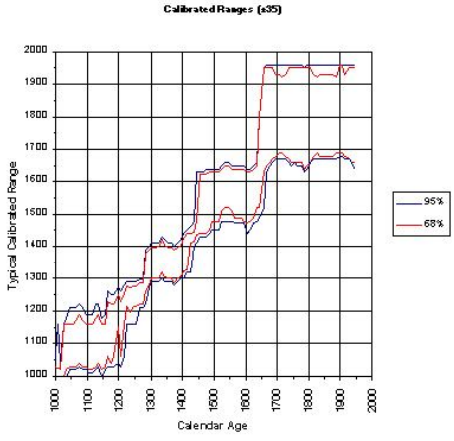

Figure A.3.: Effect of radiocarbon calibration on the radiocarbon age. Plot based on IntCal98, calibrated with OxCal using the probability method.

et al., 1992; Berger, 1992; Sonninen and Junger, 2001; Hale et al., 2003; Nawrocka, 2012). The basic principles of this particular application of the radiocarbon method were first suggested in a short paper published in the *Nature* in 1964 by Labeyrie and Delibrias. Here some of their words:

> "Old mortars are ordinarily composed of about 80 per cent by weight of coarse sand particles embedded in a matrix of calcium carbonate needles. Therefore, 1 Kg of mortar contains about 90 g of carbon dioxide, which has been incorporated through diffusion process from the ambient atmosphere when the mortar has been prepared. The carbon dioxide capture process lasts about one week after the moment when lime and sand have been mixed with water. From this moment the proportion of carbon-14 in the carbon of the calcium carbonate needles must decrease in the same way as it does after death in plants or animals, and therefore building constructed with these mortars can possibly be dated by the usual carbon-14 method" (Labeyrie and Delibrias, 1964, p.742)

To understand the basic principle of this application it is necessary first consider the lime manufacturing process.

Traditional lime is produced from limestone according to the description provided in the section 3.1. Because of the thermal treatment, carbon contained in the structure of the original limestone leaves the solid phase as gas so that at the end of the thermal process no carbon is contained in the quicklime.

Subsequently, the quicklime undergoes a slaking process described in equation 3.1.2 which, in the past, was mainly produced using an excess of water resulting in the formation of *lime putty*, one of the most widely used inorganic binders for construction.

Plasters, renders, mortars and other architectural parts were formed by mixing the lime putty with sand and, if the case, other additives.

When in place, the $Ca(OH)_2$ within the mixtures hardens by carbonation resulting in the formation of new $CaCO_3$. As the carbon that binds to the calcium during this reaction originates from the atmosphere, the $CaCO_3$ contained in the hardened mixture reflects the atmospheric radiocarbon concentration at the time of hardening. Equations 2.1.1-2.1.6 describe the hardening process of lime emphasizing the dissolution process of atmospheric CO_2 in water. As already stated, in this system, equation 2.1.1 represents the dissolution in water of atmospheric $CO_{2(g)}$ containing 1×10^{-12} parts of ^{14}C. In the meantime, solid $Ca(OH)_2$ dissolves in water forming calcium and hydroxyl ions (equation 2.1.5) and, depending on several factors, a solid $CaCO_3$ phase with specific mineralogical characteristics precipitates by reaction between Ca^{2+} and CO_3^{2-} (equation 2.1.6). In this manner the ^{14}C atoms contained in the atmosphere at the time of hardening are trapped in the structure of $CaCO_3$.

At the end of the carbonation process, the carbon (and with it also the radiocarbon) is fixed in the structure of $CaCO_3$ and it cannot be replaced by new radioactive atoms. The acquisition process stops and the radioactive decay loss is not compensated by the intake of new carbon. As a consequence, since the end of the carbonation, a lime based mixture starts to lose radiocarbon atoms and the material can be dated with the radiocarbon method.

Because the $CaCO_3$ precipitation (i.e. the hardening process of lime) occurs at the same time of construction, the radiocarbon dating of mortars is, potentially, the most reliable technique for dating old constructions (other techniques currently used to date old building are based on the use of the organic matter that can be contained within the mortars. Unfortunately, very often the relation between this matter and the mortars is not known).

A.2.1. Drawbacks and limitations

Contamination from $^{14}C-dead$

Despite the fact that the radiocarbon dating of mortars is very simple in principle, several studies have highlighted various practical challenges and factors that must be considered (Van Strydonck et al., 1986).

These arise mainly from the fact that currently is impossible to separate the $CaCO_3$ produced by the hardening process of lime from the $CaCO_3$ contained in other sources within the mortars. Sample contamination with carbonaceous substances can be due to several factors such as presence of incompletely burnt pieces of limestone[8] or aggregates of fossil origin including limestone sand.

Carbonate rocks are mainly made of $CaCO_3$ that, at the beginning of the sedimentary process, contained all the carbon isotopes contained in the earths' atmosphere at the time of the precipitation. However, in contrast to the carbon contained in the lime mixtures which have a lifetime shorter than the radiocarbon's half-life, the $CaCO_3$ of geological origin comes from times far earlier than that equivalent to the decay time of radiocarbon. This means that the carbon contained in carbonate rocks is $^{14}C-dead$ and, consequently, any piece of carbonate rock contained in a mortar sample (such as grains of carbonate sand or pieces of under burned limestone) can affect the result of radiocarbon dating.

Presence of aggregate grains or pieces of stones would not be a problem if a technique for separating them from the lime was available. Unfortunately, even if under the microscope it is possible to distinguish between the lime and the aggregate, from a practical point of view, their separation is almost impossible when both are made of

[8] These are pieces of the same stone used to produce the lime that have not been completely decomposed during the thermal process used to produce the quicklime.

$CaCO_3$.

The only case when this separation is praticable is when the aggregate is made of quartz. In contrast to $CaCO_3$, in fact, quartz does not dissolve in hydrochloric acid (HCl) or phosphoric acid (H_3PO_4) and, consequently, dissolving a lime based mortar containing quartz aggregate in acid allows capture of carbon as gaseous CO_2 as shown in equation A.2.1.

$$CaCO_{3(s)} + 2HCl_{(aq)} \rightarrow CaCl_{2(aq)} + H_2O_{(l)} + CO_{2(g)} \tag{A.2.1}$$

The CO_2 released by the acid dissolution is then transformed in the graphite useful for the isotope counting by AMS. However, this case is not frequent and, besides, there still remains the problem of under burned pieces of stone that can be contained in the mixture and behave in a similar manner of the binder under acid attack.

Over the time, improved methodologies based on the acid dissolution have been developed to separate the lime contained in the mortars from the aggregate but, despite all efforts, there still remains some uncertainties in the results of the radiocarbon dating (Folk and Valastro, 1976; Van Strydonck et al., 1986; Sonninen and Junger, 2001).

These techniques are based on complex processes that divide the carbonated lime from the aggregate contained within the mortar by mechanical and chemical separation (Heinemeier et al., 2010; Marzaioli et al., 2011). Initially the mortar is gently crushed with a pestle and mortar, and sieved using increasingly fine mesh widths up to <100 microns (typically 46-75 microns). Following the mechanical separation the resulting particles are analyzed to verify presence of contaminants.

If the sample does not contain contaminants, chemical separation is obtained by pouring 85% phosphoric acid over the powder under vacuum. Theoretically, since the carbonated lime dissolves easier than limestone (Heinemeier et al., 2010, p.174), it is possible to collect the CO_2 produced by the dissolution of the binder without contamination from the CO_2 produced by dissolution of $CaCO_3$ of geological origin. The dissolution process, in fact, starts out quite violently, at the beginning liberating CO_2 from the carbonated lime. Successively, the reaction slows down and the dissolution of geological carbonate begins (although it is impossible to recognize when the binder dissolution stops and when the dissolution of aggregate begins).

The gas produced is collected cryogenically in glass vials in 5 successive fractions (figure A.4) that are dated separately in order to create a profile age of the sample (figure A.5). Because the higher reactivity, it is supposed that the CO_2 produced by the dissolution of the carbonated lime is represented better in the first carbonation fraction collected (Heinemeier et al., 2010, p.174).

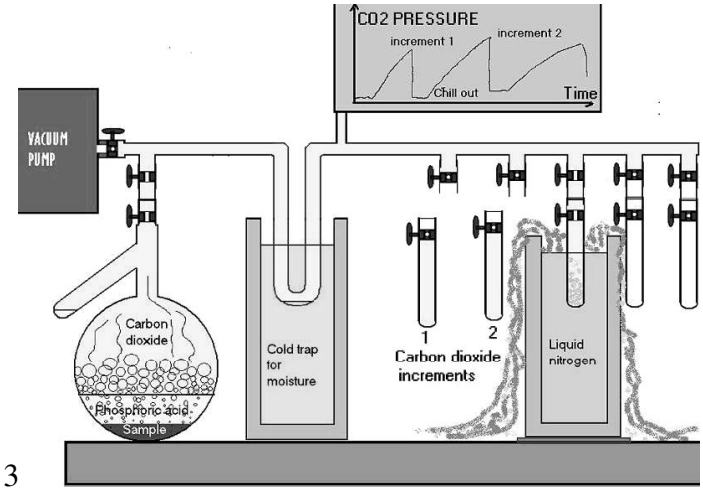

Figure A.4.: Chemical separation of CO_2 in fractions (from: Heinemeier et al., 2010, p.176).

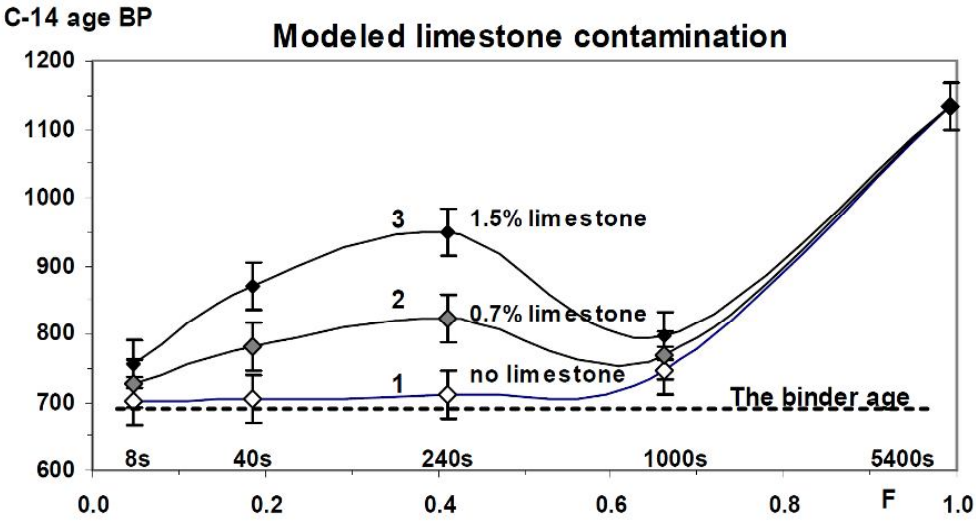

Figure A.5.: Modeled ^{14}C profiles showing the effect of limestone contamination. The sample age is set 700 before present. (from: Heinemeier et al., 2010, p.177).

Dissolution and re-precipitation of $CaCO_3$

The previous statement about the immutability of carbon contained in the $CaCO_3$ phases precipitated during the hardening process of lime has exceptions. Calcium carbonate, in fact, is soluble in water (even though its solubility is quite low) and this means that sometimes the carbonated lime contained in building materials can be affected by a process of dissolution and re-precipitation. This process leads to an exchange of carbon atoms that has a negative effect on the radiocarbon dating results (Karkanas, 2007).

Typical water sources that can produce this process are: rain (that affect mainly renders and also mortars, if the building is in a state of disrepair), ground water aquifer (mainly affecting foundation and ground floor flooring) and rising dump (mainly for plasters, renders, and mortars).

The dissolution process of of $CaCO_3$ can be described by equation 3.3.1 that shows that, once in solution, the Ca^{2+} is free from the previous bond with the carbonate ion and thus can react with new CO_3^{2-} in the same manner as described in equation 2.1.6, to produce new $CaCO_3$. However, in this case the carbon population dissolved in solution can be made of both, atoms from the dissolved $CaCO_3$ and atoms from the atmosphere.

In the latter case, it must be considered that the carbon concentration in the atmosphere at the dissolution time of the lime is different from the carbon concentration at the lime hardening time. For this reason, the radiocarbon dating of a lime mortar containing even a small amount of re-precipitated $CaCO_3$ can be affected by errors due to the radiocarbon contents of the new $CaCO_3$ phases.

To avoid this problem, the samples can be analyzed before submission to the laboratory were the radiocarbon counting is carried out. Re-precipitated $CaCO_3$ in lime mixtures can be recognized with several tehcniques such as cathodoluminescence (Gliozzo and Memmi Turbanti, 2006; Heinemeier et al., 2010), X ray diffraction and infrared spectroscopy.

Delay in the hardening process of lime

Labeyrie' statement that the CO_2 capture process of lime lasts about a week is not proved. Carbonation, in fact, as already seen is a very slow process that depends on several factors such as temperature, moisture content and pore structure. Since all these factors are quite changeable from site to site and also inside the same site, the hardening time of lime mortars can be variable.

Carbonation can stop if the environment becomes too dry, too wet or if the CO_2 access is inhibited (Van Balen, 2005; Cizer et al., 2012b). Under these conditions carbonation can only start again following a change in the conditions such as crack

formations caused by carbonation shrinkage. Scientific investigations of old buildings have already highlighted that the inner part of thick walls, such as the city walls, can contain $Ca(OH)_2$ centuries after their construction (Marchese, 1980; Moropoulou and Bakolas, 1995).

As a consequence of the delayed carbonation, it is obvious that the results of radiocarbon dating of old lime mortars depend not only on the purity of the samples but also on the depth of the sample within the analyzed structure. For this reason, superficial samples are more desirable than deep samples.

In this case, however, the sampling procedure should avoid mortars applied after the construction of the main structure such as joint sealing mortars whose date (although technically correct) are later than the building time of the main structure.

Renders and plasters are not likely to be affected by the problem of delayed carbonation because in direct contact with the atmosphere and their porous structure that permits an efficient diffusion of CO_2. However, in this case, it must be verified that these layers, often considered expendable surfaces, have not been subject to demolition and reconstruction. If this has happened, obviously, their radiocarbon age cannot be assumed as the radiocarbon age of the structure but more simply as the date of the re-plastering.

A.3. The *pure lime lumps* technique

Despite the above mentioned limitations, recent studies have shown that adoption of a special sampling procedure based on the careful selection of lumps of incompletely mixed lime, seems to provide an interesting alternative that avoids problems associated with contamination.

This technique has already been discussed at an international level in several occasions (e.g. Gallo et al., 1998; Fieni, 2002) and the more recent publications on this subject describe the results achieved using the latest sampling methodologies, together with the limitations and drawbacks (Pesce, 2010; Pesce et al., 2009, 2012).

The founding principle of this technique is the use of lumps of pure lime instead of generic pieces of mortar. These lumps are quite common in the lime mixtures predating mechanical mixing and are thought to originate from imperfect mixing of lime and sand during the building process. Previous sampling methods did not discriminate between pure lumps and contaminated samples. As pure lumps contain the same lime as that used in other parts of the mixtures but are free of contaminants (such as sand grains or under burned pieces of limestone), they can dramatically reduce the errors in radiocarbon dating.

Figure A.6.: Traditional tool for slaking the lime in the north west of Italy

A.3.1. Lime lumps: formation, characteristics, sampling problems and treatments

It is known that during the older manufacturing process of lime mortars, some lumps of lime not mixed with sand, could remain embedded within the mortars (Franzini et al., 1990; Bruni et al., 1997; Bakolas et al., 1995; Bugini and Toniolo, 1990). At that time, the slaking process was assisted by a continuous manual mixing carried out with specific tools (figure A.6). Once the quicklime was completely dissolved, the lime putty was then filtered and stored in pits dug in the ground or immediately mixed with sand and other materials to produce mixtures such as mortars, plasters and renders (Adam, 1999; Oates, 1998; Vecchiattini, 2010; Rattazzi, 2007). During this process, some small lumps of lime could remain compact and fail to intimately mix with the sand grains (probably because they were not well slaked or mixed[9]) even though they were able to combine with the atmospheric CO_2 in the same manner as the remaining matrix.

According to some research, composition of these lumps is similar to that of the surrounding matrix (Franzini et al., 1990; Bruni et al., 1997; Bakolas et al., 1995) with only differences in micro-morphology[10]. In particular, the matrix of the mortar surrounding the lumps appear to be more compact and with smaller pores compared to the surrounding matrix. Furthermore, in many cases the growth of the crystals in the matrix is greater than that in the lumps (Bakolas et al., 1995; Bugini and Toniolo, 1990, p.814).

Unfortunately, the pure lime lumps are not the only lumps contained in the old mor-

[9] There is not a general agreement about the formation process of these lumps but the above mentioned hypothesis is one of the most common (Bugini and Toniolo, 1990).

[10] For this reason, some authors hypothesize that crystals in these lumps developed over a shorter time period compared to the crystals of the matrix (Bruni et al., 1997).

tars. The internal structure of historic lime mixtures has been found to contain at least five different types of lump, each of which can be recognized individually. These comprise:

- unburned (or under-burned) pieces of limestone (Ingham, 2005; Elsen, 2006; Leslie and Hughes, 2002);
- over burned pieces of limestone (Leslie and Hughes, 2002; Ingham, 2005; Elsen, 2006; Elsen et al., 2004);
- pieces of burned limestone containing high concentrations of silica (these arise when the stone used for the lime production contains a high quantity of impurities; Elsen et al., 2004; Bakolas et al., 1995);
- concretion of re-carbonated lime;
- lumps of pure $CaCO_3$ produced by the carbonation of pure lime putty (Leslie and Hughes, 2002; Franzini et al., 1990; Bugini and Toniolo, 1990; Ingham, 2005; Elsen, 2006; Elsen et al., 2004; Bakolas et al., 1995).

Among these types only the lumps belonging to the latter group are suitable for radiocarbon dating. Over-burned pieces of lime, in fact, may have been subject to a delayed carbonation caused by the sintered CaO crystals contained in them that were less reactive with water and, consequently, slower to react with CO_2 (Elsen, 2006). Unburned pieces of limestone still contain CO_2 of geological origin (that, as previously discussed, can affect the radiocarbon dating result), while calcium contained inside the lumps of silica is mainly bonded to the silicon rather than to the CO_2 (Bakolas et al., 1995). Problems connected to the concretions have already been discussed previously.

Lumps of pure lime are easily recognizable as they exhibit a white, rounded and floury complexion (Fig. A.7). Surface hardness of these lumps is very low making them extremely delicate to handle and easily damaged. To facilitate extraction of these lumps from a mortar in an undamaged condition a two-step procedure is used:

1. on site sampling of a small amount of mortar containing the lump;
2. extraction of suitable pure lime lumps for the laboratory analysis.

The on site sampling procedure

On site sampling must be tailored to reduce problems arising from the re-carbonation of lime described previously. Moreover, sampling should be carried out to accommodate the individual requirements of the structure from which the sample is taken. Buildings out of the ground, underground walls, fresco layers, mosaic substrate, all require slight variations in the technique.

Figure A.7.: Pure lime lumps in a specimen of air lime mortar (left hand side; scale bar: 1 cm) and detail of the same lime lump (right hand side).

When walls are build with ashlar, it can be difficult to reach the inner part of the structure and proceed with the sampling work, especially if the thickness of the mortar joints is not large enough to allow selection of suitable samples[11].

When the inner part of the masonry is accessible, it is always important to consider the possible re-carbonation of lime and the depth of the sample within the wall. Care is also needed to avoid unusual situations such as water pockets and mixtures non belonging to the original structure such as plasters applied after the construction of the wall.

When a suitable depth is reached, the lumps must be identified. The minimum amount of $CaCO_3$ required for a meaningful analysis by AMS is 20 milligrams. In the case that a single lump does not contain sufficient material, multiple lumps from the same area (i.e. from the same stratigraphic unit) can be used.

Sample extraction inside the laboratory

Following on site sampling and before treatment and analysis at the AMS laboratory, it is necessary to examine the samples under an optical stereo microscope to confirm the lump nature and mechanically remove particles of aggregate that may be still attached to the surface.

Very often, in fact, it is difficult to distinguish on site lumps of incompletely burnt limestone or grains of milky quartz from the pure lime lumps. However under a magnifying glass, even at low magnification, it is possible to distinguish between these types. The surfaces of lime lumps have a floury appearance (Fig. A.7 right hand side) while those of under burned lumps and quartz grains appear denser resembling stone.

Evaluation of the superficial hardness is a useful method for distinguishing between the different types of lump. Even performing a crude test, by hand, using a needle point, allows different types of lump to be effectively distinguished.

Following successful identification, all pieces of sand still attached to the surface of lumps must be removed using tools such as scalpels or needles. In order to remove as

[11] In some cases it is only possible to proceed if a cross section of the wall is accessible.

many pieces of sand as possible, the work should be done using a stereo microscope. Great care should be taken in this phase as the lumps are very delicate and easily damaged.

When the lumps are clean, they must be weighed to check that the mass matches the requirements for the radiocarbon dating process and stored in a box with rigid walls to avoid damage during transit to the laboratory.

Treatment at the AMS laboratory

At the AMS laboratory the pure lime lumps are processed using the standard treatment for carbonate. Upon arrival, the sample is analyzed using an optical microscope to double check for the presence of macro contaminants. If necessary, further mechanical cleaning is carried out. Once cleaned, samples are treated with hydrogen peroxide (H_2O_2) to chemically remove the outside layer.

Approximately half of the minimum amount of the pre-cleaned samples (by weight) is dried in an oven where it is also treated with H_2O_2 and converted to CO_2 using phosphoric acid (H_3PO_4). The CO_2 extracted from the sample is, then, reduced to graphite using hydrogen (H_2) in the presence of an iron powder catalyst. The graphite is finally pressed into tablets which are used as a target in the AMS for measurement of the carbon isotopic ratios (Pesce et al., 2009; CEDAD, 2011).

A.3.2. Previous applications of the *pure lime lumps* technique

In 2008 a detailed example of this sampling and dating method was presented during an international conference in Cyprus. This work involved the collection of two lime lumps from the apses of the medieval church of S. Nicolò of Campodimonte (Camogli, Genoa - Italy) and dating with the radiocarbon method. Results obtained were evaluated and compared with the radiocarbon dating of organic material collected in the same apses. Results of the radiocarbon dating were compared with the results of other dating methods (Pesce et al., 2009).

Prior to this test, relatively few researchers carried out radiocarbon dating of lime lumps in archaeological sites. Exceptions being Gallo, on the alto-Medieval castle of Aghinolfi (Massa Carrara – Italy; Gallo, 2001) and Fieni on the basilica of S. Lorenzo Maggiore in Milan (Italy; Fieni, 2002).

However, since 2008, additional tests have been made by the research group of the Institute for the History of Material Culture of Genoa (Italy). To date, a total of 30 samples taken from 10 different archaeological sites were dated following the procedure described earlier. In about 85% of cases, results were found to be consistent with the respective archaeological framework and uncertainty of radiocarbon dating

was often reduced by comparison with other archaeological information. In 14% of cases (circa) the results were archaeologically meaningless and this suggest that the technique still needs to be improved.

A.4. A study on the accuracy and precision of the results achievable with the *pure lime lumps* technique

In order to evaluate accuracy and precision of the results achievable with the *pure lime lump* technique, a test was carried out at University of Bath together with the Superintendence for the Archaeological Heritage of Piedmont (Italy)[12]. Although this technique has been applied several times with interesting results, in fact, until few years ago there was not yet clear evidence of the accuracy and precision of results achievable.

This test aimed to address this issue by dating 4 lumps of pure lime taken from the same construction and comparing the results among themselves (to evaluate the accuracy) and with the archaeological framework (to evaluate precision). The construction chosen was the baptismal font found during the archaeological excavation carried out inside the St. Lorenzo Cathedral of Alba (Turin, Italy). The small size of the construction, the availability of other archaeometric dating such as those produced by application of the thermoluminescence method to some ceramic materials, and the results of the archaeological excavation perfectly suited the requirements of this test.

A.4.1. The baptismal font of the St. Lorenzo Cathedral of Alba (Italy)

The St. Lorenzo Cathedral of Alba is a Romanesque church located in Alba (Cuneo, Piedmont), in the North West of Italy. The church was built on the site of a former structure, probably found at the end of the 5^{th} century A.D. and almost totally rebuild during the high middle ages. Currently it has a Latin cross with three naves and a late Gothic architectural style (Micheletto, 2013).

From 2007 to 2012 the church was subjected to renovation works and archaeological excavations that unearthed the remains of an octagonal baptismal font which remained in use until the late 12^{th} century. It is located in the southern nave of the existing cathedral where other remains of the Romanesque cathedral are located (figure A.8 and A.9).

[12]The Superintendence for the Archaeological Heritage is the local public administration in charge of the preservation of cultural heritage.

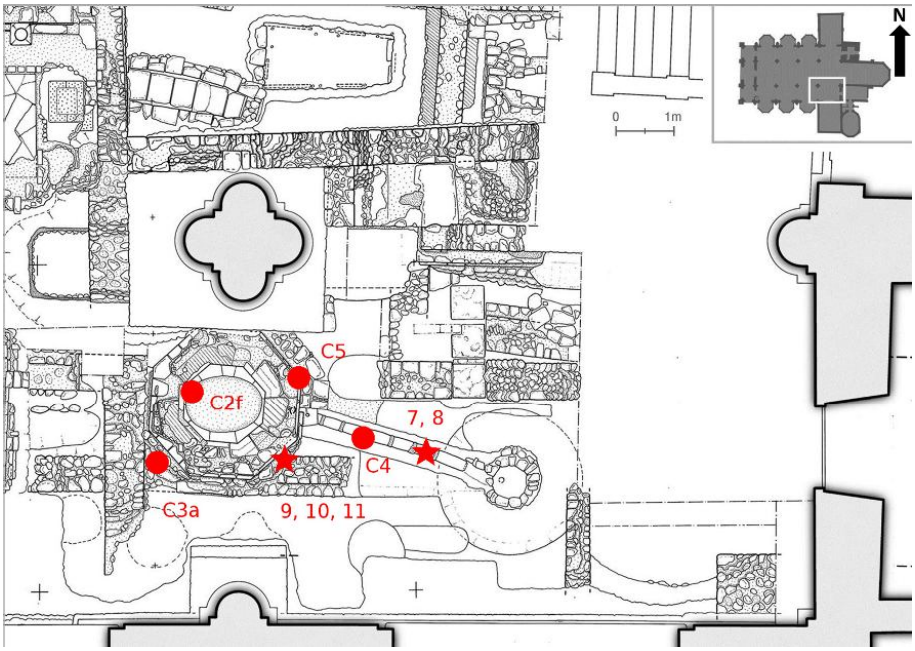

Figure A.8.: Saint Lorenzo Cathedral of Alba. Survey of the baptismal font with the drainage pipe (image from the archive of the Superintendence for the Archaeological Heritage of Piedmont and of MAE). Circles indicate the position of lime lumps while the star-shaped symbols indicate the location of the brick samples (samples n. 13, 22, 23 and 24 were taken in structures not included in this survey).

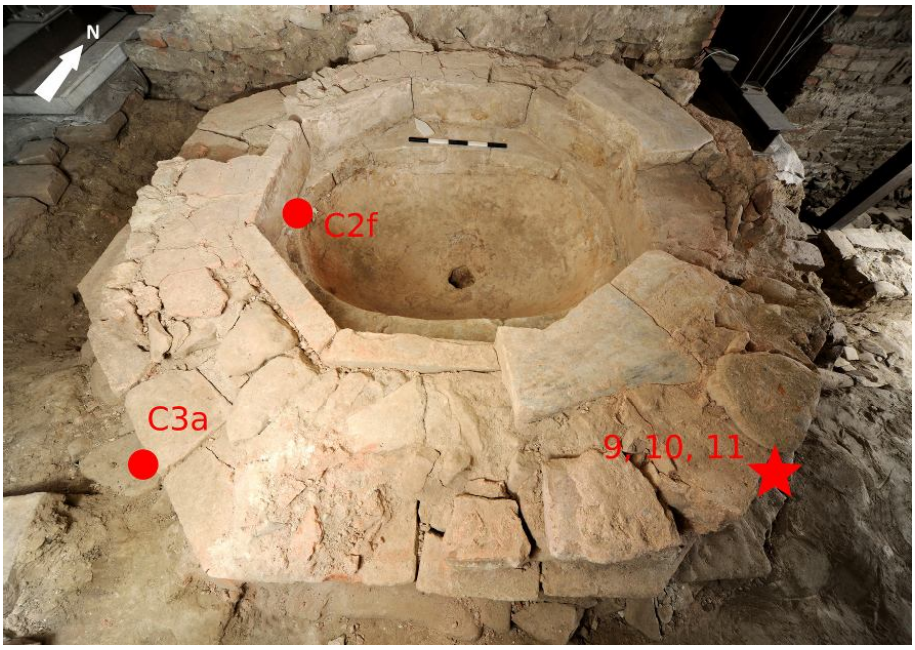

Figure A.9.: Image of the remains of the baptismal font (from: archive of the Superintendence for the Archaeological Heritage of Piedmont and of MAE). Circles indicate the position of some of the lime lumps while the star-shaped symbols indicate the location of some of the brick samples.

Figure A.10.: Octagonal perimeter of the baptismal font: detail of the special pattern called *en-chevron* scratched on the surface of some bricks (image from the archive of the Superintendence for the Archaeological Heritage of Piedmont and of MAE).

The archaeological excavation, in particular, revealed the lower part of the font and the related drainage pipe of water (Subbrizio, 2013; Ugge', 2013). The structure lays on a surface of about three square meters; each side of the octagon is about 110 cm wide. The structure was built using bricks, stones and lime mortar. The bricks have been laid on very thin layers of mortar, well refined when the lime was still wet. At the edges of the octagon, some specifically cut bricks were used for connecting the faces (figure A.9). The internal part of the baptismal font has an elliptical monolithic basin of red Verona marble of approximately 137 cm in length (semi-major axis), 100 cm width (semi-minor axis) and 40 cm deep, was surrounded by appropriately sized marble slabs. It is likely that the basin was part of an earlier Roman structure. A hydraulic plaster (the so called *cocciopesto*) made from air lime and brick powder covers the basins inner surface. The majority of bricks used in the font have sizes comparable with those of the Roman age that is 7 cm in thickness, 44 cm in length and width that, overall, reproduces the size of the so called *sesquipedales*, a roman modulus. Despite this clear identification of the bricks age the external faces of several bricks are carved with a special pattern called *en-chevron* that was widespread in the 10^{th} century (figure A.10).

In contrast, bricks used in other structures recovered during the same excavations such as a perimeter wall (stratigraphic unit USM 993) and the external side of the bell tower, were characterized by sizes more similar to the medieval modulus used since the 12^{th} century A.D. that is approximately 7 cm in thickness, 14 cm in width and 30 cm

Table A.2.: Supposed age for the different parts of the font where the lumps where sampled.

Specimen	Location	Supposed age
C2f	basin rim	From the end of the 6th century A.D. to the end of the 10th century A.D.
C3a	foundation	End of the 6th century A.D.?
C4	drainage pipe	From the end of the 6th century A.D. to the end of the 12th century A.D.
C5	mortar among the bricks with the *en-chevron* pattern	No later than the end of the 12th century A.D.

Table A.3.: Results of the radiocarbon dating and supposed age of the analyzed structure.

Specimen	Weight [mg]	$\delta^{13}C$ [o/ooo]	Uncalibrated age (B.P.)	Calibrated ages (cal A.D.)	Confidence level (partial data; %)	Confidence level
C2f	33	-32.0±0.5	1121±45	780-790	1.9	95.4
				800-1020	93.5	
C3a	109	-15.8±0.3	1154±40	770-990	95.4	
C4	86	-16.9±0.5	1188±50	760-980	83.7	95.4
				690-750	11.7	
C5	31	-20.5±0.5	1141±40	770-990	95.4	

in length (Greppi, 2013). Due to the inconsistency of these characteristics and because of the reduced volume of the remains, it was not possible to determine when the font was build and whether it was built in a single phase or more phases (e.g. if the font was modified during the time before the destruction). For these reasons archaeometric dating was required. According to the archaeological record, the font was supposed to be built between the end of the 6th century and the second half of the 12th century (table A.2), when the basin was filled up. In fact, due to a change in the baptismal ceremony and, consequently, to a change in the shape of the baptismal fonts, in the second half of 12th century, the structure was partially filled with rubble and modified according to the new needs. Among the other modifications also a new drainage pipe was built without destroying the original one. Within the previous mentioned range of time (6th-12th century A.D.), according to the *en chevron* pattern carved on the surfaces of the bricks, archaeologists supposed that the font could have been built during the 10th century A.D. but no other proof of this hypothesis was given.

A.4.2. Materials and method

Considering the available materials, the radiocarbon dating method was chosen to date the lime mortar used in the font and the thermoluminescence method was chosen

to verify the dating of bricks and pipes. For the radiocarbon dating, some lumps of pure lime were extracted from as many samples taken from the mortar used in different parts of the font and dated with the pure lime lumps technique. Each mortar sample was no more than a few cubic centimeters while the weights of the dated lumps are reported in table A.3.

Specimens were sampled in the mortar that binds the stones of the basin rim (sample C2f), in the foundation (sample C3a), in the mortar used beneath the original drainage pipe (sample C4) and in the mortar used among the bricks with the *en-chevron* pattern (sample C5). Sampling points (reported in figure A.8 and A.9) were agreed with the Superintendence for the Archaeological Heritage of Piedmont and were chosen to be as close to the surface structures as possible in order to reduce the delay in carbonation. Moreover, because of the continued presence of water in the structure (the baptismal font contained water during its use) specimens that clearly contained re-precipitated $CaCO_3$ were carefully avoided.

Before the removal of the lime lumps from the mortar samples, each specimen was analysed by the geologist Roberto Ricci in order to obtain the mineralogical characteristics of the mixes, useful to evaluate possible differences among the specimens and, consequently, to evaluate the radiocarbon dating results. Analyses were carried out at low magnification, using a Nikon SZM 800 stereo microscope and a fiber optic illuminator, on the specimens as they were taken from the archaeological site (i.e. without preparation). Results of the analyses showed that the mixture of the sample C2f contained air lime as the main binder phase and brick powder (*cocciopesto*) as the hydraulic additive. The sand, which had a poor particle size distribution, was taken from the river Po (mainly composed of quartz) with a maximum grain size of 1 millimeter. Several tiny lumps of pure lime were found inside the mixture. Mortar of the samples C3a, C4 and C5 contained air lime as binder and sand with a poor particle size distribution as aggregate, once again taken from the river Po. A high aggregate:binder ratio was observed as the maximum size of the grains that was evaluated to be about 1 millimeter. Several lumps of pure lime of a few millimeters diameter were found during the analysis.

Subsequently, the specimens were analyzed at University of Bath with a Leica Wild M3 stereo microscope for the identification and extraction of the pure lime lumps according to the technique previously described. Once isolated, the lumps were submitted for AMS ^{14}C dating at the Center for Dating and Diagnostic of the University of Salento (Lecce, Italy). The samples underwent the standard procedure used for carbonates and the obtained graphite was pressed in the target holders of the accelerator mass spectrometer for measurement of the carbon isotopic ratios. International Atomic Energy Agency (IAEA) C_6 sucrose standard with a nominal ^{14}C concentration of 150.61 pMC and C_1 Carrara marble with a nominal ^{14}C content of 0 pMC were used as stand-

Table A.4.: Results of the thermoluminescence dating (confidence interval 1σ; results of dating and methodology from: Sibilia, 2010).

Sample	Location	Dating (A.D.)	Dating average (A.D.)	Supposed age	Note
7	Drainage pipe	580±80	590±70	Roman age	
8	Drainage pipe	595±100		Roman age	
9	Foundation of the baptismal font	595±65	575±75	Roman age	
10	Foundation of the baptismal font	595±65		Roman age	
11	Foundation of the baptismal font	600±100		Roman age	
13^	USM 993	1030±60	1030±60	Medieval age	#12 not available
22	Bell tower, external	810±70	790±55	Medieval age	
23	Bell tower, external	790±95		Medieval age	
24	Bell tower, external	825±60		Medieval age	

ards for normalization and for estimation of the measurement and sample processing background, respectively. For the calibration of the ^{14}C dates OxCal Ver. 3.10 software was used.

To determine the production time of the bricks, some specimens (made of up to three pieces each) were taken and sent to the laboratory for thermoluminescence dating (TL). To verify differences in size and age, 9 samples including bricks and ceramic bodies of the old pipe were taken from the baptismal font and from other structures. In particular, specimen n. 7 and 8 (pipes) were taken in different parts of the drainage pipe of the baptismal font; specimen n. 9, 10 and 11 (bricks) in the foundation of the baptismal font; specimens 12 and 13 (bricks) in the wall US 993 and specimens 22-24 (bricks) in the external wall of the bell tower. The last three specimens, in particular, were characterized by the medieval modulus and, consequently, could have been used to evaluate the results of the thermoluminescence dating method applied to the bricks.

Thermoluminescence dating was carried out at the Dating Center – Laboratory of Archaeometry of the University Milano Bicocca (Milan - Italy) using the fine grain technique. Evaluation of the annual dose was performed using measurements of total α activity (contribution of Uranium and Thorium) and a flame photometric detector (contribute of Potassium) on the ceramic bodies. Contribution of environmental dose range was measured with the ionization chamber for environmental dosimeter. A water content of 80±20% of the saturation value was used for the data processing. All the information on thermoluminescence dating of these bricks is reported in Sibilia (2010).

A.4.3. Results and discussion

The radiocarbon dates of the mortars are reported in figure A.11-A.14 and summarized in table A.3. A graphical comparison of the results obtained with the two dating methods is reported in figure A.15.

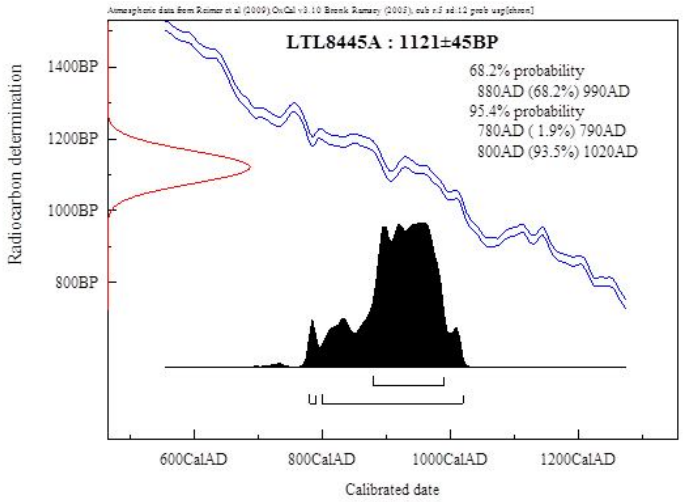

Figure A.11.: Results of the radiocarbon dating for the sample C2f.

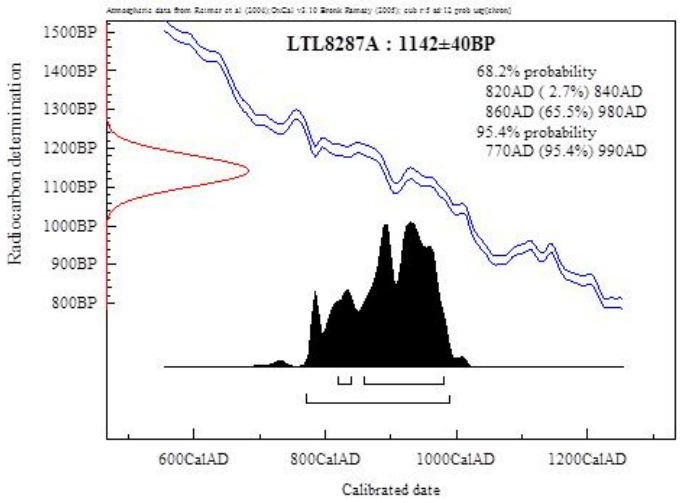

Figure A.12.: Results of the radiocarbon dating for the sample C3a.

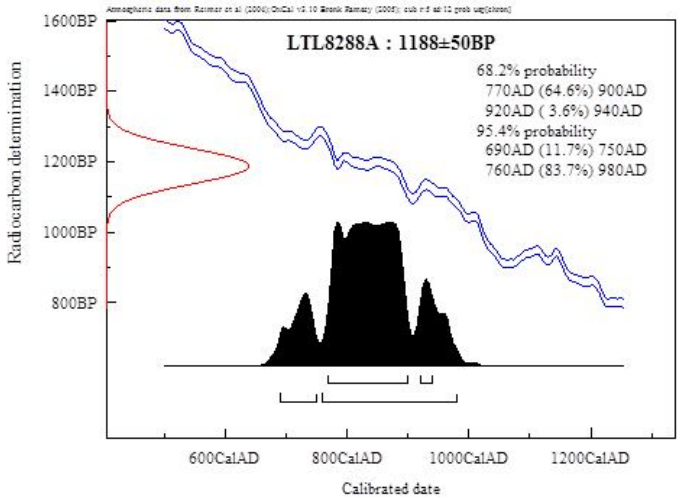

Figure A.13.: Results of the radiocarbon dating for the sample C4.

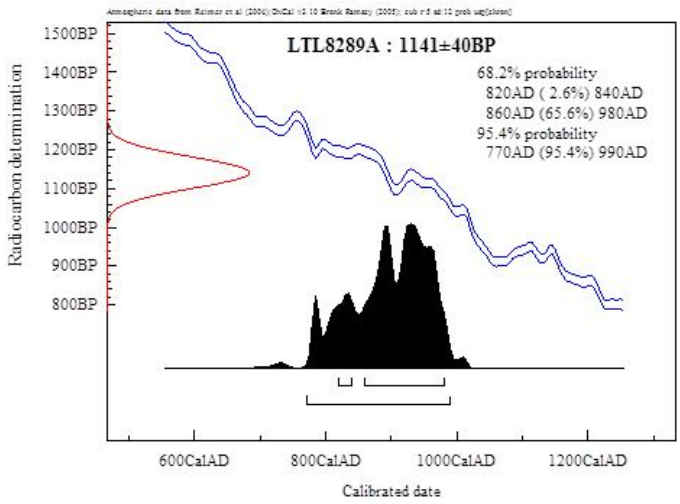

Figure A.14.: Results of the radiocarbon dating for the sample C5.

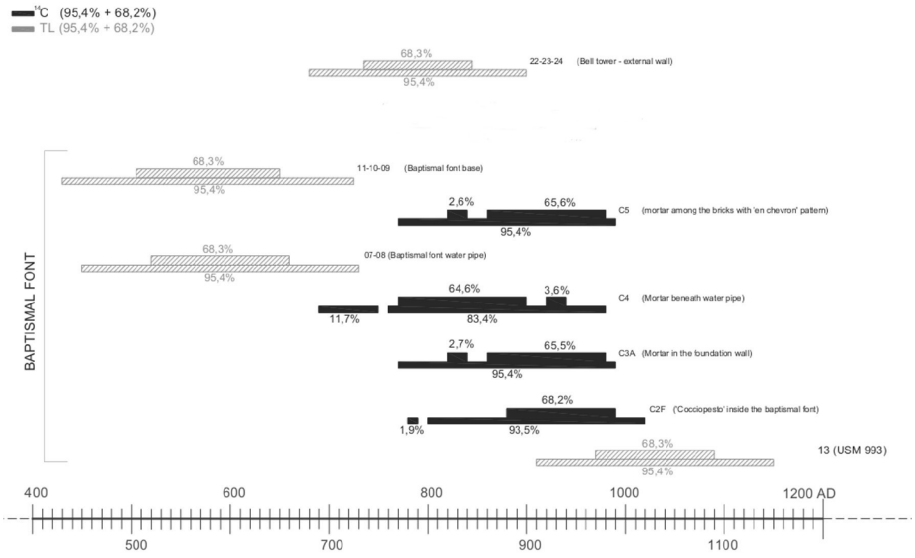

Figure A.15.: Graphical description of the results of the calibrated radiocarbon dating (black lines) and of dating of bricks obtained with the thermoluminescence method (dotted lines).

The results show that the calibrated radiocarbon dates are consistent and comprised between 690 and 1020 cal. A.D. A more careful observation of the data highlights that results of sample C4 are slightly anticipated compared to the others, whereas results of samples C3a and C5 have exactly the same radiocarbon age, very similar also to the radiocarbon age of C2f (figure A.15).

Consistency of the results suggests that a delay in the carbonation time due a delay in the penetration of CO_2 inside the mortars is unlikely as well as the effect of a dissolution and re-precipitation process of $CaCO_3$ due to the ground water or to the water originally contained in the font. In fact, even if one of these factors had taken place, the probability that the radiocarbon dating of the samples were so similar would have been extremely rare, considering the locations of the samples.

Results of the thermoluminescence dating with 1σ confidence level are reported in table A.4. According to these results, specimens 7, 8, 9, 10 and 11 are contemporaneous and dated to the 6^{th} century A.D. Different results were found for specimen 13 (11^{th} century A.D.; specimen 12 did not give results) and for the specimens 22-24 (end of the 8^{th} century A.D.). Considering the brick dimensions and the obtained results, it is possible to notice a correspondence between the bricks with Roman sizes and the thermoluminescence date. According to the thermoluminescence results in fact, the bricks with Roman modulus are actually connected with the late roman tradition whereas those with medieval modulus have been found produced later.

The thermoluminescence dates of the samples 7, 8, 9, 10 and 11 differ from the radiocarbon dates of the lime lumps; therefore, it is probable that the pipe and the bricks are older than the lime mortar binding them and likely reused. As discussed previously because a delay of about two centuries in the carbonation seems to be unlikely and because the radiocarbon dating of mortars is in agreement with the dating of the *en chevron* pattern, it is likely that the ceramic elements used in the baptismal font could have been actually reused from previous structures (or that an earlier structure could have been adapted later to the use as baptismal font). The reuse of bricks from earlier structures was a very common procedure in the past centuries, as already proved inside the cathedral itself and in many other places in the north of Italy. Confirmation of this result is the thermoluminescence dating of the bricks used in the external wall of the bell tower (specimens 22-24) and in the US 993. These bricks, in fact, have been dated to a time very similar to that of the lime lumps and their dimensions are in agreement with the dimension of the medieval modulus.

A.5. Conclusions

Consistency of the radiocarbon dating results and consistency of the results obtained from the mineralogical analyses of the mortar as well as the small size of the structure

suggest that the baptismal font of the Alba Cathedral was built in a single constructive phase between the 770 A.D. and 990 A.D. (the range of time where all the radiocarbon dating converge). Thermoluminescence dating suggests that the ceramic materials (bricks and pipes) used in the baptismal font were produced between the 500 and the 650 A.D. and reused later in the baptismal font when the *en-chevron* pattern was carved. A practice that, from an archaeological point of view, is typical of the 10^{th} century. For these reasons and considering also all the archaeological and historic record, it is possible to hypothesize that within the above mentioned range of time (770-990 cal A.D.), the most probable construction time of the baptismal font is the 10^{th} century A.D.

Overall, these tests highlight the accuracy and the precision of the radiocarbon dating results achievable with the pure lime lumps technique, that is not yet achievable by the other techniques used for the preparation of samples for the radiocarbon dating of lime mortars. Furthermore the results show that even the radiocarbon dating of a single lump produces reliable chronological information and this has a clear effect on the costs of the analysis (with the traditional technique for a single chronological date point, 5 individual gas samples should be dated).

Results achieved and experience gained to date highlight the importance and future potential of radiocarbon dating of pure lime lumps for historic constructions. Success of the method is dependent on following an appropriate sampling methodology which involves archaeological, chemical and physical knowledge of the building and of the materials being studied. Knowledge of the chemical, physical and mechanical processes involved in the carbonation reaction are of fundamental importance in the application and development of this technique.

Despite recent advances, in fact, the full potential of this technique is still to be discovered. Unknowns include the dating of mixtures containing hydraulic lime which accounts for a significant proportion of historic mortar. Re-carbonation of $CaCO_3$ is expected to affect the results of radiocarbon dating. However few studies have been carried out to address this phenomenon in lime lumps. To date, results applied to lime lumps do not suggest this problem, however their extraction from ruined walls of archaeological sites where the penetration of rising damp or rain is expected has not been carried out.

A.6. Acknowledgment

The author would like to thank the Superintendence for the Archaeological Heritage of Piedmont and of MAE for their help in this research. Help is acknowledged from Dr. Gianluca Quarta and Prof. Lucio Calcagnile at the Centre for Dating and Diagnostics, University of Salento (Lecce, Italy) and to all colleagues of the Institute of the History

of Material Culture of Genoa (Italy).

This thesis was mainly written using open source software. In particular, Lyx and MikTex were used to write and compose the whole document. JabRef was used to manage the bibliographic references. QtiPlot was used to plot the most part of the data. GIMP was used to elaborate the raster images and LibreOffice Draw was used to produce some of the vector images. A special thanks to all the contributors and developers that have been working on these beautiful pieces of software.